LEVEL II

VOLUME 1
AD-TR-81-38

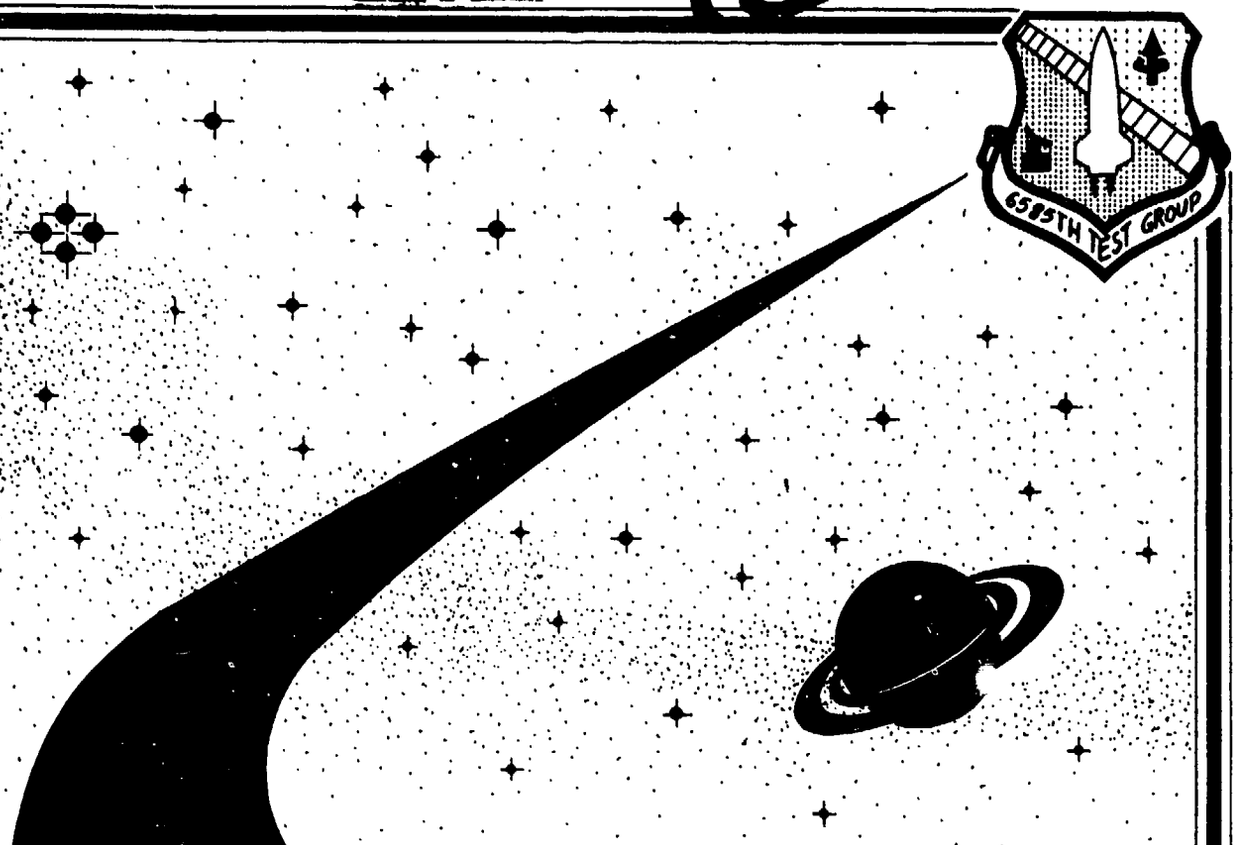

TENTH BIENNIAL GUIDANCE TEST SYMPOSIUM

7-9 OCTOBER, 1981

HOLLOMAN AFB, NEW MEXICO 88330

UNCLASSIFIED

SECURITY CLASSIFICATION OF THIS PAGE *(When Data Entered)*

REPORT DOCUMENTATION PAGE		READ INSTRUCTIONS BEFORE COMPLETING FORM
1. REPORT NUMBER AD-TR-81-38, VOLUME I	2. GOVT ACCESSION NO. AD-A107612	3. RECIPIENT'S CATALOG NUMBER
4. TITLE *(and Subtitle)* TENTH BIENNIAL GUIDANCE TEST SYMPOSIUM PROCEEDINGS		5. TYPE OF REPORT & PERIOD COVERED Symposium Proceedings 6. PERFORMING ORG. REPORT NUMBER
7. AUTHOR(s) As indicated on individual papers.		8. CONTRACT OR GRANT NUMBER(s)
9. PERFORMING ORGANIZATION NAME AND ADDRESS 6585th Test Group/GD Holloman AFB, New Mexico 88330		10. PROGRAM ELEMENT, PROJECT, TASK AREA & WORK UNIT NUMBERS
11. CONTROLLING OFFICE NAME AND ADDRESS 6585th Test Group/GD Holloman AFB, New Mexico 88330		12. REPORT DATE October 1981 13. NUMBER OF PAGES
14. MONITORING AGENCY NAME & ADDRESS*(if different from Controlling Office)*		15. SECURITY CLASS. *(of this report)* UNCLASSIFIED 15a. DECLASSIFICATION/DOWNGRADING SCHEDULE

16. DISTRIBUTION STATEMENT *(of this Report)*

DISTRIBUTION STATEMENT A
Approved for public release;
Distribution Unlimited

17. DISTRIBUTION STATEMENT *(of the abstract entered in Block 20, if different from Report)*

18. SUPPLEMENTARY NOTES

19. KEY WORDS *(Continue on reverse side if necessary and identify by block number)*

Test and Evaluation, Gyroscopes, Accelerometers, Inertial Guidance, Navigators, Modeling, and GPS

20. ABSTRACT *(Continue on reverse side if necessary and identify by block number)*

These proceedings contain papers included in the Tenth Biennial Guidance Test Symposium. This symposium, hosted by the Central Inertial Guidance Test Facility, is directed toward the exchange of information, stimulation of new ideas, and discussion of recent developments in the field of guidance testing. The papers presented include such topics as the use of the Global Positioning System, Aircraft Inertial Navigators, Component Evaluation, Advanced Guidance Methodology, Missile Guidance Systems, and Analysis Techniques. The included

DD FORM 1 JAN 73 1473

UNCLASSIFIED

SECURITY CLASSIFICATION OF THIS PAGE *(When Data Entered)*

Block 20 (Cont'd)

papers are those presented in the unclassified sessions of the symposium. Papers presented in the classified portions of the meeting are being published as Volume II.

Accession For	
NTIS GRA&I	☒
DTIC TAB	☐
Unannounced	☐
Justification	
By	
Distribution/	
Availability Codes	
Dist	Avail and/or Special
A	

AD-TR-81-38

VOLUME I

PROCEEDINGS OF THE
TENTH BIENNIAL GUIDANCE TEST SYMPOSIUM

Held At

HOLLOMAN AIR FORCE BASE, NEW MEXICO

Hosted By

6585TH TEST GROUP

CENTRAL INERTIAL GUIDANCE TEST FACILITY

7-9 OCTOBER 1981

FOREWORD

The Tenth Biennial Guidance Test Symposium was held at Holloman Air Force Base, New Mexico 7-9 October 1981. These symposia are hosted by the Central Inertial Guidance Test Facility (CIGTF). These meetings bring together approximately 300 people from industry, educational institutions, foreign governments, the Department of Defense, and other Government agencies. The goal is to provide a forum for the exchange of technical information and the stimulation of new ideas related to the testing of aided and unaided inertial guidance systems and components.

Many excellent papers were received for presentation at this meeting, but due to the time available, only a portion of those submitted could be included.

The paper selection committee, headed by Dr. F. F. Kuhn of the Central Inertial Guidance Test Facility, included Col R. E. Clark, USAF (Ret.), Systron-Donner Corp.; Dr. H. Sorenson, University of California at San Diego; Mr. D. R. McKanna, USAF Air Staff (Ret.); Col L. Sugerman, USAF (Ret.), Physical Science Laboratory, New Mexico State University; Mr. T. Sanders, Naval Air Development Center; Dr. H. Pastrick, Control Dynamics Company; Mr. Bob McAdory, Air Force Armament Test Laboratory; Lt Col Roger McLain, Ballistics Missile Organization; Dr. John Niemela, U. S. Army Avionics R&D Activity; Mr. Tom Reed, Charles Stark Draper Laboratory; and Lt Col Thomas Rowley, USAF Air Staff.

In addition to those listed above and the contributing

authors, a large number of people contributed to the success of this meeting and I wish to express my appreciation to each for his efforts. Special thanks go to our symposium manager, Mr. G. Mozer.

This document is published only for the exchange and stimulation of ideas. Its publication does not constitute Air Force approval of the documents' findings or conclusions.

Robert E. Beale

ROBERT E. BEALE, Colonel, USAF
Deputy Commander

ABSTRACT

These proceedings contain papers included in the Tenth Biennial Guidance Test Symposium. This symposium, hosted by the Central Inertial Guidance Test Facility, is directed toward the exchange of information, stimulation of new ideas and discussion of recent developments in the field of guidance testing. The papers presented include such topics as the use of the Global Positioning System, Aircraft Inertial Navigators, Component Evaluation, Advanced Guidance Methodology, Missile Guidance Systems, and [illegible] Techniques. The included papers are those presented in the unclassified sessions of the symposium. Papers presented in the classified portions of the meeting are being published as Volume II.

PROCEEDINGS

SESSION I - PERFORMANCE TRENDS - NANO g's AND NANORADIANS

SESSION II - PERFORMANCE TRENDS - NANO g's AND NANORADIANS

(CONTINUED)

SESSION III - CRUISE MISSILE AND AIDED GUIDANCE

SESSION IV - MODERN TESTBEDS AND SIMULATIONS

SLED TESTING OF THE MX ADP/AIRS SYSTEM - Eldon E. Peterson and Capt Robert S. Lawrence

PRECISION CENTRIFUGE TESTING USING AN ACCELERATION REFERENCE STANDARD - Kurt E. Steinke

DEVELOPMENT OF ROCKET SLEDS TO IMPLEMENT THE REVERSE VELOCITY TECHNIQUE FOR INERTIAL GUIDANCE SYSTEM TESTING - Jack E. Myers

A HARDWARE-IN-THE-LOOP SIMULATION FOR TESTING THE GUIDANCE, CONTROL, AND WARHEAD EQUIPMENT OF THE VOUGHT CORPORATION ASSAULT BREAKER MISSILE - Peter Schaar

SESSION V - AZIMUTH AND ERROR BUDGETS

AN INTEGRATED PROGRAM FOR DEVELOPMENT OF A LASER GYRO IMU WITH SUB-ARC SECOND AZIMUTH FINDING CAPABILITY - Jim Matthews, M. Gnese, T. Taylor and I. Smith

CONSTRUCTION OF APPROXIMATE ERROR BUDGETS FOR MULTIPLE COMPONENT GUIDANCE SYSTEMS - William J. Fitzpatrick

TITLE: PERFORMANCE TRENDS IN INERTIAL TECHNOLOGY

AUTHOR: ROBERT G. BROWN

R. G. BROWN ASSOCIATES, INC.
Topsfield, Massachusetts

PAPER NOT RECEIVED IN TIME FOR PUBLICATION

TITLE: DYNAMIC ANGULAR MEASUREMENT IN THE NANO-RADIAN RANGE

AUTHORS: HAROLD D. MORRIS
PHILIP D. FLANNER

SYSTRON-DONNER CORPORATION
Concord, California

and

ROBERT T. CALLAHAN

LOCKHEED MISSILES AND SPACE CO., INC.
Palo Alto, California

and

B. KATZ
G. BUKOW

CHARLES STARK DRAPER LABORATORY
Cambridge, Massachusetts

DYNAMIC ANGULAR MEASUREMENT IN THE NANORADIAN RANGE

A dynamic angular position transducer capable of measuring broadband angular motion in the nanoradian range is described. The inherent noise level of the device lies below 30 nanoradians (rms) in the 1 Hz to 1000 Hz band and reaches a noise floor of about 0.2 nanoradians (rms) per $\sqrt{Hz}$ above 40 Hz. The device's frequency response is essentially that of a second order high pass system rising at 12 dB per octave to a 2 Hz corner with flat response to 500 Hz thereafter. Test methods for noise determination and transfer function definition are presented, as well as a discussion of applications and projections of future developments in design and testing.

I. INTRODUCTION

Over the past several years, Systron Donner has continued the evolutionary development of a broadband Inertial Angular Displacement Sensor (IADS), the Model 8301,* which has now been shown capable of resolving angular displacements in the nanoradian range.

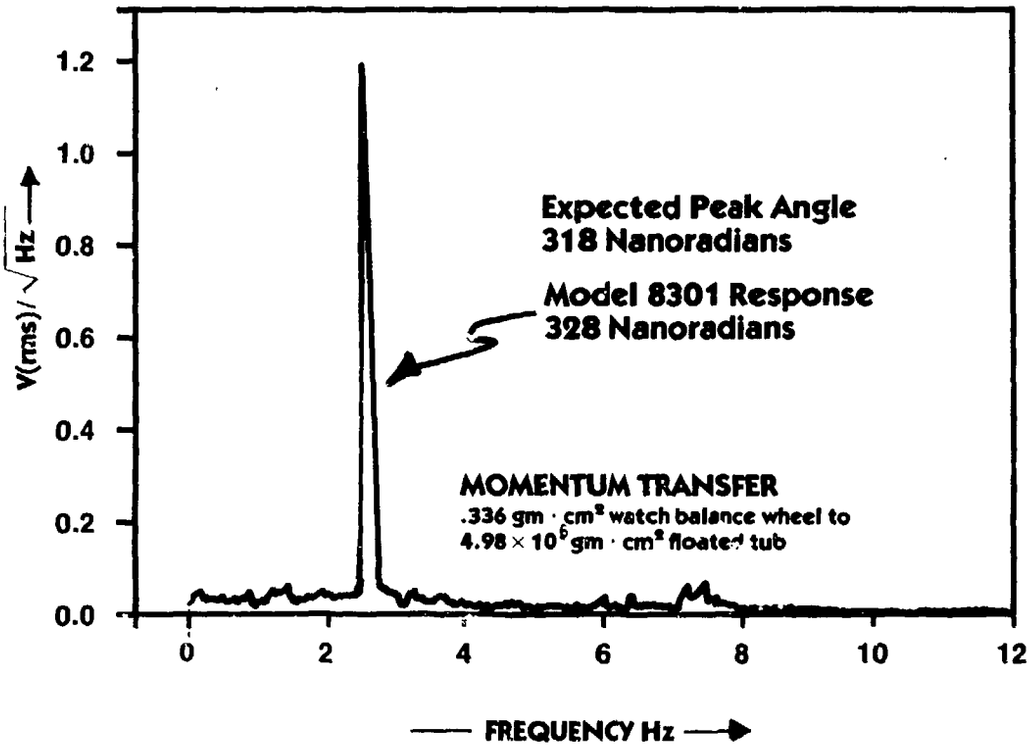

FIGURE 1

*The Model 8301 IADS is a proprietary development of the Systron Donner Corporation and is covered by one or more of the following U. S. Patents: 3,967,178; 3,967,064; 3,520,196; 3,321,753.

As a demonstration of this capability, an angular momentum transfer scheme was used to detect an estimated 318 nanoradian peak displacement at 2.5 Hz. The result is reproduced in Figure 1 above which reveals the transducer responded within about 3% of the expected value and clearly shows its ability to detect and resolve nanoradian angular disturbances. (Refer to Page 22 for a further description of the experiment.)

The transducer covered by this paper has a sensitivity of 1 Volt per microradian, an equivalent noise of less than 30 nanoradians rms and a pass band of 1 to 500 Hz.

The paper outlines the design of the transducer, describes methods of test (particularly noise level and transfer function determination), presents test results, discusses various applications, and closes with a review of future design directions and test methods.

II. DESIGN DESCRIPTION

The Model 8301 has evolved from a line of force balance, null position servo accelerometers. This transducer is essentially an angular accelerometer operated as an angular position transducer above the device's natural frequency, a technique commonly utilized in seismometry. In practice, the natural (or corner) frequency is usually set as low as possible to provide position measurements over a broad frequency band and to garner information as near zero frequency as practical. The current design of the 8301 has a corner frequency typically falling between 1.5 and 2.5 Hz, and work is continuing to lower that value into the tenths of a Hertz range.

The design is best described by reference to the transducer and servo block diagrams of Figures 2 and 3, respectively. When an input acceleration (or displacement) is applied to the transducer case, the enclosed moment of inertia, i.e., the tightly coupled vane and fluid ring, tends to remain stationary in inertial space. The case-mounted position sensors sense the rotation of the case about the vane and provide, through the detector electronics, a voltage proportional to the angular displacement which is amplified and scaled by the servo amplifier. The position voltage impressed across the torque coil creates a torquing current to restore the vane to its null position.

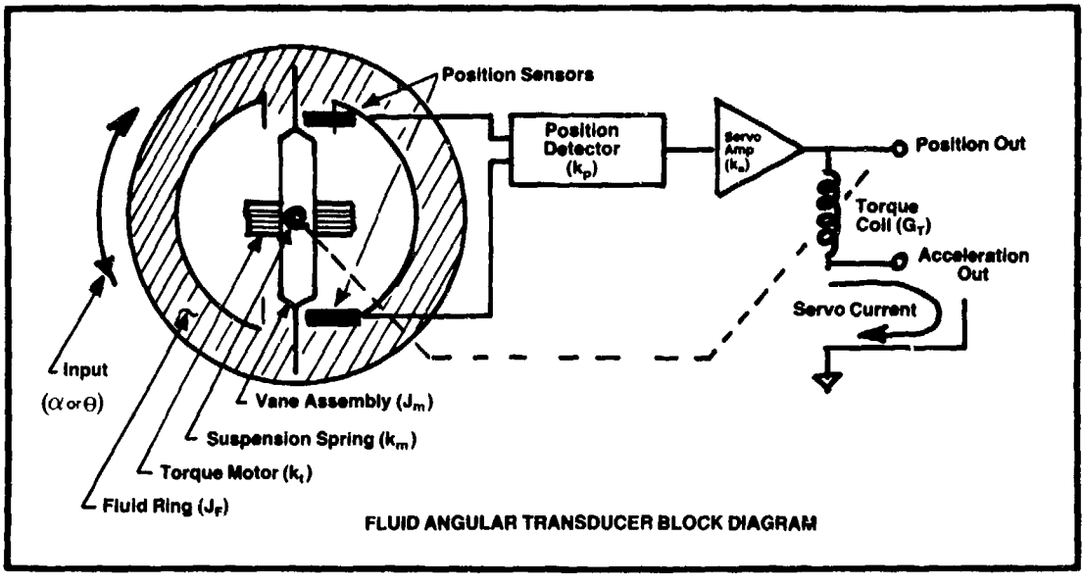

FIGURE 2

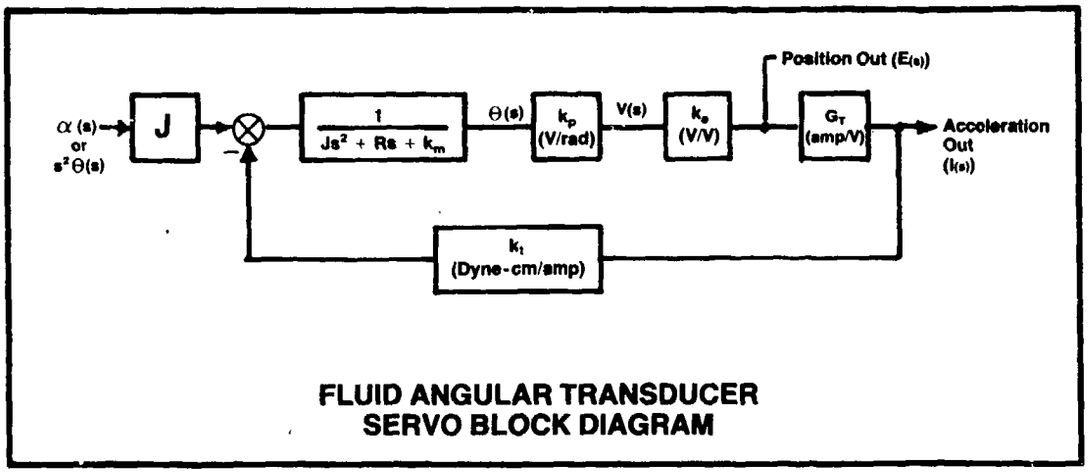

FIGURE 3

The current required to drive the vane back to null is proportional to the input angular acceleration. The transfer function to E(s) for input acceleration α(s) is

$$\frac{E(s)}{\alpha(s)} = \frac{k_p k_a}{s^2 + \frac{R}{J}s + \frac{\left(k_m + G_T k_T k_p k_a\right)}{J}} \qquad (1)$$

This is a transfer function for a simple second order system with a damping term

$$\frac{R}{J} = 2\zeta\omega_n \qquad (2)$$

and a natural frequency

$$\omega_n = \left\{\frac{k_m + G_T k_T k_p k_a}{J}\right\}^{\frac{1}{2}} \qquad (3)$$

Thus a Bode plot transfer function for constant amplitude acceleration input shows full response from dc to the second order corner ω_n followed by a 12 dB per octave roll-off above that corner. The transfer function to E(s) for input displacement $\theta(s)$ is identical except for an s^2 term in the numerator which results in a Bode plot rising at 12 dB per octave to the second order corner at ω_n and leveling off to a flat response above ω_n. The transducer behaves as an angular accelerometer below ω_n and an angular displacement sensor above ω_n. The transfer functions to I(s) are identical to those above except for a G_T term in the numerators. In practice, G_T is made very small in displacement sensors to provide a low natural frequency and a measure of I(s) becomes impractical.

The servo block diagram of the angular displacement sensor being discussed in this paper appears as Figure 4, below.

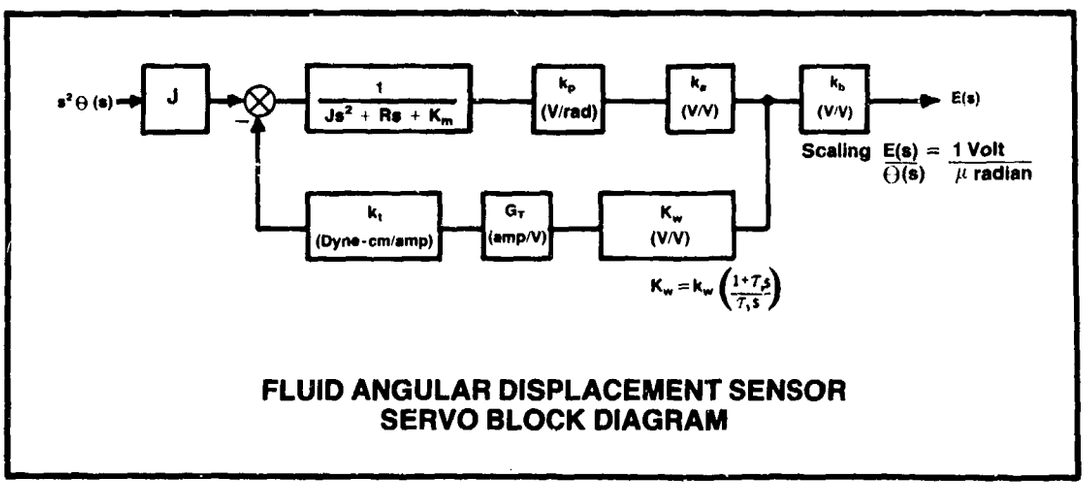

FLUID ANGULAR DISPLACEMENT SENSOR SERVO BLOCK DIAGRAM

FIGURE 4

This servo is the same as that depicted in Figure 3 except for the addition of a buffer amplifier, k_b, to achieve the desired signal level and an integrator in the feedback to provide for long-term centering of the vane assembly at the null position. The resulting transfer function is

$$\frac{E_o(s)}{\theta(s)} = \frac{k_1 s^3}{s^3 + \frac{R}{J}s^2 + \left(\frac{k_m + k_2}{J}\right)s + \frac{k_2}{\tau_1 J}} \cong \frac{k_1 s^2}{s^2 + \frac{R}{J}s + \left(\frac{k_m + k_2}{J}\right)} \cdot \frac{\tau_1 s}{1 + \tau_1 s} \qquad (4)$$

where: $k_1 = k_p k_a k_b$ (volts/radian)

$k_2 = k_p k_a k_w G_T k_T$ (dyne · cm/radian)

This transfer function results in a Bode plot (assuming a 0.7 damping ratio, a τ_1 of 0.8 seconds, and a natural frequency $\omega_n = \left(\frac{k_m + k_2}{J}\right)^{\frac{1}{2}} = 12.57$ radians/sec) as shown in Figure 5.

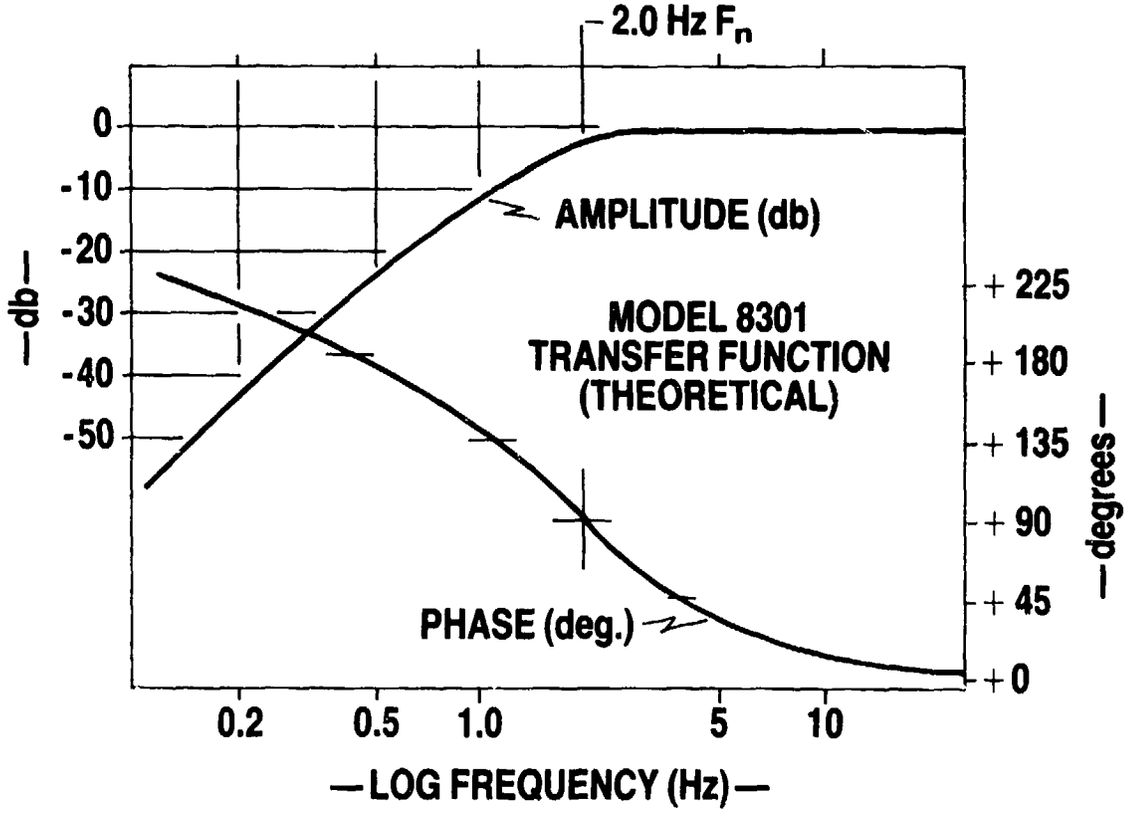

FIGURE 5

The Model 8301 is a completely self-contained transducer requiring only a ±15 Volt supply and appropriate ground to operate. The mechanism and the electronics are contained within a cylinder 1.5 inches in diameter and 3.5 inches long (see Figure 6). The fluid ring inertia and the position pick-off method are unique features of the 8301. The former allows the designer to use a relatively large self-supported moment of inertia resulting in a sensitive, rugged instrument with minimal suspension errors, while the latter, a patented "Q spoiler" scheme, gives, without amplification, a relatively noise free, high level (typically 100 Volts per radian) signal at the output of the detector electronics. This high level, "clean" signal is a key to attaining noise levels and sensitivities in the nanoradian range.

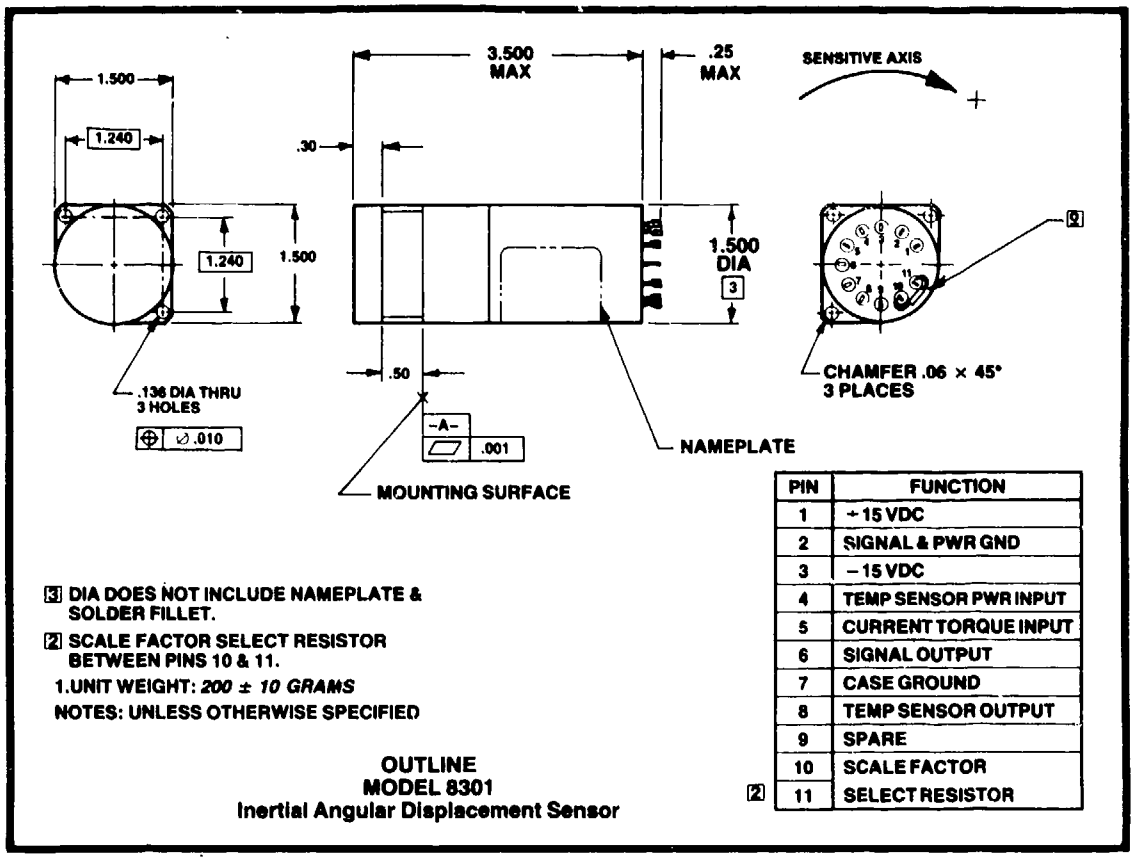

FIGURE 6

III. PERFORMANCE AND TESTING

The transducer has been scaled and used in a number of different ranges. Testing to date indicates performance specifications as typified by the listing in Table 1 are readily attainable.

Parameter	High Range	Low Range
Range	±10 milliradians	±10 microradians
Scale Factor, $k_p k_a k_b$	1 volt/milliradian	1 volt/microradian
Frequency Range	1 Hz to 2000 Hz	1 Hz to 500 Hz
Transfer Function	See Equation (4) and Figure 5	
Damping Coefficient, ζ	0.7 nominal	
Corner Frequency, $\omega_n/2\pi$	1.5 Hz to 2.5 Hz	
Rotor Unbalance, ML/J	0.02 radians/sec^2/g (maximum)	
Rotor Angular Freedom	±20 milliradians (minimum)	
Threshold	0.002 millirad (max.)	0.02 microrad (max.)
Amplitude Response (referred to 100 Hz)	±3.5% (2σ) from stated transfer function at room temperature over frequency range	
Phase Response	±3° (2σ) from stated transfer function at room temperature over frequency range	
Scale Factor Temp. Coef.	±0.05%/°F (maximum)	
Bias	30 mV	100 mV(max.)
Noise	<2.5 μrad (rms)	See Figure 20

TABLE 1

MODEL 8031 SHORT FORM PERFORMANCE SPECIFICATION

The high range, ±10 milliradian transducer was a precursor to the low range, ±10 microradian device that is the subject of this paper. The former is described in some detail in Reference 1.

Scale Factor and Transfer Function

Performance testing of a device designed for 10 microradian full scale operation can require some unique approaches to test equipment design and utilization. Measurements of scale factor and frequency response (transfer function) are particularly sensitive to and may be distorted by instrument and local microseismic or other low level ambient noise. Two approaches can be taken. The scale factor and transfer function can be determined directly in the 10 microradian range by providing calibrated inputs, or the transducer can be electronically scaled to a higher range, tested in that range to minimize the effects of noise and then rescaled to the sensitive range. Both approaches call for special steps. Testing the transducer in the 10 microradian full range requires careful design and construction of test equipment to obviate the effects of ambient noise and provide precisely calibrated (or measured) dynamic

small angle excursions within the device's range and pass band. Testing in a higher range simplifies the test equipment design but requires auxiliary measurements to define the scaling change, assure linear performance through the ranges and prove the phase response. Both methods have been utilized to test this transducer.

Lockheed Missiles and Space Company designed, built and utilized a test bed combining a small angle forcer and a real time optical angular position detector to measure scale factor and transfer function of the Model 8301. Measurements were made with the transducer operating in its low range, i.e., 1 Volt/microradian sensitivity. A schema of the test method is presented in Figure 7a. The optical position detector utilizes a diode light source to illuminate the reference mirror on the pivoted platform. The subsequent optical path (shown as dashed lines in the figure) acts as an optical "lever" to provide an amplified linear displacement at the quad detector proportional to small rotations of the reference mirror attached to the platform. The optical wedge provides a means for calibration. As the wedge is rotated (with the pivoted platform and reference mirror held stationary), the beam is displaced an amount equivalent to a 13.2 μrad peak-to-peak displacement of the platform; the scale factor of the optoelectronic link is thus defined as Volts out from the quad detector electronics per μradian in at the platform.

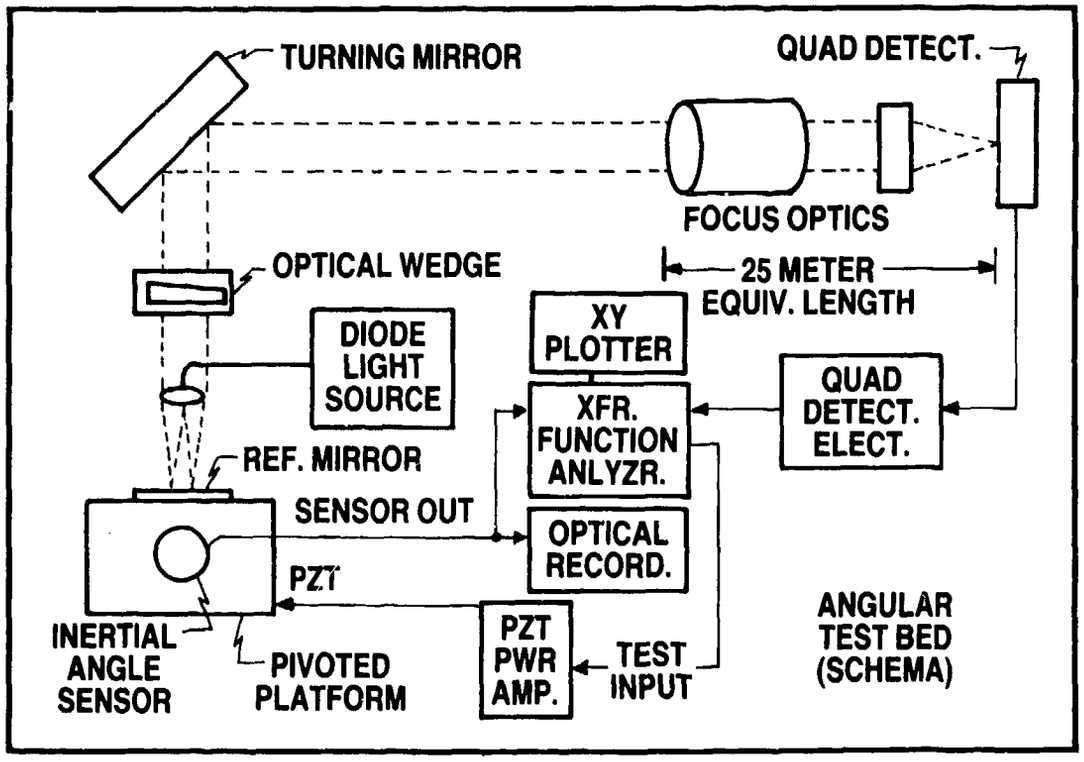

FIGURE 7a

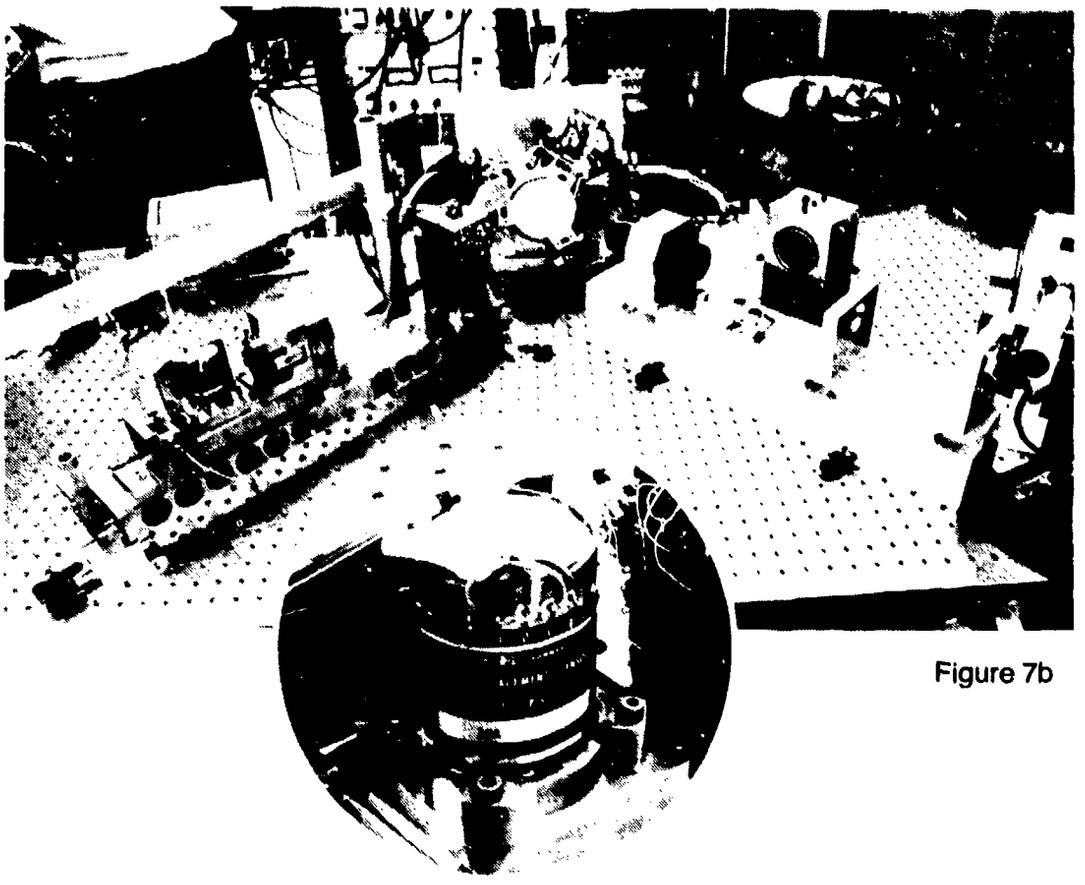

Figure 7b

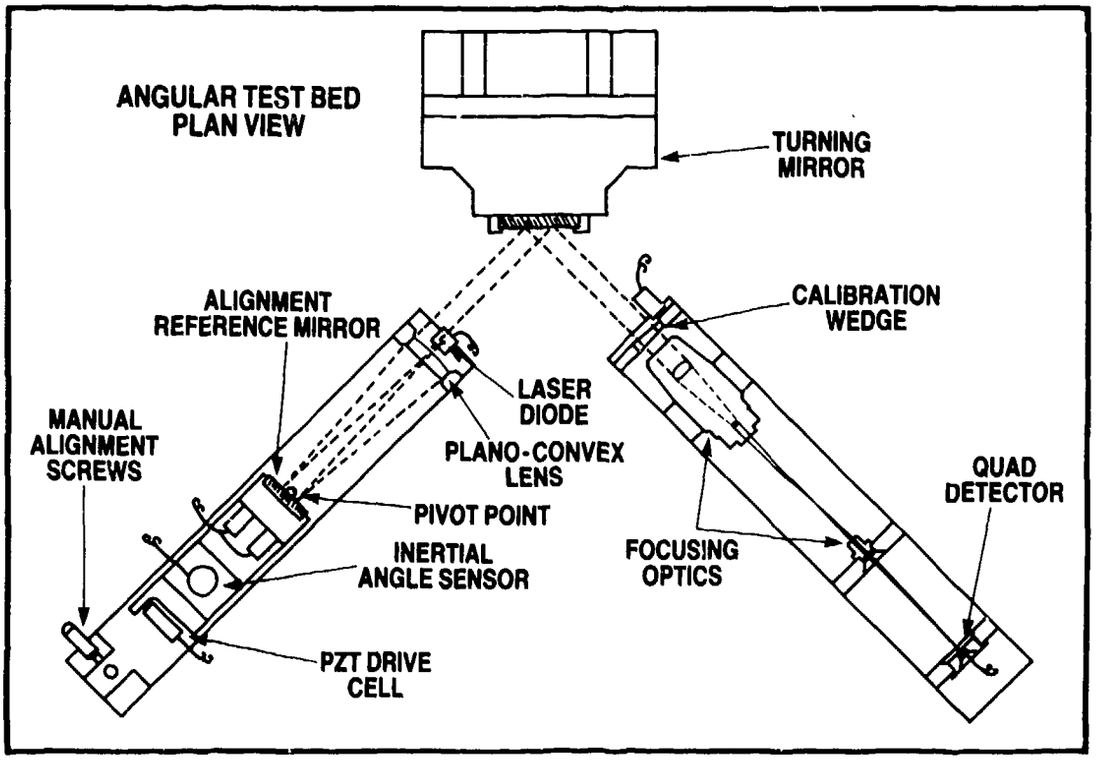

Figure 7c

A full description of the test method is best made with reference to Figure 7a, a schema of the Angular Test Bed; Figure 7b, a photograph of the test setup; and Figure 7c, a plan view of the setup shown in the photograph. The reference mirror on the pivoted platform is set at one-half the focal length of the collimated light beam from the laser diode source. The PZT forcer induces angular vibration of the platform (containing the IADS and the reference mirror) about the pivot point set below and in line with the surface of the reference mirror. The resultant rotation of the reference mirror results in translation of the light beam which, after reflection off of the turning mirror, enters the focus optics to create a diffraction limited spot on the quad detector. The focus optics consists of an inverted beam expander followed by a microscope (2X) objective. This optical train provides the equivalent path length of 25 meters. The quad detector is a silicon detector previously demonstrated to be capable of resolving motions of the spot on the order of 1/1000 of a spot size. The test configuration provides a measurement threshold of 30 nanoradians.

The Transfer Function Analyzer (TFA), a Schlumberger EMR 1170 Frequency Response Analyzer, provides a single frequency signal as a disturbance to the platform through the PZT and analyzes two separate return signals by filtering at that test frequency. In the test the two signals monitored by the TFA are the quad detector output (a measure of the angular input previously shown to have a bandwidth of greater than 1 KHz) and the IADS signal. A transfer function between a calibrated, measured angular input and the IADS output is thus generated. The transfer function generated by sequencing the TFA from 1 Hz to 1 KHz in steps of 60 points per decade is reproduced, in two sections, as Figures 8a and 8b, respectively. The IADS response is shown in Figure 8b to be within ± 1 dB from 10 Hz to approximately 400 Hz. The resonances starting between 400 and 500 Hz were determined by separate test to be associated with test equipment structural modes.

Systron Donner has taken the second approach to testing the transducer. The gain of the output amplifier, k_b, (see Figure 4), is re-scaled to provide 1 Volt per 0.1 milliradians (a 100 to 1 gain reduction) and an input of approximately 150 microradian rms is applied.

The test table is described in both References 1 and 2. It is simply a ball bearing supported vertical axis table with a closed loop angular displacement servo and mechanical stops at ± 10 milliradians. The table is periodically calibrated (usually once per shift) by statically checking the angular position pickoffs; a check based on using a differential photodetector, set 175 inches from the table, to measure the angular displacement of a laser beam reflected from a mirror attached to the table. Independent tests of the table angular pickoffs,

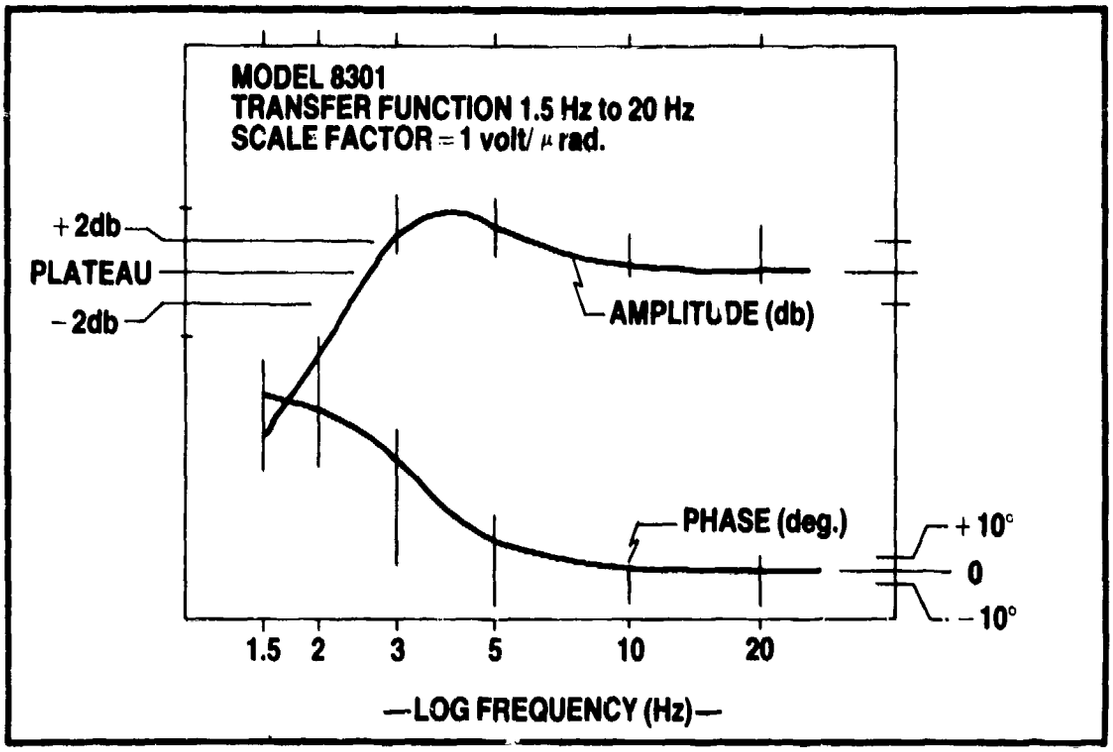

FIGURE 8a

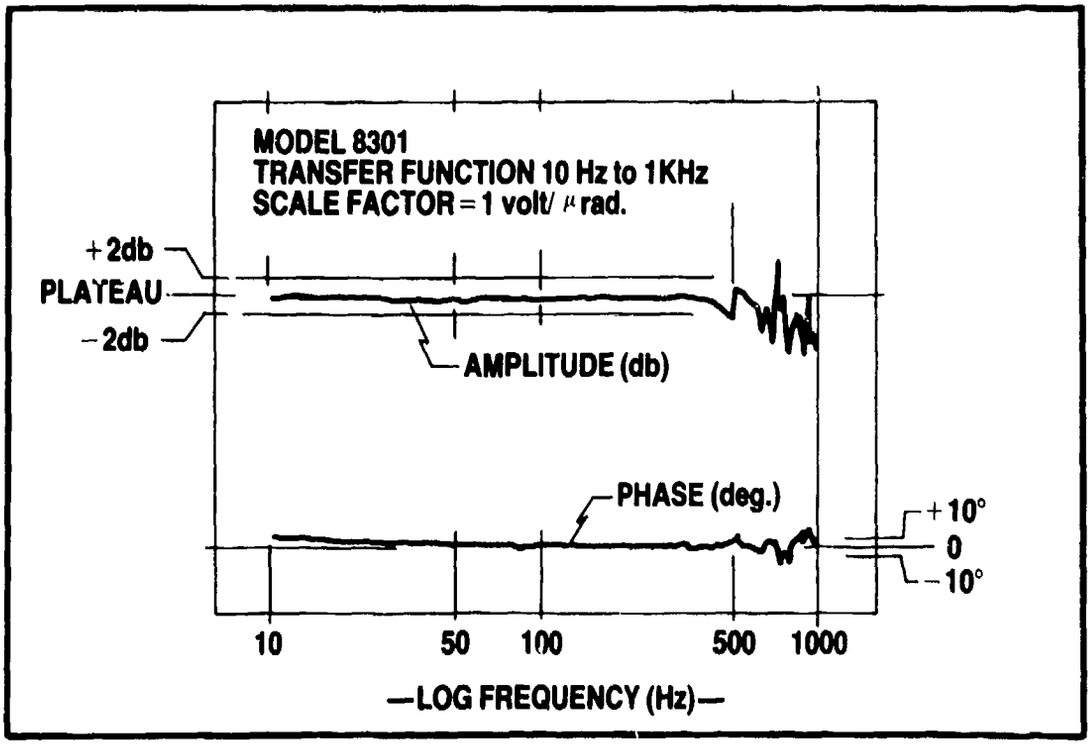

FIGURE 8b

pickoffs similar to those used in the Model 8301 transducer, assure their flat response and linearity over the test band.

The transducer scale factor in the higher range is determined at some frequency in the pass band, typically 100 Hz, by driving the table to some peak displacement between 0.5 and 1 milliradian and comparing the transducer output to the output from the calibrated table pickoff. The scale factor in the lower range is then derived from the high range value by either of (a) calculating the scale change from resistor ratios that set the gain, or (b) measuring the gain, k_b, of the two configurations of the output amplifier. The required voltage measurements are most conveniently made with dual channel equipment, e.g., digital analyzers such as the Hewlett-Packard Model 5423A Structural Dynamic Analyzer. This method of scale transfer of course leaves open the question of the mechanical sensor response to the very low inputs it is designed to measure when scaled for 1 Volt per microradian, i.e., is the device linear down to the nanoradian range and will it truly measure inputs in that range? Our approach to this has been to mount the unit on an isolated platform and utilize angular momentum transfer to provide small angle excursions. (See discussion of noise below and Figure 1.) Work is continuing on this measurement at Systron Donner. One possible approach is described under Future Directions at the end of this paper. Linearity in the high range is simply measured by demonstrating that the scale factor is constant for various level inputs. Figure 9 shows the results of a linearity measurement.

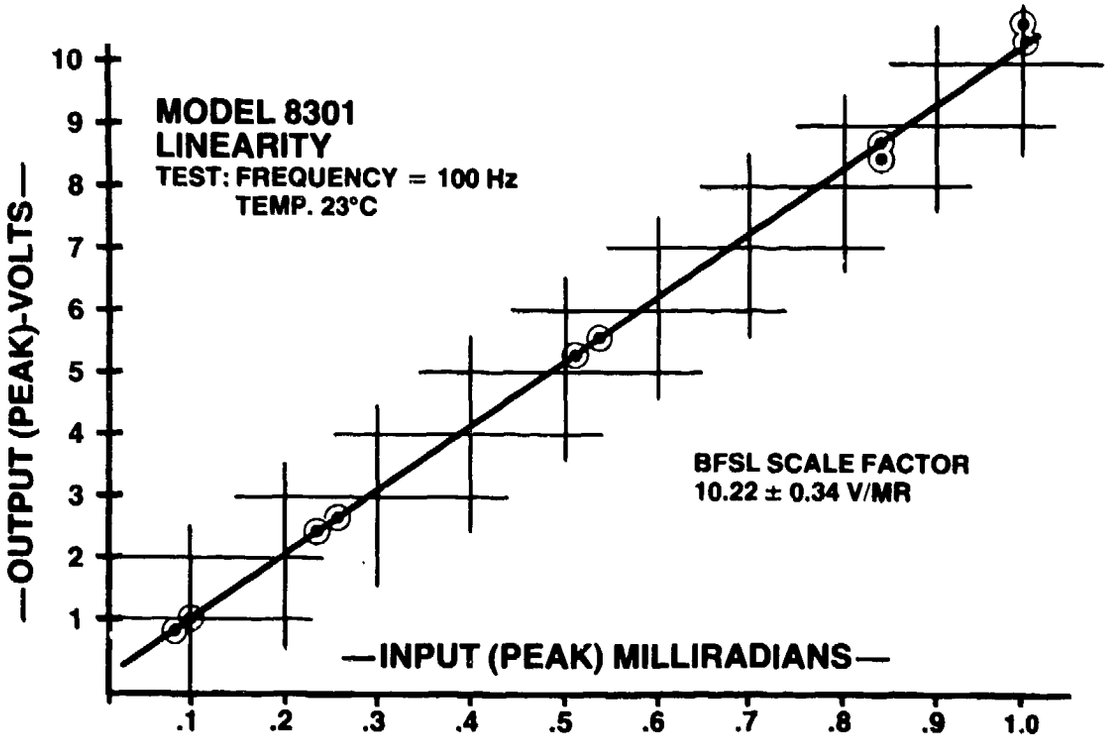

FIGURE 9

Transfer function measurements are accomplished by examining the response of the transducer to inputs in its pass band. In essence the test is the same as the scale factor test, except that both the amplitude and phase are determined and the measurements are made across the frequency band of interest. Two basic methods have been used. In one, a digital memory scope is used to garner phase and amplitude readings at discrete frequencies for single frequency sine wave inputs, while in the other, a random noise is used to drive the table and a Fast Fourier Transform Analyzer is used to derive the transfer function. The latter method requires significantly less time to obtain acceptable results. The analyzer used, the Hewlett-Packard Model 5423A, also has a tape storage feature and can be used to drive a digital plotter. A typical transfer function taken by the second method is given in Figure 10. The same question asked in conjunction with scale factor concerning response in the nanoradian range can be posed here. At present we have only the methods described in the scale factor discussion. Again, see the description of future possible mechanizations at the end of the paper.

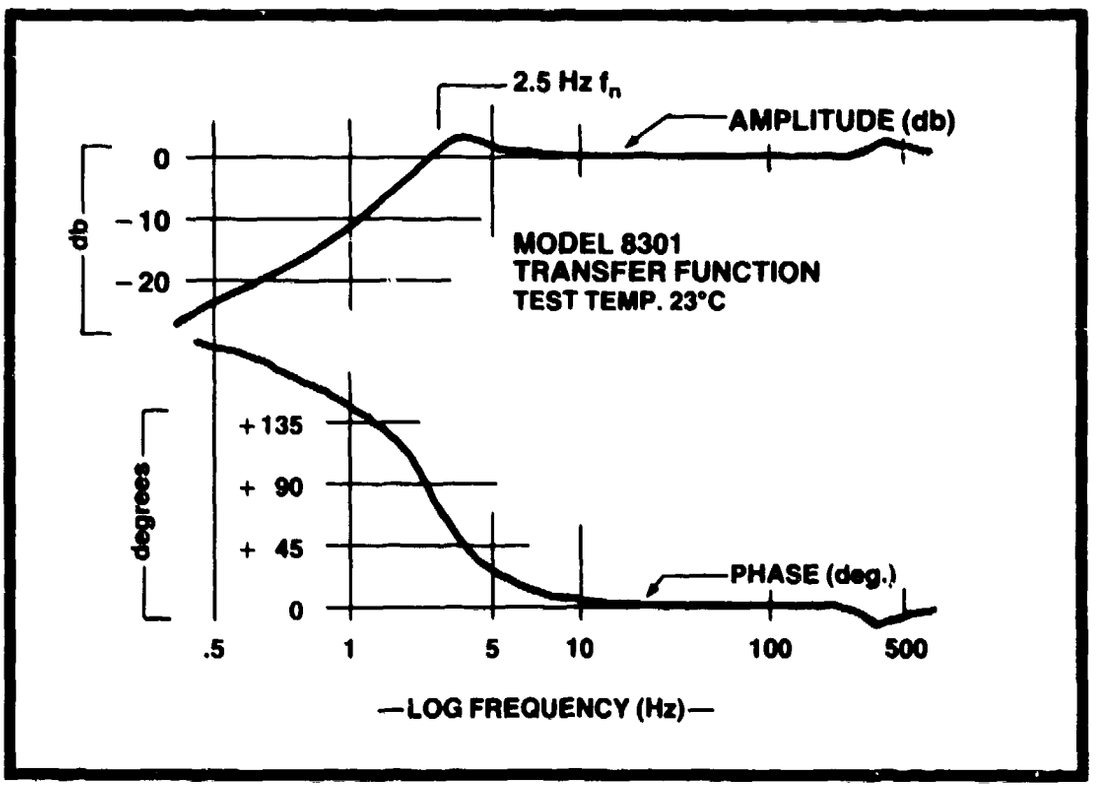

FIGURE 10

Since transfer function values are also concerned with phase, the contribution of the scaled amplifier must be considered. As with scale factor measurements, this can be done either by calculation (relying on gain bandwidth products) or by measurement.

Noise

Measurement of the true self-generated noise of the transducer is an interesting problem. Needless to say, a transducer scaled to respond with signals of volts per microradian of input is ultrasensitive to ambient disturbances responding, for instance, to voices, paging systems and other minute man-made or natural local disturbances. A degree of isolation even greater than that needed for scale factor and transfer function measurements is called for. Various approaches ranging from massive isolated platforms, with and without air bearing supports and active controls, to simple angular isolators have been taken.

Two Systron Donner 8301 angle sensors were subjected to special noise evaluation tests at The Charles Stark Draper Laboratory, Cambridge, Massachusetts. One unit (hereafter called the reference sensor) was a facility item maintained at the Laboratory and of an earlier 8301 design. Its calibration had previously been verified by comparing its output to that of a precision rate integrating gyro. The second unit (hereafter called the test sensor) was obtained from Lockheed Missiles and Space Division, Palo Alto, California and was specially designed for ultrahigh sensitivity.

The testing was performed as part of a continuing effort at the Laboratory to evaluate noise limitations for a wide range of inertial instruments.

The two instruments were placed on the concrete pad of the inertial test laboratory with their sensitive axes vertical and approximately parallel. Previous testing with seismometers and other inertial instruments had shown the concrete pad to be seismically the most quiet location in the test laboratory.

The instrument outputs were fed into two channels of a time series spectral analyzer. The estimated power spectral densities obtained for the frequency band from 2 to 100 Hz are shown as log-log plots in Figures 11 and 12. The principal features in the spectral curves of both instruments are the significant amount of noise measured from 2 to 5 Hz and a smaller amount of noise in the band from 8.5 to 13.5 Hz, with a 10.5 Hz peak. Smaller peaks appear at frequencies around 20, 30 and 40 Hz, with a larger peak at 60 Hz representing the 60 Hz pickup of the sensors. Some of these noise frequency components have been detected in the laboratory environment in previous tests with the reference sensor and other test instrumentation, such as seismometers and precision gyros.

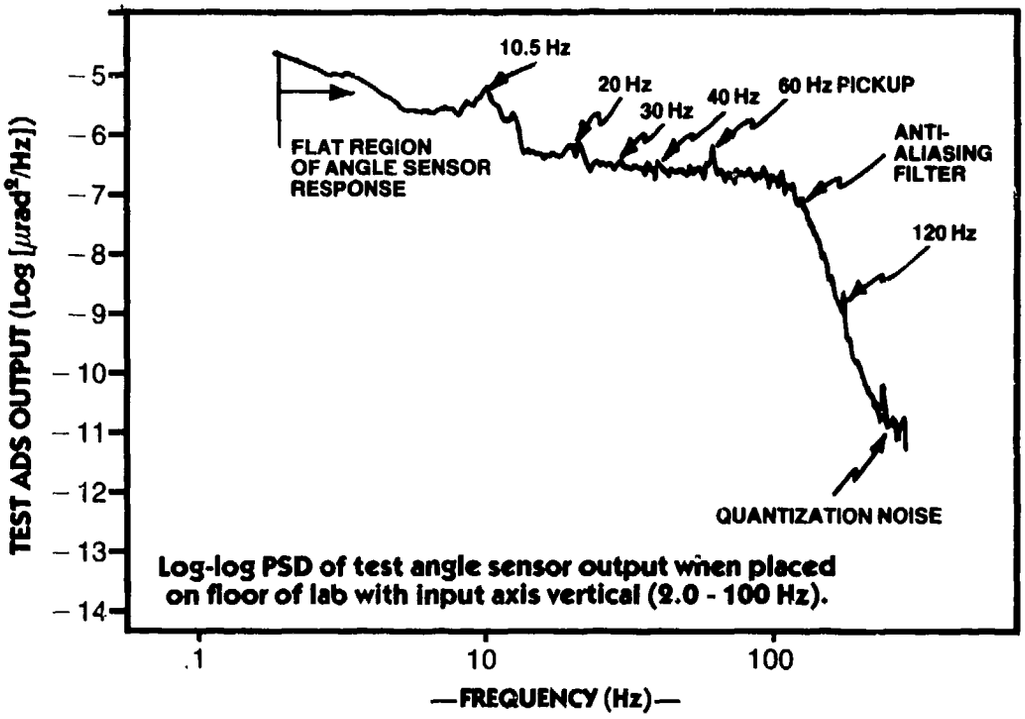

FIGURE 11

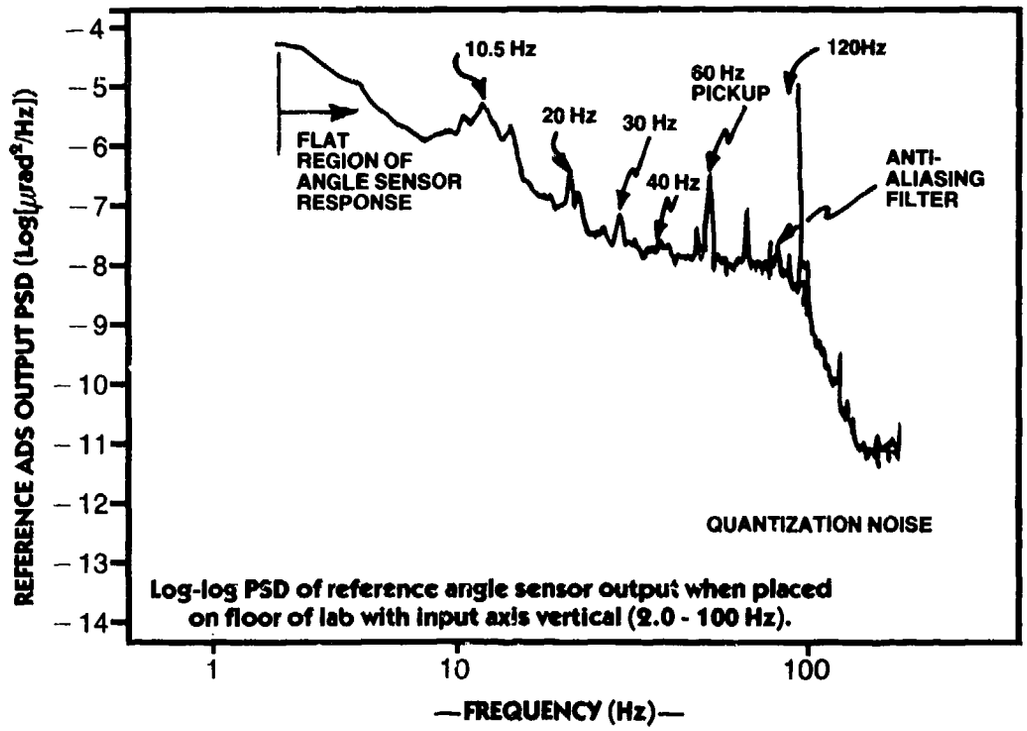

FIGURE 12

Figure 13 shows the coherence between the two sensor outputs in the band from 2 to 30 Hz. It is interesting to note that the outputs in the 2 to 5 Hz band are not correlated between the two instruments, indicating that it is primarily instrument noise rather than noise due to floor motion inputs. The test sensor measures an rms noise of approximately 0.018 μrad in this band while the reference sensor indicates a corresponding rms noise of 0.012 μrad.

Both instruments do measure about the same rms noise in the 8.5 to 13.5 Hz range, approximately 0.005 μrad. These disturbances are thought to be ground motion since local disturbances at about 10 Hz have been measured in previous tests. The above conclusion is further strengthened by Figure 13 where the coherence between output data from both units shows high coherence between 8.5 and 13.5 Hz.

Over the 2 to 100 Hz band, the reference sensor exhibits an rms noise of approximately 0.015 μrad while the test sensor has a corresponding value of 0.020 μrad.

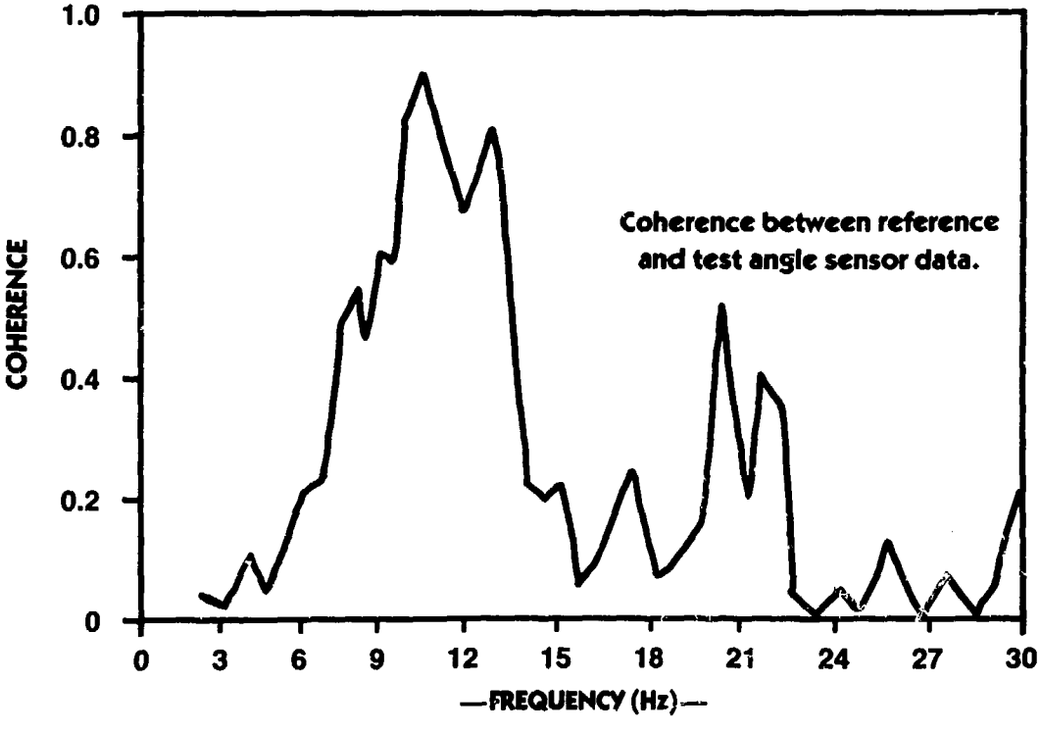

FIGURE 13

The wide band spectra of the angle sensors are shown in Figures 14 and 15 for a filter cutoff frequency of 2000 Hz. Note the relatively high noise peaks in the test sensor PSD plots at around 950, 1300 and 1900 Hz and smaller peaks at various other frequencies which are not measured by the reference sensor. A closer look at the figures indicates that the reference sensor has an inherent noise threshold which appears to be higher by approximately an order of magnitude than that of the test sensor in the band above 30 Hz. Thus the minor disturbances exhibited in the test sensor output cannot be sensed by the reference sensor.

However, the large noise spikes on the test sensor above 800 Hz should have been sensed by the reference sensor if they were actual disturbances. Since they were not sensed, we conclude that they are electronically generated within the test sensor itself.

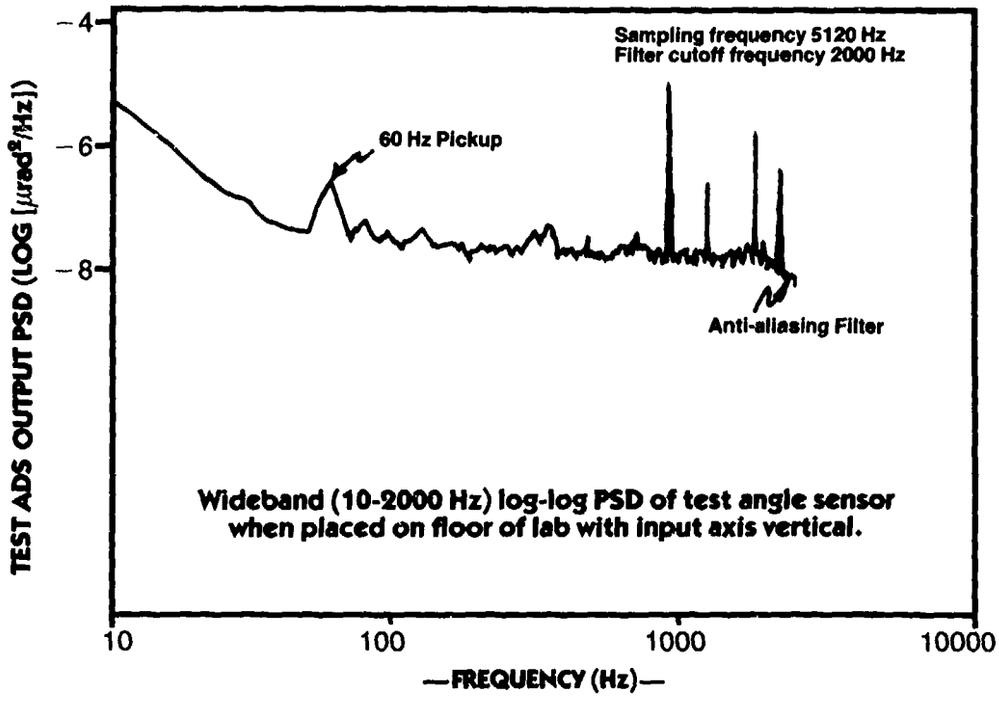

FIGURE 14

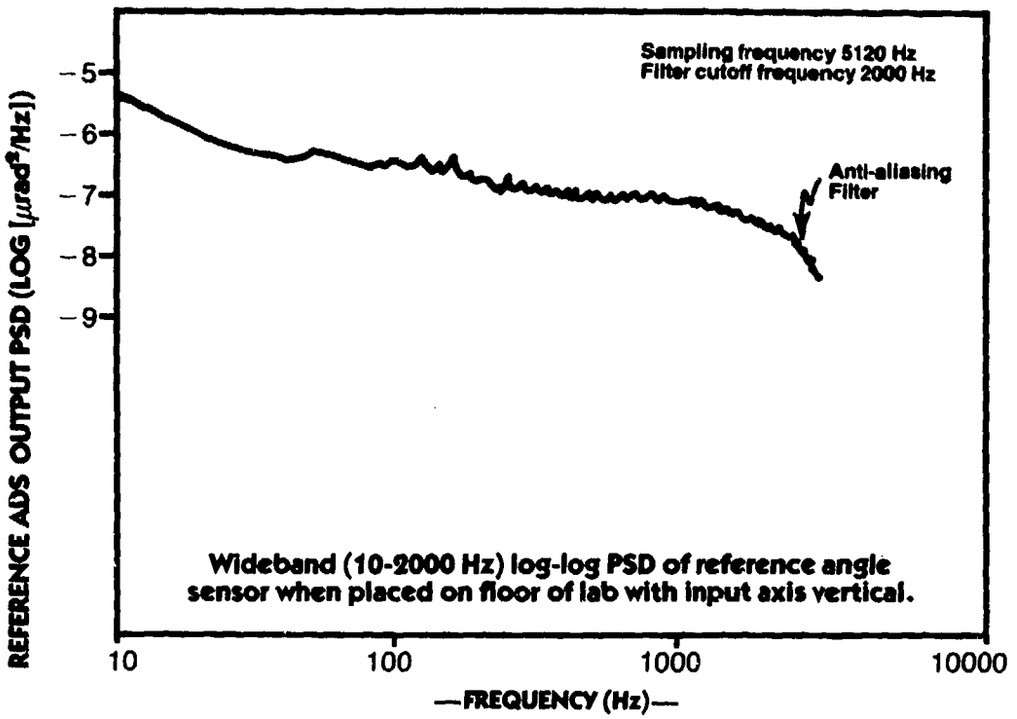

FIGURE 15

A plot of the coherence between the outputs of the two instruments is shown in Figure 16. There is no indicated coherence above 100 Hz.

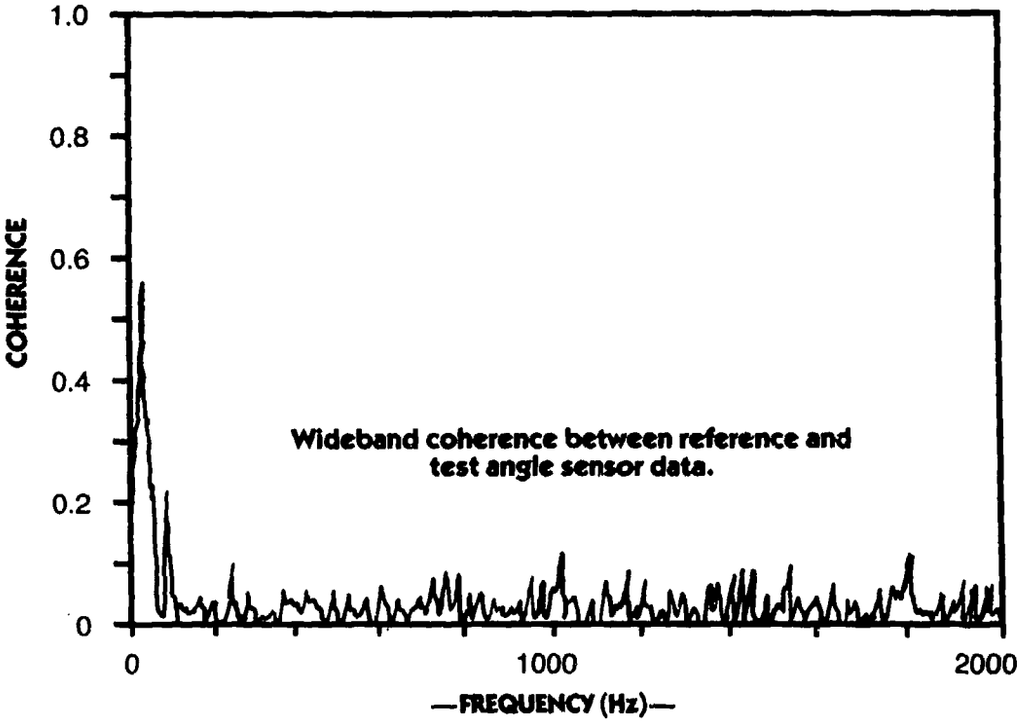

FIGURE 16

Over the total frequency band 2 to 2000 Hz, the reference sensor exhibits an rms noise of 0.020 μrad. The rms noise of the test sensor still is 0.020 μrad since so little noise is present in the band above 100 Hz.

The Model 8301 IADS designated as the test angle sensor in the noise tests at the Draper Laboratory was also tested for noise at the Palo Alto Research Laboratory of the Lockheed Missiles & Space Company. To minimize the effects of local noise, the test was run early on a Sunday morning with air conditioners switched off. The sensor was mounted on a Newport Research optical table configured to attenuate seismic inputs using air isolation support columns. The output signal of the IADS was recorded on a high bandwidth (>1 KHz) Honeywell optical recorder. A tracing of the recording is given in Figure 17. The predominant 7 Hz waveform resulted from a local seismic disturbance. The noise in the 1 KHz band was estimated to be 30 nanoradians (rms). Thus, independent measures, at widely separated laboratories, resulted in noise level determinations of 30 nanoradians (rms) or less for the same transducer. In both cases, the noise output was shown to contain some residual local disturbances; the inherent noise of the transducer was certainly less than 20 nanoradians (rms).

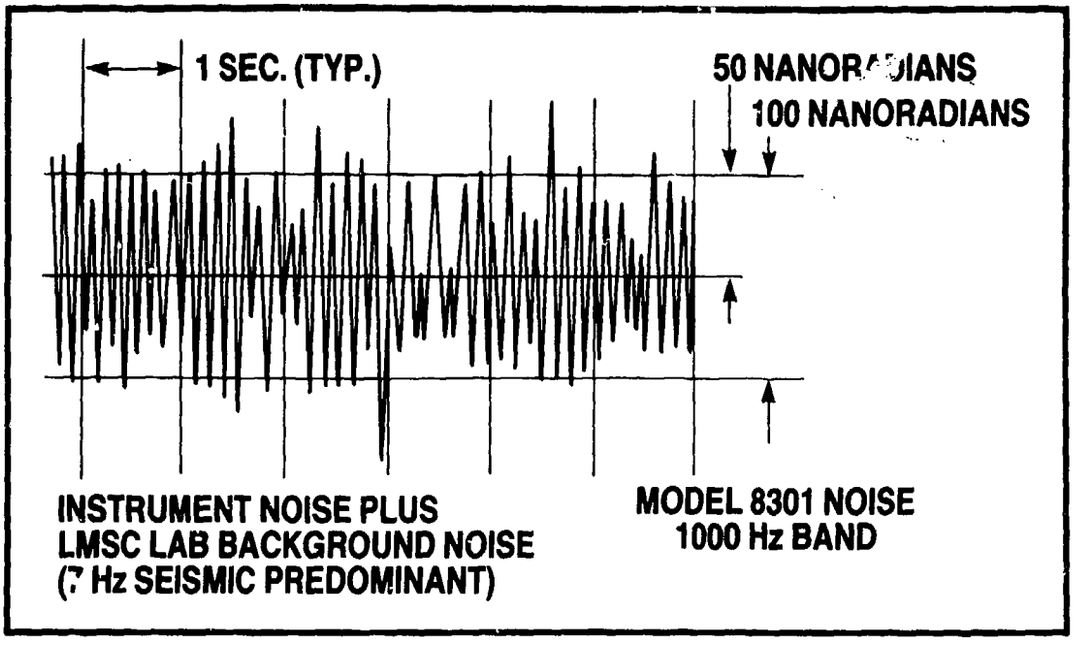

FIGURE 17

Inherent noise level evaluations of a sensitive (1 Volt per microradian) Model 8301 have also been made at Systron Donner. Recognizing that isolation to zero frequency was not required to evaluate this high pass transducer, a crude but effective angular isolation system was constructed and used for the test. The isolator, shown in Figure 18, was simply a nest of three galvanized washtubs of decreasing diameters floated in one another with tap water, mounted on a plywood platform and set on foam pads on the floor.

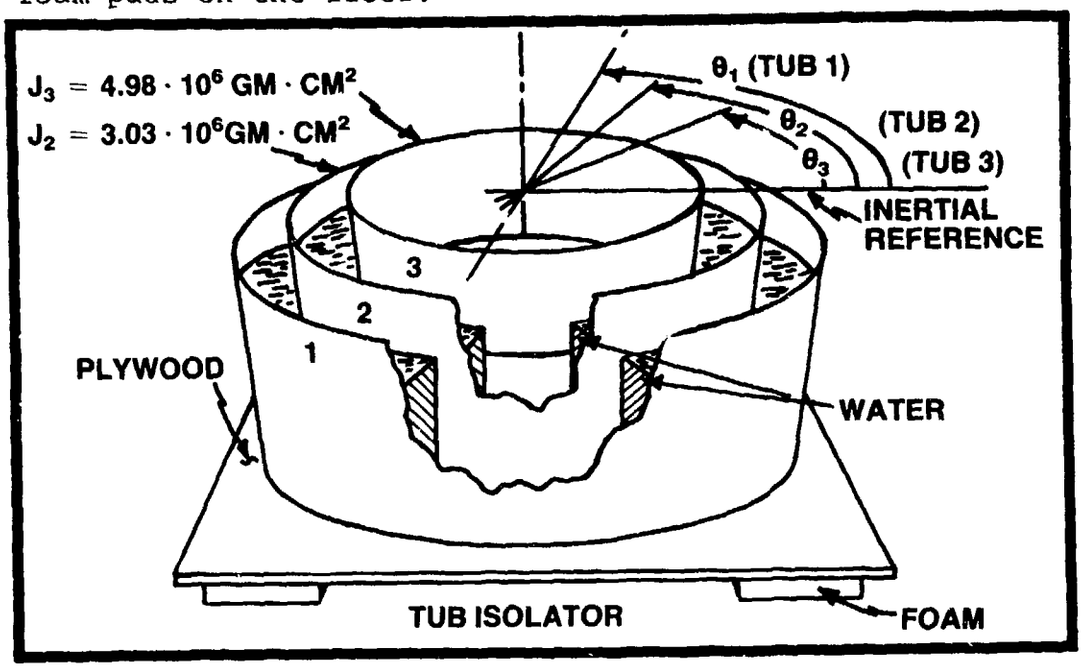

FIGURE 18

Neglecting the effect of the foam, the transfer function of the system was

$$\frac{\theta_3(s)}{\theta_1(s)} = \frac{1}{s^2\tau_2\tau_3 + s\left[\tau_2 + \tau_3\left(1 + \frac{\tau_2}{\tau_{23}}\right)\right] + 1}$$

where: θ_3 = the displacement angle of Tub 3 with respect to the inertial reference

θ_1 = the displacement angle of the input at Tub 1 from the inertial reference--the noise source

$\tau_2 = J_2/R_2$ where J_2 is the inertia of Tub 2 and R_2 is the velocity dependent torque between Tubs 1 and 2

$\tau_{23} = J_2/R_3$ where R_3 is the velocity dependent torque between Tubs 2 and 3

$\tau_3 = J_3/R_3$ where J_3 is the inertia of Tub 3

This function behaves as a system of gain 1 at dc followed by two first order poles resulting in a 12 dB per octave rolloff above the higher first order corner. The transfer function of this system was measured by hanging the platform from a beam and applying angular excitation through two opposed 20 Watt speakers. Two Model 8301's were used, one on the plywood platform and one in Tub 3 of the isolator. The resultant transfer function is reproduced in Figure 19. The system provides effective angular isolation for the frequencies of interest in the 8301.

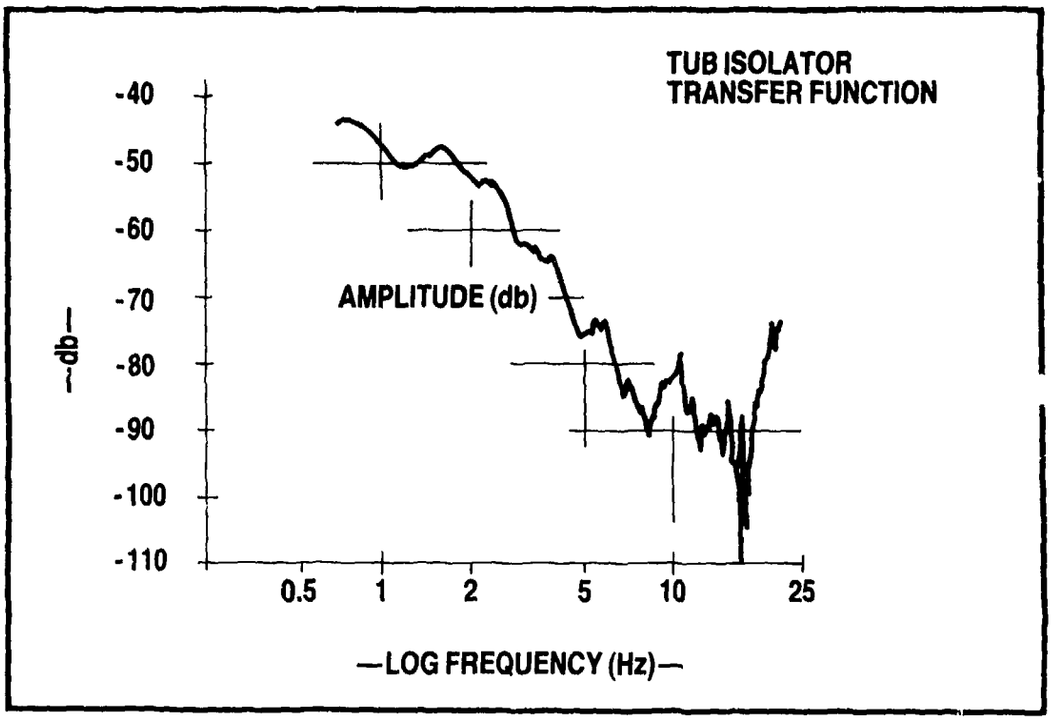

FIGURE 19

The noise measurements were made by mounting the transducer in the center of Tub 3 and supplying power from batteries disposed about the periphery of the floor of the tub. Using an H-P Model 5423A in the autospectrum mode, the noise level in the bands 0 to 10 Hz, 0 to 100 Hz and 0 to 1000 Hz (see Figure 20) was measured and recorded. In addition, the noise power in the bands 1 to 10 Hz, 10 to 100 Hz and 100 to 1000 Hz was calculated. The results were similar to those obtained by Draper Laboratories on a "sister" unit. The preponderance of the noise, some 0.028 microradians rms or about 75% of the total noise in the band 1 to 1000 Hz, was found in the 1 to 10 Hz band. Although the investigation is not complete, our supposition is that this low frequency

noise is generated in the feedback amplifier, k_w (see Figure 4). An interesting artifact in these plots is the sharp peaks appearing in the 850 to 1000 Hz range; they are generated by choppers in the stabilized amplifiers used in the electronics.

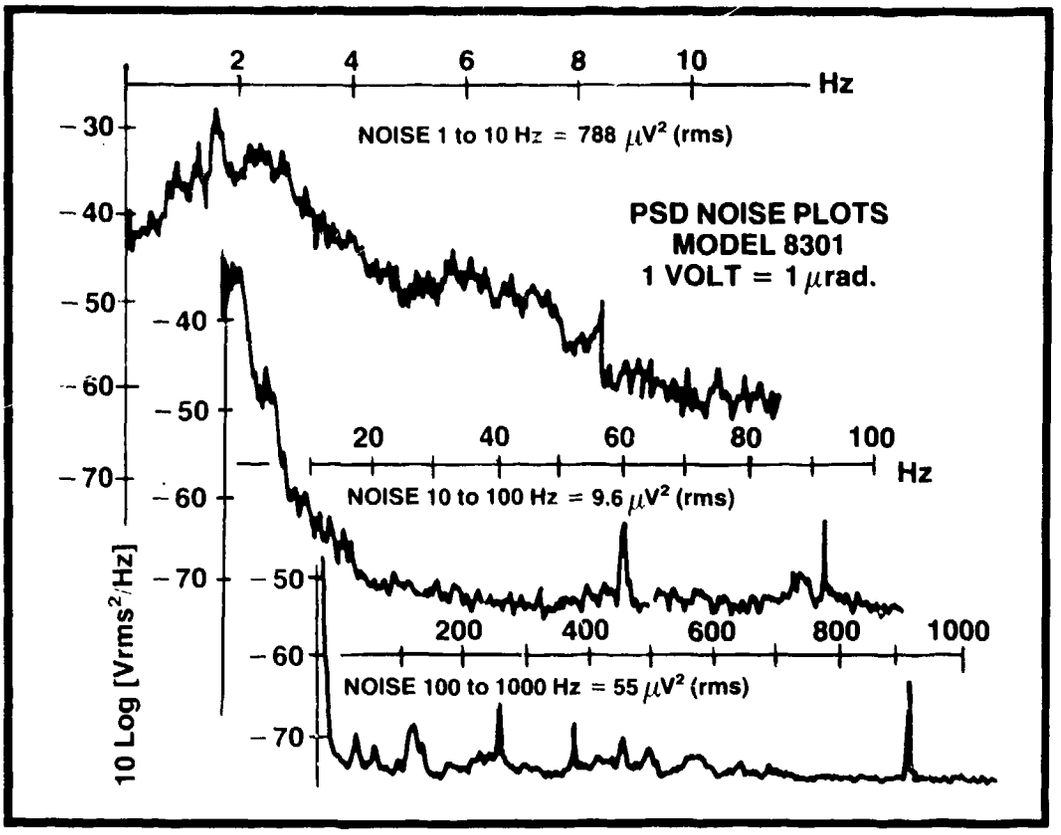

FIGURE 20

Momentum transfer was mentioned above as one approach to testing these transducers in their most sensitive range. A striking demonstration of this approach was made by placing a Hamilton 992B Railway Special watch on the floor of Tub 3 during a session of noise measurements. Figure 1 shows the result. The balance wheel of the watch had a moment of inertia of 0.336 gm cm and a peak displacement of 4.71 radians at 2.5 Hz. Considering conservation of angular momentum, the expected peak response, $\emptyset$, of Tub 3 was

$$\phi = \frac{J(\text{watch wheel}) \times \text{Amplitude (watch wheel)}}{J \text{ (Tub 3)}}$$

$$= \frac{0.336 \times 4.71}{4.98 \times 10^{6}}$$

$$= 0.318 \times 10^{-6} \text{ radians}$$

The measured value for ϕ was 0.328×10^{-6} radians.

Applications

The Model 8301 is an inertial transducer and as such faces a wide spectrum of possible applications. In this section, we point out three general areas of usage, namely, image stabilization, vibration instrumentation, and control systems. The section is not exhaustive and we leave the task of extending the list to the interested reader.

The low range (10 microradian full scale) version of the Model 8301 IADS has been available for about a year. Its applications history is thus embryonic, whereas the high range version, being available now for a number of years, has an extensive history of utilization for stabilization, instrumentation and control. The former can certainly be used in the same general categories of applications as the latter and as system technology is refined, calling for higher sensitivity and resolution, the low range IADS application history will grow.

Image Stabilization

Versions of the IADS have been used to stabilize images in a number of systems. The first usage of the transducer was to stabilize a Forward Looking Infrared (FLIR) image. The FLIR system, supplied by Hughes Aircraft Company, was flown on the B-1 bomber. The IADS provided real time line of sight stabilization. In about the same time frame, Aerojet Electrosystems Company used the IADS for similar purposes in a laboratory evaluation of a FLIR system (Reference 3). More recently, a version of the high range IADS has been selected and is currently being delivered for use on the LANDSAT-D earth resources satellite. In this latter application, the signal from the IADS will be used in data reduction to dejitter and enhance the resolution of the image from the thematic mapper.

The low range IADS can be similarly applied to stabilization problems. The continuing growth of systems technology will call for its finer resolution and, in fact, the transducer has recently been used to demonstrate line of sight jitter removal into the nanoradian range in a fine pointing system.

Vibration Instrumentation

The Air Force has utilized a tri-axis package configuration of the high range IADS to measure angular vibration in a number of aircraft, including the DC-10, L-1011, 747 and NKC-135 Airborne Laser Laboratory. Data from the latter tests were used to study dynamic bending moments in the aircraft. These tests are described in References 1, 4, 5 and 6. We foresee similar applications on large space structures wherein sensitive angular transducers will be used to monitor the structure motion and perhaps be utilized as control elements.

The noise tests run at the Draper Laboratory suggest the IADS provides a practical means for evaluating and monitoring the angular base motion of stabilized inertial test pads. The data presented in this paper show the low range IADS is capable of resolving and measuring into the nanoradian range. A test engineer could certainly devise methods for characterizing test beds down to the noise limit (see, for example, Figure 20) of the IADS. With proper application of coherence or correlation techniques, time averaging and a pair of IADS, broadband angular vibration measurements down to 10 nanoradians (rms) or less are possible.

Control Systems

The IADS, being an inertial transducer, can be utilized for stabilization in angular motion control systems. The engineers at Contraves Goerz Corporation have recently applied a high range IADS as a high pass compensation element in a rate table control system and demonstrated significant improvement in angular rate and position jitter.

A system block diagram is given in Figure 21. The significant point to note is that the IADS high pass signal complements the low pass signal of the Inductosyn to provide wideband compensation. When configuring a system of this nature, the system engineer quickly discovers that, if the low pass instrument has a second order corner, control is lost at the crossover frequency, since at that frequency the low pass signal phase is -90° and the high pass signal phase is +90°. Contraves Goerz has solved that system design problem by inserting a crossover filter in series with the Inductosyn signal.

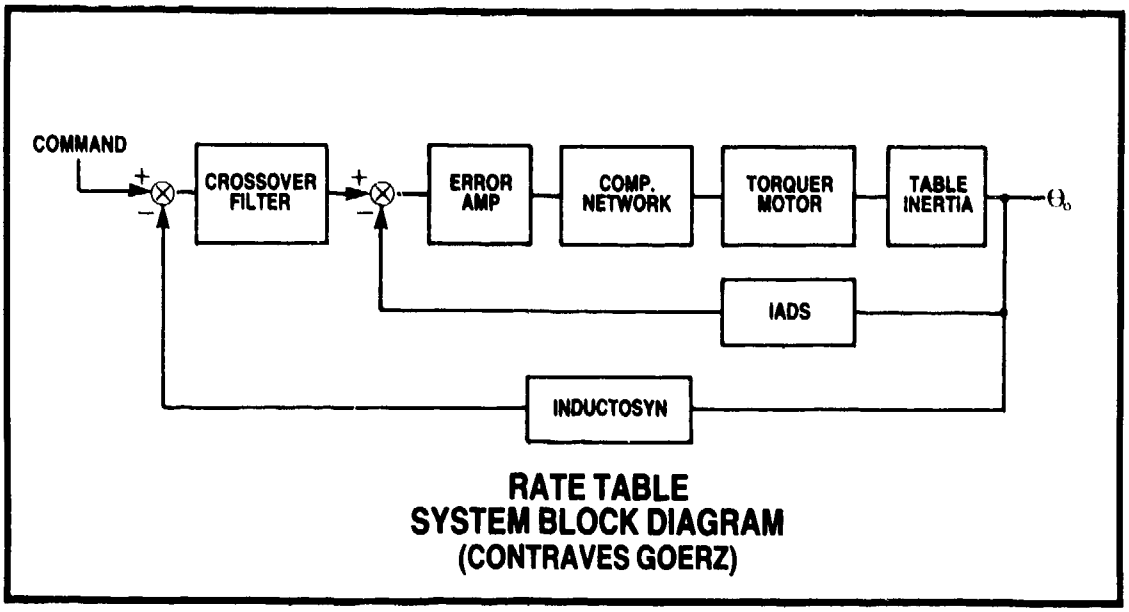

FIGURE 21

The results of a series of tests with the IADS in and out of the control loop are given in Figures 22, 23 and 24. Figures 22 and 23 show a performance comparison of rate and positional jitter, respectively, with the IADS in and out of the control loop. Figure 24 gives another comparison of performance. Plots of motor current (applied torque), position and rate at table speeds of 0.01°/sec and 10°/sec show significant reduction of the noise content in these signals when the IADS is switched onto the control loop. It is interesting to note that, relatively, rate jitter improvement exceeds positional jitter improvement, especially over a wider range of table speed. At present, no explanation is offered but the phenomenon is being investigated. In both cases the improvement factor falls off as table speed is increased. The conjecture is that this effect is related to the 30 Hz control loop bandwidth. This phenomenon is also now being investigated.

Contraves Goerz ran their series of tests on a Model 611 table supported with ball bearings. In the immediate future, tests will be run on an air bearing table to assess its performance with and without an IADS compensator. In any case, the test results so far give a convincing demonstration of system jitter reduction through inclusion of the IADS in the control loop.

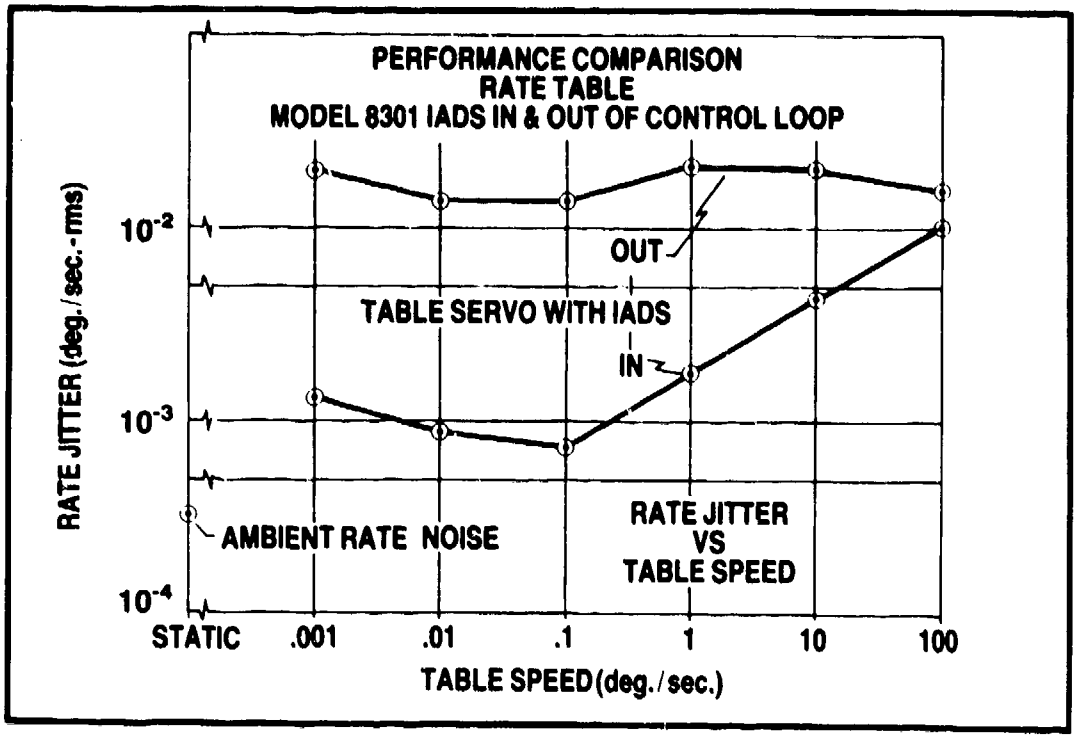

FIGURE 22

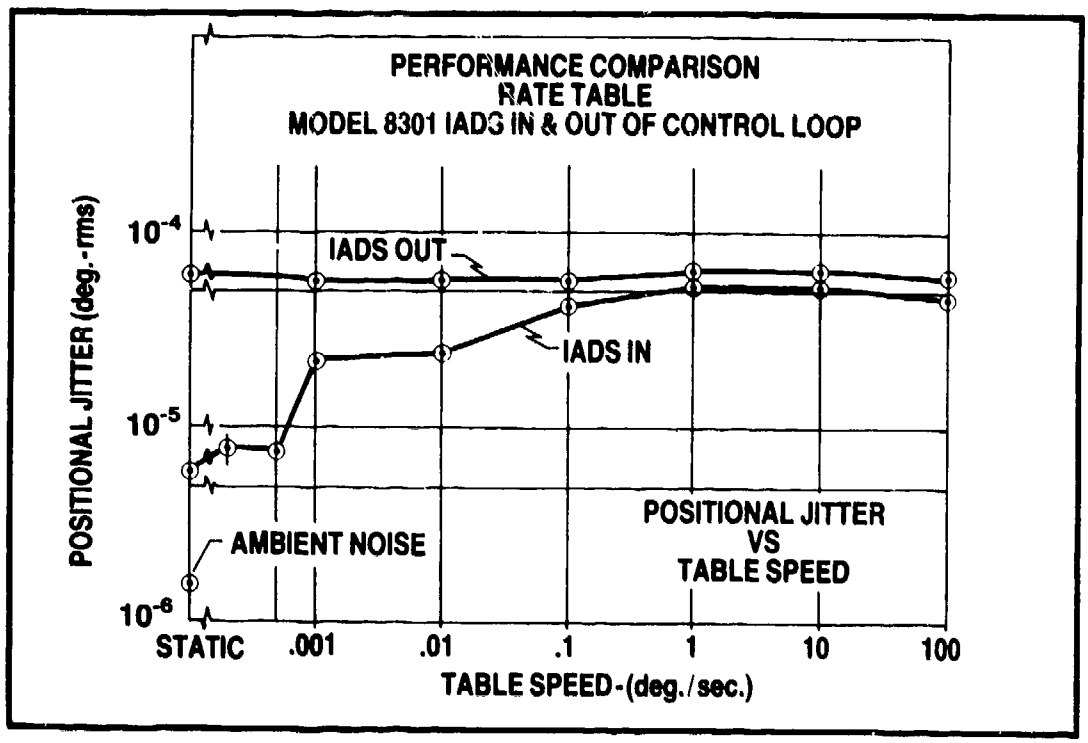

FIGURE 23

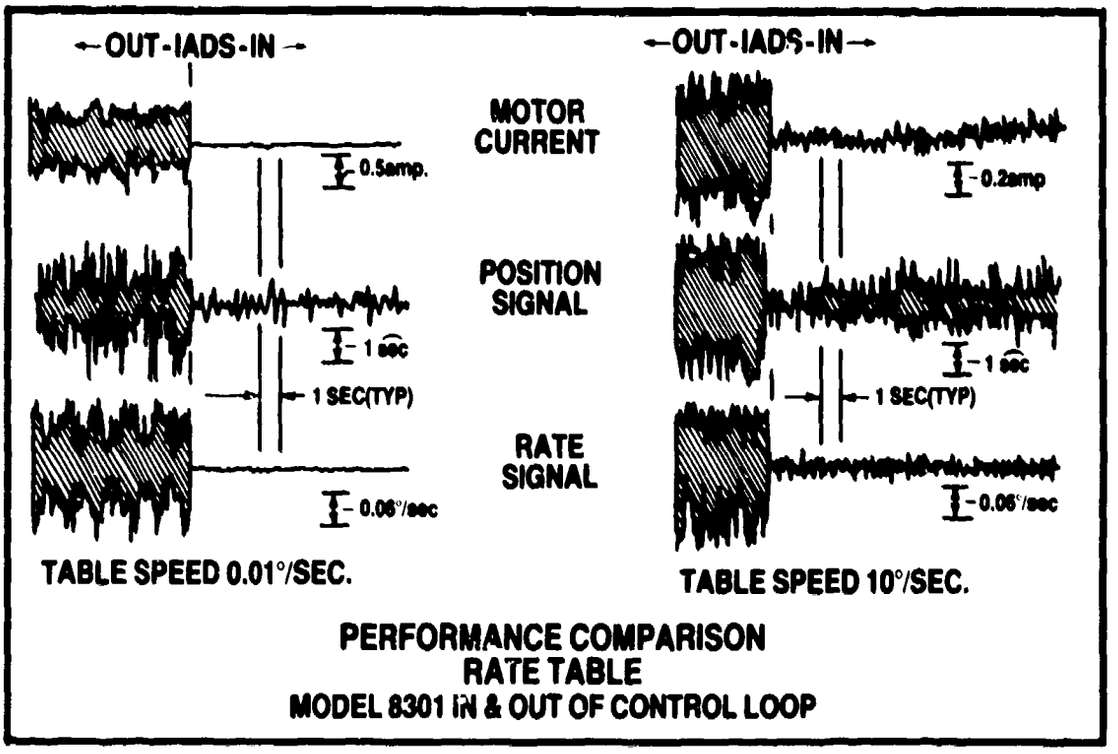

FIGURE 24

Future Directions

The Model 8301, being a descendent of an angular accelerometer, can be configured, with suitable electronics and sensor design, to measure angular jerk, acceleration, velocity or position. The objective in these closing paragraphs is to present our view of the future evolution of this device as a dynamic Inertial Angular Displacement Sensor (IADS) and to consider methods that can be developed for testing to keep pace with the design advances.

Design

The evolutionary development of this transducer has not reached the inherent limits of the major design elements. For example, a simple angular position sensor comprised of an inertia, J, and a velocity dependent torque, R, has a fundamental mechanical system time constant, J/R, defining the limit of the lower corner, a limit not yet reached in the 8301. In the near term, further evolution of this transducer design will thus consist of design refinements rather than large variations in design approach.

In applications where the transducer is used to complement the signal derived from a low pass instrument, the system design problem usually is simplified if the flat phase region is brought nearer zero frequency. Even setting that consideration aside, applications can be conceived wherein a transducer of this type replaces the more traditional instruments, such as gyros, for angular position determination. Again, bringing the response nearer zero frequency would enhance the unit's utility. Both of the foregoing considerations engender a drive to move the lower corner, residing between 1.5 and 2.5 Hz in the present design, down in frequency. We have reason to believe that corners down to 0.5 Hz are attainable and have run a breadboard feasibility demonstration of a unit set up for a nominal 1 Hz corner. The resultant transfer function is compared to the original in Figure 25. The change was effected by lowering the spring rate about 5.8 to 1. As expected, the damping ratio rose accordingly since no steps were taken to modify the system's time constant, J/R. Design refinements will lead to a 90° phase point at 0.5 Hz with a nominal 0.7 damping ratio (See Figure 26).

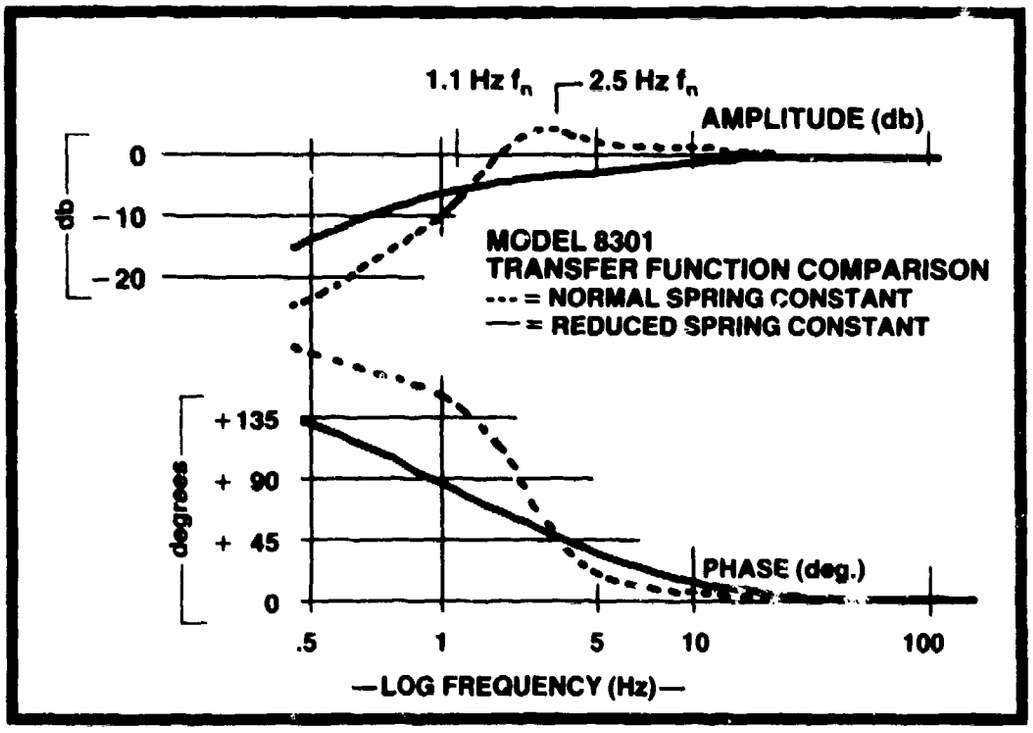

FIGURE 25

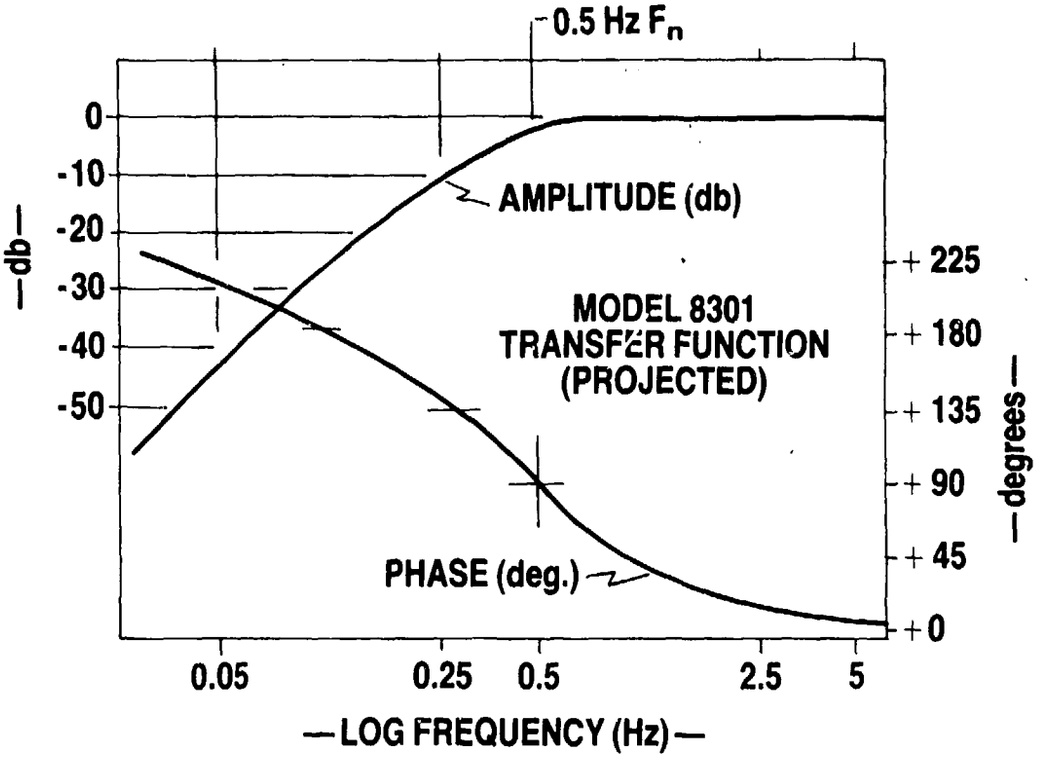

FIGURE 26

All the noise measurements have shown the broadband noise of the current design to lie in the 20 to 30 nanoradian (rms) level with the preponderance of the noise lying below 10 Hz. For applications such as the first in the preceding paragraph, the noise "peak" lies in the system transition region. Although the noise level is already very low, we foresee applications of this device for which the low frequency noise content may need to be reduced. Lowering the corner frequency will lower the noise "peak" frequency and, with refined amplifier design, we project a value of 5 to 10 nanoradians (rms) as achievable below 10 Hz.

At least three other performance parameters listed in Table I are of prime import in a transducer intended for general system use, two are explicit and one is implied. They are, respectively, rotor unbalance, scale factor temperature coefficient and transfer function temperature dependence. Rotor unbalance is primarily a function of the manufacturing process. Reduction in unbalance requires refinement of both the mass and volume balancing steps. A reduction of 5 or 10 to 1 in the noted value is projected as a reasonable value to attain in the next generation of this design. Significant reduction of the thermal dependence of scale factor and transfer function calls

for modification of the internal geometry of the transducer. While both parameters are at least partially dependent on gain constancy of the position sensing electronics, they also depend on the interaction of the self-supported inertia (the fluid ring) and the vane assembly. This interaction is dependent on geometry and viscosity, with the latter being a strong function of temperature. We believe a 5 to 1 reduction in scale factor temperature coefficient is achievable over a preselected 50°C range, but cannot currently forecast the expected level of improvement in transfer function thermal dependence.

Table II below provides a summary of the projected near-term evolution of the low range transducer's performance parameters.

Parameter	Present Design	Near Term Evolution
Range	±10 microradians	Same
Scale Factor, $k_p k_a k_b$	±1 Volt/microradian	Same
Frequency Range	1 Hz to 500 Hz	0.25 Hz to 500 Hz
Transfer Function	See Figure 5	See Figure 26
Damping Coefficient, ζ	0.7 nominal	Same
Corner Frequency, $\omega_n/2\pi$	1.5 Hz to 2.5 Hz	0.5 Hz
Rotor Unbalance, ML/J	0.02 rad/sec^2/g (max.)	0.002 rad/sec^2/g (max.)
Rotor Angular Freedom	±20 millirad (min.)	Same
Threshold	0.02 microrad (max.)	Same
Amplitude Response (referred to 100 Hz)	±3.5% (2σ) from stated transfer function at room temperature over frequency range	Same
Phase Response	±3° (2σ) from stated transfer function at room temperature over frequency range	Same
Scale Factor Temp.Coef.	±0.05%/°F (maximum)	±0.01%/°F (max.) preselected 50°C range
Bias	100 mV (maximum)	Same
Noise	See Figure 20	10 nanoradians (rms) to 1000 Hz

TABLE II

PROJECTED NEAR-TERM EVOLUTION
MODEL 8301 TRANSDUCER PERFORMANCE

Testing

As these devices are refined, especially as low corner, high pass, high sensitivity angular position transducers, parameter testing will similarly have to be refined. Measures of scale factor, linearity and transfer function at displacement levels commensurate with the end usage if not already needed will shortly become a necessity. There are undoubtedly myriad means for satisfying that necessity. At least two basic methods have been or will be used to generate small angle inputs to test the current design: momentum transfer and offset torquing, with the latter having two variants we are aware of.

The description given beforehand of the transfer function testing at Lockheed is one variant of offset torquing, i.e., application of force at some finite distance (lever arm) from a "table" center. The test method is straightforward and worthy of consideration for use in future testing. The other offset torquing variant utilizes a rotating, purposely unbalanced (eccentric) mass to couple reaction forces as torques to a suitably suspended vertical axis table. The test input torque is given by (neglecting the induced motion of the vertical axis table) (See Figure 27)

$$T = -m\Omega^2 dD\cos\Omega t$$

where: T = applied torque
m = eccentric mass
Ω = angular velocity of the offset mass
d = radius of mass on the satellite table
D = radius of satellite table on the vertical axis table

This latter method is practically constrained to apply single frequency displacements at any given instant of time, while the former could be adapted for application of multispectral inputs, white noise for instance, with the transfer function being developed by any of the now available dual channel Fast Fourier Transform Analyzers, e.g., the Hewlett-Packard Model 5423A mentioned beforehand. When utilizing these two techniques, the test engineer must consider the possible effects of linear acceleration on a transducer of this type. Rotor unbalance results in a finite response to linear motion albeit there is always a direction of minimum sensitivity associated with the transducer.

Momentum transfer holds some promise (as does the method of offset torquing developed by Lockheed) as a precise, sensitive test method useful for production, i.e., a test that can be

mechanized for fast turnaround with low cost per unit. Suppose that the offsct mass, m, were removed from the satellite table shown in Figure 27 and the table was driven by an oscillating torque.

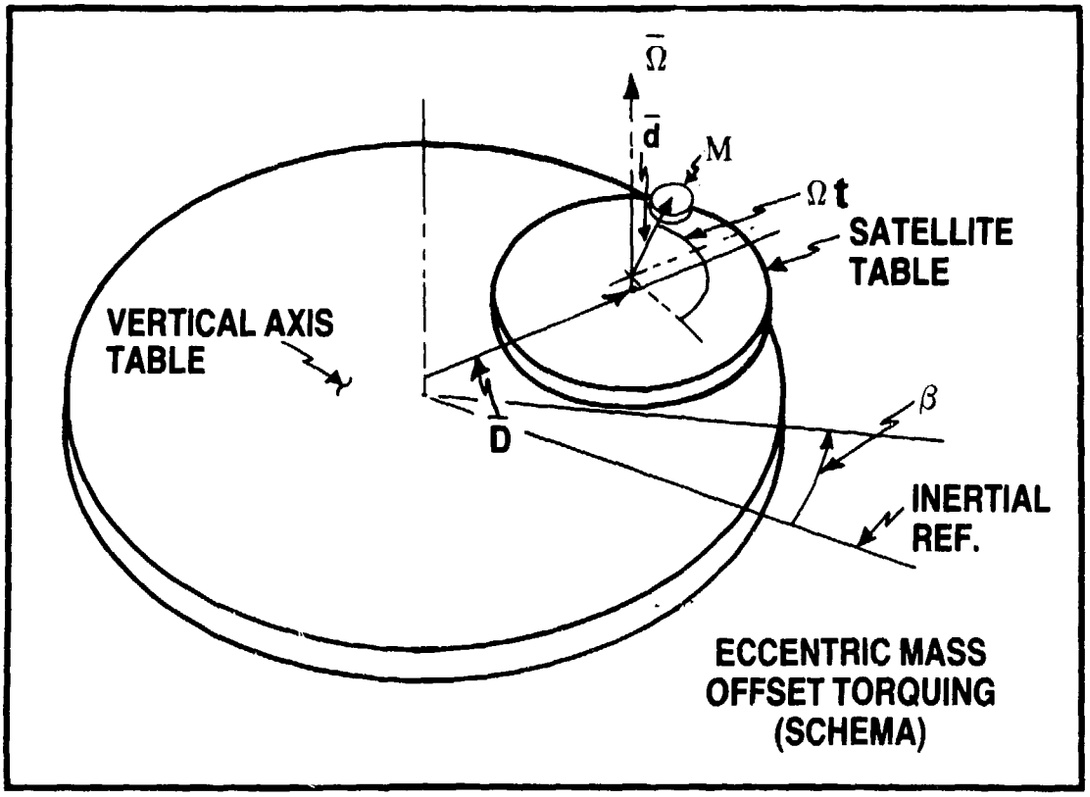

FIGURE 27

Then, considering conservation of momentum, the vertical table will respond as

$$\beta = \Delta \frac{J_s}{J_v}$$

where: β = displacement of the vertical table
Δ = displacement of the satellite table
J_S = inertia of the satellite table
J_V = inertia of the vertical table

and with suitable selection of J_S, J_V ($\frac{J_V}{J_S}$ ranging from, say, 10^4 to 10^6) and the character of Δ, the test setup could be

used for rapid determination of the transducer's transfer function. This method is of particular interest since it has already been demonstrated that suitable design will result in a test bed for measuring noise which, in turn, implies transfer function and scale factor would be measured in a quiet environment.

Testing of other performance parameters is straightforward once the noise and transfer function/scale factor test problem is resolved. References 1 and 2 provide further information on parameter testing.

CONCLUSION

This paper has described the design, performance and testing of an Inertial Angular Displacement Sensor (IADS), the Systron Donner Model 8301, with measurement capability extending into the nanoradian range. The inherent noise level of this high pass transducer (1 Hz to 500 Hz band) has been shown to be below 30 nanoradians (rms) and nanoradian range displacement measurement has been demonstrated.

Various applications of angular displacement sensors, including image stabilization, angular vibration monitoring and active control, have been pointed out as past or projected utilizations.

Near-term evolution to a pass band of 0.25 Hz to 500 Hz with an inherent noise of less than 10 nanoradians (rms) has been predicted. In addition, the next generation device has been projected to have a lower sensitivity to linear acceleration and improved (lowered) thermal coefficients.

The Model 8301 IADS is a versatile tool presenting to the design engineer an expanded capability for resolving systems problems. Extension of performance into the nanoradian range is timely--we now see systems technology demanding the resolution and sensitivity offered by this instrument and foresee a continuing growth in that demand.

REFERENCES:

1. H. D. Morris, R. B. Peters and P. H. Merritt, "A Precision Inertial Angular Vibration Measuring System," The Shock and Vibration Bulletin of the Naval Research Laboratory, September 1980, Bulletin 50 (Part 2 of 4 Parts).

2. R. B. Peters, "A Dynamic Angular Calibration System for Broadband Microradian Inertial Sensors," Proceedings of the AIAA Guidance and Control Conference, August 1978; Paper Number 78-1253.

3. H. B. Ellis, "FLIR High Frequency Stabilization Study Program," Aerojet Electrosystems Company, Final Report, AFAL-TR-76-78.

4. "The Boeing 747-100 Airborne Linear and Angular Vibration Measurements," AFFDL/FBG/79-5, May 1979, distribution limited to U. S. Government Agencies.

5. "Douglas DC-10 Airborne Linear and Angular Vibration Measurements," AFFDL/FBG/79-4, May 1979, limited distribution.

6. "Lockheed L-1011 Airborne Linear and Angular Vibration Measurements," AFFDL/FBG/79-7, May 1978, limited distribution.

TITLE: BOREHOLE GRAVIMETRY (CHASING NANO-G'S)

AUTHORS: NORMAN R. BURNFIELD
WILLIAM L. WINSTROM

BELL AEROSPACE TEXTRON
Buffalo, New York

A-1

INTRODUCTION

Recently there has been an increasing interest in obtaining gravity profiles of boreholes to assist in interpretation of the nearby sub-surface structure. This information is particularly useful in the search for gas near a depleted well.

The profiles require measurements of +1g to accuracies of a few nano-g's. The subject of this paper is the design and development of a BoreHole Gravity Meter (BHGM), including investigation of various error sources, some solutions to reduce errors and test results.

REQUIREMENTS OF A BOREHOLE GRAVIMETER (THE PROBLEM)

Borehole gravity measurements are made by lowering a gravimeter into the hole to the desired depth, leveling the gravity sensor and recording the data. This process is repeated at various levels, depending on the sub-surface structure, to obtain vertical gradient measurements. The vertical gradient measurements are transformed into bulk density measurements by the following, as shown in Figure 1.

$$\rho_b = 3.686 - 39.185\ \Delta g/\Delta Z$$

This bulk density information is the information required in the analysis of a borehole.

The bulk density resolution is shown in Figure 2 for gravimeter accuracies of 5 and 10 μgal.

Since the holes are not vertical, provision is required to level the gravimeter. Repeatability of 1 μgal requires leveling repeatability of 10 arc seconds.

Temperature within these holes rises very rapidly. Figures 3 and 4 show a survey in two holes and the associated temperature profile.

The specifications agreed upon for the first development unit were:

Diameter	3.56 inch
Temperature	0 to 130°F
Hole Angle	±15°
Reading Time	5 minutes
Accuracy	5 μgals (5×10^{-9} g's)

DESCRIPTION OF BHGM (THE SOLUTION)

Figure 5 shows a block diagram of the Borehole Gravimeter. The Bell Model XI pendulous force rebalance accelerometer is used as the gravity sensor. The accelerometer and its constrainment electronics are housed in a double oven. The assembly is mounted on a 2 axes platform which uses electrolytic bubble levels as the level sensors and stepper motors for control.

The output of the accelerometer is a d-c signal proportional to gravity. A zener diode in combination with an amplifier is used to subtract 974 μgal (0.994g) from the gravity signal. The residual analog signal is converted to a 0 to 50 kHz pulse rate with a nominal scale factor of 240 μgal/Hz. The zener diode and amplifier are also in a double oven and the A/D converter is in a single oven.

The pulse rate is counted for one second. The one second samples are conditioned for transmission to the surface where a small computer records, filters and converts the data to μgals.

ACCELEROMETER (MODEL XI)

The single-axis, pendulous proofmass, force rebalance device uses a capacitive bridge pickoff to detect acceleration forces acting on the spring supported proofmass.

Rebalancing of the proofmass is accomplished by electromagnetic forces produced when an electric current flows through the torque coil (wound on the proofmass), positioned in a permanent magnetic field.

Movement of the proofmass from the null position, caused by acceleration acting on the mounting base, unbalances a capacitive bridge causing amplitude and phase (direction) modulation of the excitation carrier. The detected error signal is demodulated and amplified to provide a restoring current which is passed through the proofmass-mounted torque coil. By monitoring the restoring current, a measurement of input acceleration is obtained. The accelerometer is 1.3 inches high and 0.9 inch in diameter with seif-contained analog constrainment electronics.

NOISE ERRORS

The threshold or minimum detectable acceleration that the gravimeter can measure is limited by random noise generated by the accelerometer and its associated electronics. Tests conducted in the laboratory have shown that this noise, not the capacitive pickoff or suspension system, determine the threshold level. The following analysis describes the major noise sources and their contribution to the overall gravimeter noise.

a) Accelerometer Noise

The random thermal noise acting on the accelerometer pendulum produces random torquer or "acceleration noise" and shows up as an error since the current required to constrain the pendulum is used to measure the acceleration input. These random torques are due to random electron flow in the pendulum coil support reacting with the torquer magnetic field and random collision of gas molecules with the pendulum. The magnitude of the thermal noise is given by:

$$\text{RMS Torque Noise} = \frac{\sqrt{4\,k\,TC\,\Delta f}}{P}\ \text{g's}$$

For the Model XI, $K = 1.38 \times 10^{-16}$ erg/°K

$T = 300$°K

$C = 85$ dyne-cm-sec

$P = 116$ dyne-cm/g

Δf = Bandwidth (Hz)

The system bandwidth is determined by the system filtering time constant which is 300 seconds. Substituting the above parameters yields:

RMS noise = 1.0 μgal

b) Constrainment Loop Electronics

A diagram of the accelerometer constrainment loop electronics is shown in Figure 6. The constrainment loop limits the deflection of the pendulum to less than 10^{-5} rad/g and provides a dc output current proportional to acceleration input. The electronic noise in the loop interacts with the suspension spring to produce noise in the dc constrainment current output. The major constrainment loop noise source is the preamplifier. Its noise contribution in g's is given by:

$$V_P = \frac{E_N \sqrt{\Delta f}\, K_S}{G_P}$$

where: E_N = spectral density of preamp noise = 12×10^{-9} volts/$\sqrt{Hz}$

Δf = system bandwidth

G_P = pickoff gain = 5 volts/radian

K_S = spring constant = 5 g's/radian

Therefore, V_P = 0.36 μgal

c) Bias Generator

Since variations in gravity over a 5 microgal to 6000 milligal range are to be measured, the nominal 1g acceleration is biased out to provide an analog output voltage scaling from the accelerometer of 1 v/g. The noise contribution of the bias generator is as follows:

$$V_B = \frac{E_N \sqrt{\Delta f}}{KB}$$

where: E_N = bias reference noise spectral density = 2×10^{-7} v/$\sqrt{Hz}$

KB = bias = 6.4 volts/g

Δf = system bandwidth

for: V_B = 1.0 μgal

d) Scaling Amplifier Electronics

The accelerometer output voltage is amplified by a scaling amplifier to provide a dc output voltage of 1 microvolt per microgal. This signal may then be read directly or converted by an analog to digital converter to a digital format. The noise contribution of the scaling amplifier is as follows:

$$V_S = \frac{E_N \sqrt{\Delta f}}{K_A}$$

where: E_N = scaling amplifier noise spectral density = 4×10^{-7} v/$\sqrt{Hz}$

K_A = system scale factor = 1000 v/g

Δf = system bandwidth

V_S = 0.01 μgal

ENVIRONMENTAL ERRORS

1. Temperature Errors

The gravimeter temperature control requirements are determined by the changes in ambient temperature expected during borehole operation. Errors due to ambient temperature changes are minimized by a combination of temperature compensation and control. The thermally related error sources are discussed below.

a) Accelerometer

The major thermal errors in the accelerometer are due to bias and scale factor variations. The bias error is due to change in suspension torques acting on the pendulum and scale factor due to magnetic flux density change. A sensor in the accelerometer whose resistance varies with temperature is used to compensate the bias and scale factor. The uncompensated bias and scale factor error of 25 ppm/°F is reduced to 250 microgal over the oven temperature control variation of ± 0.01°F. The compensation network shown in Figure 1 uses a selected resistor in the output sampling network to compensate the output voltage with temperature. Its value is determined by varying the accelerometer oven temperature 0.01°F and setting the resistance value to obtain no net output change.

b) Electronics

The accelerometer contrainment loop, biasing, and scaling electronics temperature errors are shown below for an oven temperature variation of ±0.01°F.

Source	Error (μgal)
Constrainment Loop dc Torquing Amplifier Voltage Offset	± 0.005
Bias Reference Source Voltage Variation	± 4.7
Scaling Amplifier Voltage Offset	± 0.0004
Scaling Network Resistors	± 9.0
Scaling Amplifier Resistors	± 0.003
Uncompensated R_{SS} Error	10.0
Compensated Error	2

2. Dynamic Errors

The instrument is subjected to vibration while it is moving from one station to another as well as when it is in a stationary reading mode. The accelerometer is constrained to withstand up to 10 g's dynamically during transit in the borehole so that no damage occurs to the suspension system. During the reading mode with gimbals locked some vibratory motion is present and must be filtered in order to obtain reading resolution in the 5 microgal range.

The other errors of concern are those due to nonlinearties in the Model XI accelerometer. The accelerometer dynamic error model may be represented by:

$$A_{IND} = K_0 + K_1 a + K_2 a^2 + K_3 a^3$$

where a = input acceleration

A_{IND} = indicated output acceleration

K_0 = accelerometer bias

K_1 = accelerometer scale factor

K_2 = accelerometer 2nd order nonlinearity

K_3 = accelerometer 3rd order nonlinearity

If a vibration input of $a_V \sin \omega\tau$ is present, a rectification error $K_2 a_V^2/2$ will occur. If the vibration input were constant from one station to another, this error would not be significant when the readings are differenced. However, it is likely that the vibration inputs at each station will be the same.

Centrifuge tests on the Model XI have shown that $K_2 = 5 \times 10^{-7}$ g/g^2. For a dynamic error of less than 5×10^{-9} g (5 μgal), the vibration amplitude should be less than 0.1g.

3. Magnetic Sensitivity

The accelerometer is constrained by electromagnetic forces generated by two permanent magnets and the current in the pendulum torque coil. Although the system operates in a closed magnetic circuit, the accelerometer scale factor will not be completely insensitive to external magnetic fields because some external flux will couple into the magnetic circuit. Test conducted on the Model XI show a magnetic sensitivity of 5 ppm per gauss with no shielding. The unit is therefore, shielded to provide a residual sensitivity of 5μgal/gauss.

DRIFT ERRORS

The gravimeter output contains a drift component in addition to random noise. The drift error is minimized by post data correction. Additional data corrections for tidal variations and vertical gravity gradient changes must be made. Correction of the drift during post data analysis can therefore, be accommodated provided the magnitude of the drift and its uncertainty are reasonably low. For a typical survey period of 12 hours with four station readings per hour, a total of 48 data points can be obtained to fit a best straight line drift curve. The system design goal is to obtain a 1σ uncertainty in the slope of the drift curve of 5 μgal and an absolute drift over a 12 hour survey of 20 μgal per hour.

The major source of gravimeter drift is the accelerometer bias and scale factor. Typical Model XI drift data taken over a 70 day period is shown in Figure 7. The absolute drift was 214 μgal/day.

TEST RESULTS (THE REALITY)

Laboratory Tests

Components

Separate noise tests were run in the laboratory on the zener and the operational amplifier, digitizer combination.

Zener Tests

The noise test station for the zener diode is shown in Figure 8. The approach is to compare the zener with a bank of standard cells, digitize, filter and record the output. It is recognized that the noise of the standard cells may contaminate the results but this method provides a quick and simple method to screen out obviously unuseable diodes.

Figure 9 is a plot of output of the zener test station and shows the zener noise to be within the system equivalent of 10 μgals, rms.

System Test

A stability test was run on the completed system. The data is shown in Figure 10 compared with the theoretical lunar/solar effects.

Field Tests

The prototype system was tested in a borehole in April, 1980. After lowering into the hole, the accelerometer was erected to the vertical and allowed to stabilize. The stability data was collected and corrected for temperature variations, drift and lunar solar effects. The plot of the data (Figure 11) shows a residual error of 8 μgals, rms.

During the test, it was found that the stepper motor disrupted thermal equalibrium during the leveling process and created thermal transients. The unit was returned to the laboratory where the leveling control modes were modified to reduce the thermal impact of the stepping motor. Temperature monitors were added to improve the capability of correcting for temperature.

The system is scheduled for another down hole test in the fall of 1981.

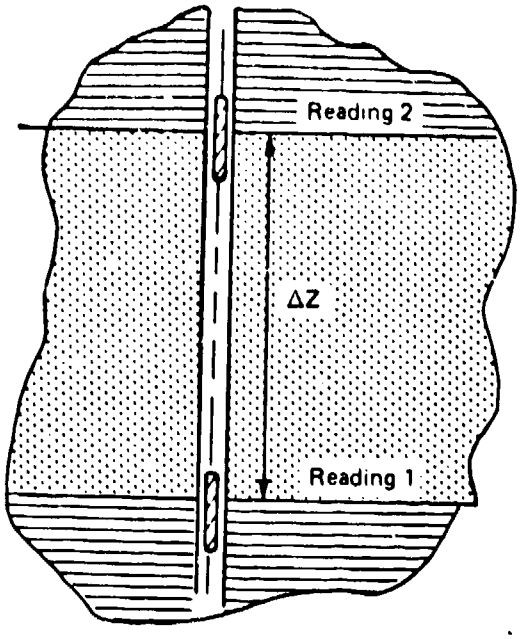

ρ_b = 3.686 - 39.185 Δg/ΔZ

Δg = Reading 1 - Reading 2

ΔZ = Thickness

ρ_b = Bulk Density

Cross Section View

Figure 1. Basic Density Equation

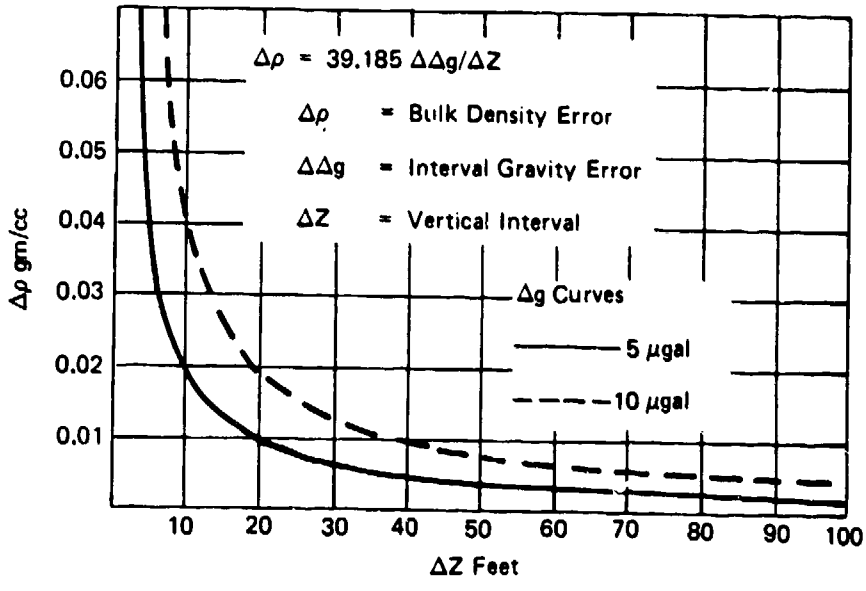

Figure 2. Error Equation

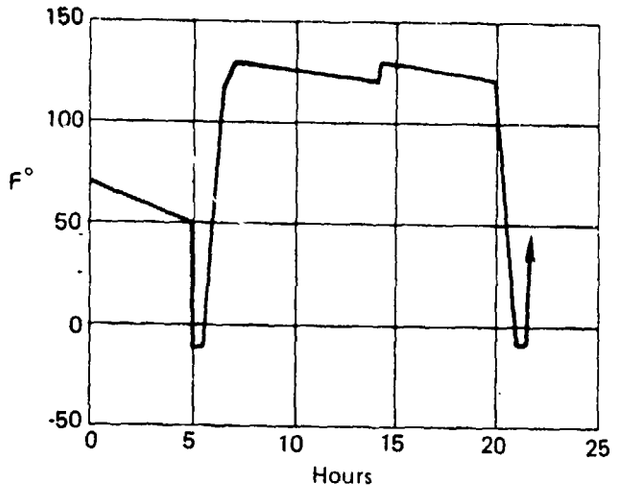

Figure 3. Survey - Northern Michigan in Winter

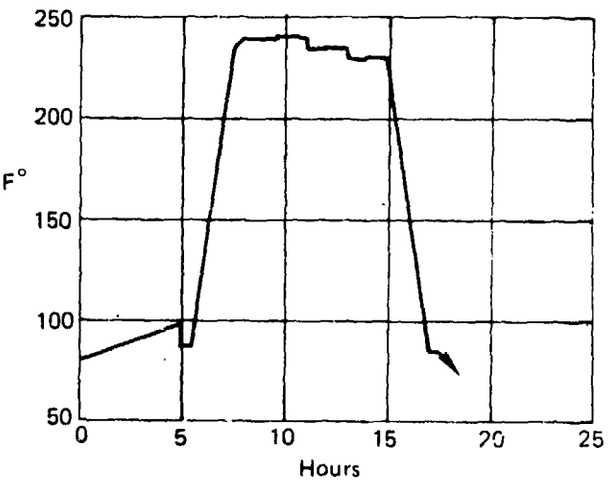

Figure 4. Survey - 12,500 ft Gulf Coast Well

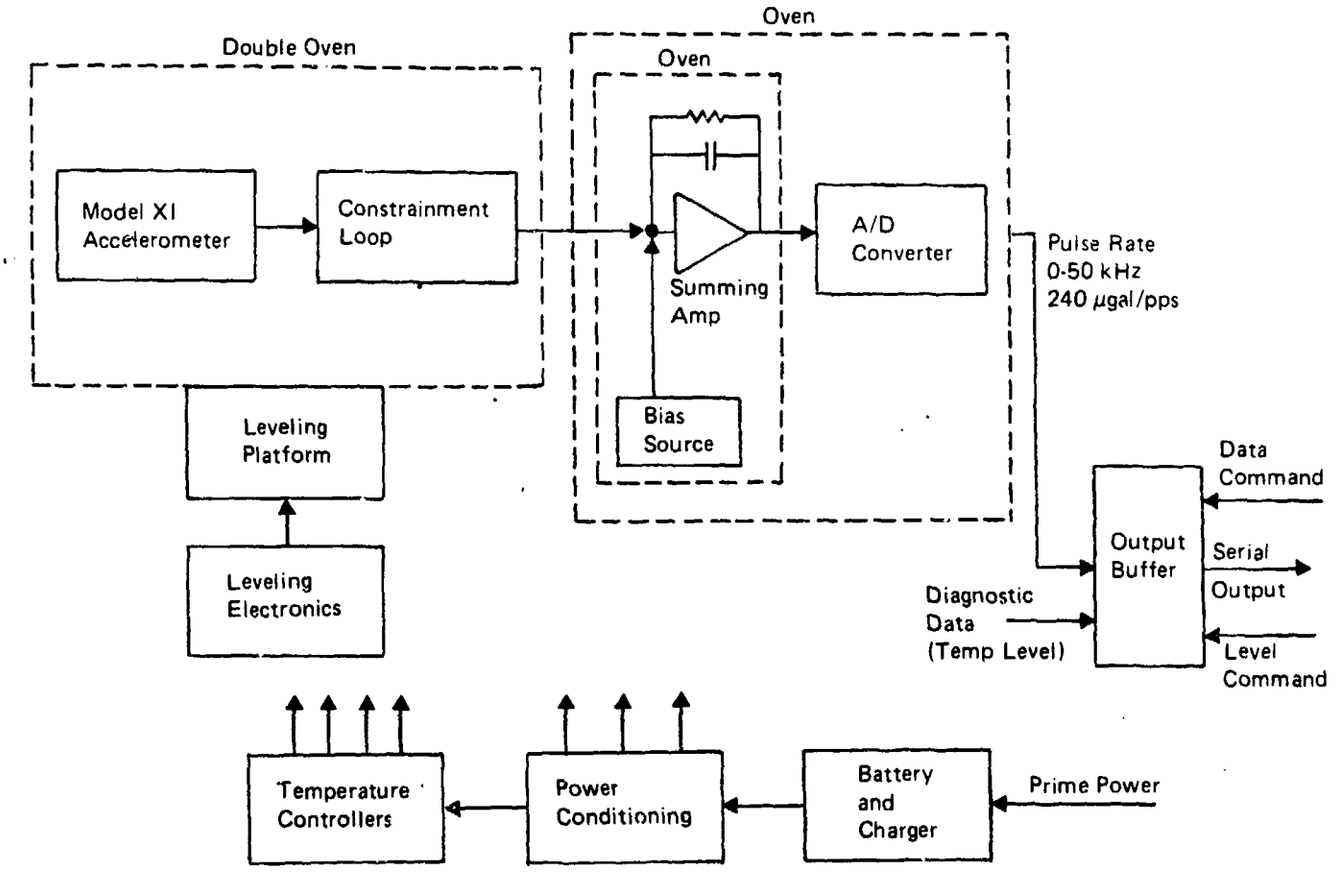

Figure 5. Borehole Gravity Meter Block Diagram

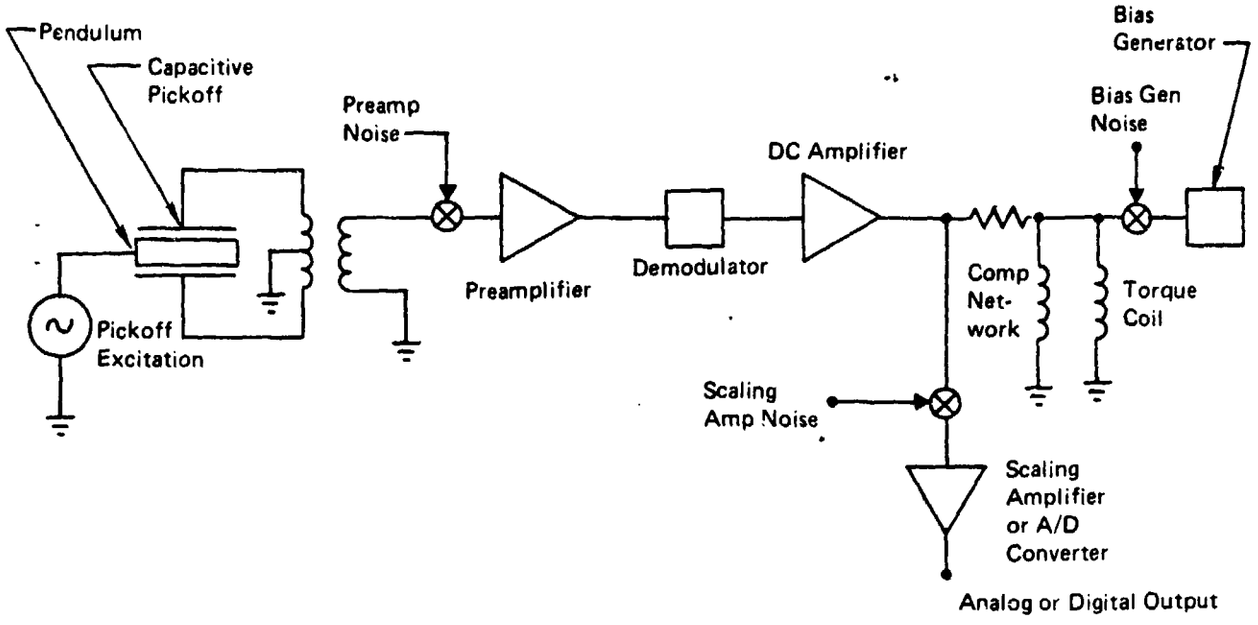

Figure 6. Electronics Block Diagram

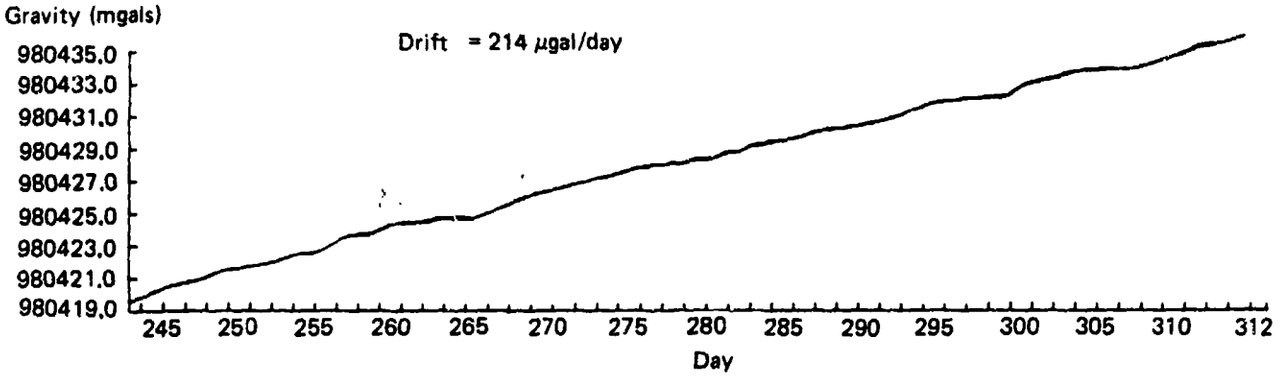

Figure 7. 70 Day Drift Test

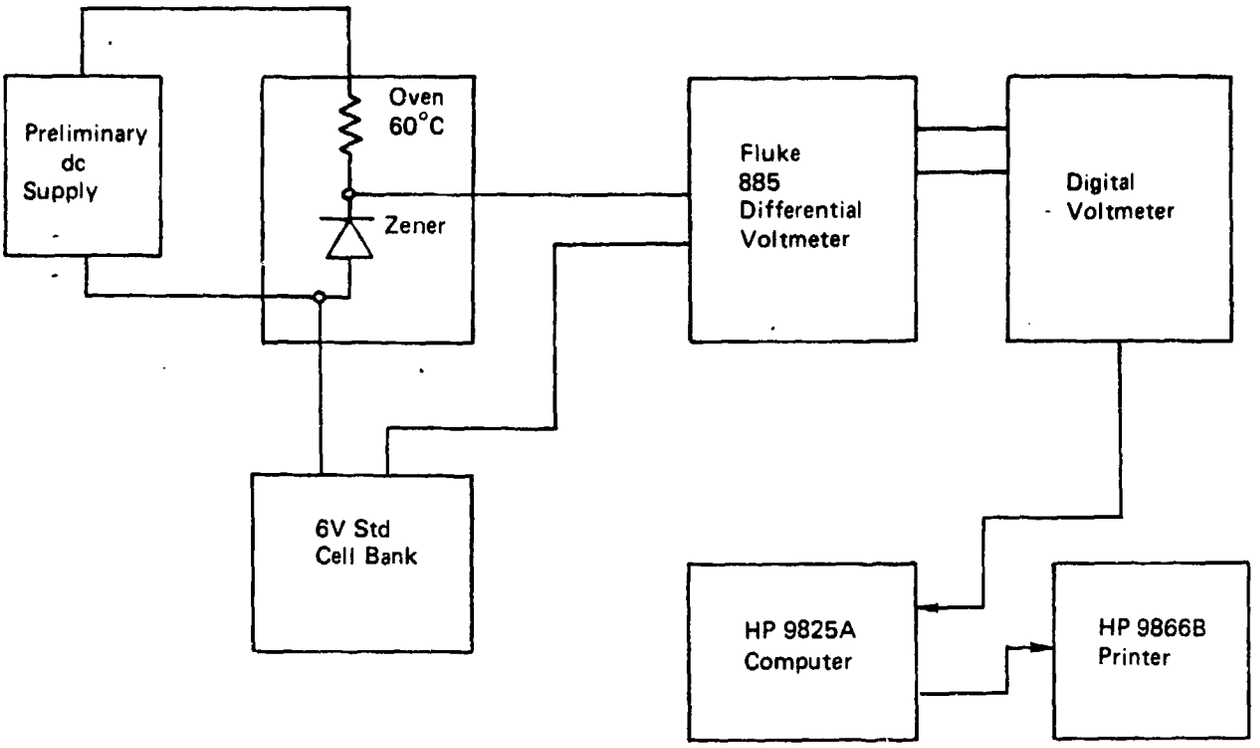

Figure 8. Zener Test Set

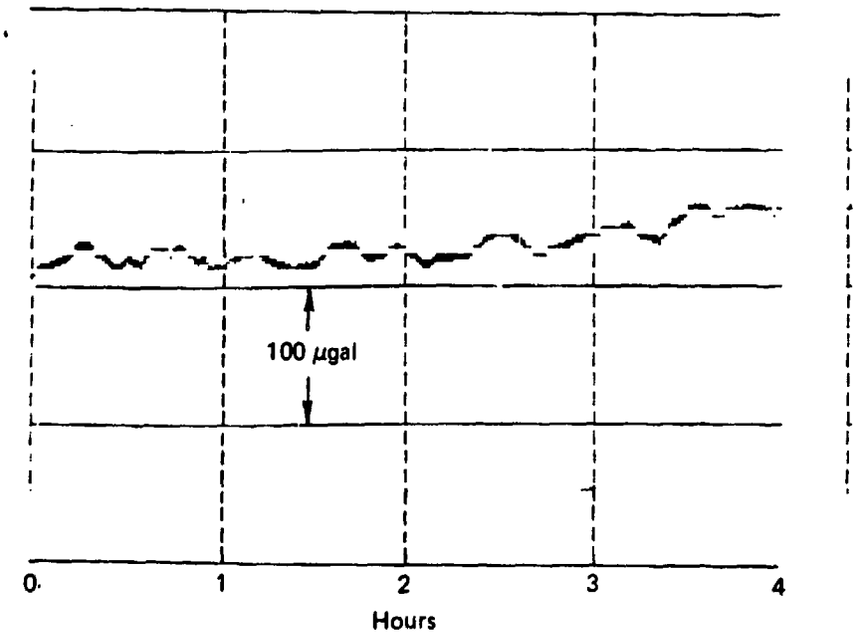

Figure 9. Zener Diode Noise Test

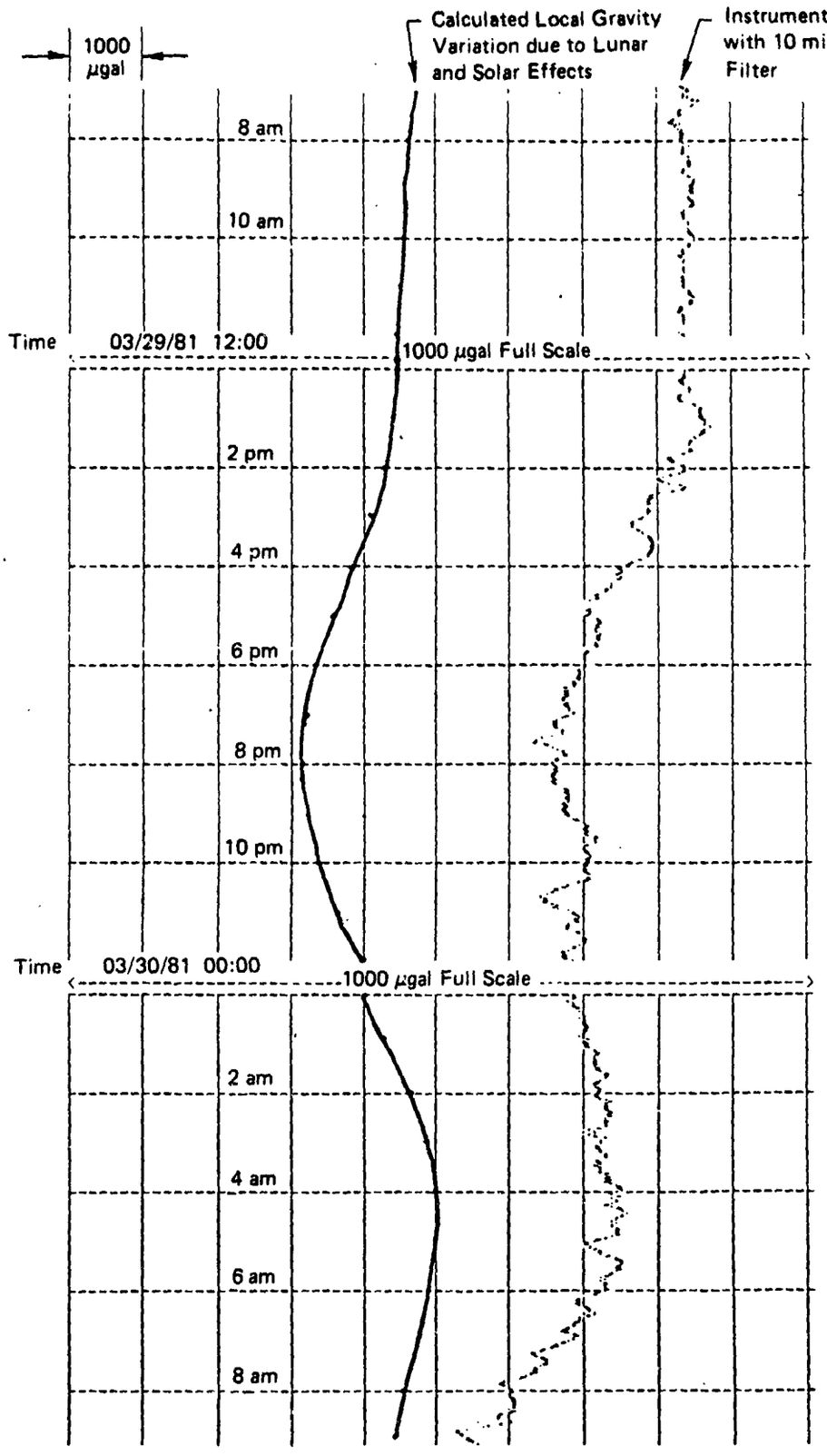

Figure 10. 24 Hour Stability Data on Borehole Gravimeter

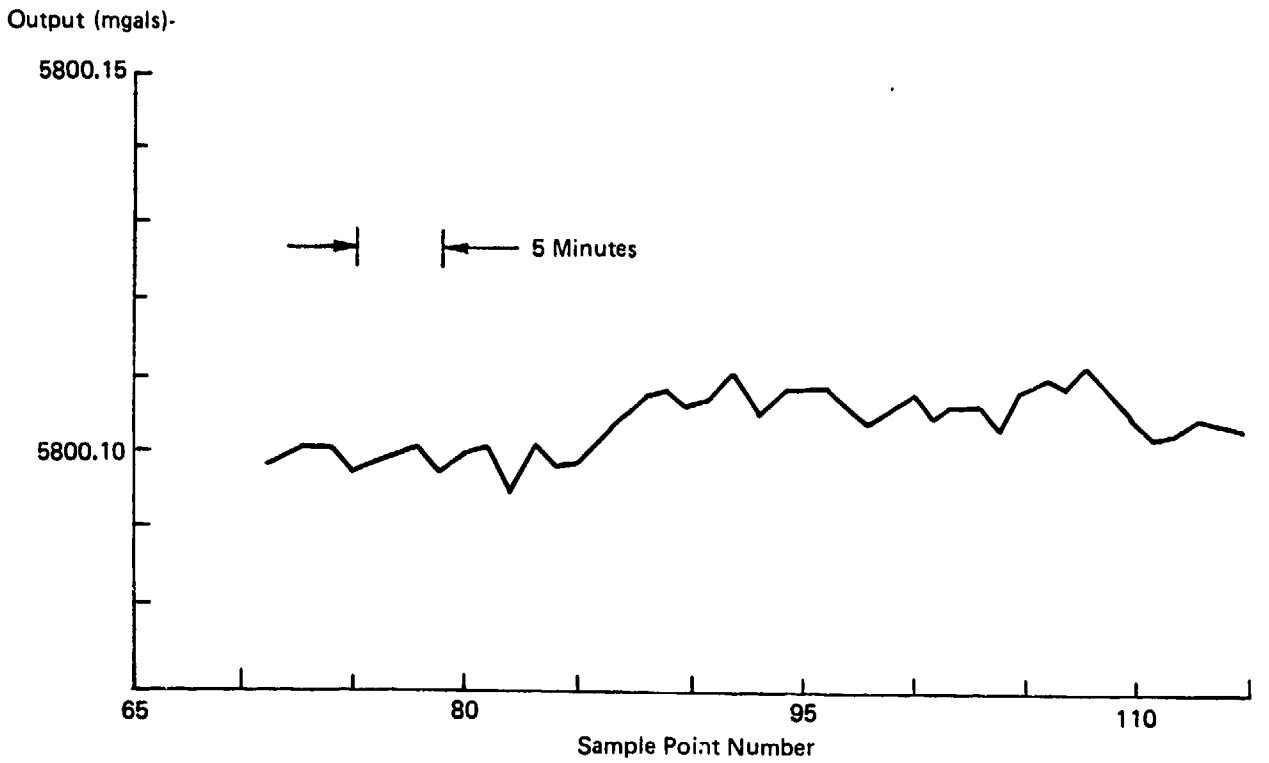

Figure 11. Down Hole Test

TITLE: EXPERIENCE AND TEST LIMITATIONS IN THE PRECISION MEASUREMENT OF GYRO ANGULAR OUTPUT STABILITY IN RATE ENVIRONMENTS

AUTHORS: ROBERT B. IRVINE
JOHN W. RITTER
ROBERT L. VAN ALSTINE

TELEDYNE SYSTEMS COMPANY
Northridge, California

TABLE OF CONTENTS

LIST OF ILLUSTRATIONS

ABSTRACT

Attitude control requirements for a number of military and NASA programs are predicated on having a stable attitude reference in the sub-arc second region. Total jitter requirements as low as 30 nanoradians RMS with strap-down loop bandwidths as high as 100 Hz have been specified. Other current requirements include noise equivalent angle (NEA) performance, as defined in one specification for the NASA Standard Inertial Reference Unit (DRIRU II), to less than one arc second accuracy w[illegible] input rates up to 200°/hr.

Recent noise and jitter tests conducted on dry-tuned gimbal gyros and the DRIRU II have revealed that a limitation in inertial test capability appears to exist. This limitation is evident when attempting to measure precision gyro power spectral noise and noise equivalent angle performance under constant angular rate inputs up to 10 degrees/second as required by some current agile vehicles.

Extensive efforts have been expended by Teledyne Systems Company and other manufacturers and agencies to measure the required output stability performance under these conditions with little success to date. The lack of success in demonstrating this performance is mainly due to test table limitations such as flutter and wow, servo instabilities and readout inaccuracies. Teledyne has been able to demonstrate low noise performance of the SDG-5 gyro and the DRIRU II under static (Earth's rate) conditions (e.g., 25 nanoradians RMS over 50 Hz for the SDG-5 gyro and NEA of less than 50 milli-arc seconds on a modified DRIRU II), but has been unsucessful in attempts to provide a stable input for the higher rate tests. Operation of two gyros "back-to-back" in order to determine and analytically eliminate common mode environmental input noise components has been employed and resulted in only limited sucess due to the difficulties in matching each gyro's specific control loop performance characteristics. Representative data are presented that supports the validity of this approach and analysis is discussed that specifies the requisite levels of matching.

Other potential test methods which warrant further investigation are suggested and discussed. In the near term, testing using the CIGTF large centrifuge in the coast down mode or a high inertia rate table could satisfy this need. In the long term, it appears that dedicated, certified test facilities will be required for constant rate and rate/slew reversal tests in order to support a large number of emerging programs including high energy laser, particle beam and other weaponry and scientific precision pointing applications.

Results of some recent testing conducted on SDG-5 gyros on a single axis air-bearing table with large inertia operating in the coast-down mode are presented. The test setup utilized is briefly described and sample data are presented demonstrating performance levels in the 40 nanoradian RMS region with 100 Hz bandwidth for coast-down varying rates from 3 degrees/second.

1.0 INTRODUCTION

There exist in the literature numerous publications and reports on noise performance tests conducted on various types of gyroscopes for a variety of applications. Typical recent test results for high accuracy dynamically tuned gyros have shown drift rate noise levels in the region of 10^{-6} to 10^{-8} $(°/hr)^2/Hz$ for frequencies from 0.01 to 10 Hz. However, these tests have invariably been conducted under "static" test conditions, i.e., under zero input rate other than the Earth's rate component at the test site [1] [2]. The major concern in obtaining this type of data has generally been to provide a stable test environment which is isolated from spurious mechanical, thermal and electrical inputs. However, with the continuing demand for higher accuracy attitude determination and control for space and terrestrial applications, it has been necessary to extend these noise measurements to include the effects, if any, of dynamic rates (typically 1 to 3°/sec) as currently required for a number of high accuracy pointing and tracking systems. While it has been presumed that there would be no deleterious effects on gyro output noise (based upon a knowledge of dry tuned gyro design and construction), [3] it has been difficult in practice to demonstrate this by actual test.

The Model SDG-5 dry tuned gyro has been extensively tested for power spectral density (PSD) noise performance over the last five years. A chronology of the more significant tests conducted is presented in Table 1. The majority of the tests were conducted under the "static" conditions previously described. This paper focuses on the experience and limitations of noise performance test under rate. Considerable efforts were expended by Teledyne Systems Company, the Jet Propulsion Laboratory, NASA Goddard and the Charles Stark Draper Laboratory to measure the DRIRU II noise equivalent angle (NEA) performance under constant input rates without real success. Additionally, Martin Marietta Aerospace conducted a series of PSD tests on SDG-5 gyros under rate. Tests conducted on a single gyro in this series showed similar unacceptable performance caused mainly by test table limitations such as flutter and wow, servo instabilities and readout inaccuracies. Operation of two gyros "back-to-back" in order to determine and eliminate common mode or correlated noise components demonstrated the validity of the approach, but has limited success due to mismatching of the specific gyro and control loop characteristics.

Some recent testing conducted on a pendulous air bearing single axis table operating in the coast-down mode from 3°/sec has been completed which did demonstrate the requisite PSD noise performance levels under varying input rates. While these test results are most rewarding and demonstrate that the noise performance of the SDG-5 gyro is independent of rate inputs up to 3°/sec, it appears that dedicated, certified test facilities are required in order to support a large number of emerging precision pointing and tracking applications.

This paper describes the experience and results of PSD noise tests conducted on the SDG-5 gyro to date and makes recommendations for future test efforts including facility considerations.

Table 1. Chronology of PSD Noise Tests on SDG-5 Gyro

TEST FACILITY	PURPOSE OF OF TEST	TEST TYPE	1976	1977	1978	1979	1980	1981
BOEING AEROSPACE CO. 4 GYROS, 1 HZ LOOP	SPACE TELESCOPE EVALUATION	STATIC PSD	△					
MARTIN MARIETTA CORP. 2 GYROS, 7 Hz LOOP	SPACE TELESCOPE AND CLASSIFIED PROG.	STATIC PSD	△					
HOLLOMAN CIGTF 1 GYRO, 7 Hz LOOP	SAMSO-HAARS TEST SERIES	STATIC PSD	△					
BOEING AEROSPACE CO. 1 GYRO, 7 Hz LOOP	SPACE TELESCOPE EVALUATION	STATIC PSD	△					
LOCKHEED MSC 1 GYRO, 7 Hz LOOP	SPACE TELESCOPE EVALUATION	STATIC PSD		△				
TELEDYNE SYSTEMS CO. 1 GYRO, 20 Hz LOOP	FINE POINTING APPLICATIONS	STATIC PSD/NEA			△			
MARTIN MARIETTA CORP. 2 GYROS, 20 Hz LOOP	CLASSIFIED PROGRAMS	STATIC & DYNAMIC PSD			△			
HOLLOMAN CIGTF 1 GYRO, 20 Hz LOOP	NASA, STANDARDS DIVISION	STATIC PSD				△		
TELEDYNE SYSTEMS CO. & JPL, 7 HZ LOOP	NASA STD DRIRU-II TEST PROGRAM	STATIC & DYNAMIC PSD			△	———	△	
TELEDYNE SYSTEMS CO. 1 GYRO, 100 Hz LOOP	WIDE LOOP BAND-WIDTH GYRO TESTS	STATIC PSD					△	
HUGHES AIRCRAFT CO. 2 GYROS, 100 Hz LOOP	NOISE PERFORMANCE UNDER RATE	STATIC & DYNAMIC PSD						△

T130887

2.0 EARLY EXPERIENCE

2.1 Back-to-Back Gyro Tests Under Rate

A series of tests was conducted in late 1978 by the Martin-Marietta Corporation, Denver for the purpose of evaluating noise performance of SDG-5 gyros under rates up to 0.5°/sec for fine pointing applications.[4] Teledyne supplied to Martin a standard production gyro (S/N 082), as used in the DRIRU II NASA standard redundant inertial reference unit, along with laboratory capture and readout electronics for the evaluation program.

Initial static testing yielded drift rate noise levels consistent with previously reported low frequency data on SDG-5 gyros (e.g., 10^{-6} to 10^{-5} $(°/hr)^2/Hz$ below 1 Hz), but results of testing under rate using a single axis commercial air bearing rate table yielded results several orders of magnitude higher. Typical results of these initial static and rate tests are shown in Figure 1. The data has been smoothed for clarity. Because of the extremely high indicated noise output under rate, it was suspected that the gyro was sensing noise inputs due to spurious rate table motions. However, no independent measure of table motion was available to verify this.

A second gyro and set of electronics were supplied by Teledyne for comparison testing with the gyros mounted on the rate table "back-to-back," i.e., with the gyro input axes colinear. This was done in order to determine to what extent the output noise signatures of the two gyros were correlated.

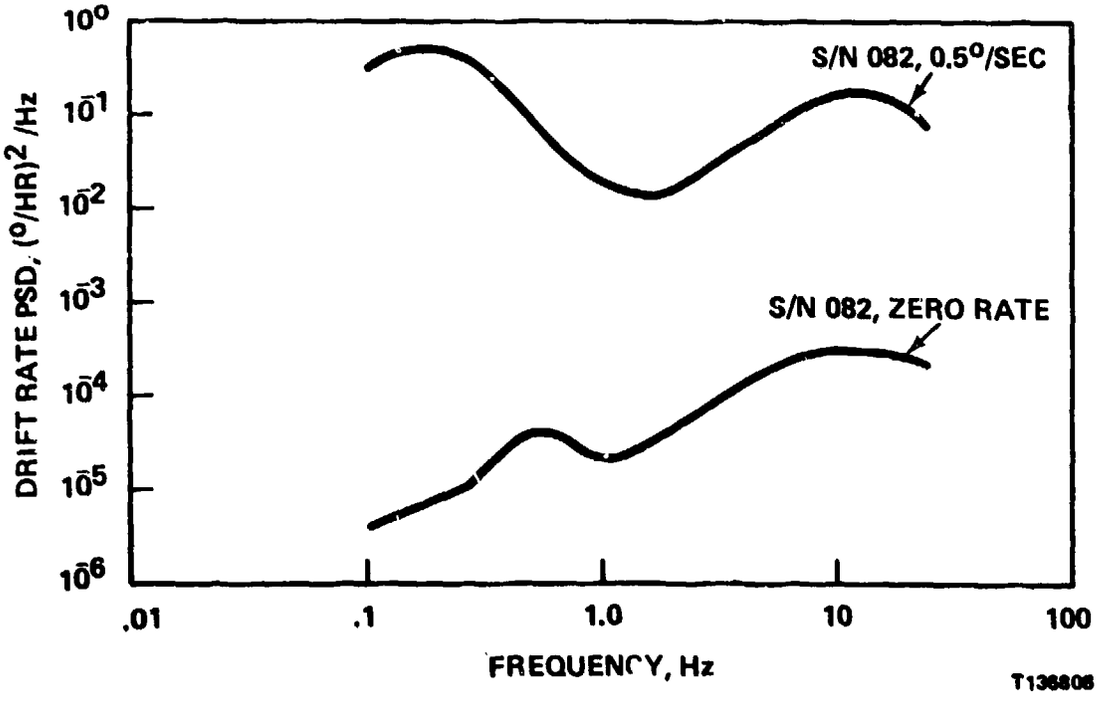

Figure 1. Drift Rate PSD for Static and Rate Inputs, Uncompensated

The presence of correlated or common mode output signals would indicate that there was either a common input source or separate correlated sources. Since the gyros were operating with completely different support electronics, including individual spin motor and pickoff excitation supplies, it could be concluded that there would be little probability of separate correlated sources within the gyros and that any correlated components of the gyro output signals would be caused by a common input stimulus, namely, rate table noise or other environment effects.

It can be shown mathematically that common mode components of two noise signals can be eliminated by differencing the two signals before performing the power spectral density analysis. [5] Any remaining noise components in the PSD signature would then be non-correlated.

The block diagram shown in Figure 2 illustrates the various signals present in a system with two gyros mounted on a rate table for back-to-back testing. The frequency response functions of the gyros are represented by $G_1(f)$ and $G_2(f)$. The common mode input noise of the table sensed by the gyro is represented by its power spectral density function $\Gamma_{cc}(f)$. The gyro noise sources that are independent of table noise are represented by their respective power spectral density functions $\Gamma_{Z_1Z_1}(f)$ and $\Gamma_{Z_2Z_2}(f)$. The output of each gyro is the sum of the noise due to table induced motion plus its own noise as shown in Figure 2.

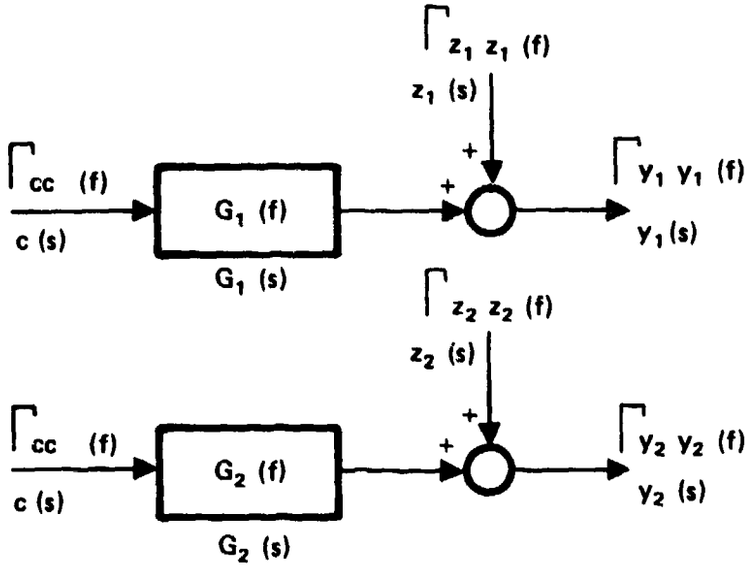

Figure 2. Noise Model for Two Gyros Operating Back-to-Back

Using the Laplace variable notation C(S), G(S), Z(S) and Y(S) for each of the variables, we can write,

$$Y_1(S) = G_1(S)\, C(S) + Z_1(S) \quad (1)$$

$$Y_2(S) = G_2(S)\, C(S) + Z_2(S) \quad (2)$$

The power spectral density functions are related by,

$$\Gamma_{Y_1Y_1}(f) = \left|G_1(f)\right|^2 \Gamma_{CC}(f) + \Gamma_{Z_1Z_1}(f) \quad (3)$$

$$\Gamma_{Y_2Y_2}(f) = \left|G_2(f)\right|^2 \Gamma_{CC}(f) + \Gamma_{Z_2Z_2}(f) \quad (4)$$

The difference between the two gyro outputs is,

$$X = Y_1(S) - Y_2(S) = \left[G_1(S) - G_2(S)\right]\ C(S) + Z_1(S) - Z_2(S) \quad (5)$$

The power spectrum of this difference function is given by,

$$\Gamma_{xx}(f) = \left|G_1(f) - G_2(f)\right|^2 \Gamma_{cc}(f) + \Gamma_{Z_1Z_1}(f) + \Gamma_{Z_2Z_2}(f) \quad (6)$$

Note that the first term on the right side of equation (6) contains two factors, the common mode input and the square of the difference between the two gyro transfer functions. This term will approach zero as the transfer functions of the gyros (including capture servo electronics) are matched. The remaining terms, which are the independent noise components of each gyro, will be root-sum-squared together when represented on an overall PSD plot of the difference data.

This method of data anlaysis was used on the output data from the two back-to-back test gyros under rate inputs up to 0.5°/sec. Figure 3 shows the individual gyro noise test data (Curves A and B) and the results of differencing these data as described above (Curve C). A two order of magnitude reduction in noise level is evident, indicating that a part of the noise existing at the output of each gyro was due to input table motion (or other correlated inputs), not noise generated independently by the gyros.

Although the above results showed a large improvement over the single gyro output data, the remaining uncorrelated noise levels were still significantly higher than would be acceptable for the fine pointing applications under consideration. It was suspected that a major part of the remaining noncorrelated noise was the result of differences in the capture loop electronics used for the two gyros. The frequency response characteristics of the two loops were not precisely matched since they had been originally designed

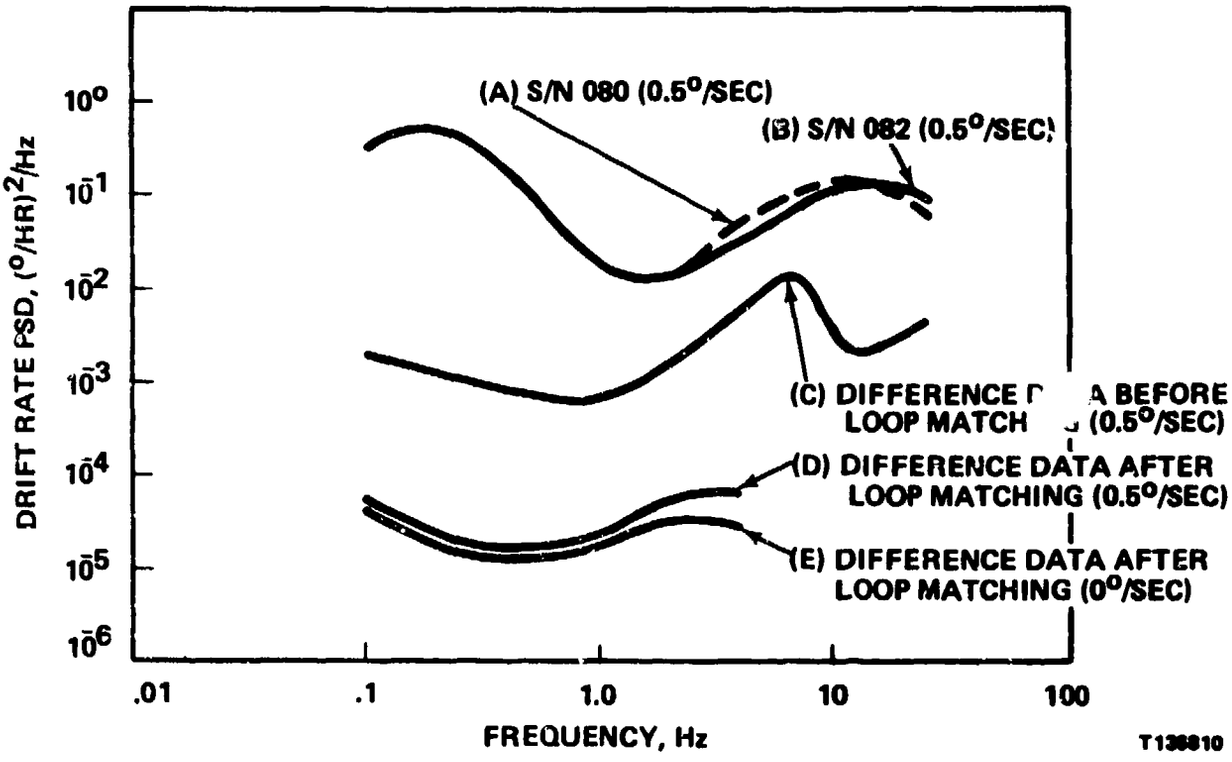

Figure 3. Drift Rate PSD for 0.5°/Sec Input Rate, Individual Gyros and Residual After Removal of Correlated Components

for different purposes and were not of the same configuration. Frequency response tests showed amplitude differences of 3 to 4 dB for frequencies up to 10 Hz.

An attempt was made to better match the response characteristics of the two loops by adding external compensation circuitry consisting of second order low pass filters with break frequencies between 7 and 10 Hz. This resulted in frequency response amplitude differences of less than 1 dB for the two loops (although phase matching degraded somewhat). The back-to-back tests were repeated for this condition and the difference data showed a further one to two order of magnitude improvement. These results are shown in Figure 3, Curve D. Note that this curve has not been extended beyond 5 Hz because of the effects of the filtering on the raw gyro output data. Also shown (Curve E) is the difference data obtained at zero rate after loop matching.

Overall, the process of removing the correlated noise components by differencing the back-to-back gyro output data using loops with amplitude responses matched to within 1 dB yielded residual uncorrelated noise levels three to four orders of magnitude below the raw noise data measured individually on each gyro for rates up to 0.5°/sec. These residual levels approached the static noise levels obtained on individual gyros and from differencing the individual gyro data. Better loop matching undoubtedly would have reduced the differences to insignificant levels.

2.2 DRIRU II Noise Equivalent Angle (NEA) Under Rate

NEA performance requirements of 1.0 arcsec peak-to-peak maximum under orbital rate conditions of 200 arcsec/sec are specified for the NASA Standard High Performance Inertial Reference Unit (DRIRU II). [6] [7] Although analysis of the system operating characteristics revealed no identifiable reason for the 200 arcsec/sec NEA performance to be different from that measured under static conditions (Earth rate input only), this requirement prompted a significant test effort at Teledyne and subsequently at the Jet Propulsion Laboratory in an attempt to verify the validity of this conclusion. Tests were performed with the system operating in the "low" range (nominal pulse weight = .05 $\widehat{\text{sec}}$) and were based on accumulating 200 ms samples over a one hour test period, then processing the data to remove the constant input rate (200 arcsec/sec) to obtain the NEA.

Initial tests at Teledyne conducted during the period of late 1978 to February 1980 involved the use of a single axis, ball bearing rate/positioning table together with supporting thermal control equipment, all of which was located in a moderately temperature controlled laboratory. Data from two different gyros within the system were sampled simultaneously to allow for elimination of the "common mode" table inputs by subtracting the output of one gyro from the other. Typical NEA performance measured with 200 arcsec/sec input rates under these test conditions were 6 to 25 arcseconds (p-p).

The problems associated with the test facility which prevented more precise measurements were:

a. Noise inputs from the test chamber blower motors and the environmental hose/electrical connections to the test chamber. These items were needed to perform tests at a constant 66°C (gyroscope temperature) per the contract test requirements.

b. Variations in the laboratory temperature which were up to 15°F per hour forcing the chamber control system to input heating or cooling air to maintain the desired temperature.

c. Cultural inputs due to vehicular traffic including an adjacent railroad, equipment and personnel movement in the laboratory.

d. Rate table noise and error effects due to the table mechanical arrangement and its control electronics during the rate tests.

Upon recognizing these test facility limitations, an effort was initiated to locate an improved test facility with superior test equipment. Discussions with the Charles Stark Draper Laboratory and the Jet Propulsion Laboratory ultimately led to the selection of an available test laboratory, at JPL, for a second series of tests.

This second attempt to measure NEA with 200 arcsec/sec rate inputs was performed in March 1980 in a well controlled temperature environment (±1°F). The DRIRU II was mounted on a gas bearing supported rate table, and then

the system and table structure were totally enclosed within a rigid box fabricated from plastic foam as shown in Figure 4. All test cables to the DRIRU II/Rate Table were mounted in a manner to minimize mechanical coupling between the table and the surrounding structure. An HP 9845 computer system with its CRT display and a PDP-11/05 computer system were simultaneously interfaced with the DRIRU II.

After allowing the DRIRU II and all test equipment to stabilize for approximately 14 hours, preliminary test runs were initiated to check out the measurement systems and inherent noise of the table servo loop. Temperature changes at the DRIRU II were measured using DRIRU II telemetry thermistors in the gyros and temperature was found to be stable within 0.03°C/hour. This level of temperature stability was maintained throughout the test period.

Attempts to measure NEA with 100 and 200°/hr table input rates revealed data acquisition problems in both the PDP 11/05 system and the HP 9845 systems. Since the HP 9845 system provided for rapid data reduction and plotting of data compared with the data reduction time of the PDP 11/05, the decision was made to abandon further efforts with the PDP 11/05 and to acquire all subsequent data using the HP 9845 system.

NEA measurements were also made with zero rate inputs with the table both supported and unsupported for comparison. The zero rate NEA agreed well with previous measurements at Teledyne and other facilities.

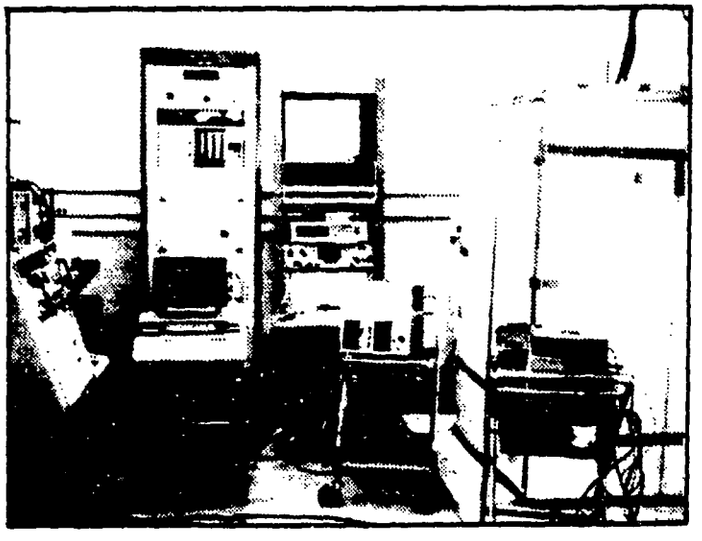

Figure 4. NEA Test Setup at JPL

Subsequent tests revealed the importance of minimizing the "axis/axis sampling delay time interval" which results from the fact that each gyro channel has its own master reference clock from which the computer measurement system samples data. The nonsimultaneous sampling of data from the two axes resulted in the high frequency noise present in the difference data. The noise level increased with an increase of the sampling delay time.

The test results obtained using the JPL test facility were significantly better than previously observed. The NEA performance obtained by subtracting the output of one gyro from the other (to remove common mode noise from the table) typically varied between 1.5 to 2.5 arcseconds (Figures 5 and 6) for test periods of up to 900 seconds. Subsequent analysis performed after completion of these tests by Goddard Space Flight Center personnel revealed that further improvement in the data might have been achieved if the data sampling of the two gyro output axes had been accomplished simultaneously rather than sequentially as necessitated by the hardware configuration.

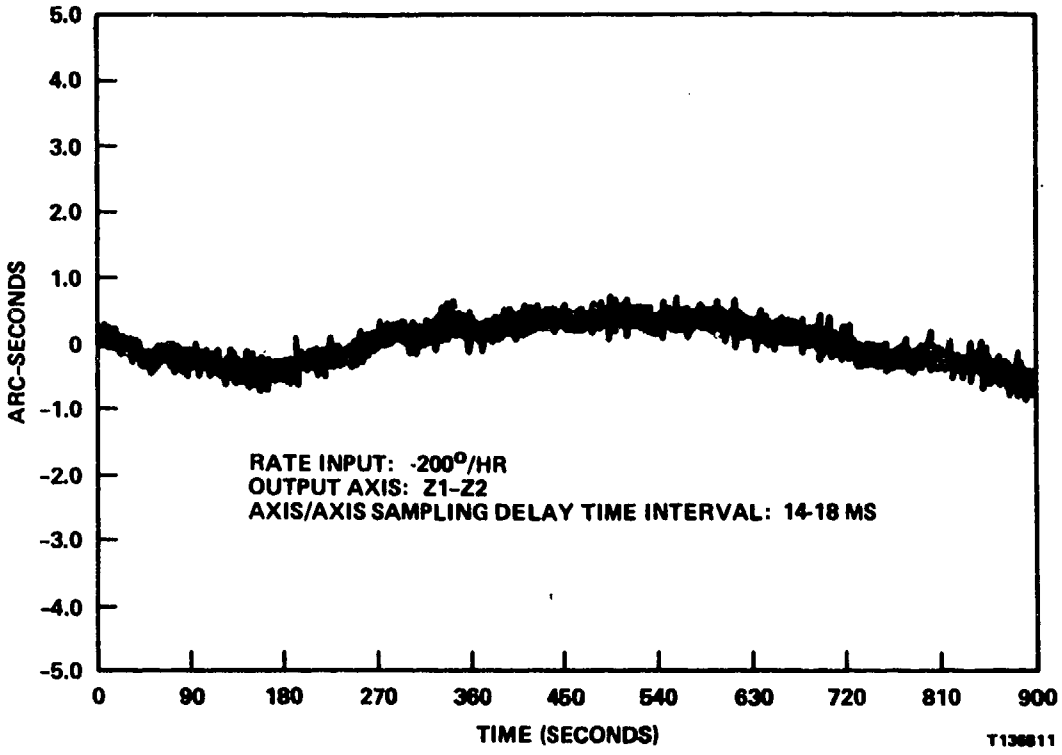

Figure 5. DRIRU II NEA Test Under -200°/Hr Rate at JPL

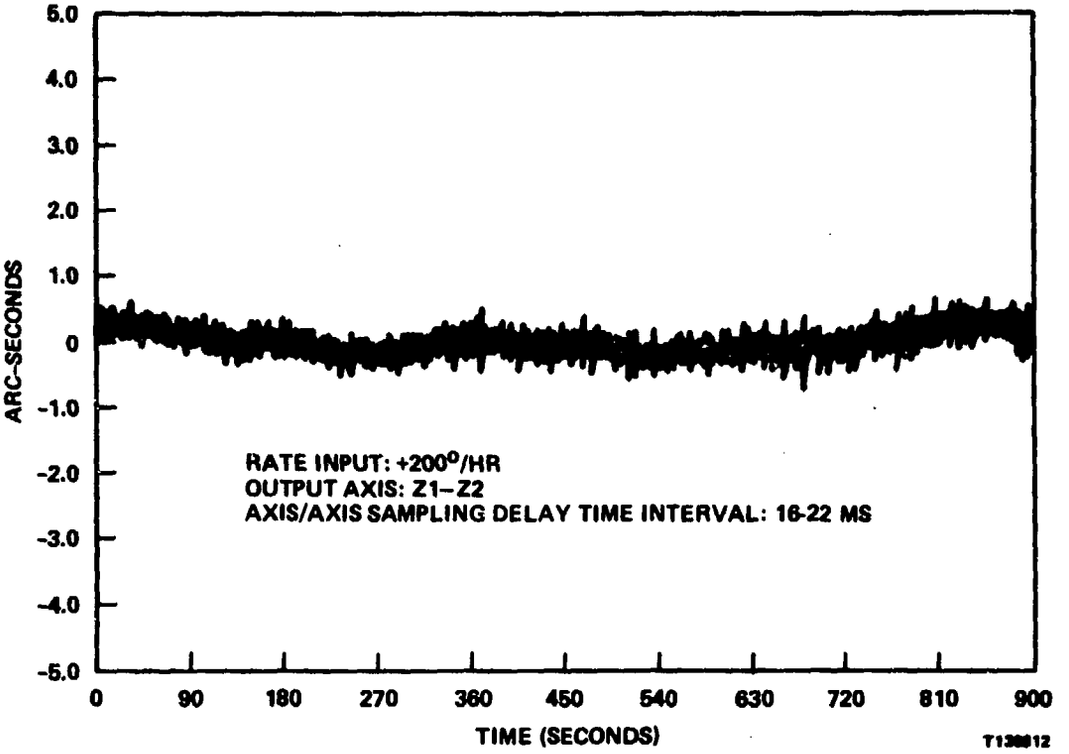

Figure 6. DRIRU II NEA Test Under +200°/Hr Rate at JPL

3.0 RECENT EXPERIENCE

3.1 DRIRU II Orbital Performance

More conclusive data, substantiating the hypothesis that NEA performance is independent of the magnitude of rate, was recently obtained from the Solar Maximum Mission (SMM) spacecraft which was launched into Earth orbit with the first DRIRU II system aboard in February 1980. The data presented in Figures 7 and 8 were obtained in the first quarter of 1981 with the DRIRU II operating in the high rate range (nominal pulse weight = 0.8 $\widehat{\text{sec}}$), as the spacecraft was experiencing a 0.75°/sec (2700 arcsec/sec) rate about the spacecraft roll axis. There was also some coning of the roll axis due to minor rates about the pitch and yaw axes of the spacecraft. Temperature varied less than 1°C during the test runs.

Examination of the data presented in Figures 7 and 8 reveals NEA performance of approximately 11 $\widehat{\text{sec}}$ worst case for the two 17.5 minute test runs with the system in the high rate range. Data were accumulated in 512 millisecond samples. Since the NEA performance is directly related to the pulse weight of the output, the equivalent low rate range performance (nominal pulse weight = 0.05 $\widehat{\text{sec}}$) may be determined by dividing the high rate range data by a factor of 16, yielding an equivalent low rate range (up to 400 arcsec/sec) NEA performance of 0.69 $\widehat{\text{sec}}$ p-p. This agrees well with static NEA performance measured in the test laboratory.

Attempts to reduce the angular rate experienced by the Solar Maximum Mission spacecraft to less than 400 arcsec/sec are scheduled for mid 1981. If these attempts prove successful, Goddard Space Flight Center plans to perform additional NEA performance tests with the DRIRU II system in the low rate range which should verify the above conclusions.

3.2 Gyro Testing at Hughes Aircraft Company

Measurement of SDG-5 gyro noise performance during rate input was successfully accomplished at the Hughes Aircraft Company facility in Culver City, California in May 1981. Since a survey of existing test facilities had revealed no suitable test table for low noise gyro testing under rate, Hughes decided to design and build a specialized rate table for this purpose. The result of this effort is a table which provides smooth rates up to 3°/sec with measured noise levels in the range 3 to 5 nanoradians (less than 0.001 arc sec).

The rate table and support structure are shown in Figures 9 and 10. The design employs several levels of isolation from cultural disturbances including a 20 ft deep seismic block, pneumatic isolators used with a pendulous suspension to provide three degrees-of-freedom isolation for the tripod assembly, and a pendulous rotating test table weighing 2000 pounds supported by a large, low pressure air bearing. An air jet drive minimizes disturbances to the table as it is accelerated to the desired rate and does not contribute any frictional disturbances when turned off.

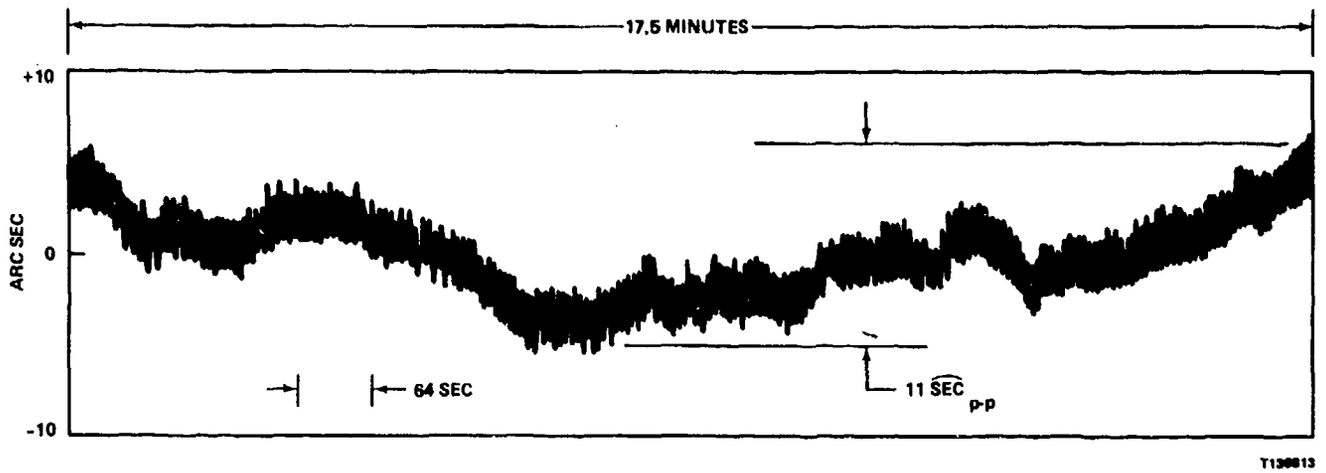

Figure 7. DRIRU II NEA Under Rate On-Orbit From SMM Spacecraft

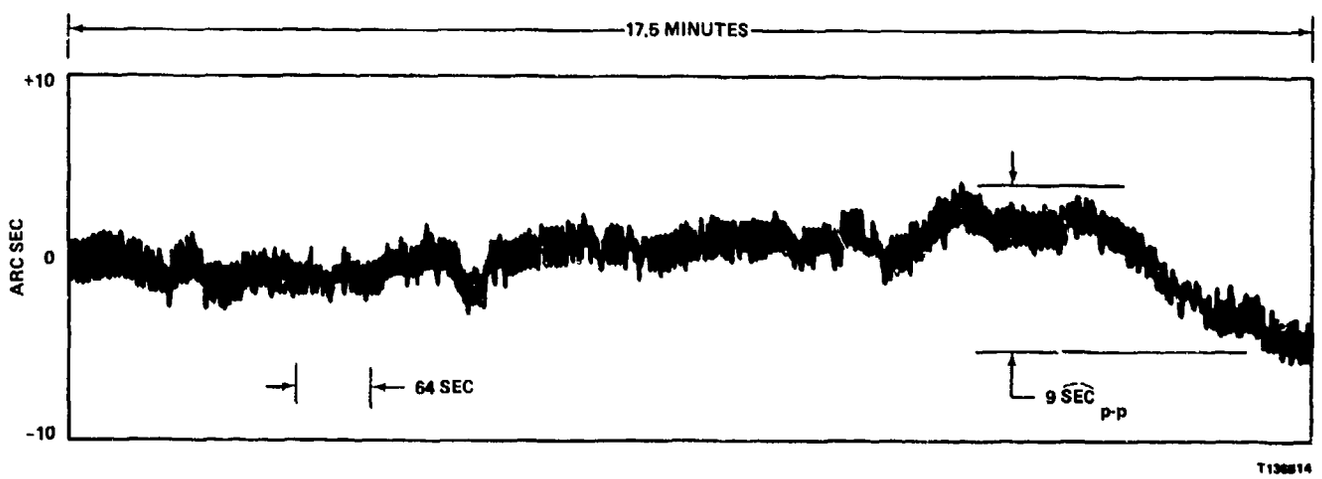

Figure 8. DRIRU II NEA Under Rate On-Orbit From SMM Spacecraft

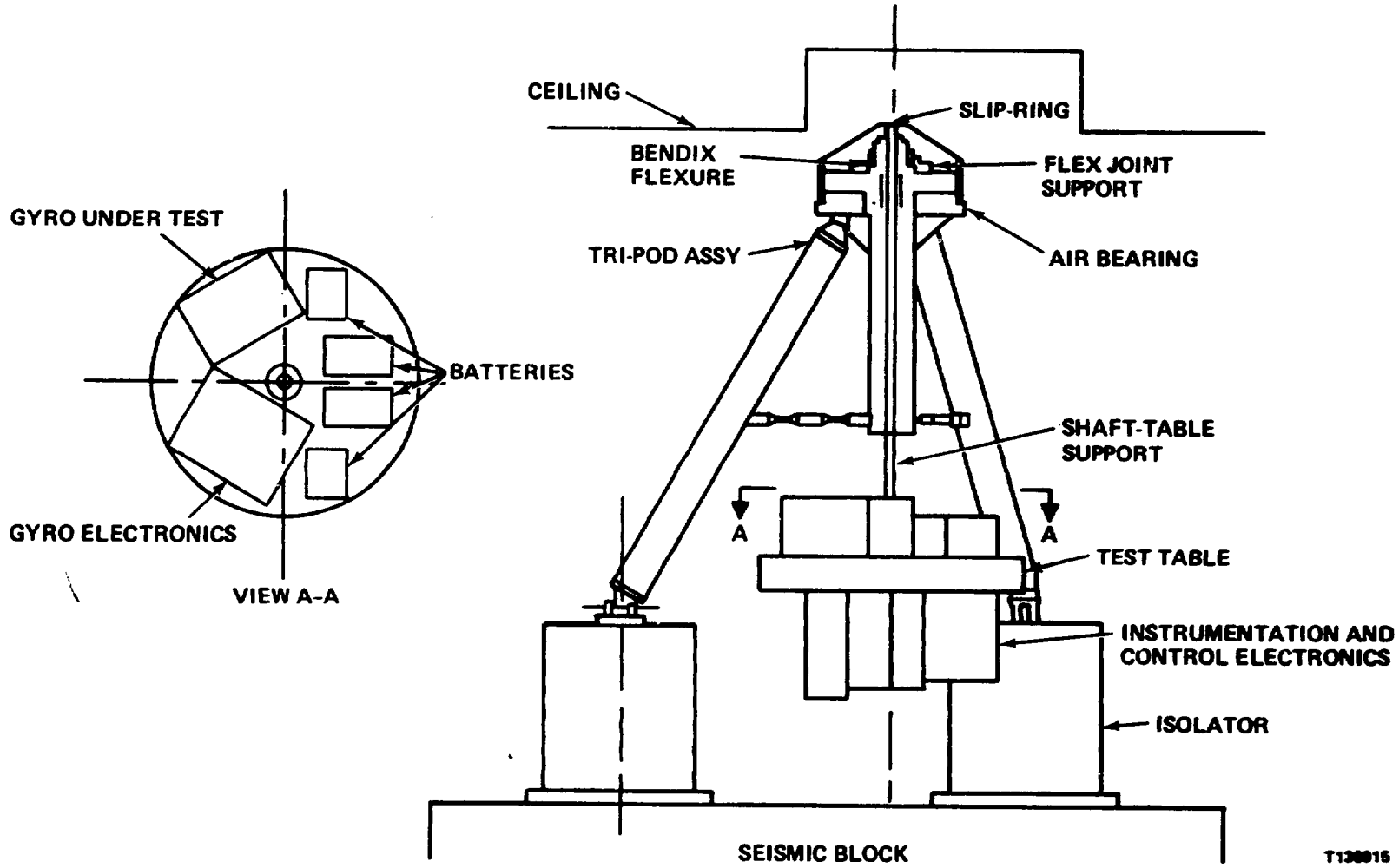

Figure 9. Schematic Drawing of the Hughes Low Noise Rate Table

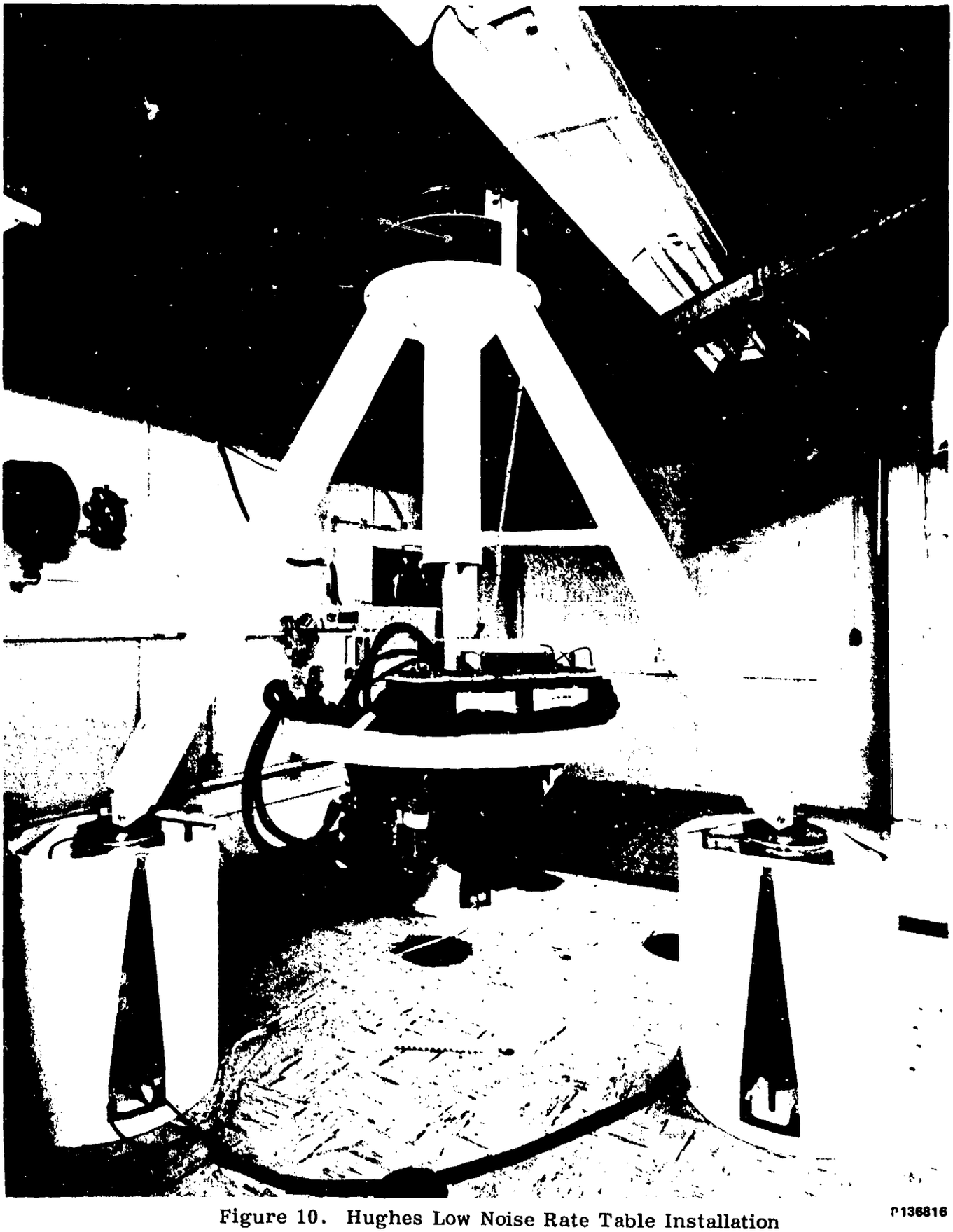

P136816

Figure 10. Hughes Low Noise Rate Table Installation

Actual testing is accomplished with the table in the "coast down" mode. The table is accelerated by the air jets to a rate higher than the desired test rate. The air drive is then removed and the table is allowed to coast down to the desired rate for data taking. During this coast period, residual table motions at the resonant frequencies of the drive and support systems are damped out and a smooth, but slowly decaying table rate is achieved. Since the coast time is long (typically 30 minutes from 3°/sec to zero rate) compared to the noise frequencies of interest (1 to 100 Hz), a reasonable sampling of data can be achieved at a table rate which decreases by much less than 0.1% over a given sampling interval. This mode of operation is entirely satisfactory for acquiring high frequency noise data while it would not be useful for accurately measuring gyro torquer performance parameters such as scale factor linearity and symmetry. For the latter type of testing a precisely controlled rate is needed.

For the noise testing conducted at the Hughes facility, the test gyro and support electronics were mounted on the table surface along with necessary balance weights. All voltages required for energizing and controlling the gyro were generated within the table mounted electronics except for one dc voltage required for the spin motor drive. This voltage was supplied through sliprings as was the output signal, a dc voltage proportional to sensed rate.

The gyro control electronics consisted of 100 Hz bandwidth analog capture loops with both direct and cross axis compensation. A commutating notch filter was included in the loop to attenuate noise components at multiples of the 100 Hz gyro spin frequency. The output signal, proportional to rate, for the axis under test was acted upon by a modified integrator to produce a signal proportional to angle in the frequency range of interest. This signal was analyzed and displayed on a Hewlett Packard Model 3582A Spectrum Analyzer as a linear plot of angle noise versus frequency. The noise signal was analyzed over a frequency range of zero to 100 Hz using an analysis bandwidth of 1.2 Hz.

The data obtained during this test series is summarized in the noise spectra presented in Figure 11 and 12. Both figures are plotted to the same amplitude and frequency scales and show typical data for zero rate input and 3°/sec input. Note that the spectra are essentially identical except for the noise spike at approximately 8 Hz which is only present in the high rate data. This frequency component occurs at a known resonance of the rate table and was caused by residual table motions excited by start-up transients. It was demonstrated during the testing that the amplitude of this component varied depending on the length of time allowed for stabilization after removal of the table drive air pressure.

The remaining frequency components are essentially identical for zero rate and 3°/sec. Those at 30 Hz, 60 Hz, 79 Hz, 90 Hz, and 100 Hz were also present on a similar noise spectrum plot (Figure 13) obtained with the input of the measurement instrumentation shorted (i.e., with the gyro out of the loop). These components, therefore, were externally induced and are not considered part of the gyro noise spectrum. The single remaining component with any significant amplitude, at approximately 34.5 Hz, is caused by

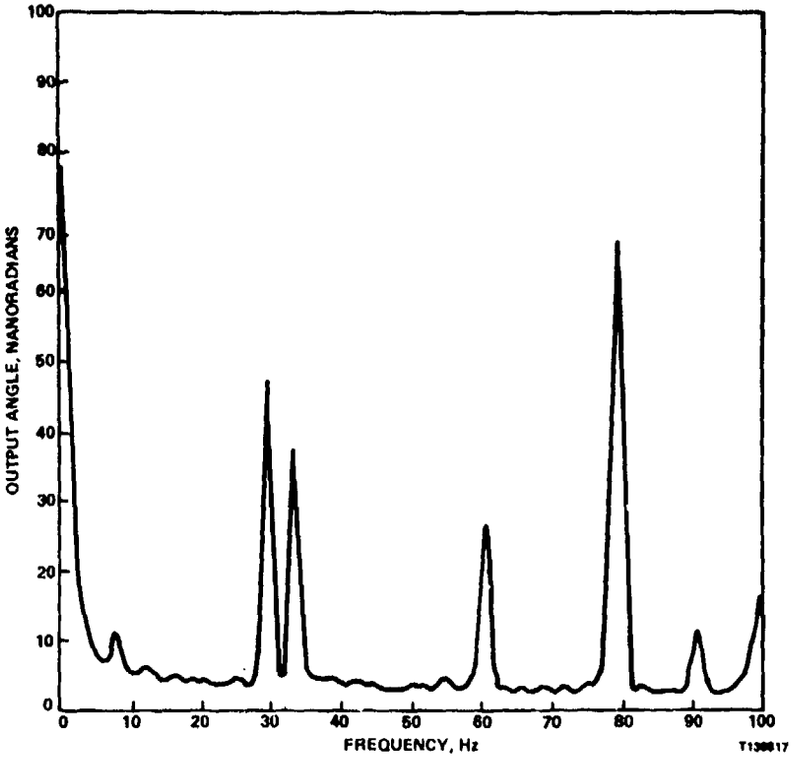

Figure 11. Typical SDG-5 Noise Spectrum at Zero Rate From Hughes Tests

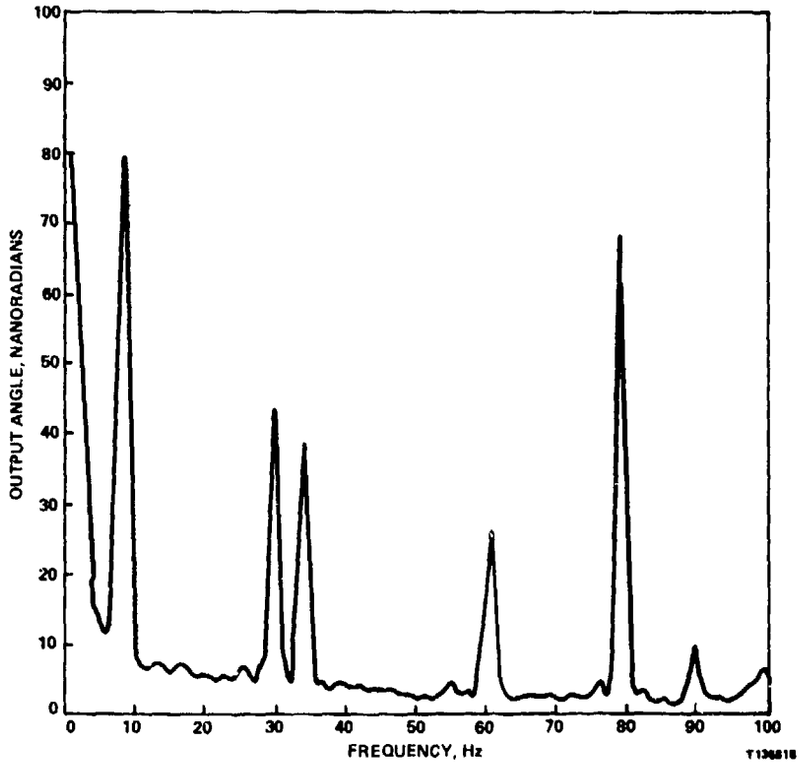

Figure 12. Typical Noise Spectrum at 3°/Sec From Hughes Tests

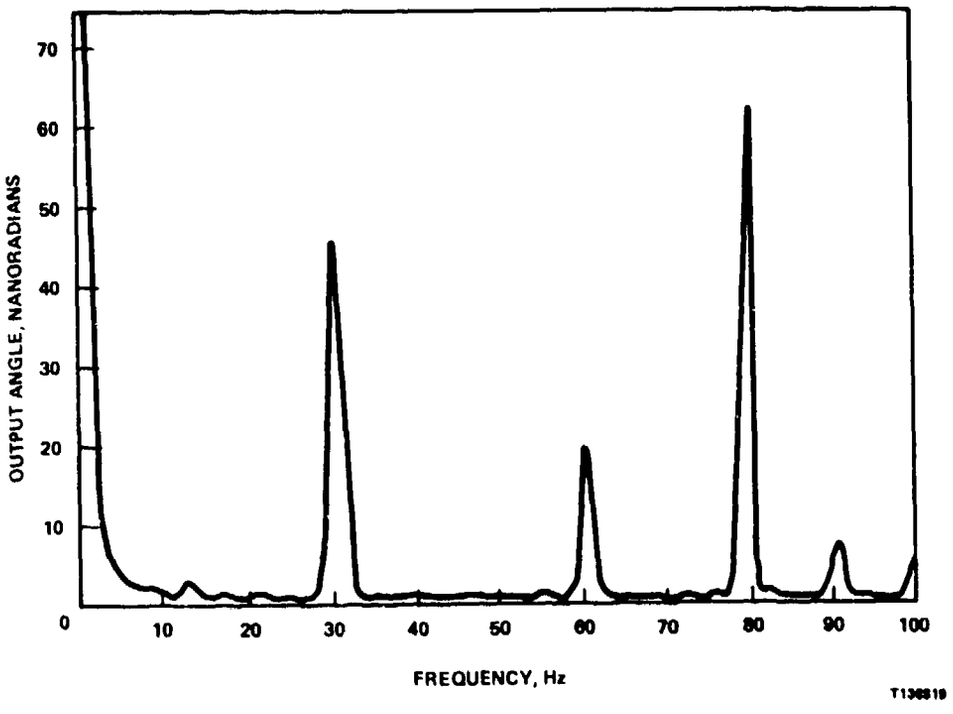

Figure 13. Noise Spectrum of Instrumentation Electronics With Input Shorted

motion of the ball cages within the gyro spin bearings. The amplitude of this component was 35 to 40 nanoradians for one of the two gyros tested and approximately 45 nanoradians for the second gyro. Since these gyros are standard production units, built approximately two years apart, it is expected that the results are typical of SDG-5 gyros built to the current configuration.

The overall noise level throughout the 100 Hz frequency range has been calculated from the 3°/sec data in Figure 12 to be 44 nanoradians rms exclusive of the noise spikes attributed to the table resonance and cultural inputs. This overall level includes the 37 nanoradians of bearing generated noise. A similar calculation for the zero rate data yields the same value within the accuracy of the test. This similarity between the zero rate and high rate noise levels confirms the previous conclusions that SDG-5 output noise is not a function of input rate and that static tests can therefore be used to characterize gyro noise for high rate applications. Although not shown in this paper, data were also obtained for the gyro axis which was orthogonal to the rate input axis. These data showed similar noise spectra to those shown in Figures 11 and 12.

For those applications where even lower noise levels than those demonstrated during the Hughes tests are required, the SDG-5 could be modified to reduce the overall noise output and more specifically the 34.5 Hz component generated in the gyro bearings. Presently, the bearings are bought to a specification control drawing which controls many bearing parameters but does not address specifically the amplitude of the torques related to ball cage motion. For special applications, low noise bearings could be selected from the standard production run or specific controls could be placed on cage dynamic balance and other related parameters.

In more general terms, the overall gyro noise output could be reduced by a factor of two to three by modifying the gyro suspension design to include a single gimbal rather than the standard three gimbal design. For applications where the full environmental capability of the SDG-5 (>225g) is not required, and where some dynamic rectification of spin-speed correlated inputs can be tolerated, this modification could be very beneficial.

4.0 SUMMARY AND RECOMMENDATIONS

This paper described recent experience in precision attitude stability measurements under rate in terms of gyro output angle and drift rate noise spectra. The test data presented showed that there is no significant difference in gyro noise performance between static test conditions and high rate environments. The gyro output is dominated by bearing induced noise at the ball cage rotation frequency (34.5 Hz), and has an overall rms level less than 50 nanoradians. Methods of reducing these noise levels were discussed.

The Hughes Aircraft Company test facility, used for the most accurate of the reported testing, utilizes an air bearing supported rate table operating in the coast down mode and has demonstrated angular stability in the 5 nanoradian region. As current and projected system performance requirements are in the same region, it appears that attention should be given to establishing a dedicated, certified test facility with broader capabilities. Ideally, this facility should be capable of providing continuous, controlled rates up to 10°/sec with noise levels in the sub-nanoradian region. The availability of such a test facility appears necessary for the performance of validation and acceptance testing in support of a number of present and future precision pointing and tracking systems. The establishment of such a facility should be considered by Holloman CIGTF or other government test agencies so that it would be available to all potential users.

ACKNOWLEDGMENT

Teledyne Systems Company expresses its appreciation to the Hughes Aircraft Company for providing the test facilities and excellent technical support that permitted the recent gyro noise measurements under rate. The DRIRU II noise equivalent angle testing was supported in part by the Jet Propulsion Laboratory, California Institute of Technology, under NASA Contract NAS-7100 and by NASA Goddard Spaceflight Center. Teledyne further expresses its gratitude to the Martin-Marietta Corporation, Denver, for the work performed in back-to-back gyro noise testing performed in December 1978.

REFERENCES

(1) Green, K., Oshika, E. and Van Alstine, R., Spectral Noise Performance of a High Accuracy Dry Tuned Gyroscope and the NASA Standard Redundant Dry Rotor Inertial Reference Unit (DRIRU II), Presented at the Ninth Biennial Guidance Test Symposium, Holloman AFB CIGTF, ADTC-TR-79-11 (Volume I), October, 1979.

(2) Drift Tests on the Teledyne Systems Company Model SDG-5 Gyroscope, Conducted by CIGTF, 6585th Test Group, Holloman Air Force Base, New Mexico, August, 1979.

(3) Irvine, R. and Van Alstine, R., Performance Advantages of Dynamically Tuned Gyroscopes in High Accuracy Spacecraft Pointing and Stabilization Systems, Presented at the Symposium on Gyro Technology, Stuttgart, Germany, September, 1979.

(4) Green, K., SDG-5 Power Spectral Density (PSD) Tests at Martin-Marietta, Denver, December 5 through 19, 1978, Teledyne Internal Memorandum DRIRU/786, January, 1979.

(5) Reddy, P., Back-To-Back Gyro Rate Testing, Teledyne Internal Memorandum SDG: 165, September, 1980.

(6) Irvine, R. and Ritter, J., DRIRU II - The NASA Standard High Performance Inertial Reference Unit, Presented at the AAS Annual Rocky Mountain Guidance and Control Conference, Keystone, Colorado, AAS 79-021, February, 1979.

(7) DRIRU II Noise Equivalent Angle (NEA) Performance of the NASA Standard High Performance Inertial Reference Unit, Teledyne Systems Company Document 60999, April, 1980.

TITLE: SEISMIC EVALUATION OF THE AIRBEARING FACILITY FOR SPACE TELESCOPE TESTING

AUTHORS: C. RODONI
A. BRADY
H. DOUGHERTY

LOCKHEED MISSILES AND SPACE CORPORATION
Sunnyvale, California

and

J. DAWSON

BENDIX GUIDANCE SYSTEMS DIVISION
Teterboro, New Jersey

J-2

SEISMIC EVALUATION OF THE AIRBEARING FACILITY FOR SPACE TELESCOPE TESTING*

C. Rodoni, A. Brady & H. Dougherty
Lockheed Missiles and Space Co.
Sunnyvale, CA 94086

J. Dawson
Bendix Guidance Systems Division
Teterboro, NJ 07608

Abstract

The Lockheed Missiles and Space Company Airbearing Test Facility is used for testing of the Space Telescope Pointing Control System. Detailed testing to characterize the environmental noise was performed using LMSC seismometers and comparing them with the data taken by personnel and equipment from the Central Inertial Guidance Test Facility of Holloman Air Force Base. In addition, laser unequal path interferometer data was taken to characterize the short term "cultural noise." The data from the instruments was used to characterize the rotational amplitude of the airbearing due to seismic motion in terms of power spectral densities.

A simplified airbearing spring-mass dynamics model was developed for understanding the various dominant frequency disturbances observed at frequencies below 5 Hz. The seismic test data was correlated with the model.

In summary, the Holloman measurements corroborated the Lockheed seismic data which show that the rotational amplitude of the airbearing table due to seismic motion was consistent with Space Telescope objectives, and that the simplified airbearing model allows prediction of the effect of changes in airbearing configuration.

The paper describes the seismic test set up, techniques used, data and results.

Introduction

The Space Telescope performance objectives require stabilizing the telescope to allow near-diffraction limited images to be obtained while maintaining the pointing stability for 10 hours of observation. Precision tracking of solar objects ([1] and [2]) is also required.

The Space Telescope Pointing Control System (PCS) is designed to meet the fine pointing performance of 0.007 arc sec stability and to maneuver the telescope 90° in 20 minutes, or less.

*Work sponsored by NASA Marshall Space Flight Center, Huntsville, Alabama, under contract NAS8-32697.

The PCS objectives are met using Fine Guidance Sensors (FGS) for rate and attitude information to achieve fine pointing, rate gyro assemblies (RGA) for rate and attitude information during maneuvers, and reaction wheel assemblies (RWA) sized to provide both the torque required for maneuvering and the precision control torques during fine pointing. A digital computer is used for calculating the control law, attitude reference, momentum management law and the command generator. The command generator shapes the acceleration and incremental angle commands to the control system in order to limit structural mode excitation.

Many of the mission operations are performed using the fine pointing mode consisting of RGAs and RWAs. A major objective of PCS tests on the airbearing table is demonstration of operation in this fine pointing mode. Fig. 1 shows a schematic of the airbearing.

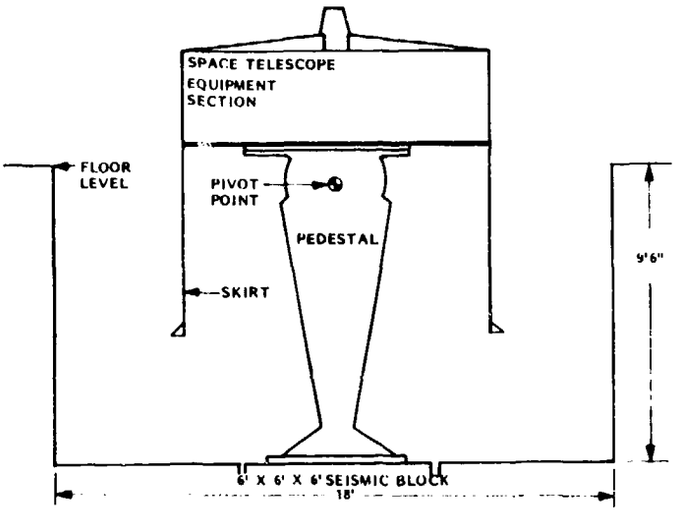

Figure 1 Airbearing table installation

The facility is located in a test area 36 ft x 39 ft, adjacent to a 28 ft x 40 ft control room with a 4 ft x 8 ft view window between rooms. The airbearing table capacity is 20,000 lb. The bearing table is approximately 10 ft high and is located in an 18 ft x 18 ft x 9 ft 6 in. deep pit. The airbearing sits on a 6 foot cubical concrete block embedded in the bottom of the concrete pit.

The objectives of the airbearing test are to demonstrate interface compatibility of the hardware and software and the validity of the mathematical models used in predicting on-orbit control system performance. This latter requirement is the most stringent relative to overall test accuracy requirements. Each of the hardware components, e.g., rate gyro assembly (RGA) and reaction wheel assemblies (RWA), undergo extensive small signal level dynamics and noise testing at the vendors. Hence, the primary purpose of the airbearing model verification is to ensure the overall system response of the components in a control system is as predicted and there is no unexplained interaction. It was determined that a test environment with less than 0.03 to 0.05 arc sec (RMS) environmental disturbance was adequate for evaluating the mathematical models. These values were derived based on an inertia of the test article on the airbearing which is one-eighth the inertia of Space Telescope, and the fact that the software can be tested to levels below Space Telescope jitter requirements by a functional simulator which contains electronic models of the Pointing Control System components. The reduced inertia allows the commands to the RWAs to equal those expected on-orbit. The RGA operates over comparable levels to those experienced on-orbit. Hence, the airbearing will provide a realistic assessment of the analytic models used to predict on-orbit Space Telescope performance. Additionally, since the control system has a nominal bandwidth of slightly greater than 1 Hz, the control system attenuates low frequency effects. Hence, the concern is with seismic disturbances which may not be adequately attenuated by the control system.

A program was initiated to characterize the seismic environment of the test facility with the rotational characteristics of the airbearing of particular concern.

A Portable Seismic Monitor (PSM) had been developed by the Holloman Air Force Base Central Inertial Guidance Test Facility (CIGTF) and F. J. Seiler Laboratory at the Air Force Academy for the purpose of evaluating base motion at potential locations for an advanced inertial component test facility.

The CIGTF equipment consisted of tiltmeters for low frequency data as well as seismometers and geophones, which provided overlapping frequency coverage to 30 Hz. This equipment was augmented by geophones provided by LMSC and by a laser unequal path interferometer (LUPI), which was used to evaluate cultural noise transients.

Seismic Characterization

All of the seismic measurements were made with an existing "mini-balance" structure mounted on the airbearing. This "mini- balance" consists of 4 spider-like arms which join at right angles at the top and which support a safety ring at their base. A sketch of the airbearing table with the mini-balance is shown in Figure 2. The measurement instruments were mounted on top of the mini-balance or on small equipment platforms on the legs. More instruments were mounted at the base of the table on the seismic block.

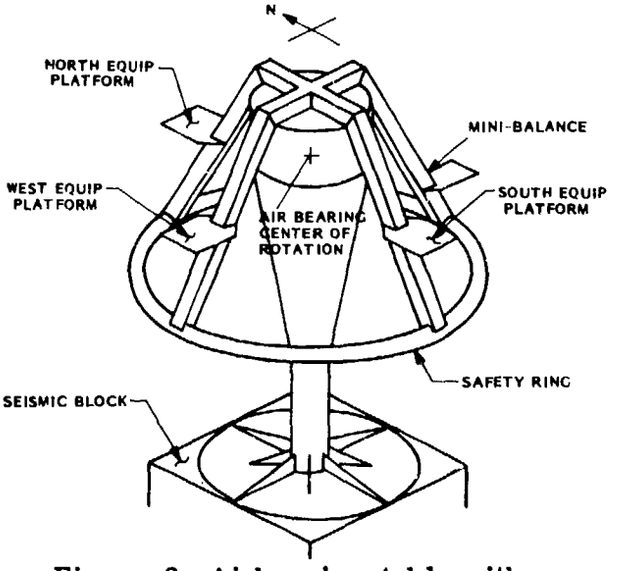

Figure 2 Airbearing table with mini-bearing

The instruments used in the tests were:

Lockheed geophones		No.
Geospace HS-10-1	Vertical	2
Geospace HS-10-1	Horizontal	4

CIGTF Seismometers	No.
Electro-Technical Labs EV-22C (horiz. & vert.)	6
Geotech SL-210 (Vertical)	2
Geotech SL-220 (Horizontal)	2
CIGTF Tiltmeters	
Autonetics A1-001A (2 axis)	2

The instruments all had different frequency characteristics as shown in Figure 3. The HS-10-1 geophones have a 1 Hz resonant frequency. The SL-210 & 220 seismometers have a .1 Hz resonant frequency as well as break frequencies due to the CIGTF-installed .03 Hz high pass and 30 Hz low pass filters. The EV-22C seismometers (in conjunction with the CIGTF amplifiers) have a sharply peaked response at 7.5 Hz.

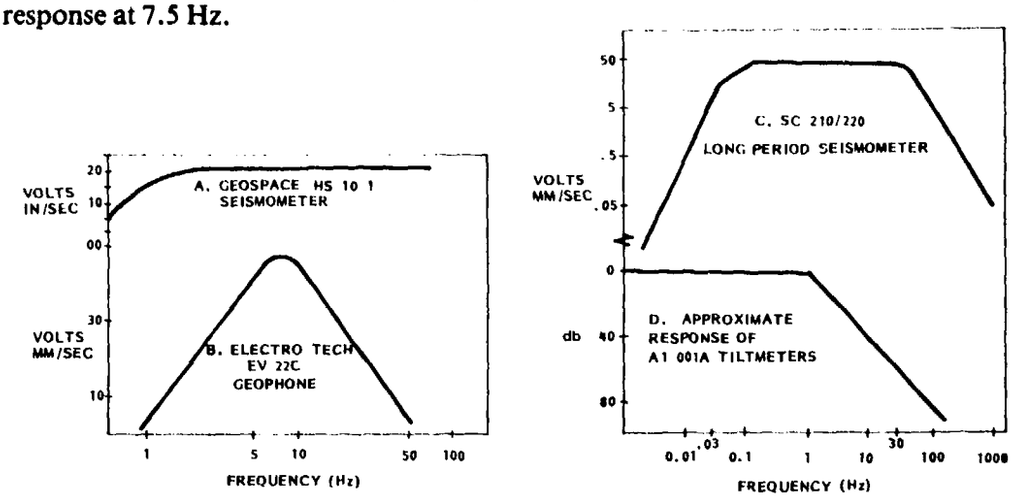

Figure 3 Frequency response of installation

The CIGTF measurements were fed directly into a HP 5420A signal analyzer while the Lockheed measurements (including CIGTF instruments) were recorded on a Honeywell 96 FM tape recorder to be processed later using LMSC data reduction software.

Each seismic test case consisted of approximately 5 minutes of data. Tests were run both with the airbearing "caged," i.e., supported by the pedestal structure, and with the airbearing "floated", i.e., free to rotate with respect to the pedestal. Multiple cases were run for both the "caged" and "floated" conditions in order to record different instrument combinations, as not all instruments could be recorded simultaneously.

The Lockheed data was recorded with a 60 Hz, single pole, low-pass filter across the recorder input. The recorded data was later sampled at 200 Hz and converted into Power Spectral Densities (PSDs) using fast Fourier transforms. The data was filtered using a modified Hanning window to minimize "leakage". A total of 100 seconds of data was used for each PSD. The data was plotted from .25 to 100 Hz using a .5 Hz bandwidth average (50 degrees of freedom), and then replotted from .05 to 10 Hz using a .1 Hz bandwidth (10 degrees of freedom). The lower number of degrees of freedom doubles the uncertainty in the data, but allowed finer resolution of the low frequency characteristics.

Test Results

The first objective of the test was to verify that the LMSC geophone data agreed with the CIGTF instruments. This objective was readily satisfied as illustrated in Figure 4. It can be seen that all of the geophones measured the same resonances with the same amplitudes. The only significant variations are encountered at the high and low frequencies and result from the different frequency response characteristics of the sensors.

The second test objective was to characterize the airbearing table seismic environment. It became apparent that structural dynamics of the airbearing table were a dominant contributor to the seismic environment. Also, the problem of deriving angular motion from linear measurements had to be addressed.

Figures 4 and 5 show the seismic spectrum to be dominated by a series of resonant frequencies, most notably 6 Hz, 13 Hz, and 20 Hz, with some additional low frequency dynamics. However, comparisons of other measurements show that the frequency of the dominant resonant peaks change depending on the instrument type (horizontal or vertical), the instrument location (top or base of the airbearing), and the airbearing configuration (caged or floated).

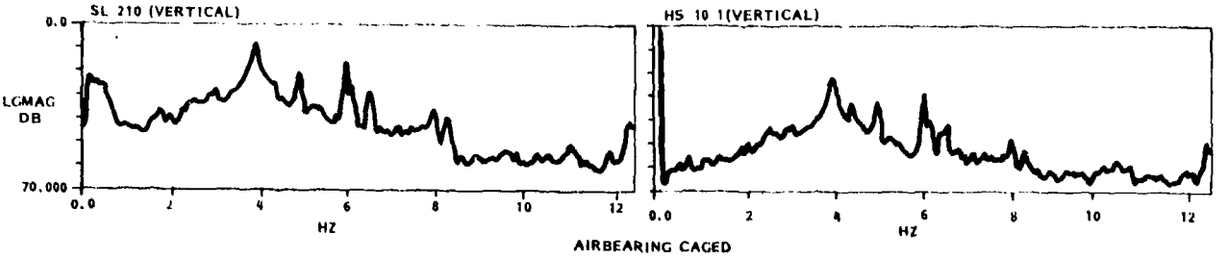

Figure 5 Comparison of SL-210 and HS-10-1 data taken with realtime analyzer

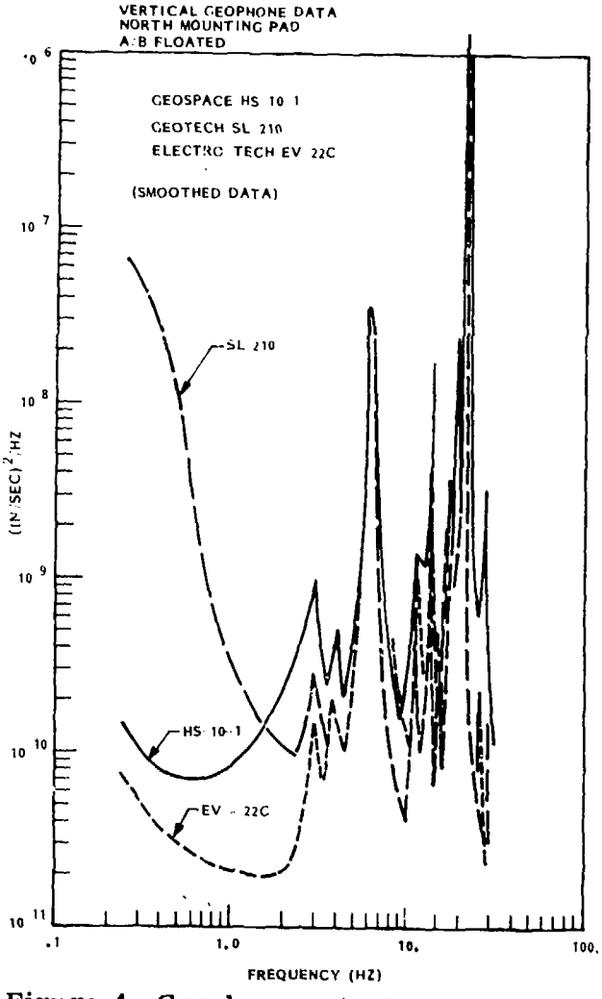

Figure 4 Geophone output comparison

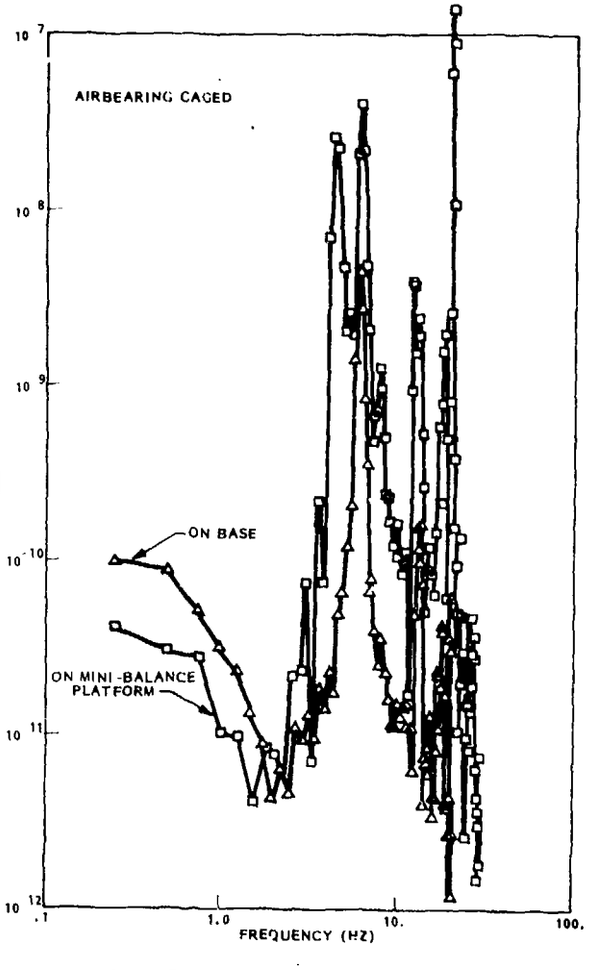

Figure 6 EV-22C on mini-balance base

Figure 6 shows vertical seismic measurement from 2 EV-22Cs mounted on the mini-balance and at the pedestal base. Figure 7 shows a similar comparison between two horizontal and one vertical HS-10-1s. Here one horizontal geophone was on the top of the air bearing while the other was at the pedestal base, and the vertical geophone was on the mini-balance platform. For both figures the airbearing was caged. These figures show that the 20 Hz resonance which is so dominant in Figure 5 is only dominant in the vertical measurements on the mini-balance platform. This peak is much less significant in the vertical measurements at the base or in either of the horizontal measurements. These figures also show that the the dominant 4.4 Hz peak only appears in the horizontal and vertical measurements made at the top of the air bearing and are absent in the measurements at the pedestal base. In addition, the 6 and 13 Hz peaks which dominate the vertical seismic data are insignificant in the horizontal data measured on the top of the airbearing.

The conclusions drawn from these observations are that the airbearing structure has a 4.4 Hz (4.0 Hz E-W) rocking mode which produces both horizontal and vertical motion at the mini-balance platforms. The 6 and 13 Hz resonances are "flapping" modes of the mini-balance legs which produce vertical motion at the mini-balance platforms and at the base, but very little horizontal motion.

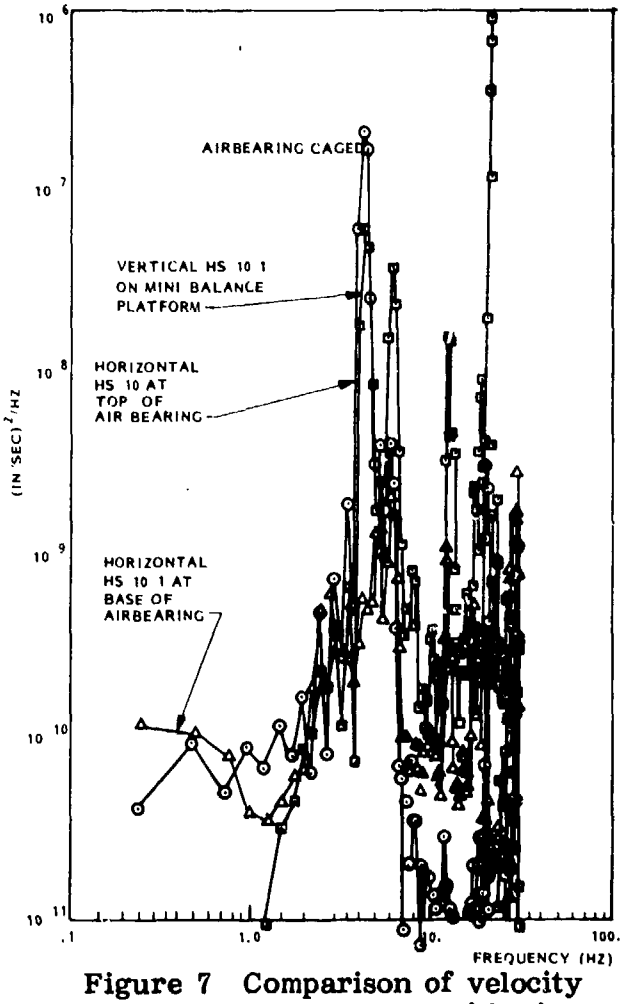

Figure 7 Comparison of velocity measurement with airbearing caged

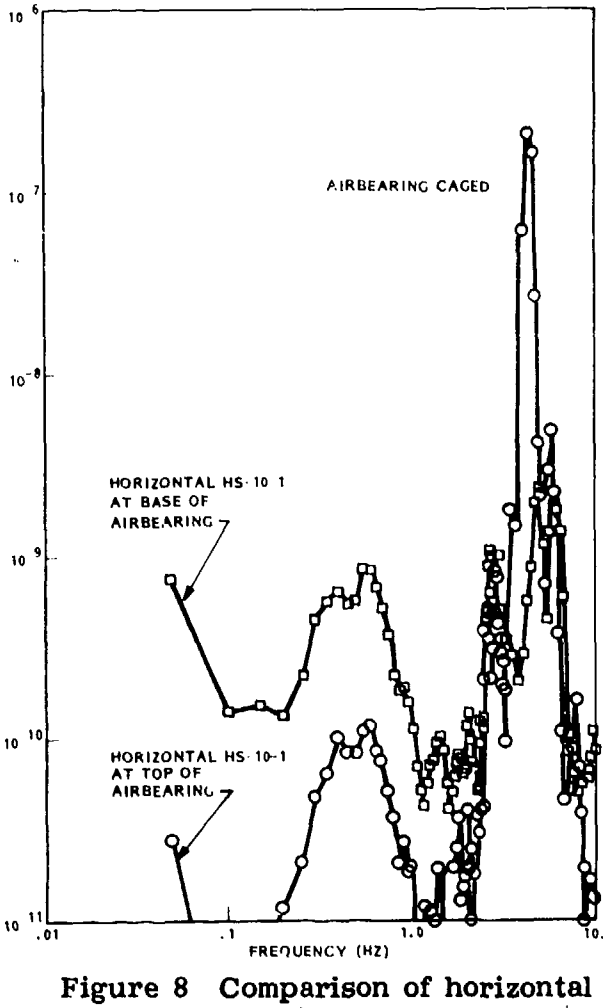

Figure 8 Comparison of horizontal velocity measurement with airbearing caged

The 20 Hz resonance is acoustic in origin, and not seismic, since it is only dominant in the vertical measurements on the mini-balance platforms. The amplitude of this mode also shows large variations between tests. Since the resonant frequency of a simple air column 10 ft deep is 27 Hz, it is reasonable to expect that the 18 ft x 18 ft dimensions of the air bearing pit could reduce the air column resonance within the pit to the observed 20 Hz. The observed peak could also be the result of the interaction of an air conditioner harmonic and the pit resonance. In any event, the 20 Hz resonance peak will not cause significant rotation of the air bearing, and thus, will not effect control system testing.

Figures 6 and 7 show that, with the exception of the 20 Hz mode, all the significant data resonances occur below 10 Hz. The data was therefore replotted from 0-10 Hz with the data averaging bandwidth reduced from .5 to .1 Hz.

Figure 8 shows a comparison of the top and bottom horizontal measurements with the airbearing caged. As observed in Figure 7, the 4.4 Hz mode is not visible at the base of the pedestal. However, the horizontal data now shows a broad resonance peak at 0.5 Hz which was not previously visible. The data also show a 2.7 Hz resonance.

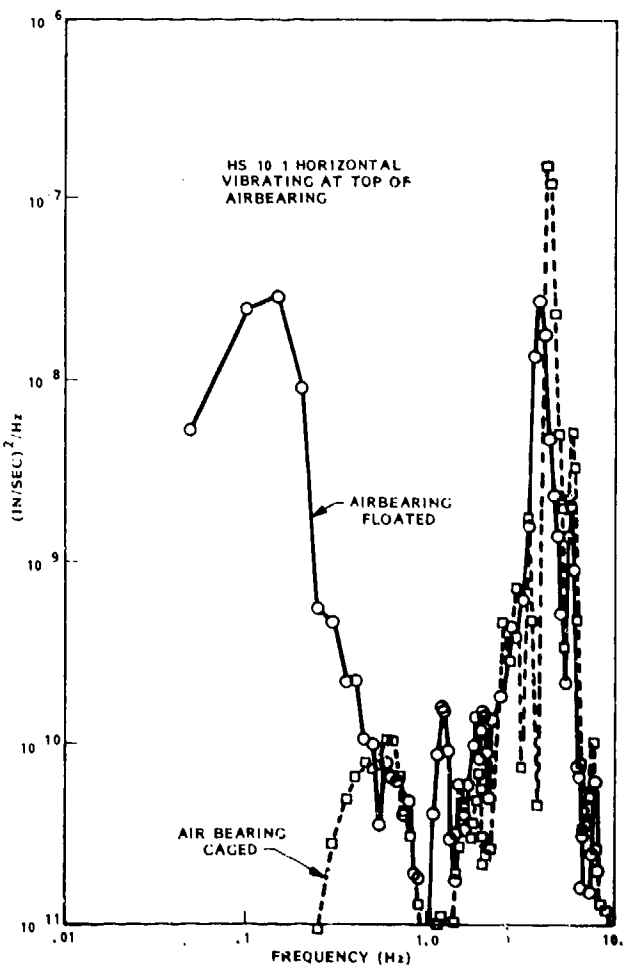

Figure 9 Horizontal spectra, caged and uncaged

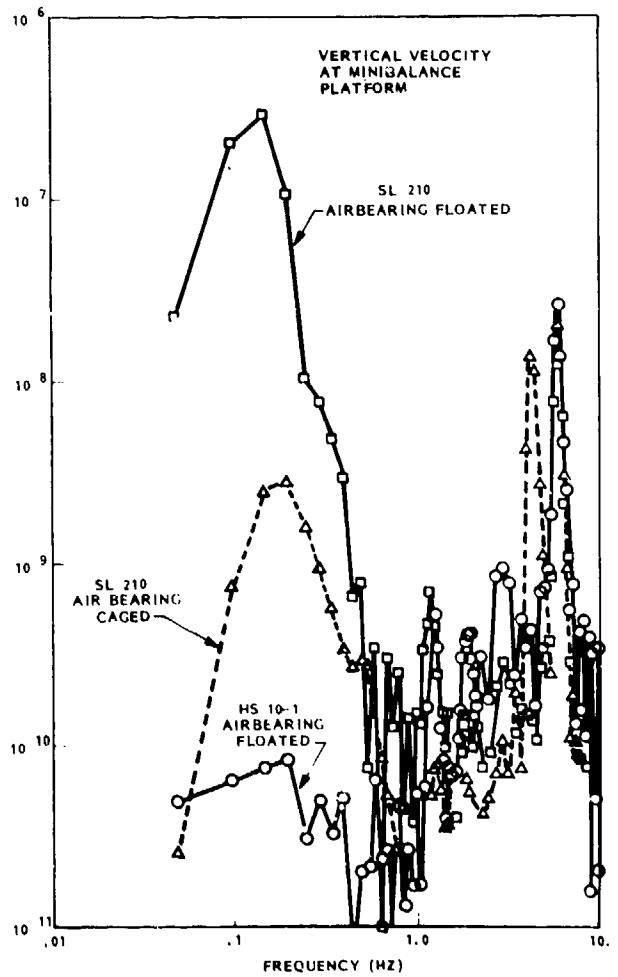

Figure 10 Vertical spectra, caged and uncaged

Figures 9 and 10 compare the horizontal and vertical measurements on the airbearing when the airbearing is caged and when it is floated (allowed to rotate). In both figures the floated data is characterized by a large low frequency peak at 0.15 Hz. In the horizontal data the 4.4 Hz peak shifts in frequency to 4.0 Hz and drops in amplitude as the bearing is floated.

In the vertical case the 4.4 Hz peak disappears entirely.

Figure 11 compares the top and bottom horizontal signals for the floated airbearing. Here the most significant factors are the absence of the large 0.15 Hz peak and the 4.0 Hz peak from the bottom data. The bottom data shows a 0.5 Hz peak instead, as well as a 2.7 Hz peak.

It is obvious from this data that floating the airbearing introduces a large 0.15 Hz resonance into the horizontal and vertical signals at the top of the mini-balance. Floating the airbearing also isolates the vertical seismometers from the 4.0 Hz pedestal mode.

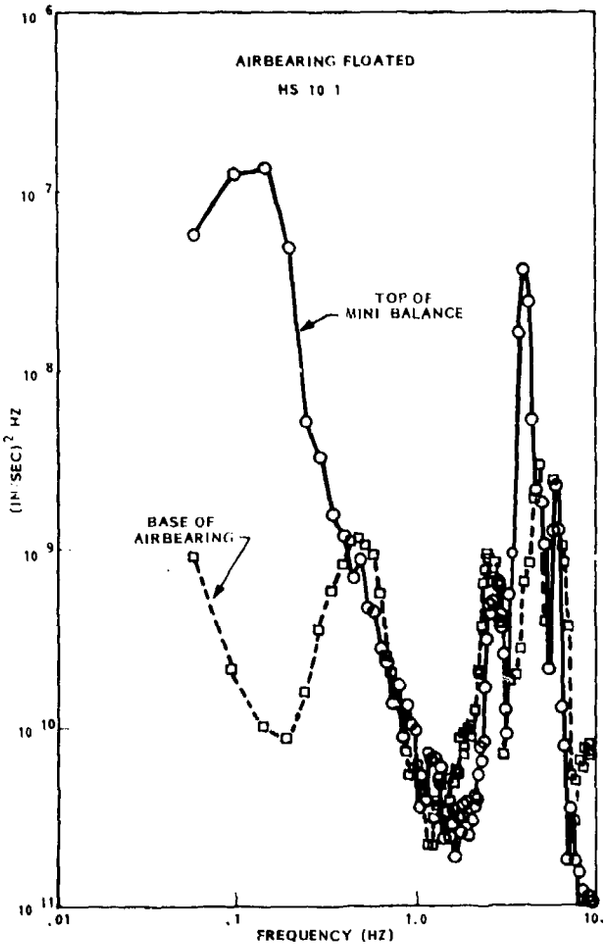

Figure 11 Comparison of horizontal velocity with airbearing floated

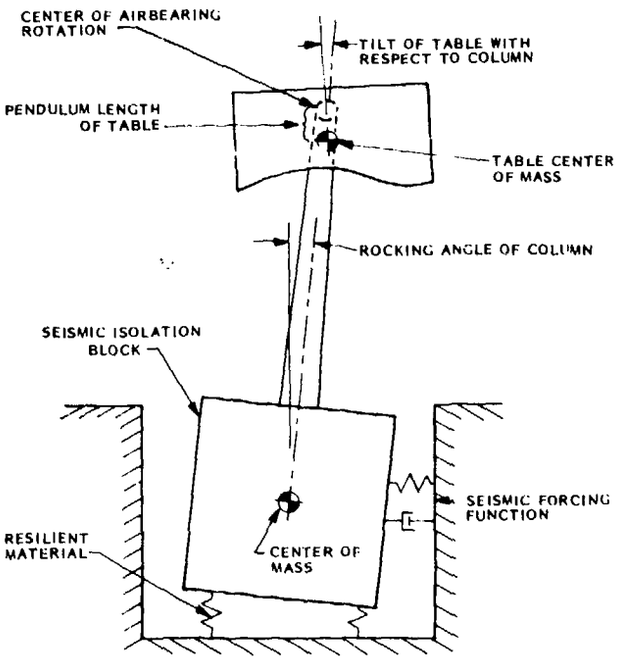

Figure 12 Dynamic model of airbearing table

Since the airbearing dynamics which would cause these observations was not readily apparent, a simple airbearing dynamic model was created to help understand these phenomena.

Airbearing Table Dynamic Model

In order to understand the relationships between the PSD characteristics of the various types of seismometers with the airbearing caged and floated, a very simple airbearing table dynamic model was developed. This model did not attempt to describe any of the structural flexibility characteristics which are obviously present in the airbearing table and mini-balance, but only addressed the rigid body dynamics of the isolated seismic block, the airbearing support column, and the airbearing and mini-balance on top of the column.

The dynamic model of the airbearing was limited to matching only three of the resonances found in the seismic PSDs: the 0.15 Hz mode when floated, the 4 Hz column rocking mode and the 0.5 Hz mode which appears to be translation of the seismic block. Figure 12 illustrates the basic elements of the dynamic model, which include a large mass for the seismic block, a long, "massless" column, and a secondary mass element on top of the column which may either rotate freely, as a pendulum, or be rigidly attached to the column.

The spring constants for the model were chosen to match the 0.15 Hz, the 0.5 Hz, and 4 Hz modes of the data. The 0.15 Hz mode was modeled as the pendulum frequency of the floated table, the 0.5 Hz mode as the resonance of the resilient material between the seismic block and the ground, and the 4 Hz mode as the rocking of the column.

Horizontal Seismometer Transfer Function

By itself, this airbearing model cannot explain the sharp horizontal seismometer resonance observed at 0.15 Hz with the air bearing floated. Since the 0.15 Hz resonance was modeled as the pendulum frequency of the table, this mode should contribute very little horizontal velocity to the seismometers.

However, by expanding the seismometer models of reference 4 to account for the effects of gravity, it was found that low frequency tilt angles could produce large horizontal seismometer outputs. The transfer function for the measured velocity with respect to the actual velocity was found to be:

$$\hat{\dot{X}}(S) = \frac{S^2 \dot{X}(S) - \dot{Y}(S)\, g}{S^2 + 2\zeta\omega S + \omega^2}$$

where $\hat{\dot{X}}(S)$, $\dot{X}(S)$, and $\dot{Y}(S)$ are the Laplace transforms of the measured velocity, the actual velocity, and the tilt rate of the seismometer, respectively. ω and ζ are the resonance frequency and damping ratio of the seismometer, and g is the acceleration of gravity.

Dynamic Model Comparison with Test Data

By including the horizontal seismometer measurement transfer function into the airbearing dynamic model, the model results compare well with the test data at low frequencies. The input to the model is a white noise horizontal acceleration. A lack of correspondence at higher frequencies is to be expected because of the simplicity of the dynamic model.

Figures 13 and 14 show comparisons of the horizontal geophone outputs at the top and base of the airbearing column with the dynamic model predictions. It can be seen that the dynamic model picks up the low frequency characteristics quite well, predicting that the top geophone output would be dominated by the .15 Hz table pendulum frequency, while the bottom output shows only the .5 Hz translation resonance.

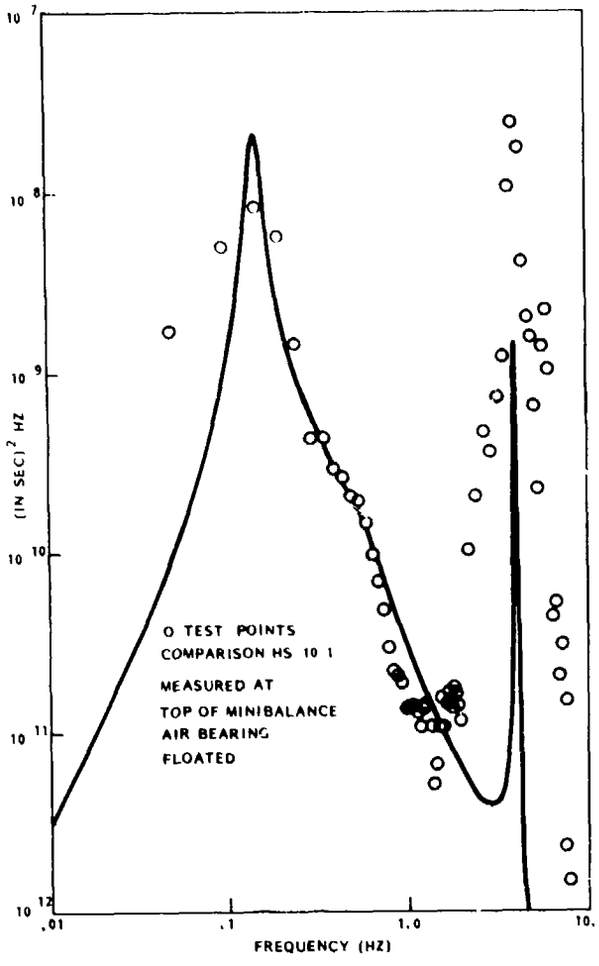

Figure 13 Comparison of geophone at top of table with dynamic model

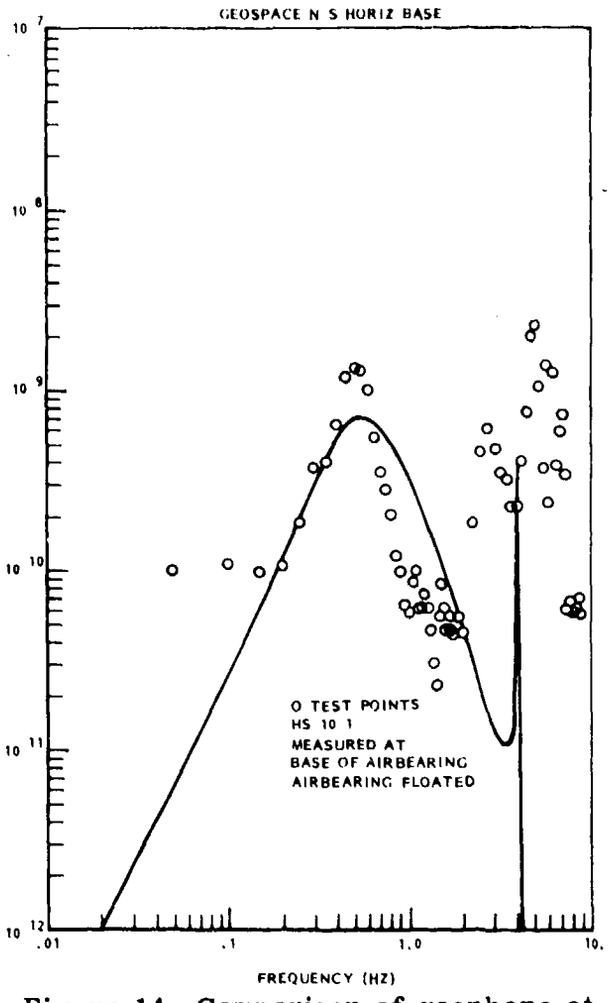

Figure 14 Comparison of geophone at bottom of table with dynamic model

Figure 15 shows how this model predicts the actual airbearing tilt angles and velocities which correspond to the measured seismometer outputs. It can be seen that the actual predicted tilt angles for the airbearing floated are significant only for the very low frequencies.

Observations Based on the Dynamic Model Results

Prior to the seismic testing, it was believed that the difference between the outputs of horizontal seismometers at the top and base of the airbearing would be a valid measure of the angular tilt of the column. While this may be true with the airbearing caged, the corruption of the top seismometer output by the low frequency tilt of the floated airbearing makes this data unreliable as an angular measurement.

Since the vertical seismometers are unaffected by the gravitational effects of the table tilt, the vertical seismometers will give a much better tilt measurement in the low frequencies. Unfortunately, the mini-balance test setup also resulted in a 6 Hz structural and a 20 Hz acoustic mode which were measured by the vertical seismometers and distort the angle data.

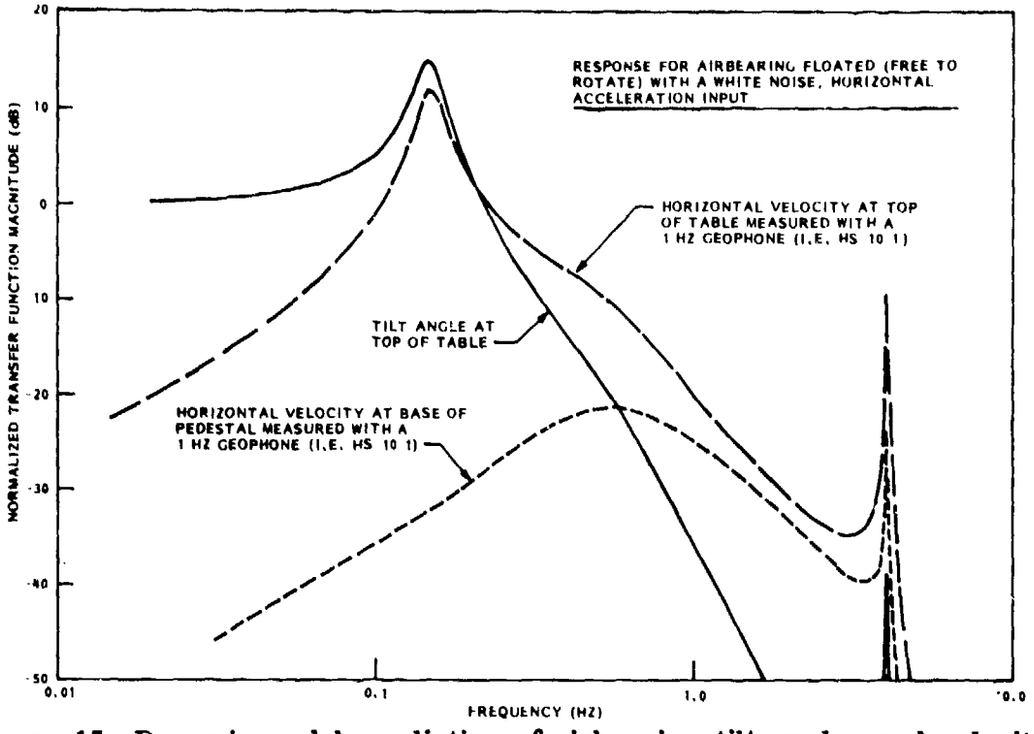

Figure 15 Dynamic model prediction of airbearing tilt angles and velocities

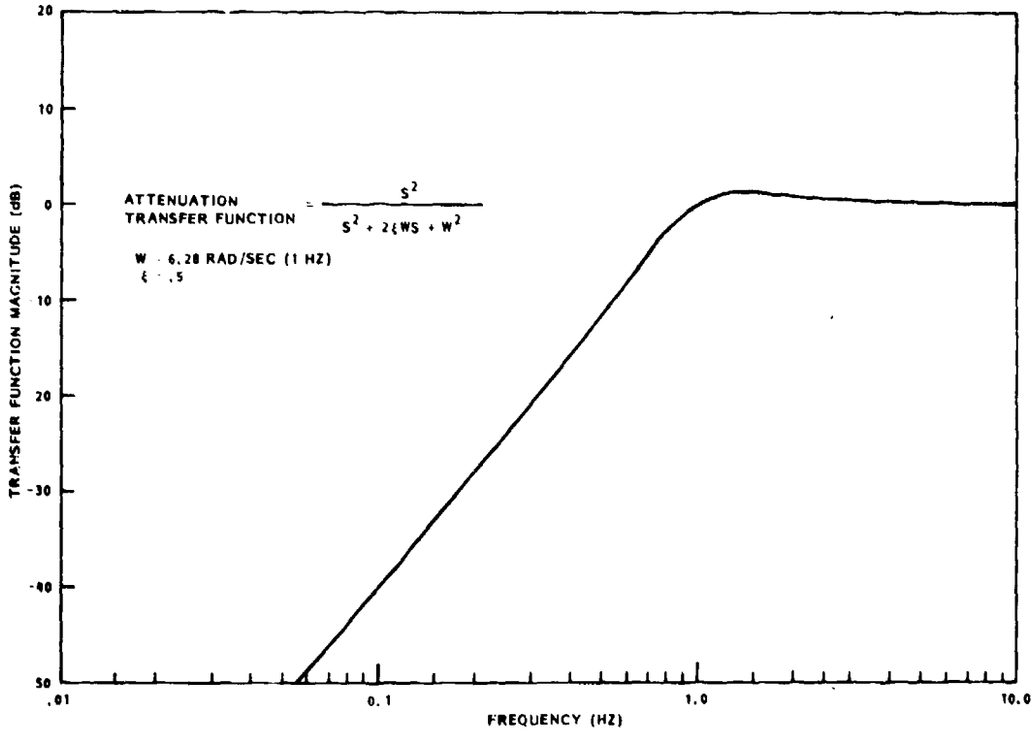

Figure 16 Seismic noise attenuation by an active control system

Seismic Noise Environment for Attitude Control Testing

As shown in Figure 15 the primary angle disturbance to the airbearing table occurs only at low frequencies. The Space Telescope Pointing Control System and other typical control systems which are to be mounted on the airbearing and active during testing have approximately a 1 Hz bandwidth and will therefore damp any angular disturbances with a frequency below 1 Hz as shown in Figure 16.

Since the Pointing Control System can be relied upon to attenuate the low frequency peaks observed in the seismic tests, the major contributors to the seismic disturbances affecting the control system will be the resonances at 4 Hz and higher. To bound the angular disturbance which might result from the seismic excitation of these resonances, the entire measured seismic disturbance (0-100 Hz) was assumed to result from a single 4 Hz rocking of the airbearing column. The seismometer outputs were translated into angles by assuming the center of rotation to be the base of the column (120 inches high). Because the RMS value of a sinusoid is related to its maximum amplitude by 0.707, the maximum amplitude of the seismic noise for this single mode model could be derived.

$$\text{Peak Angle (arc-sec)} = \frac{\text{RMS Horizontal velocity (in/sec)} \times 2.1 \times 10^5}{120 \times 25.13 \times .707}$$

The maximum sinusoid amplitude resulting from this simple (and conservative) model was found to be less than .05 arc seconds. The actual value of the main resonance at 4 Hz was determined by Holloman and Lockheed to have a peak displacement of 0.013 arc sec. This amplitude of disturbance is within the Space Telescope test requirements.

Tiltmeter Data Concern

The CIGTF instrumentation included two, two-axis tiltmeters. The tilmeter data is not believed to be accurate over the 0 - 100 Hz bandwidth of the PSD's, and has not been included in the preceeding analysis. Like other instruments which use the acceleration of gravity (g) to measure angles (references 5 and 6), the tiltmeters will respond to horizontal accelerations as well, and will interpret a horizontal acceleration (a_h) as a tilt angle of magnitude a_h/g.

Although the low bandwidth of the tiltmeters (Figure 3) tends to reduce the sensitivity to the horizontal accelerations, the error in the measured tilt angle can still be significant. For example, a .05 arc second peak amplitude, 4 Hz oscillation of the airbearing column will produce a tiltmeter output of .44 arc seconds RMS. Figure 17 compares the tiltmeter measurement at the top of the airbearing table with the vertical velocity measurement of an SL-210 seismometer. The seismometer data has been scaled to represent angle rate and then integrated to obtain angle. As expected, the tiltmeter yields a significantly higher tilt measurement above approximately .3 Hz. The tiltmeter measurements also provided data reduction problems because of their extreme sensitivity to tilt angle. While the tiltmeters were carefully leveled initially, whenever the airbearing was floated relatively large tilt angles could result, and when the airbearing was recaged, the caged angle could differ considerably from the initial angle. These angle offsets resulted in large bias outputs from the tiltmeters which, at times, saturated the tape recorder inputs and made subsequent data reduction questionable.

Optical Measurements of Seismic Environment

Consideration was also given to the effect of the overall environments, e.g., seismic, thermal, air turbulence, on any optical instrumentation which would be used in control system testing. In particular, the mounting of precision optical references in the airbearing pit was evaluated.

The test configuration is shown in Figure 18. A laser unequal path interferometer was rigidly mounted on the seismic block that supports the airbearing pedestal. A reflector was added to the interferometer to redirect the horizontal sampling beam to a vertical direction, up to a spherical mirror that was mounted on the airbearing table structure. Three translational adjustments of the interferometer were available to accurately place the source point in the interferometer at the center of curvature of the spherical mirror. The major advantage of the laser unequal path interferometer is that the translational adjustments are integral with the instrument.

The vertical nature of the air path tended to minimize the beam deviation effects due to thermal stratification. Tests were made to characterize the thermal environment using 19 thermocouples distributed in the airbearing pit for long term, i.e., greater than one week, thermal mapping of the pit. In addition, two fast thermocouples, with time constants on the order of five seconds were

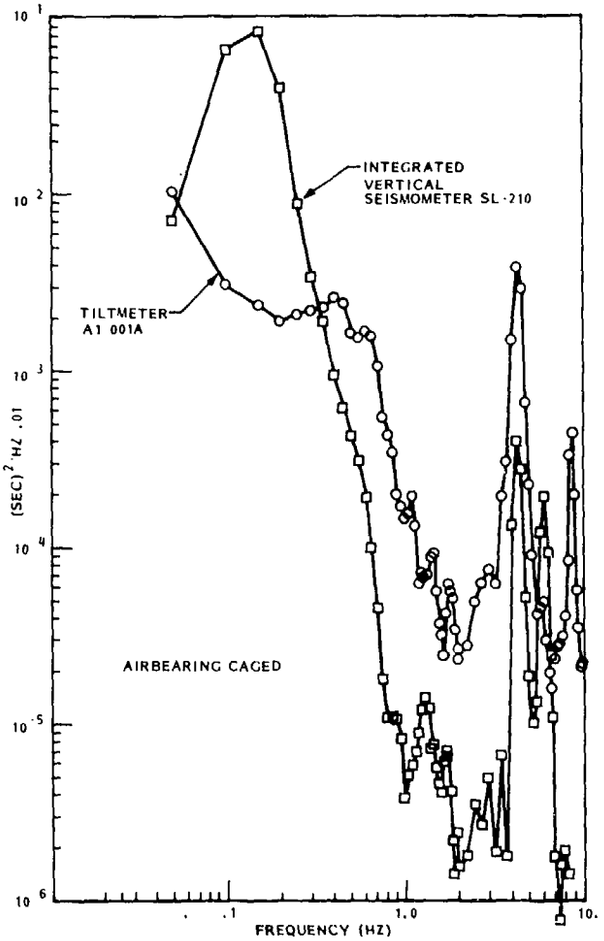

Figure 17 Comparison of tiltmeter with integrated seismometer output

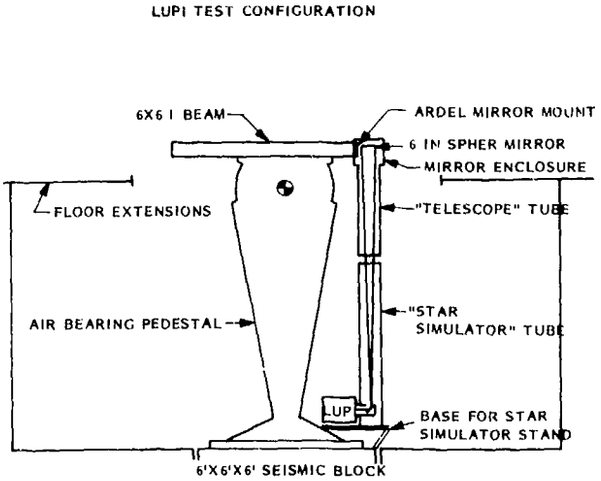

Figure 18 Laser unequal path interferometer test configuration

moved to various positions in the pit to characterize "transient" thermal conditions. No horizontal thermal gradients were detected. Stable vertical gradients of 0.35°F for the bottom 6 feet of the pit, and 1.1°F for the top 3 feet of the pit were observed. These gradients remain basically stable. Short term variations, which are a measure of turbulence, are on the order of ±0.017 to ±0.027°F. In summary, the thermal environment is basically benign.

The tests were conducted with two tubes enclosing most of the air path between the interferometer and the spherical mirror. This configuration minimized the small convection disturbances that might be expected due to thermal stratification of the pit, and any potential effects of turbulence due to continuous air flow through the airbearing to keep the bearing "clean." The lower tube was supported by the same platform that mounted the interferometer. The upper tube was mounted to the metal box that enclosed the spherical mirror, attached to the airbearing table structure. At the gap between the two tube sections (between 1 and 4 inches) each tube was closed with an optical window.

The basic approach to evaluate the seismic environment is as follows. The light from a point monochromatic source i.e., a laser, mounted on the seismic block is reflected by a spherical mirror that is mounted on the airbearing table and returned toward the source. An interference pattern can be formed with a local "reference" beam obtained by taking off part of the laser signal with a partial reflector (beam-splitter).

Non-systematic distortions of the interference fringe pattern are caused by localized variations in the refractive index of the air through which the beam traverses. Lateral shifts of the fringe pattern (in the local reference interferometers) are caused by changes in the separation between the interferometer and the spherical reflector. Changes in spacing between the fringes, or in the orientation of the fringes, are caused by differential rotations between interferometer and spherical mirror.

The interference fringe patterns were recorded on high-speed 16mm film by means of an instrumentation camera. Frame rates of 40 to 200 frames per second were used.

Test Results

During an early series of tests, several large transients (>1 arc second peak) were observed. Further investigation of these transients showed that some of the instrumentation components were not effectively damped, and were oscillating widely in response to external "seismic" inputs. A construction project was underway within 100 to 200 yards of the airbearing facility involving heavy earth-moving and earth-compacting equipment. By adding suitable amounts of damping material at strategic locations in the optical train, most of the resonances were successfully controlled. Data was then collected after 4 PM to avoid the interference from the strongest source of cultural "seismic noise".

The second series of tests yielded film sequences which showed only a few transients, which rarely exceeded ±0.5 arc second. The high sensitivity of the interferometer fringe pattern to longitudinal displacements (along the optical axis) causes the fringe pattern to shift a full fringe when the end of the supporting beam moves 0.000012 inch. With a lever arm of approximately 45 inches, this corresponds to a rotation of the supporting beam of 0.06 arc second. The data taken at 200 frames per second yields consistently sharp fringes (no smear due to longitudinal displacement during the exposure).

Data covering a typical one second interval (200 successive frames) was reduced, and optical axis differential orientations between the interferometer and the spherical mirror were determined for each frame. Figure 19 shows a typical sequence of three frames. The subtle changes in the interference patterns of the outer frames correspond to a rotation of 0.031 arc second (in 0.01 second)

about the X axis. The "RMS" angular deviations (vector quantity in two axes) obtained from this data is less than 0.11 arc second, with the low-inertia supporting beam. The level of angular deviations is expected to be substantially reduced, i.e., to levels of .03 to .05 arc seconds, when the moment of inertia is increased by addition of the equipment section and airbearing skirt. In the final test configuration, the table inertia is effectively 1/8 the Space Telescope moment of inertia. Floating the table will also reduce some of the seismic disturbance coupling.

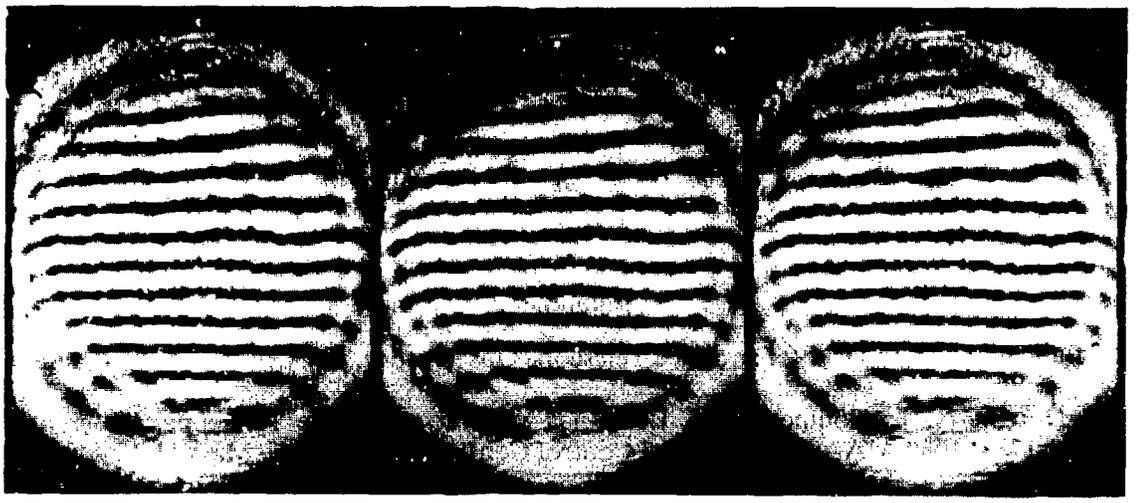

Figure 19 Typical sequence of interference fringe patterns

Due to the limited sample of data, no spectral analysis of the interferometer data has been made.

The RMS data obtained from interferometer data is over limited time periods, e.g., one second, and, tends to be difficult to reduce and measure. Hence the optical data tends to lead to larger values than these obtained from the seismometer data. The seismometer data is considered the more accurate. The interferometer data has been used to evaluate short term "cultural" noise, e.g., spikes, which might be masked in the seismometer data.

Comparison of 4 selected frames with the same beam orientation, recorded at time intervals of approximately 0.25 second, allows a preliminary evaluation of air turbulence levels. The free air gap between the windows on the tubes surrounding the beam was set at one inch. The gap was located at 30 inches from the spherical mirror, where the beam aperture is about 4.5 inches. The peak-to-peak local wavefront distortions observed between the compared frames do not exceed 1/8 of fringe spacing ($\lambda/16$). Extrapolated to a 12-inch aperture, the maximum beam deviation due to air turbulence should not exceed 0.015 arc second, peak to peak. It is recognized that limited sample of data was used, but it is evident that the air turbulence effect on any optical instrumentation would be less than the .03 to .05 arc second (RMS) requirement for Space Telescope Testing.

Conclusions from the Testing

Based on the results of the Lockheed and Holloman seismic evaluation of the LMSC airbearing facility, it was found that:

1) The LMSC seismic instrumentation agrees with the CIGTF instrumentation and is adequate for the monitoring of testing.
2) The seismic measurements are consistent with a simple dynamic model of the airbearing table when the gravitational effects on the horizontal seismometers is taken into account.

By recognizing that an active control system will attenuate any seismic disturbances below 1 Hz during testing, the seismic tilt angle disturbance is estimated to be .013 arc sec for the main resonance and bounded by .05 arc seconds. These values are within the requirements for the Space Telescope testing.

References

1) J. N. Bahcall, C. R. O'Dell, "The Space Telescope Observatory," NASA TM-78301, June 1979.

2) H. J. Dougherty, K. Tompetrini, J. Levinthal, G. Nurre, "Space Telescope, Observatory in Space", 80-1784, 1980 AIAA Guidance and Control Conference, Danvers, Mass 11-13 Aug. 1980.

3) "Data Package For A Seismic Environment Test at Lockheed Missiles and Space Center, Sunnyvale, California, 22-28 February 1980," Lt. L. P. Schelonka, Central Inertial Guidance Test Facility, 6585th Test Group, Holloman AFB, N. M., March 1980.

4) "Seismometer and Accelerometer Response," Dennis W. Gilstad, Appendix 2 of FJSRL-TM-7904-00-8, CIGTF, Oct 1973

5) "Stabilization of a Seismic Isolation Block Inertial Instrument Testing," Emil Brodersen, AIAA paper #74-857, Aug 1974

6) "Detection and Compensation for Milliarcsecond Motions of Precision Inertial Instruments," B. J. Simmons and D. R. Stevens, AIAA paper #76-1965,

TITLE: CRUISE MISSILE GUIDANCE SYSTEM (CMGS) TESTING AT THE CENTRAL INERTIAL GUIDANCE TEST FACILITY (CIGTF)

AUTHOR: WILLIAM T. RITTER

TEST TRACK DIVISION, 6585TH TEST GROUP
Holloman AFB, New Mexico

TABLE OF CONTENTS

K-2

ILLUSTRATIONS

K-3

I. INTRODUCTION:

In 1975, both the United States Air Force and Navy were interested in developing Cruise Missiles. The Navy Cruise Missile Program Office was involved with selecting a guidance contractor for their version of the Cruise Missile. The Air Force had decided to use the same guidance system that the Navy had selected for their air launched version.

The flight testing of two different Cruise Missile Guidance Systems (CMGS), was conducted by the 6585th Test Group at Holloman AFB, New Mexico, from 18 July 1975 through 26 November 1975. One system was supplied by E-Systems and the other by McDonnell-Douglas Astronautical Corporation (MDAC). This paper will cover only the MDAC CMGS. This testing was one factor in the selection of a winning Navy Contractor.

Two phases of testing were conducted. A "Competitive Phase", which provided technical data on the CMGS performance to the Naval Air Systems Command. This phase of testing was limited by time rather than by the number of flights. A target date of 5 September 1975 had been established as the last day of the Competitive Phase. The MDAC CMGS arrived at HAFB on 18 July 1975 and this phase of testing was completed on 5 September 1975. During this period of time, one shakedown and nine competitive flights were flown.

The "Follow-on Phase" of testing began after MDAC

was chosen as the winning contractor. This phase lasted from 22 October to 26 November 1975. Nine standard flights and two pure inertial flights were flown. This resulted in a total of 21 flights for the entire MDAC CMGS program. Ten of the flights were scored plus one successful pure inertial flight was made. The remaining ten flights were not counted due to a variety of reasons (CMGS system problems, reference system problems, aircraft aborts, instrumentation problems).

All flights were conducted on board a C-141 aircraft specially modified to accept pallets with the MDAC CMGS and the Completely Integrated Reference Instrumentation System (CIRIS). The C-141 was modified to allow the CMGS to provide steering information to an aircraft crew member who controlled the lateral movement of the aircraft.

CIRIS was used as the reference system for the computation of errors throughout the flight. For the scoreable flights, errors were computed for two designated ground targets and two specified time durations, all of which occurred after the last update of the MDAC CMGS.

II. CMGS & TESTBED DESCRIPTION

A. CMGS MAJOR COMPONENTS

MDAC supplied the following major components for test and support of the CMGS. A block diagram of the equipment is shown in Figure 1.

1. Cruise Missile Guidance Set, Consisting of the following:
   a. Inertial System - Litton LN-35M, consisting of a P-1000 platform with special shock absorbing mount and LC-4516 computer.
   b. Honeywell- GG 1500AF01 Rate Gyro and accelerometer package.
   c. Honeywell APN-194 Radar Altimeter.
   d. McDonnell-Douglas analog filter assembly.
2. Control Display Unit (CDU) - to provide an operator with system control, status, and position display for "Quick Look" analysis.
3. Interface Panel - to provide signal conditioning of the signals between the aircraft and the CMGS.
4. Power Distribution Unit (PDU) - to provide control and fusing of power to the CMGS.
5. Battery - to provide a backup power source during any momentary power interruption.
6. Cooling System - to provide liquid cooling of the CMGS, simulating liquid fuel cooling of the system in the actual missile.

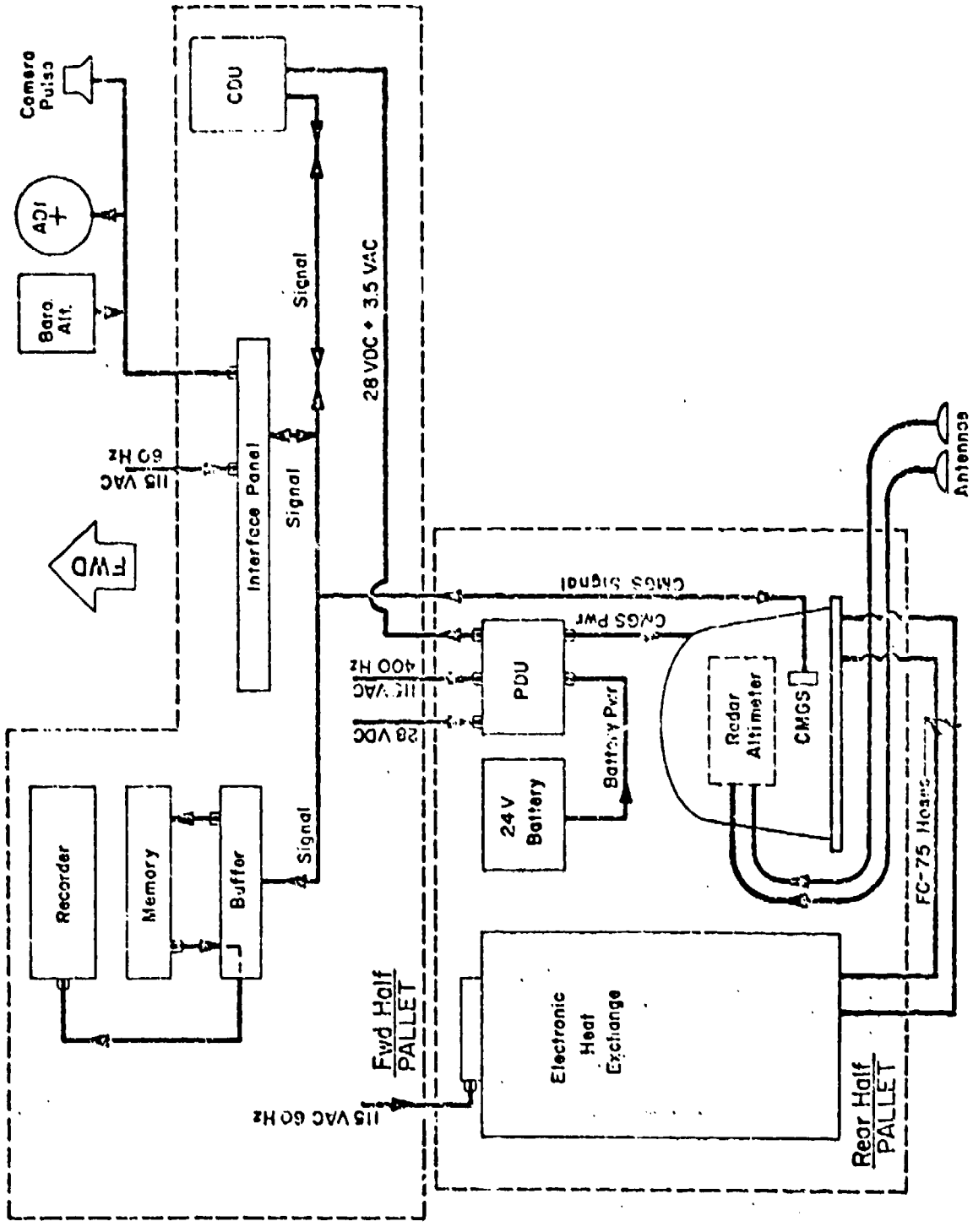

FIGURE 1 CMGS MDAC BLOCK DIAGRAM

7. Manual Control Unit (MCU) - Litton unit used to provide access to the computer program.

8. Paper Tape Reader - used with the MCU to load system program and map data into the computer.

B. C-141 AIRCRAFT

The C-141 Aircraft (NC-141/SN62-12776) is utilized exclusively for the Central Inertial Guidance Test Facility (CIGTF) testing under formal agreement with the Aeronautical Systems Division (ASD). Mechanical and electrical interfaces have been standardized. Palletization techniques provided in the testbed enable systems to be easily moved between the laboratory and the aircraft environment. The C-141 has been modified to accommodate five system test pallets. Pallet Station 1 is occupied by the CIGTF's CIRIS. The remaining stations are available for the systems under test.

Power change over from external ground power source to aircraft power was accomplished in 50 milliseconds and in accordance with MIL-STD-704.

The following items were made available for project use on the testbed aircraft:

1. Attitude Director Indicator (ADI)
   - P/N 143222-01-02
2. Barometric Pressure Transducer
   - P/N 502000-39 HTL Industries INC.

3. Two Radar Altimeter Antennas - AS 2595/APN-194

4. Camera Pulse Signal

The ADI was used to display the CMGS generated cross-track steering commands and the target event signal. Analog barometric pressure signals were supplied to the CMGS from a pressure transducer on the aircraft. The radar altimeter antennas were flush mounted to the bottom of the aircraft and connected directly to the radar altimeter component of the CMGS. The on-board vertical camera was manually activated by a crew member upon receipt of the target event signal.

C. REFERENCE SOURCE - CIRIS

1. The Completely Integrated Reference Instrumentation System (CIRIS) provides a highly accurate position, velocity, and attitude reference over long flight paths, for real-time use, in testing guidance and navigation systems. The CIRIS is an airborne automated system that is operationally independent of National Ranges (White Sands Missile Range, etc.). CIRIS advances flight testing of navigation systems in two areas:

   a. Highly accurate continuous reference data is usable for aircraft testing over long periods of time.

   b. Real-time and near real-time data provides

immediate evaluation of systems under test.

2. CIRIS generates the reference data by using four measurement devices that are controlled and time-coordinated by a minicomputer to provide inputs to a 15-state Kalman filter. The real-time filtered reference data which is generated in a second minicomputer can be distributed to test data acquisition computers and recorded with the raw measurement data on magnetic tape. Further processing (backward filtering and smoothing) can be done post-flight as required.

   a. CIRIS data meets the following specifications:

      (1) Position accuracy to 13 feet (1 sigma) in three-axes.

      (2) Velocity accuracy to .10 feet/second (1 sigma) in three-axes.

      (3) Attitude accuracy to 6 arc minutes (1 sigma).

      (4) Real-time reference data every 10-15 seconds.

      (5) Post-flight reference data every 1-4 seconds.

      (6) Continuous reference for longer than 84 minutes in any direction (limited only by transponder availability).

Some of the specifications can experience degradation where transponder coverage is limited.

b. The measurement hardware includes an inertial navigation system stabilized by barometric altitude from an air data computer, a precision radio range/range-rate system, and eventually a doppler radar. The inertial system data is used in the filter as continuous reference for data propagation and reference for the filter error states. The error states can be updated by incorporation of barometric altitude, doppler velocities, and precision range and range-rates to precisely surveyed ground sites. The CIRIS accuracies are directly dependent on the measurements obtained from the range/range-rate system which includes an airborne interrogator that is used to selectively interrogate one ground based transponder every two seconds. The use of four transponders nearest the current aircraft location provide in a time-phased triangulation scheme, range and range-rate estimates, including one redundant measurement. The transponder and its associated omni-directional antenna are

portable and are designed for remote operation. They are deployed in a triangular pattern separated by approximately 150 miles in a line along the flight path. Degraded CIRIS data can occur when flight paths leave areas of radio range coverage (200 nautical miles line-of-sight). Future plans to incorporate doppler radar data will minimize degradation during periods of limited transponder coverage.

III. TEST DESCRIPTION

A. PHILOSOPHY

The Navy required that the competitive phase of testing provide for a realistic capability test, from which a fair and impartial data base would be compiled for final evaluation. This was accomplished by utilizing verification testing techniques and near operational profiles. To meet requirements, the Applied Physics Laboratory of John Hopkins University was desginated by the Navy to select a route for the test. The route was selected without knowledge or consultation of either contractor and was provided to them simultaneously.

Along the route seven areas were available for gathering data. The contractor was allowed to

select any portion within these areas for fixing. The selected data within these fix areas was digitized for storage in the MDAC CMGS. The actual flight path of a normal flight and short flight are shown in Figures 2 and 3, respectively. Figures 2 and 3 also show the CIRIS transponder locations in addition to the actual CIRIS flight position. The numbers indicate the locations of the various transponders. The C-141 was flown over the path shown by commands from the CMGS using the cross-track steering indicator which was used by an operator at the second station autopilot.

B. TARGETS

Initially, two ground targets were selected to evaluate the accuracy of the system. These targets were specified distances from the last fix area. After the testing started, the Navy decided that errors at designated time durations following the last system update would be beneficial since the errors in an inertial system are functions of time rather than functions of distance. Since the velocity of the C-141 varies from mission to mission, the timed targets would provide a common point for comparison of data from flight to flight. Specific time durations were established based on an actual Cruise Missile profile.

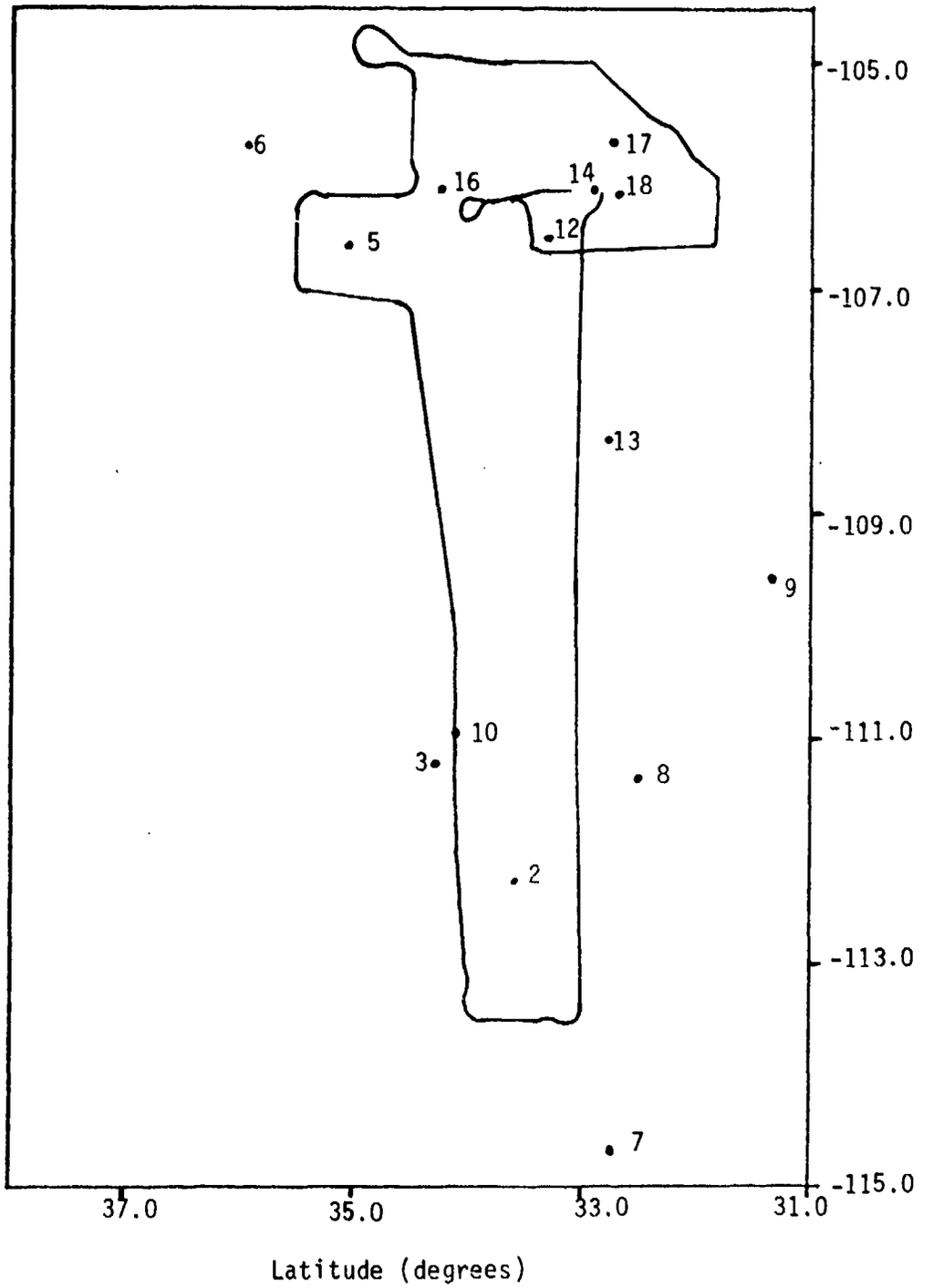

FIGURE 2 ACTUAL - NORMAL FLIGHT PATH

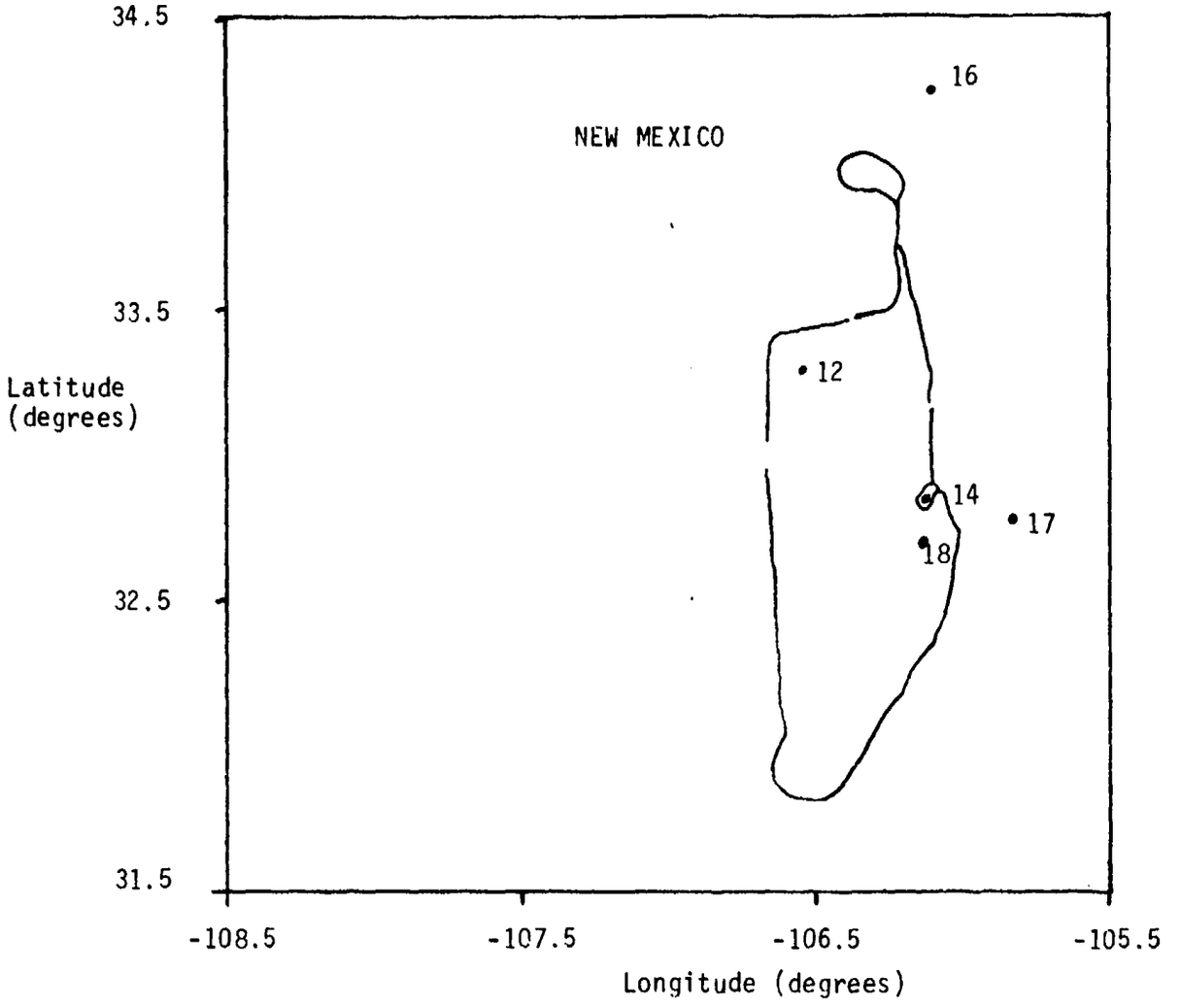

FIGURE 3 ACTUAL - SHORT FLIGHT PATH

C. CONTROL OF C-141

Pilots performed the normal aircraft take-off procedures. Due to the requirement to navigate to the various fix areas, the course of the C-141 had to be under the control of the CMGS. This was accomplished, after flap and gear retraction, by having the CMGS provide crosstrack steering information to the steering bars on the Attitude Director Indicator (ADI). Lateral control of the C-141 was based on an operator steering the aircraft using the output of the ADI. Since the C-141 was following the lateral commands of the CMGS, a malfunction could result in the aircraft going too far off course. Therefore, the contractor provided error bounds along the route which, if exceeded, would signal a system failure. The pilots would control altitude and airspeed. Deviations from the CMGS commanded guidance occurred only when thunderstorm avoidance was necessary. Although this was a rare occurrance, it did prevent overflight of a fix area on one flight and resulted in an unscored flight. Overflight of fix update areas was maintained close to that of an operational Cruise Missile, at low flight altitude. Throughout the flight the status, performance, and operation of the system was monitored and hand written records were taken of planned and unplanned

events. The aircraft was flown at low level only over fix update areas. Between these areas flight was accomplished at altitudes ranging between 16 and 28 thousand feet. After the last fix update area, a climb was initiated and target overflight was made at approximately 8,000 feet above the target. System target overflight was indicated to the second station by the appearance of the vertical steering bar "Off Flag" on the ADI. Upon this indication the operator announced "target" and activated the vertical camera. This procedure provided a means of estimating a "Quick Look" miss distance. After overflight of the last target the pilots took complete control and landed the aircraft.

Prior to reaching the first fix area, the CMGS navigated using its inertial system only. Between fix areas and from the last fix to the targets the system navigated using the inertial system only. Therefore, the quality of the CMGS's inertial performance is critical to the overall system performance.

Since the competition was time limited and the customer desired as large a sample of data as possible, an alternate short route was established during the flight test. It was identical to the normal flight route except that it covered only the

last hour of flight, starting just prior to fix area #5. The short route was flown three times during the competitive phase of testing.

D. CMGS ADJUSTMENT, MAINTENANCE, AND REPAIR

No adjustment, maintenance, or repair was made to the system hardware or software at any time after presentation of the program and data tapes to the project engineer without the approval of the Naval Air Systems Command (NAVAIR). The Aeronautical Test Division insured that the system was not made available to the contractor for adjustment, maintenance, or repair without the consent of NAVAIR.

E. SCORING CRITERIA

1. Failure of Test

A test was declared a failure if any of the three following conditions were not met.

a. Every time a test system was aligned for a competitive flight, standard alignment procedures were followed and the system had to be ready to navigate in 23 minutes or less.

b. The test system had to navigate for 100 percent of every test mission unless shutdown was accomplished due to or as protection against external disturbances such as excessive heat, power

fluctuation, etc.

c. The test system had to position update the inertial system after flying over the last matrix area and not indicate a system failure at anytime during the flight.

2. Invalid Tests

An invalid test was designated for all tests yielding no useful performance information over the designated targets due to:

a. System malfunction caused by operator error.

b. Occurrence of some incident beyond the control of the system under test, which seriously impacted the CMGS performance.

c. Failure of the test instrumentation or other testbed support equipment.

3. Valid Tests

All other tests were considered valid.

4. Successful Tests

All valid tests completing the planned profile for which final (or target) reference position data was available with an accuracy of +/- 50 feet were recorded as a successful test.

5. Scoreable Tests

In order for a flight to be considered a

scoreable flight, the fix areas had to be overflown and data collected during the time of overflight. If this did not occur, the flight was not considered to be representative of successful performance and therefore not scoreable.

IV. TEST RESULTS

A. TEST HISTORY

The MDAC version of the CMGS underwent competitive flight evaluation during the period from 18 July through 5 September 1975, and follow-on evaluation during the period 22 October through 26 November 1975. Table I summarizes the number of turn-ons, operational hours, navigation hours, flight hours, scoreable flights, valid flights, and invalid flights.

TABLE I

PROGRAM TEST TOTALS

	COMPETITIVE PHASE	FOLLOW-ON PHASE	TOTAL
Turn-on's	84	113	197
Operational Hours	144	117	261
Navigation Hours	80	83	163
Flight Hours	31	45	76
Scoreable Flights	5	5	10
Valid Flights	6*	5	11
Invalid Flights (CMGS Prob.)	0	2	2
Invalid Flights (Not CMGS Prob.)	4	4	8

* One Flight Not Scoreable.

One shakedown flight plus nine other flights were made during the competitive phase of the testing and eleven flights were made during the follow-on phase of the testing. A flight summary of the C-141 cargo flight tests is shown in Table II. Of the 21 flights, 11 were considered valid flights and 10 were considered scoreable. The reasons why specific flights did not provide scoreable data are given below.

Flight SD-001 was a shakedown flight.

Flight MC-002 was classed as an invalid flight for two reasons. First, the aircraft had to fly around storm centers that were located on its programmed flight path prior to reaching fix area #4. During these periods of flight, the CMGS was not steering the aircraft laterally. Second the duration of the navigation time (approximately 20 minutes) while setting at a ground level of 4040 FEET, caused a register overflow problem in the software. This problem will not happen during the operation of a submarine launched missile because the navigation time prior to firing is very short (1-2 seconds) and its altitude relative to sea level is very small. A patch to the software was made to complete the flying tests, but the modification will not be incorporated into the final software package.

DATE 1975	FLIGHT NUMBER	TYPE	NAV TIME (HRS)	FLIGHT TIME (HRS)	SYSTEM FAILURE	INVALID FLIGHT	VALID FLIGHT	SCOREABLE TERCOM	COMMENTS
6 Aug	SD-001	Shakedown	7.0	6.1			x	NA	
14 Aug	MC-001	Normal	5.4	4.7			x	x	
21 Aug	MC-002	Normal	5.5	5.0		x			Weather Abort
25 Aug	MC-003	Normal	6.0	4.6			x	x	
27 Aug	MC-004	Normal	3.2	2.6		x			Aircraft Abort
28 Aug	MC-005	Normal	5.0	4.4			x	x	
3 Sep	MC-006	Short	.5	.0		x			Weather Abort
3 Sep	MC-007	Short	1.6	1.3			x	x	
4 Sep	MC-008	Short	3.8	1.3		x			Instrumentation recorder problem
5 Sep	MC-009	Short	3.0	1.2			x	x	
14 Nov	MC-010	Normal	4.6	4.3	x	x			
19 Nov	MC-011	Normal	4.6	4.3			x	x	
20 Nov	MC-012	Normal	2.8	2.2		x			CIRIS Abort
21 Nov	MC-013	Normal	4.6	4.2			x	x	
21 Nov	MC-014	Normal	5.0	4.4			x	x	
22 Nov	MC-015	Normal	6.2	4.6		x			CIRIS Abort
23 Nov	MC-016	Normal	5.0	4.4			x	x	
24 Nov	MC-017	Normal	6.5	4.3			x	x	
24 Nov	MC-018	Pure Inertial	2.6	1.5	x	x		NA	
25 Nov	MC-019	Normal	5.3	4.8		x			Instrumentation recorder Problem
26 Nov	MC-020	Pure Inertial	6.1	5.6		x		NA	
				TOTAL	2	10	11	10	

TABLE II

FLIGHT SUMMARY

Flight MC-004 was classed as an invalid flight because of aircraft problems during the flight. The aircraft commander aborted the remainder of the flight as a result of these problems.

Flights MC-006 and MC-019 were classed as invalid flights because no data was recorded by the instrumentation system during the flights.

Flight MC-008 was classed as an invalid flight because of weather problems.

Flight MC-010 was classed as an invalid flight because of a system failure. The system did not update itself after fix area #7 and therefore would not have armed a real missile. The contractor attributed the problem to a large navigation error caused by erratic gyro performance.

Flights MC-012 and MC-015 were classed as invalid flights because the CIRIS reference system aborted during the flights.

Flight MC-018 (pure inertial flight) was classed as a system failure because a correlation was erroneously attempted by the system during flight. This was not supposed to occur with the aircraft flying East and below the latitude of the first fix area. However, the system did attempt to correlate which resulted in erroneous system performance. The contractor attributed this problem to a computer malfunction in the memory.

Flight MC-020 was a pure inertial flight. It was classed as an invalid flight because it did not meet the original scoring criteria.

B. DATA REDUCTION

1. DATA PROVIDED TO MDAC

After unpacking and editing the data from the raw CMGS data tape, position comparison was accomplished by interpolating the reference data (CIRIS) to the system data at the system output times, which occurred every five seconds. The IRIG time used for this comparison was appended to each record of the CIRIS and CMGS data tapes during the flight. This comparison produced system errors for each flight from approximately the time of aircraft take-off to aircraft landing. Plots were made of the system position errors over the entire flight, with blow-ups covering the period of time after the last update, through all four targets. The plots were annotated to show all update locations and reasons for no data coverage. Listings of all data was provided as required.

In order to present the miss distances in a form which provided an indication of system performance, CEP data was generated for the ten scoreable flights. Two methods were used which

are explained as follows.

a. METHOD 1

Autonetics developed this method of finding the CEP (50th percentile and 90th percentile), and the associated confidence limits (92, 85, 65 percent) of each. This method assumes that the latitude and longitude errors were uncorrelated and Chi distributed. Data was presented showing the resulting CEP with its respective confidence limits for each of the four targets. Reference #1 gives details of this method.

b. METHOD 2

This is a simplier method of finding the CEP of four targets for the 10 flights. A scatter plot of the miss distances was made and a circle was drawn halfway between the 5th and 6th (working out from the center) target miss coordinates. Mathematically this is the median of the RSS values for the ten flights.

Data was presented showing the CEP, Median Root Sum Square (RSS) error, and 90th percentile of the two designated ground targets

and the two specified time targets. In addition, the confidence intervals for 65, 85, and 92 percent were presented.

In order to gain a further estimate of the pure inertial accuracy of the system, the error prior to the first update was examined. Data was presented showing the position errors of the system for each flight just prior to updating at fix area #1. Although no statistical methods were used and the Schuler oscillation of the errors can be misleading, this data did give some indication of the pure inertial performance.

2. DETERMINATION OF EVENT TIMES

The time of the last update was difficult to precisely identify. Within fix area #7 a 3-correlation voting scheme was used. Immediately following the last of the three correlations the CMGS generated position residuals which were recorded on the system data tape. Since the CMGS data was output at 5 second intervals, the actual residual change could have occurred at any time within the 5 seconds preceeding the change indicted on the system data tape. Therefore, the midpoint of this interval (2.5 seconds prior to indicated change) was chosen as the point for computing

the starting time for the two time targets.

After testing began, the Navy requested that the CMGS error be computed after the last update. The time used above for computing the timed targets was not appropriate for this computation since the voting mechanization had not been completed at this time, resulting in the latitude and longitude outputs not being updated yet. Therefore, the error at the last update was computed at the first time when the latitude and longitude had been updated by the CMGS. This was generally in the next 5 second data interval. An additional requirement for computing the miss distance at the last update was that CIRIS data be available. Since CIRIS coverage was optimized for the targets and not at the last fix area, and the aircraft was at a low altitude, there were flights where CIRIS data was degraded or not available. In those cases, the error was computed as soon as good CIRIS data became available.

The ground target error was computed by comparing the CIRIS output to the CMGS at the point of closest approach to the target, as indicated by the CMGS latitude. Since the aircraft was flying almost due South, the system indicated latitude had to coincide with

the target latitude at some point in time. This time was selected as the time to make the comparison between the system position and CIRIS position.

3. TIME BIAS ERROR

No known time bias errors were detected on flights MC-001 through MC-008. A timing bias error was detected on flights MC-009 through Mc-017. This problem was caused by the instrumentation system and not the CMGS under test. The problem was associated with the IRIG-B time that was appended to the CMGS output buffer (recorded on tape). The bias was found to be constant during a given flight, but variable from flight to flight.

In order to recover the data, a standard method for determining the timing bias on each individual flight had to be developed. The method arrived at was based on the knowledge of how North-to-South or South-to-North aircraft heading changes affect the longitude error of a system during the inertial phase of the flight. Figure 4 shows an example of how timing biases and/or system errors influence the longitude error when these types of heading changes are made. This condition occurrs when the system experiences a heading change from 90 to 180

degrees. When a timing bias exists, a sine wave characteristic is induced on the longitude error as shown in the bottom plot.

The following procedure was used on each flight that exhibited the timing bias.

a. An initial plot of the latitude, longitude, and RSS errors was made covering a time span that included a 90 degree heading change. From these plots, visual detection of a timing bias was possible.

b. The system IRIG time was then biased by +0.5, +0.75, +1.0, +1.25, and +1.50 seconds. The latitude, longitude, and RSS errors were plotted for each time bias.

c. By visual inspection of the plotted data, the actual timing error bias contained in the data could be identified as falling between any two of the generated time biased plots. Too much of a timing bias correction will reverse the sine characteristic on the longitude error.

d. Another iteration followed, this time at +0.05 second intervals within the selected .25 second area.

CMGS ERROR WITH NO TIMING BIAS ERROR

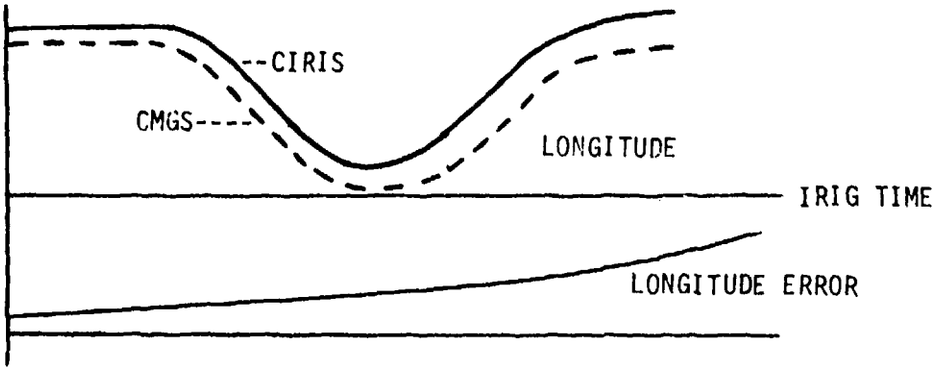

TIMING BIAS ERROR WITH NO CMGS ERROR

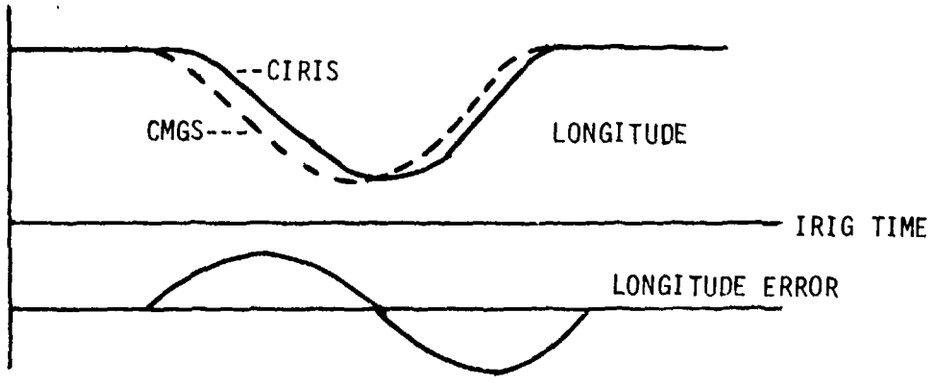

TIMING BIAS ERROR AND CMGS ERROR

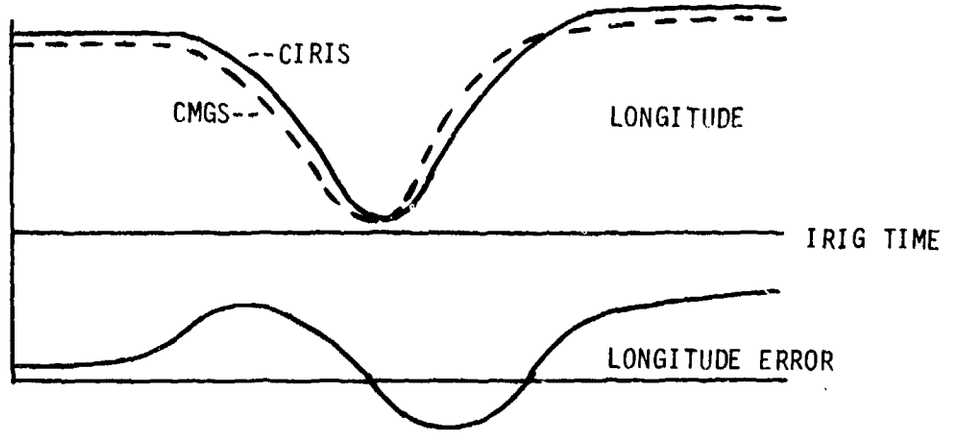

FIGURE 4 TYPICAL TIMING ERROR AND/OR CMGS ERROR

e. From this latest set of plots, the timing bias could be visually identified as falling between two of the 0.05 second intervals.

The accuracy of the system position error data after determining the timing error to within +/-.025 seconds is +/-12.50 feet at 500 ft/sec aircraft speed. TABLE III shows the timing bias that was used to recover the position error data of the affected flights.

TABLE III

CALCULATED TIMING BIAS ERROR (SECONDS)

FLIGHT NUMBERS						
MC-009	MC-010	MC-011	MC-013	MC-014	MC-016	MC-017
1.05	0.70	1.05	0.80	0.95	1.15	0.55

4. PHOTO DATA

There were three flights during which the CMGS guided the C-141 to the targets, but no errors could be computed (MC-008, MC-015, MC-019). On all of these flights, photos were taken of the ground targets using the checkpoint camera aboard the C-141. These photos were examined to see if they could be used to provide valid system miss distance

information for these flights.

To establish the validity of the photo data, eight flights were analyzed which had both CIRIS and photo data available. The miss distances from the photo were compared with the miss distances from the CIRIS. The results ranged from 50 to 550 feet difference. This demonstrated the validity of the camera for quick-look indication of system performance. However, discrepancies of 500 feet or greater prevented using the photo miss distances in any quantitative assessment of system performance. A qualitative assessment of the performance from these three flights does indicate that the system did provide accuracies on these three flights equivalent to those experienced on the other scoreable flights.

5. INERTIAL FLIGHTS

Two pure inertial flights were flown near the end of the program. However, the first flight on 24 November was classified as a system failure. This resulted from a computer memory failure according to the diagnosis of the contractor. No problems were encountered during the second pure inertial flight on 26 November. The C-141 flew west along the

standard verification flight route and returned along the same route. The flight covered approximately six hours. Photographic checkpoints approximately 5 minutes apart were used as the reference system. A plot of the system errors was provided to MDAC. A growth rate radial position error was calculated and presented in the report. Although this is only one flight and several are needed to specify system performance, it does give an indication of the accuracy of the inertial system used during this test program.

V. CONCLUSIONS

The MDAC portion of the CMGS Competitive Navigation Flight Test, Follow-on Flight Test, and Final Report were completed on schedule. The data was presented to the customer in sufficient time for utilization in the selection process.

From the project's planning stage in late May 1975 through the Final Report in February 1976, a very short time elapsed for such a very important project. The MDAC CMGS, as well as the CIRIS System, functioned very well during this period with few problems. The time bias problem could have resulted in no valid data, but a method to recover the data was developed and applied so that no loss of data or test time occurred.

REFERENCE

1. "Inertial System Performance Evaluation" by L. L. Rosen and D. L. Harmer, Autonetics Corporation, Third Inertial Guidance Test Symposium Proceedings, MDC-TR-66-106, Vol I, 19-21 October 1966.

2. "Cruise Missile Guidance System (CMGS) Fly-Off and Follow-On-Test McDonnell/Douglas Final Report," by Central Inertial Guidance Test Facility, 6585th Test Group, Holloman AFB, NM 29 February 1976.

TITLE: FLIGHT TEST OF THE ALCM NAVIGATION SYSTEM

AUTHORS: M. D. MOBLEY
J. I. BROWN

BOEING AEROSPACE COMPANY
Seattle, Washington

FLIGHT TEST OF THE ALCM NAVIGATION SYSTEM

M. D. Mobley

ALCM Developmental Engineering Manager

Boeing Aerospace Company

J. I. Brown

ALCM Navigation Design Manager

Boeing Aerospace Company

ABSTRACT

This paper describes Boeing's Air Launched Cruise Missile (ALCM) Navigation System Test Program. Although the emphasis of the paper is on development and test of the navigation system as it is mechanized in ALCM operational software, system hardware is also discussed. ALCM navigation, terrain correlation, and Kalman filter mechanization are described. ALCM navigation system success is largely due to the orderly progression of its development from simulation to live launch. Details of these tests and a summary of major system test results are presented so that others with a similar development task may benefit from the studies and test methods used by ALCM navigation personnel.

I. INTRODUCTION

The Air Force has ordered production of the ALCM, a nuclear tipped, turbofan powered, long-range strategic cruise missile developed specifically for air launch. The ALCM is designed for compatibility with either the current B-52/SRAM avionics or the avionics being added to the B-52 as part of the offensive avionics system (OAS) update. This paper covers testing the ALCM navigation, terrain correlation, and Kalman filter mechanizations, including hardware and software.

ALCM design and development began at Boeing in 1972 with a contract award for the subsonic cruise armed decoy (SCAD). However, Boeing developmental efforts on the terrain correlation updated guidance system started well before that. Reference 1 summarizes Boeing's early terrain correlation work. The SCAD program was stopped in 1973 and was redirected to a technology demonstration.

After six successful launches in 1976, Boeing prepared for a full-scale engineering development program, but was redirected to a competitive flyoff, using a different configuration missile, AGM-86B. Boeing won this competition, and the navigation performance was listed as one of three major factors that led to Boeing's success (ref. 2). The navigation simulations and tests leading to this competitive flyoff program are described. A follow-on launch program for further evaluation is currently in progress and will include launches from an OAS-modified B-52.

Boeing's test program was designed so that test conditions represented operational conditions as closely as possible for the flight and for missile checkout and maintenance and mission planning. This ensured that test results represented expected system performance in an operational environment. Development and test of

the ALCM navigation system progressed from simulation, ground test, T-33 flight test, and captive flight test to live missile launch. This orderly progression, defined at the outset of program development, played an important role in the success of the system. Each test along with its major objective is discussed in the paper.

II. ALCM NAVIGATION SYSTEMS DESCRIPTION

Figure 1 shows the navigation hardware used during the competitive flyoff. The equipment on the left is onboard the carrier aircraft and is operational B-52 hardware with one exception—the bulk memory unit (BMU) that was added as part of Boeing's B-52 modification for the flyoff. This unit contains a small, removable, easily portable tape transport unit (TTU). The TTU uses a magnetic tape to store mission data for the entire complement of ALCM's on a fully loaded B-52. The OAS program will use a tape storage device very similar to that used by Boeing during the competitive flyoff.

Equipment on the right of figure 1 is the avionic equipment of the ALCM and short-range attack missile (SRAM). The B-52 system can align and launch ALCM's or SRAM's carried on wing-mounted pylons or on a rotary rack carried in the bomb bay. Carrier avionics include a master computer that provides initialization and alignment data to ALCM and SRAM and sequences the missiles through launch. The carrier inertial measurement unit (IMU) provides a stable reference for the launch platform.

The B-52 airplane avionics, Doppler heading systems, and position fix radar provide data for IMU initialization and alignment. The carrier aircraft equipment is equivalent in function to the equipment that will replace it with the B-52 OAS modification.

The primary ALCM avionics forming the navigation system are the computer, inertial reference unit, radar altimeter, static pressure sensor, and temperature sensor. The missile computer memory has 65,536 16-bit words;

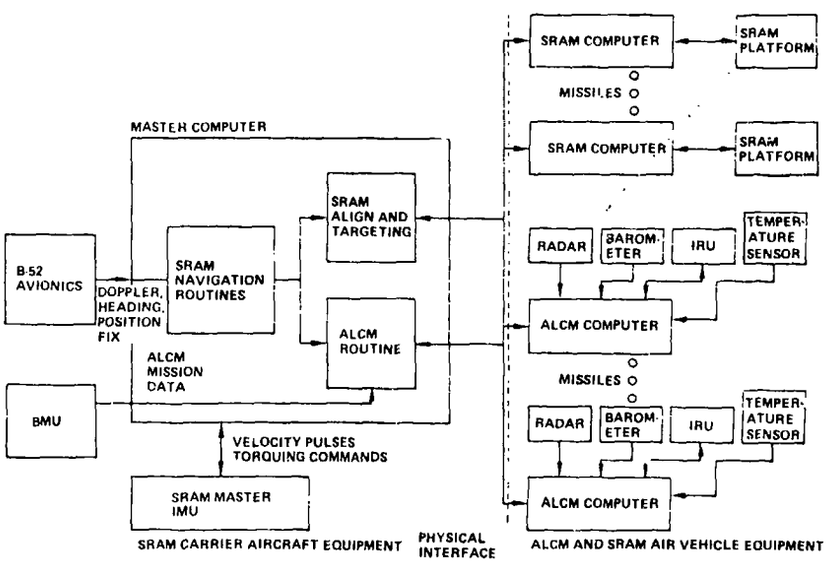

Figure 1. ALCM-SRAM System

approximately half of the computer memory is used for storage of mission data and the other half for operational flight software. The missile computer controls all missile freeflight functions, including navigation and missile guidance along a preplanned horizontal and vertical path. The IMU provides an accurate reference for ALCM navigation functions. The radar altimeter is used by the flight control for terrain following and by the terrain correlator. Pressure, temperature, and inertial vertical velocity are used for accurate vertical position determination during altitude-hold flight segments and terrain correlation flight segments. Figure 2 shows primary navigation functions and how those functions are allocated between the master computer in the carrier and the ALCM computer. The Kalman filter used for

Carrier	Missile
• Carrier navigation functions	• Free-flight navigation
• ALCM alignment initialization	• Vertical channel
• ALCM status and fault monitoring	• Terrain correlation
• Mission data transmittal	• Alignment Kalman filter
• ALCM launch initialization	

Figure 2. ALCM Navigation, Alignment Functions, and Allocations

alignment of the missile IMU to the carrier IMU is also used for processing the terrain correlation fixes in freeflight. Missile filter states are shown in figure 3. During missile alignment, the filter is updated every 60 seconds by comparing missile change in position to carrier change in position during this period. Based on this comparison, updates are made to all modeled states. During the alignment process, special corrections are used to account for carrier alignment taking place at the same time the missile is being aligned to the carrier. This dual alignment can easily cause filter divergence unless properly handled (ref. 3). During alignment the vertical channel of the missile is slaved to the carrier's vertical channel, using periodic updates

	Element	Definition
1.	ΔX	Position error - X
2.	ΔY	Position error - Y
3.	$\Delta \dot{X}$	Velocity error - X
4.	$\Delta \dot{Y}$	Velocity error - Y
5.	θ_x	Platform tilt - X
6.	θ_y	Platform tilt - Y
7.	θ_z	Platform tilt - Z
8.	ϕ_z	Computer coordinate t... - Z
9.	ϵ_x	Gyro drift - X
10.	ϵ_y	Gyro drift - Y
11.	ϵ_z	Gyro drift - Z
12.	G_x	Gyro scale factor - X
13.	G_y	Gyro scale factor - Y
14.	K_x	Accelerometer scale factor - X
15.	K_y	Accelerometer scale factor - Y

Figure 3. ALCM Alignment Matrix

to calibrate the missile vertical channel accelerometer bias. In freeflight the missile uses a third-order constant-gain filter to damp the inertial altitude with temperature-corrected pressure.

Figure 4 shows primary mission functions, time sequencing, and functions of missile and carrier computers during each mission stage. After ground testing of the airplane and missile systems, the B-52 with missiles uploaded is placed on alert. For an operational scramble, there is no time to warm up or align the avionics prior to takeoff. Once airborne, the B-52 navigation system uses heading systems, continuous Doppler radar velocity and position updates when available from the mapping radar for initialization and alignment. The alignment process is continuous and improves (to within limits imposed by system noise) the longer it takes place. As soon as carrier errors are acceptably stable, inflight alignment of ALCM's or SRAM's may begin.

Once power is applied to the missiles by the operator, ALCM's are sequenced under software control through coarse alignment and then fine alignment; this process aligns the ALCM platform to the carrier and also calibrates the platform. The alignment process continues until launch and mission data for

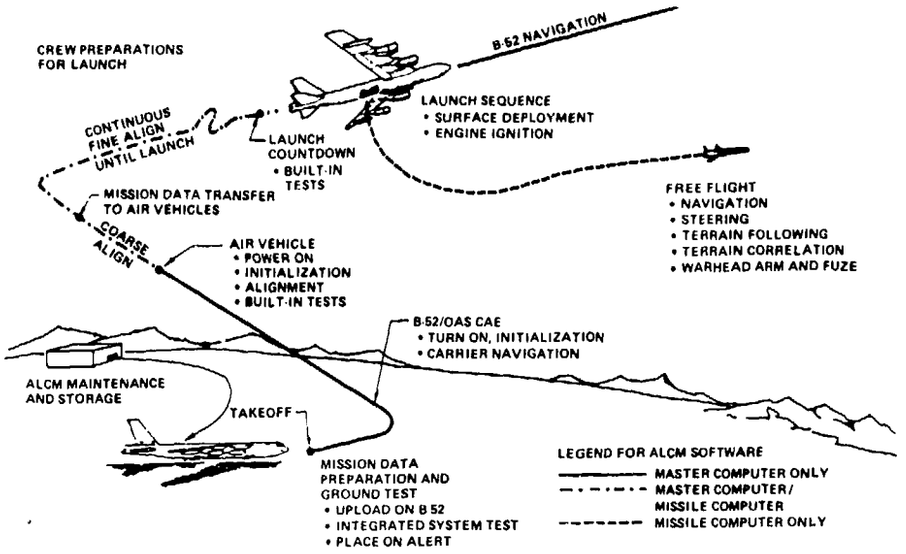

Figure 4. Typical Mission Functions

a specific trajectory are transferred from the B-52 bulk memory unit (BMU) to the missile computer memory some time before launch. These data, loaded in the TTU, are carried to the B-52 by the crew. The missions may be changed by reloading mission data prior to launch.

After launch the missile will follow the preplanned mission to the target, using terrain correlation position fixes to update position, further trim platform drifts and scale factors, and improve the estimate of missile velocity.

All ten of Boeing's missile flights during the competitive flyoff were launched following operational conditions described in figure 4. This approach provides assurance that obtained test results represent system performance likely to be achieved in an operational environment.

A conceptual view of the terrain correlation system is shown in figure 5. Hardware involved in terrain correlation is shown in figure 6 and was designed with error budgets compatible with terrain correlation and terrain following system needs. The correlating data for this system are a single string of terrain height data. This string is obtained with measurements from the radar altimeter, providing the height of the missile above ground level and measurements from the pressure-temperature-inertial system that provide a reference height of the missile above mean sea level.

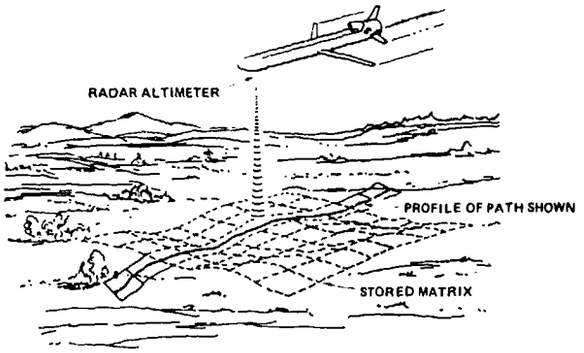

Figure 5. Terrain Correlation Concept

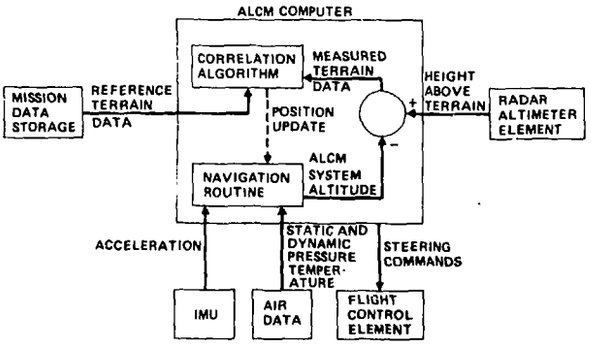

Figure 6. Terrain Correlation Flight Hardware

Use of the temperature probe to correct pressure and inertial vertical sensors significantly increases accuracy of reference height measurements. Radar and mean sea level altitude measurements are subtracted to obtain variation of the terrain elevation under the missile flightpath. This sample of sensed data is compared, a column at a time, with the reference data in the ALCM computer. The computer memory contains all columns of reference terrain elevations that ALCM should be flying over at that point in the mission. This matrix of reference elevations is commonly called a terrain correlation map.

By computing best possible match of measured data with stored elevation data, the navigation system estimates its position when over the map center and then updates itself. The stored maps are selected to be wide enough so that there is a very high probability of crossing the maps, and long enough so that there is a very high probability of obtaining a successful fix.

III. ALCM TEST PROGRAM

The entire development and test of the ALCM navigation system will be covered in this section. The phasing of ALCM navigation system development is shown in figure 7 and was designed so that test data could be used to affect subsequent tests. The objectives of the test were defined to fit in with the testing sequence and are listed in figure 7. In all of those design activities and tests, two important precepts were followed as closely as possible: (1) test in an orderly sequence, with new tests building on previous successes and (2) test in the same manner the system will eventually be used. Specific applications to ALCM development and test of these simple, common sense rules are described, and the effect on the test program is itemized in the following sections.

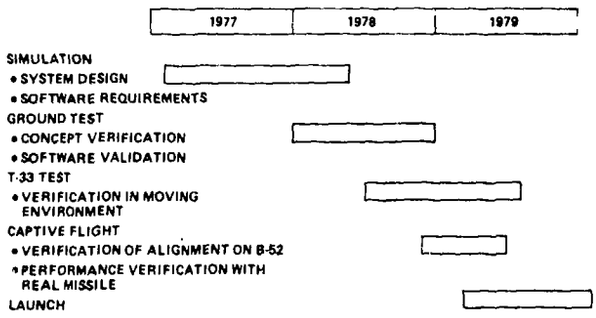

Figure 7. ALCM Navigation Tests

Simulation

The primary tool used in developing requirements for navigation software is the Alignment Navigation Simulation and Error (ANSER) analysis program described in reference 3. This is a Monte Carlo simulation program developed by Boeing over the past 15 years to develop and accurately model inertial navigation systems updated by a Kalman filter, using a wide array of sensors.

Figure 8 is a block diagram showing primary parts of the ANSER program; this program includes simulation of carrier and ALCM navigation mechanization. The simulation includes a very complete reference error model and a truncated error model that represents the filter in the missile computer. Missile and carrier simulations reside in the same program, allowing real-time interaction between missile and carrier filters to be determined and properly accounted for.

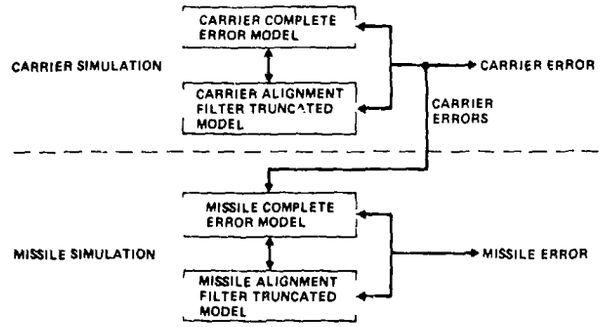

Figure 8. Alignment Navigation Simulation and Error (ANSER) Program

The ANSER program simulates the carrier navigation, missile alignment, missile freeflight navigation, and missile ground calibration and is the basic tool used to develop all navigation software requirements for the onboard missile filter.

Figures 9 and 10 contain data typical of that generated by ANSER: a plot of position error versus time from launch to target as well as the calibration of the platform from initial application of power through freeflight to target. Figure 11 shows data typical of trade results obtained with ANSER. In this case the number of states in the Kalman filter is the trade variable.

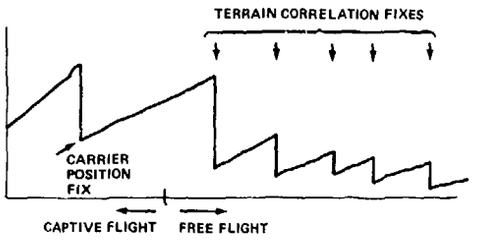

Figure 9. Typical ANSER Data

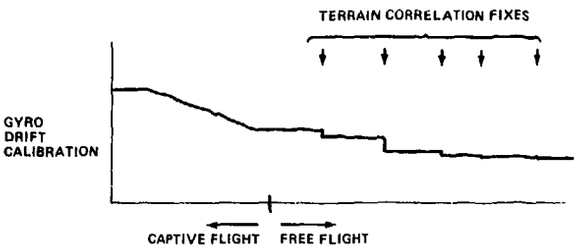

Figure 10. Typical ANSER Data

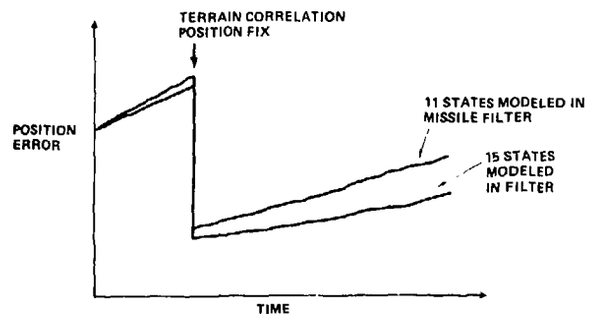

Figure 11. ANSER Trade Data

Figure 12 shows a simplified block diagram of the simulation program used to design and validate software requirements for missile terrain correlation and the vertical channel system. The simulation generates the sensed altitude strip (including all inherent system errors) and then performs the correlation function against the true terrain to estimate actual position. System errors include radar system errors (noise, scale factor, and beamwidth of the antenna), reference altitude errors (pressure errors, temperature errors, and angle-of-attack induced errors), vertical accelerometer errors (noise, scale factor, and biases), and reference map errors. This program was used to (1) establish requirements for design of the terrain correlation mechanization, (2) establish error budgets, and (3) perform detailed design of the vertical channel reference system.

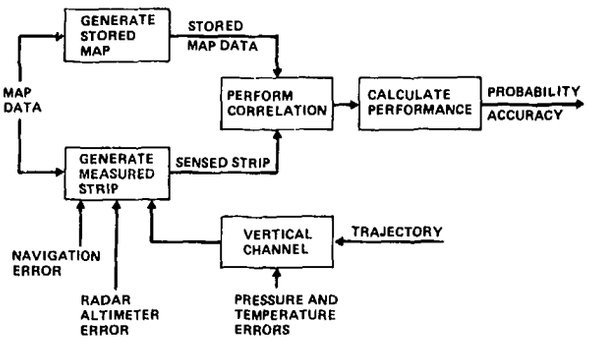

Figure 12. Terrain Correlation Simulation

Figure 13 shows the system vertical errors while terrain following. Vertical channel errors are particularly critical during terrain correlation while terrain following. In this mode, all of the sensors are subject to large errors. The vertical accelerometer is excited by large vertical acceleration, and the pressure system is excited by large vertical position and angle-of-attack excursions (affecting the pressure reading). Vertical channel gains were selected using this simulation so that the total vertical channel error was within the error budget.

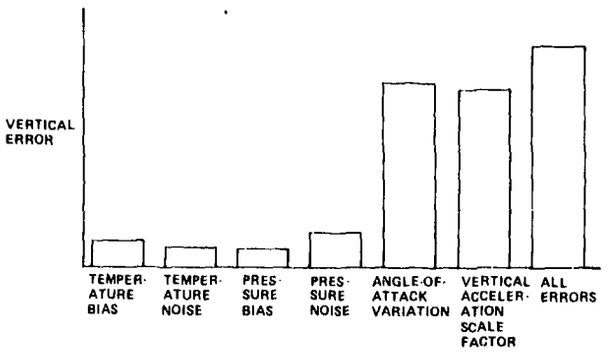

Figure 13. Vertical Channel Error Sensitivities

In addition to use in designing the system, the programs are used in analyzing flight test data (fig. 14). On a mission during the flyoff a false fix occurred, and this degraded performance throughout the remainder of the mission. Position error versus time on this mission is shown in figure 14 along with predicted performance, using ANSER with the false fix at the indicated point as the only error source. Clearly the false fix is the error source causing degraded performance at the target. The ANSER program was used in this case to isolate the cause of poor performance at the target, and the terrain correlation program was used to pinpoint the cause of the false fix.

Navigation Software Validation

After the basic design is validated via digital simulation, the next step is to document the design and write the program code. Actual disciplines and methods used by ALCM to design software are beyond the scope of this paper but described in detail in reference 4.

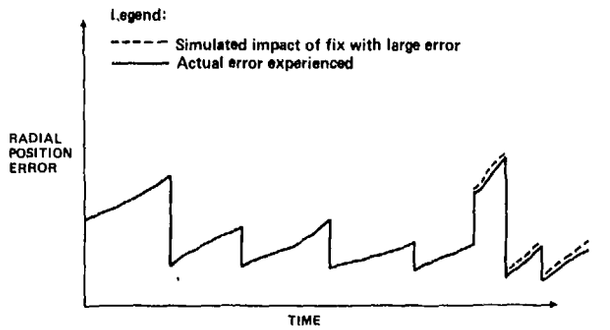

Figure 14. Use of ANSER in Analyzing Flight Results

The subsystem simulator is the primary tool in final validation of flight operational software. Validation takes place in a laboratory dedicated for this purpose. A block diagram of the primary simulator functions is shown in figure 15. Actual missile avionics used as part of the simulation are shown on the left of figure 15 and simulated components on the right. The simulation uses operational software residing in the flight computer and then simulates the external equipment so that the missile computer responds as if it were flying an actual mission from initialization through alignment, launch, and finally to target. Terrain correlation is also simulated during the mission.

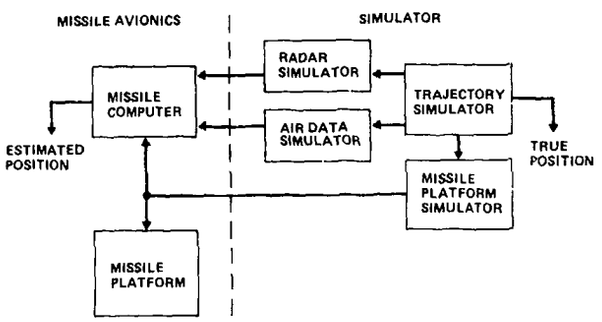

Figure 15. ALCM Subsystem Simulator

The trajectory and desired platform errors for the missile are input to the simulation. Placement of terrain correlation fixes is defined. Some platform errors that can be introduced include tilts, gyro drifts, and gyro and accelerometer scale factors. Instead of using the actual platform, the simulator inputs accelerometer pulses to the computer in place of the platform. The torque commands from the computer are sent to the simulator to be applied to the platform simulation. The simulator keeps track of true position.

Comparison of computer estimates of position with true position provides a measure of software and mechanization performance in a well-controlled environment with motion simulated. This can be done in the laboratory prior to flight commitment. In this manner the software and mechanization can be debugged in a controlled environment in which the risks associated with problems are much less than in a real launch. Typical results from a test run are shown in figure 16.

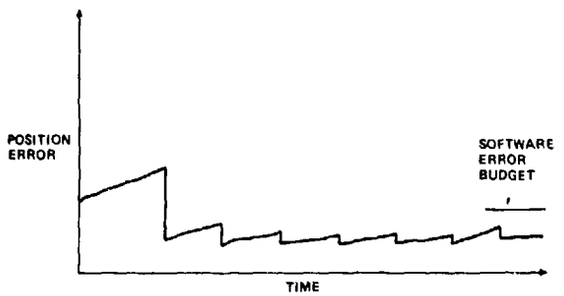

Figure 16. Subsystem Simulator Typical Results

There is an error budget for the navigation system that assigns certain error and error growth to the software. These test runs are used to ensure that the software error budget is met. The vertical channel and the terrain correlation system are validated in essentially the same manner. Each time a new software release is made, similar navigation runs are made even without a major navigation change, ensuring navigation performance for all software releases.

T-33 Flight

Once navigation requirements are validated in digital simulation and in the laboratory, the system should be tested in a real moving environment. For this test the ALCM program uses the T-33, which is a company-owned aircraft used exclusively for ALCM testing. The T-33 is used for testing cruise missile avionics because (1) speed and maneuvering capabilities of the T-33 are similar to the missile capabilities; (2) the T-33 can terrain follow, inducing all the errors caused by this into the navigation system and terrain correlation system; and (3) the environment is representative of the missile environment.

The T-33 is configured with prototype hardware of all missile flight avionics; ALCM equipment is located in the avionics bay. Inertial navigation element (INE), radar altimeter, air data computer, and the temperature probe and its electronics are part of the ALCM equipment used. The INE is sequenced, using a control and display unit accessible by the operator in the T-33 second seat. The two antennas used by the missile to measure altitude above ground are mounted in the T-33 with the same spacing used on the missile. The antenna mounting plane relative to the ground is the same as that on the missile. So that adequate reference data can be obtained in almost any condition or range, the T-33 carries instrumentation to determine its position.

The T-33 follows the path prescribed in the ALCM mission data by the computer. The computer displays horizontal and vertical steering commands that the pilot follows. In this way the T-33 flies as the missile would but with the pilot in the loop instead of an autopilot. Errors in navigation and terrain correlation systems caused by maneuvering in vertical and horizontal directions are the same as those introduced by the missile.

To ensure that data obtained from the T-33 represent data obtained from ALCM, great care was taken in using operational prototype hardware and in placement of external sensors. To further ensure that the data are valid, the T-33 software uses ALCM missile modules for navigation, Kalman filtering, outer loop steering, terrain correlation, and executive control. Figure 17 lists modules common to the T-33 and the ALCM computer code.

- Executive control
- Navigation
- Kalman filter and scheduling
- Terrain correlation
- Air data
- Outer loop control
- Platform sequencing
- Ground align
- Data library
- Utility input-output

Figure 17. T-33/ALCM Common Key Software Modules

Almost any parameters in the Kalman filter, terrain correlation, and navigation routines can be plotted for analysis. Data recorded on any particular flight can be changed, allowing flexibility for examining particular problems. The T-33 offers a valuable tool for debugging the navigation mechanization and for extending the terrain correlator data base. The allowed flight areas for the T-33 are much less restricted than that of the missile, and it can fly over maps with widely varying types of terrain to ensure performance under all operating conditions. Figure 18 shows the data compiled and miles logged by the T-33 since its initial use in 1977.

• Total number of flights	127 flights
• Total number of hours	200 hours
• Total number of fixes	880 fixes
• Nautical miles flown	55,000 miles

Figure 18. T-33 Summary Data

Captive Flight

Because of the progress in simulation, laboratory validation, and T-33 flight testing, tests with real missile hardware should be needed only for additional verification. No serious problems should be experienced. The captive flight is the next step in the progression to launch. In this mode the missile experiences operational alignment and launch countdown, except that the missile is electronically, not physically, separated.

Steering commands are presented to the B-52 pilot (as in the T-33); and the B-52 flies the mission with the missile sequencing through normal modes of terrain following, terrain correlating, ascents, descents, and altitude hold.

The missile is mounted on a pylon or on the bomb bay launcher in the down position so that the ground can be seen by the altimeter. The pressure sensor does not sense correct pressure near the B-52 flown field; therefore, in the captive mode the B-52 system provides vertical information to ALCM. This step in the progression to launch tests the navigation hardware and software in a totally dynamic environment prior to commitment to launch. This test guarantees compatibility with the B-52 navigation system and demonstrates integration of mission data for the planned profile.

Freeflight

At the freeflight stage of the test sequence, all errors in navigation mechanization have been removed and the system is ready for launch. This is the final proof of performance but is anticlimactic in many ways because of all the tests completed up to the point of launch. The hardware is subjected to stresses of ejection and ALCM engine vibration, which were not experienced until this point. However, although not emphasized in this paper, missile hardware receives qualification with a combined environmental and burn-in test, verifying that the equipment can withstand freeflight environment. During all the competition flyoff, there was no failure of any avionic hardware that affected mission success.

IV. TEST RESULTS

This section covers test results of the T-33 and live missile launch. During all tests, the operational scenario was stressed. Conditions shown in figure 2 were used during all captive and live launches during the competition. All systems were cold on takeoff, inflight alignment of ALCM occurred after the B-52/SRAM systems were aligned in flight, terrain correlation was performed while terrain following, the INE calibration constants were degraded to simulate a long operational storage prior to launch, operational-type terrain data were used for terrain correlation, and mission data were transferred to the missile before launch.

Because of careful attention to ultimate operational use of the system and great attention to operational conditions during the competition, the demonstrated performance is a good representation of what the operational user can achieve.

Live missions flown by ALCM fall into the general category shown in figures 19 and 20; these missions were either flown solely on the Utah Test Range or launched off the California coast with a route inland, ending on the Utah Test Range. The primary reason for using this inland route from an overwater launch was to simulate more operational conditions. It is interesting to note that there was no statistical difference in the accuracy of these two missions. This is consistent with ANSER accuracy predictions. There are three major accuracy measures of the ALCM system: (1) accuracy on target, (2) accuracy at map entry, and (3) terrain correlation accuracy.

The following sections cover each of the accuracy measures. In all the data presented, range instrumentation and optical and radar systems at the test ranges were used as reference; no adjustments were made in any data. In each case all requirements imposed on the navigation system were met.

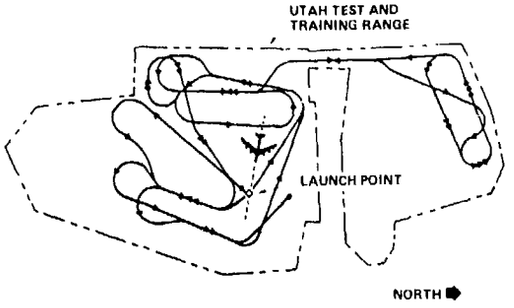

Figure 19. ALCM On-Range Mission Scenario

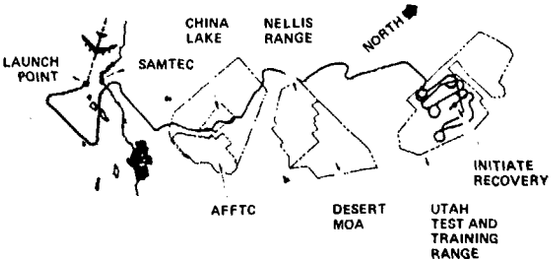

Figure 20. ALCM Overland Mission Scenario

Accuracy on Target

ALCM has two basic accuracy-on-target requirements: the first (case I) is circular error probability (CEP) after a normal long-range mission, and the second (case II) is CEP after a shorter range mission with fewer maps. Accuracy data demonstrated in the competitive flyoff are shown in figure 21. In both cases the demonstrated median radial errors are within the desired performance. Figure 22 shows T-33 accuracy on target compared to the expected performance. Here again, the performance was well within expected limits.

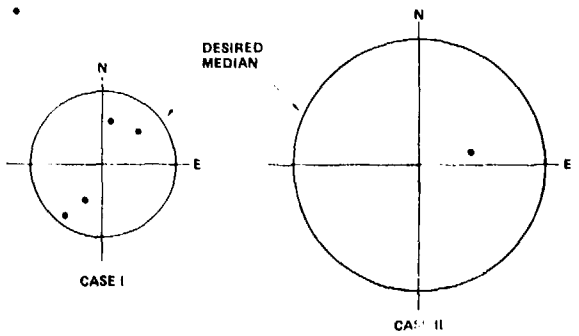

Figure 21. Missile Accuracy

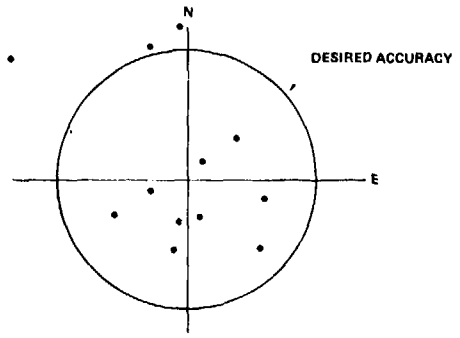

Figure 22. T-33 Accuracy Data

Accuracy at Map Entry

Error at map entry, given as a percentage of map width versus distance traveled from the previous map, is shown in figure 23. Percentages are well within requirement.

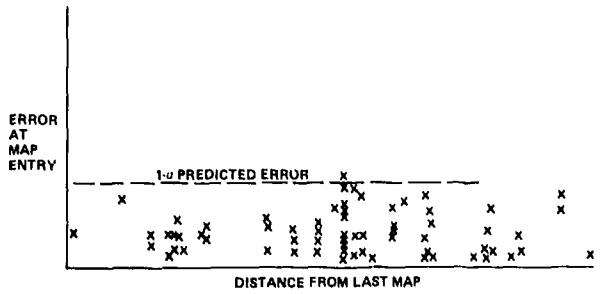

Figure 23. Error at Map Entry

Terrain Correlation Accuracy

Figures 24 and 25 show the terrain correlation accuracy for missile and T-33 flights. Terrain correlation accuracy is met in both cases. Similarity in performance between the T-33 and missile again shows that T-33 data accurately represent missile data.

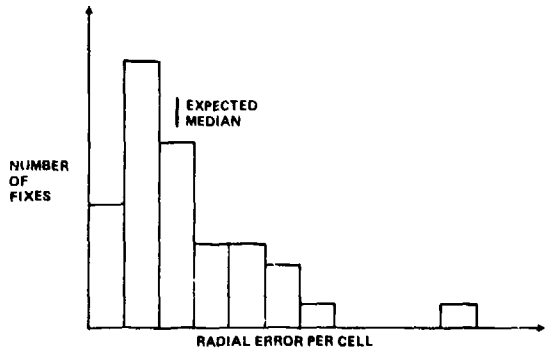

Figure 24. Correlator Accuracy—T-33

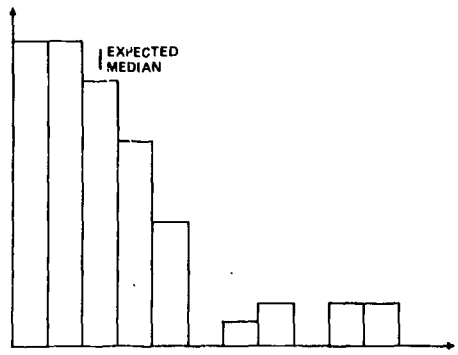

Figure 25. Correlator Accuracy—Missile

V. SUMMARY

The approach used in developing and testing the ALCM navigation mechanization is described above. This approach is to test the mechanization as it will be used and design the test to be orderly, leading finally to a live launch. These ground rules are simple but have contributed enormously to the success of the ALCM test program. Specific uses of these ground rules in the ALCM navigation system test are presented so that others may benefit from this approach.

REFERENCES

1. M. W. Johnson; "Analytical Development and Test Results of Acquisition Probability for Terrain Correlation Devices used in Navigation System"; AIAA paper No. 72-122; Boeing Aerospace Company.

2. "Software Key to ALCM Choice"; Aviation Week and Space Technology; March 31, 1980; pp. 18-22.

3. G. H. Yamamoto and J. I. Brown; "Design Simulation and Evaluation of the Kalman Filter used to Align the SRAM Missile"; AIAA paper No. 71-948; Boeing Aerospace Company.

4. J. E. Bloodworth, M. H. Stieglitz, and J. R. Elston; "Minimizing Air Launch Cruise Missile Software Life Cycle Cost"; AIAA paper; 1978; Boeing Aerospace Company.

TITLE: UTILIZATION OF GPS DATA IN EVALUATING GUIDANCE SYSTEMS ACCURACY

AUTHOR: GERALD GRIMALDI

ROCKWELL INTERNATIONAL
Anaheim, California

ACKNOWLEDGMENT

The author wishes to acknowledge the diligent work performed by the members of the Guidance System Evaluation Unit at Autonetics. Their effort in support of the post flight test accuracy evaluation of the Minuteman III Production Verification Missiles 18 and 19 (Air Force Contract F04704-78-C-0038) made this paper possible.

Lt. Col. G. Green and Capt. K. Jackson of the Air Force Ballistic Missile Office are also acknowledged for their interest, enthusiasm, and suggestions during the evaluation of these two flight tests.

ABSTRACT

Two Minuteman III missiles having a unique configuration were flight tested during 1980. These missiles contained a Missile-Borne Receiver Set (MBRS) which, in conjunction with transmitted signals from four Global Positioning Satellites (GPS), provided missile trajectory measurements for use in post flight analyses.

The role of this new form of instrumentation system data was integrated into the overall post flight test accuracy evaluation data flow. Also, detailed GPS/MBRS data flows were established, including a definition of all necessary corrections which need be applied, and new evaluation software tools were developed.

GPS/MBRS data gathered during the prelaunch mode of the missile test were used to estimate the location of the launch point. A comparison of this estimate with the "known" launch point coordinates was made to assess the reasonableness of the data and the data processing methodology.

GPS/MBRS data obtained during missile flight were corrected, synchronized, and compared to guidance system data to form missile trajectory comparisons in various coordinate frames. These trajectory comparisons were used as observables in a Kalman filter estimation technique to provide estimates of modeled errors in the Inertial Measurement Unit (IMU) of the guidance system. Also, the GPS/MBRS data were used in another manner, namely, to provide a gross indication of total guidance system accuracy. The indicator, termed Navigation Miss, is similar in nature to the presently employed Miss Other Than Reentry measure of system accuracy.

The results of both the detailed IMU hardware evaluation and the gross "Navigation Miss" determination were compared with the results achieved using standard radar tracking data. Based on these evaluations and comparisons, an assessment of the overall accuracy evaluation capability of the GPS/MBRS instrumentation system, as experienced on PVM 18/PVM 19, was estimated.

I. INTRODUCTION

A. GPS AND MINUTEMAN

The Global Positioning System (GPS) is a satellite navigation system which provides data to various users for the purpose of accurately determining user position and/or velocity relative to the earth.

In January 1980, and again in March 1980, the Air Force experimented with applying GPS for the purpose of missile trajectory determination leading to an assessment of guidance system accuracy. This unique and challenging experiment was employed on the last two Minuteman III R&D flight tests; Production Verification Missile (PVM) 18 and PVM 19, launched from Vandenberg Air Force Base t the Kwajalein test area.

Each missile carried a Ballistic Receiver Evaluation Wafer/Spacer (BREW/S), which contained a Texas Instruments (TI) developed Missile-Borne Receiver Set (MBRS). This receiver accepted signals transmitted by four satellites and received through the Missile-Borne Antenna (MBA). The MBRS provided pseudorange and range rate data plus an onboard solution of missile earth fixed position and velocity, and receiver clock bias and drift rate effects. This information was telemetered to ground receivers through the Autonetics Flight Data Handling Group (FDHG) hardware located in the BREW/S (see Figure 1). Guidance and Control (G&C) system data from a second, passive, Inertial Measuring Unit (IMU) was also telemetered by onboard computer control (D37 computer) through the FDHG. This paper discusses the results of the guidance system accuracy evaluation, obtained on PVM 18/PVM 19, using the unique GPS pseudorange and range rate measurement data.

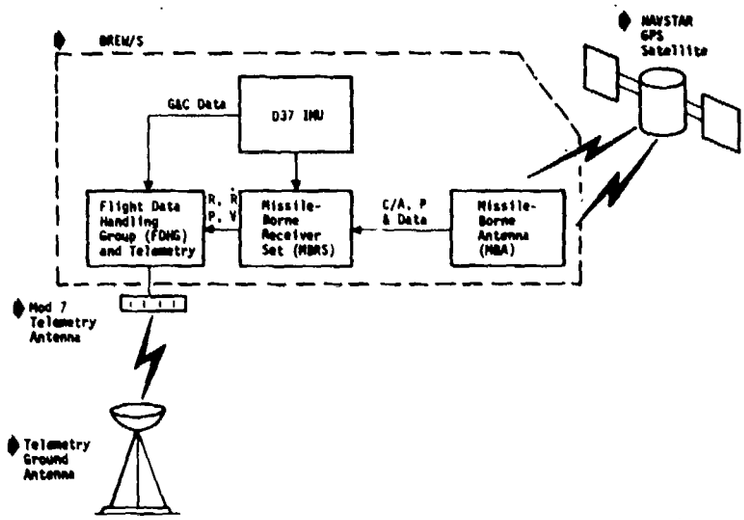

Figure 1. Data Flow Through BREW/S

B. FLIGHT TEST EVALUATION OVERVIEW

A typical ICBM flight test sequence is depicted in Figure 2. The sequence starts with the pre-launch mode and then progresses through the launch, boost/post-boost, reentry vehicle (RV) deployment, RV freeflight, and reentry phases and ends with RV impact.

The total weapon system impact error is defined as the distance that the RV misses its intended target. This total error is caused by the summation of separate individual error sources. Figure 2 depicts the common set of error subsets used on the Minuteman Program, ie, targeting, guidance and control (G&C), geodetic and geophysical (G&G), RV deployment/separation, and RV reentry errors. The time during which each error subset actively affects the RV impact is also shown in Figure 2.

The post flight test evaluation activity addresses the various error subsets*, and their members, to assess their contribution to weapon system miss. The specific process used by Autonetics to evaluate missile accuracy on a typical R&D flight test is depicted in Figure 3. The evaluation of ground program, flight program, and targeting associated errors is accomplished via the use of telemetered guidance system data and does not require direct use of external tracking system data. The evaluations in these areas are directed to assessing software precision and/or known mechanization approximation errors.

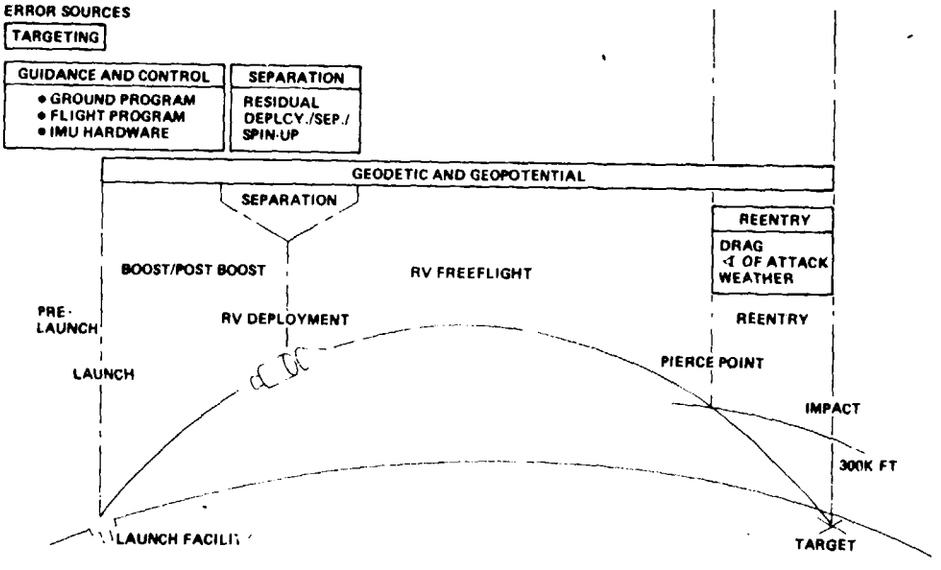

Figure 2. Flight Test Time Sequences and Error Sources

*G&G errors are generally unknown and act as corrupting influences in characterizing other error subsets.

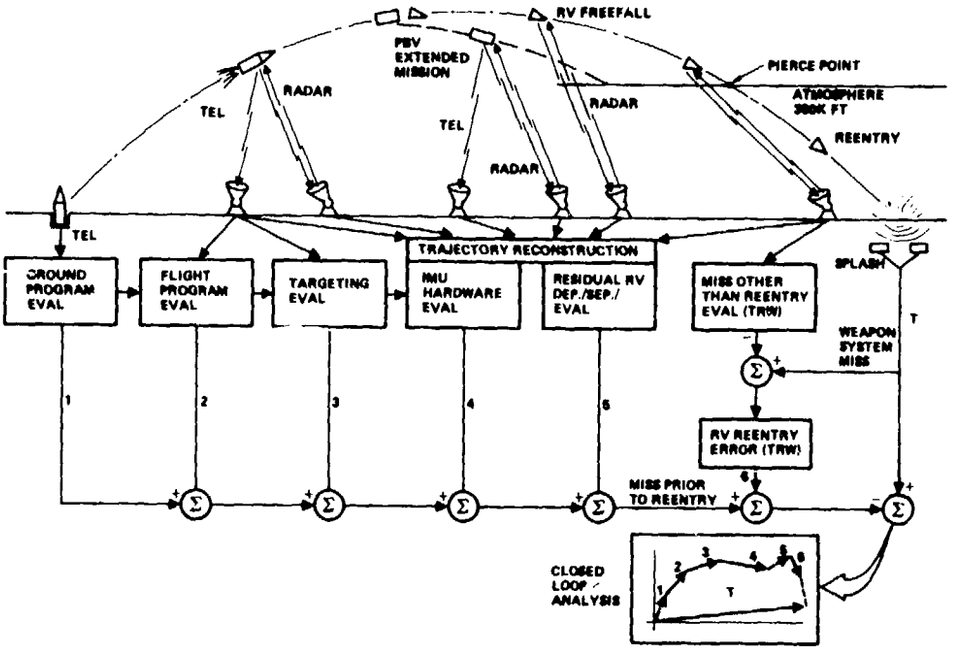

Figure 3. Standard Flight Test Evaluation Process

The evaluation of IMU hardware (accelerometer, gyro, and platform misalignment) is more complex and involves the comparison of the guidance system indicated missile trajectory, generated post flight from telemetered guidance system data, and the trajectory as measured by external tracking systems. In the standard Minuteman evaluation process, the external tracking is provided by uprange (California), midrange (Hawaii), and downrange (Kwajalein) radars. These radars provide slant range measurements which are used in a multilateration approach to assess IMU hardware performance.

In addition, since instrumentation data are not available to measure residual RV deployment/separation/spin-up errors, such errors are modeled and estimated simultaneously with the estimation of IMU hardware errors via the combined use of radar RV freefall tracking data and radar post-boost vehicle (PBV) tracking data.

Estimates of RV reentry error are provided to Autonetics by the TRW Corporation. This error is generally computed as the difference between the measured weapon system miss minus the estimated Miss Other Than Reentry (MOTR). MOTR is estimated via the assessment of the RV freefall trajectory using downrange radar and optical tracking system data.

Finally, the closed loop evaluation step, which completes the evaluation process, consists of an assessment of the total evaluation effort. Specifically, the magnitude of each individual error source contributing to impact miss is added and the sum is compared with the total RV impact miss as measured independently by external splash detection devices. The difference in impact estimates is referred to as the unaccountable impact error. The magnitude of this unaccountable error should be compatible with an expected uncertainty calculated from the uncertainties estimated for each of the individual error estimates. If this condition occurs, the probability of the evaluation process being valid is considered to be acceptable.

C. ROLE OF GPS/MBRS

The GPS/MBRS data obtained on PVM 18 and PVM 19 were factored into the overall data evaluation flow and were used separately from, and together with, radar tracking data in the evaluation of IMU hardware errors. In this capacity, the GPS/MBRS data provide a measure of the PBV trajectory, equivalent to radar PBV tracking, which is the reference for evaluating IMU hardware accuracy.

In addition to IMU hardware evaluation, the GPS/MBRS data were used to obtain an estimate of total G&C accuracy via a free-fall analysis of the GPS/MBRS indicated state (velocity and position) of the PBV, adjusted for nominal PBV/RV effects. This type of analysis provides an estimate of "Navigation Miss" which, although not exactly equivalent to radar-determined MOTR, characterizes the major portion of weapon system miss. The major portion of this paper is devoted to describing the IMU hardware and Navigation Miss evaluations using the GPS/MBRS data.

II. GPS/MBRS DATA EVALUATION

A. DATA FLOW

The use of the GPS/MBRS data in the overall data flow during the post flight accuracy evaluation of guidance system IMU hardware errors is illustrated in Figure 4. Briefly stated, the telemetered GPS/MBRS data are processed through a series of evaluation programs which extract, correct, synchronize, and compare the data with reconstructed guidance system trajectory data (from GIMLET program). The trajectory comparisons in the range and range rate domains (from MISEUS program), or an earth fixed velocity domain (from MERGE program), are used as observables in a Kalman maximum likelihood estimation program (KEEP) to estimate modeled IMU hardware errors. These observables may be used with other observables, such as guidance/radar slant range and range rate comparisons (from SACRED program) and/or guidance/guidance* Fly-2 velocity comparisons (from COMERS program).

Functional flow charts for each of the four key GPS/MBRS data processing programs, EXPRT, CORSYN, SACRDG, and MISEUS are shown in Figures 5 through 8, respectively. The basic function of EXPRT is to extract and reformat telemetered data. CORSYN computes and applies certain corrections, as illustrated, to the high rate (0.03 s/sample, during flight) data and aligns range and range rate data in time. SACRDG time synchronizes the GPS/MBRS data to the guidance

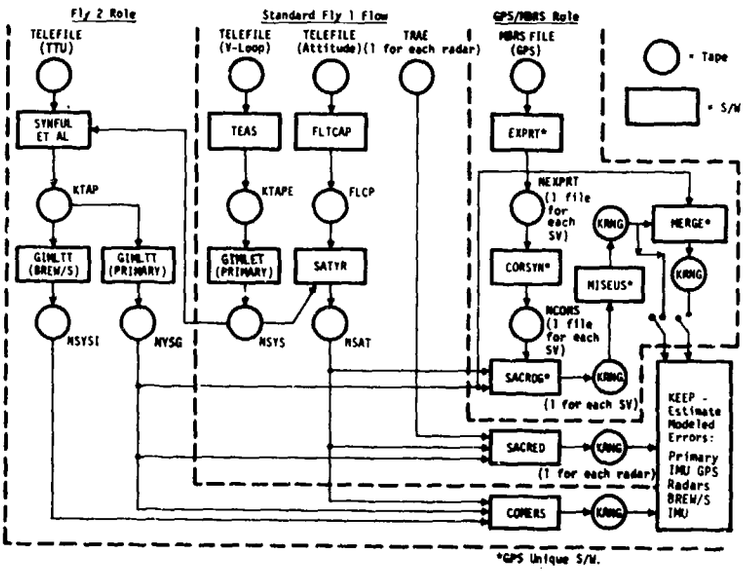

Figure 4. Data Flow - Guidance System IMU Hardware Evaluation

*One guidance system is passive and provides additional data for evaluation.

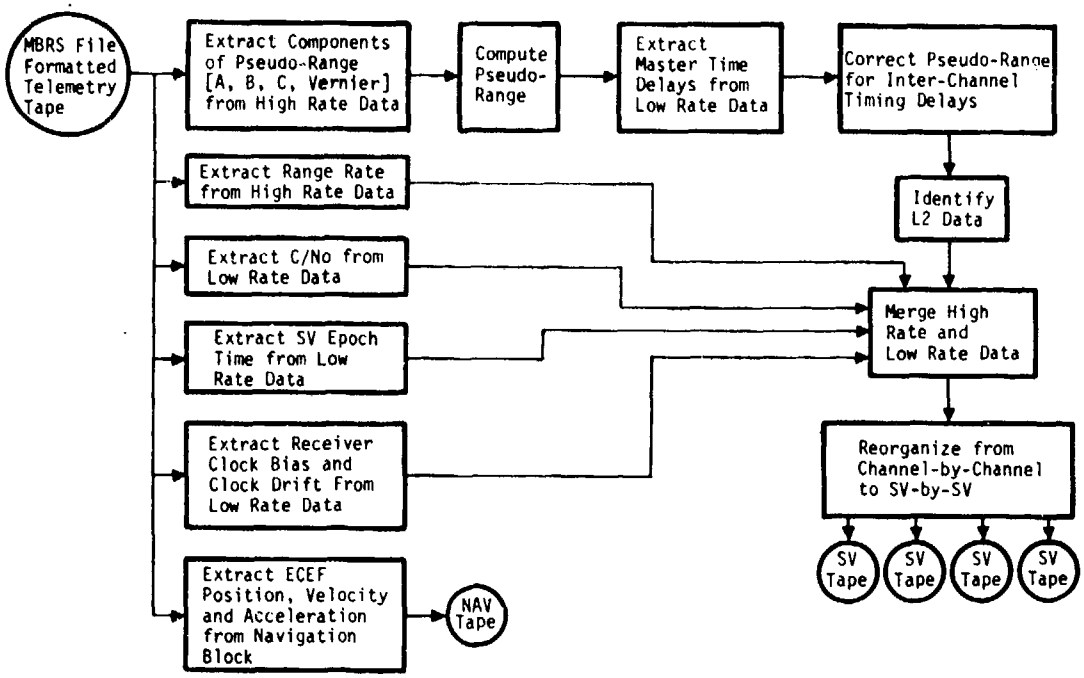

Figure 5. EXPRT Functional Flow

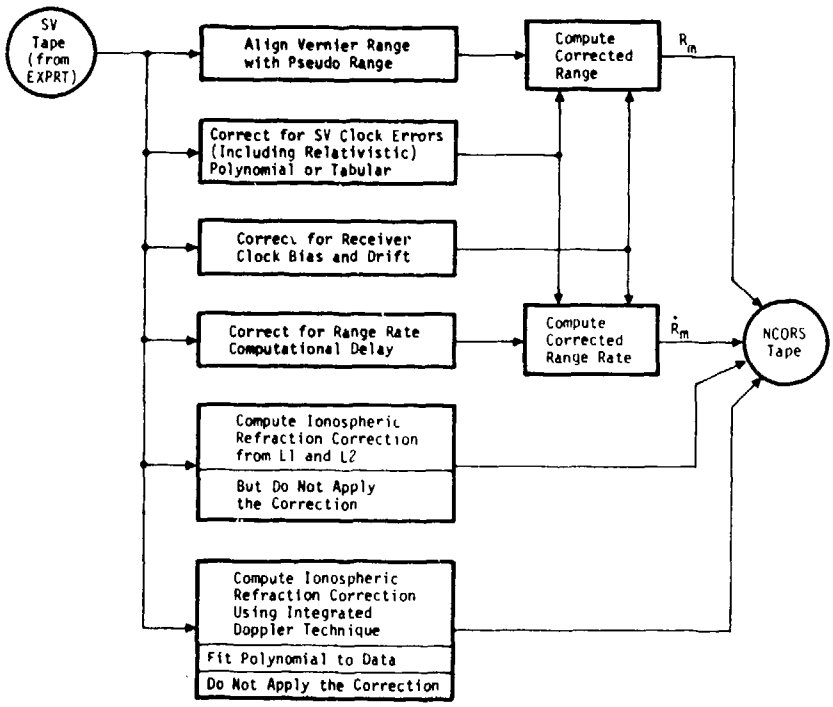

Figure 6. CORSYN Functional Flow

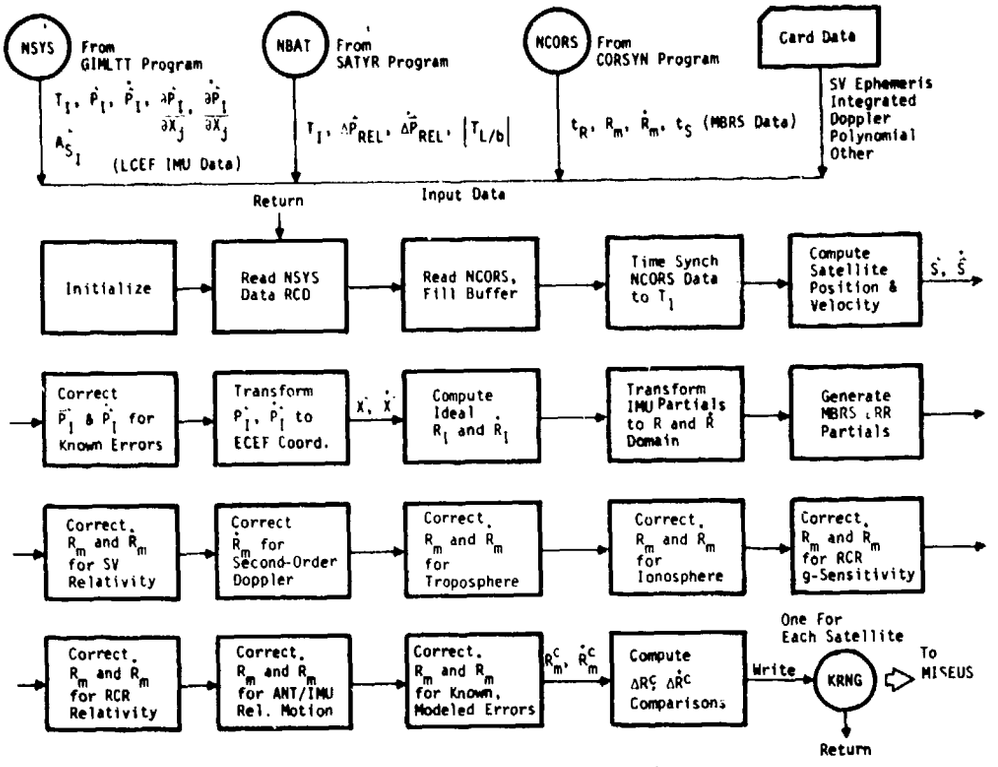

Figure 7. SACRDG Functional Flow

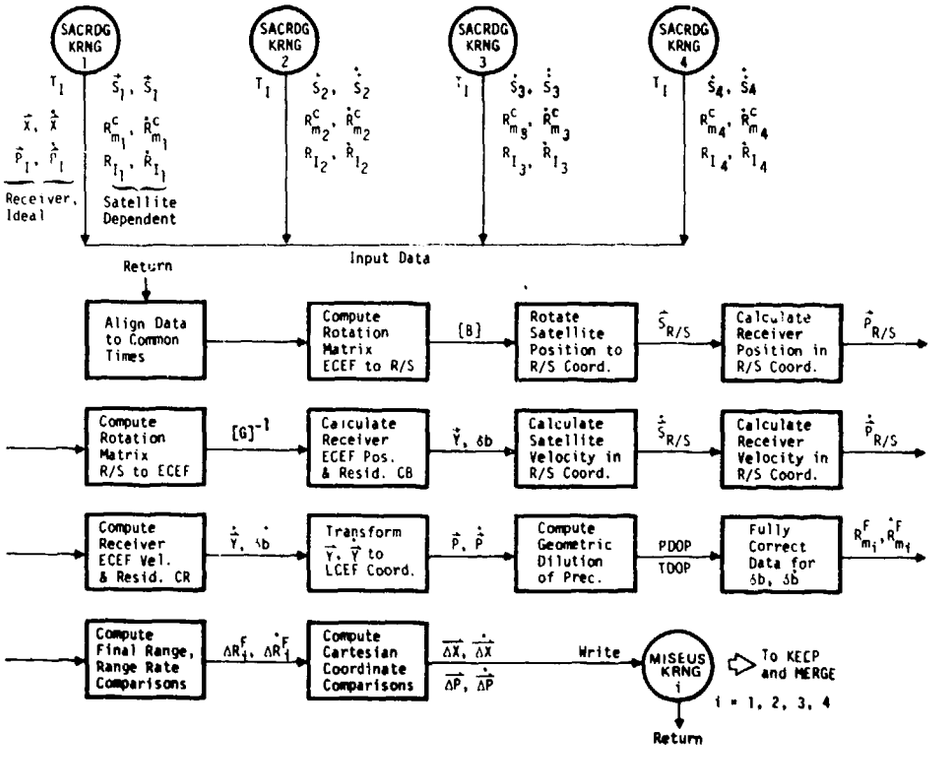

Figure 8. MISEUS Functional Flow

system sample times, corrects for additional errors in the data, and forms range and range rate trajectory comparisons. IMU error model partials are also transformed to the range and range rate domain for later use in forming the measurement matrix during the IMU hardware error estimation process. The MISEUS program is designed to use the four range and four range rate measurements to deterministically compute position and velocity in an earth fixed coordinate frame, plus receiver clock bias and drift rate effects. The computed clock effects are also removed from the range and range rate data to provide "fully-corrected" GPS/MBRS range and range rate data, and guidance minus GPS/MBRS range and range rate trajectory comparisons (observables) for the estimation process. MISEUS also forms earth fixed trajectory comparisons between the guidance system data and the GPS/MBRS deterministic solution. The MERGE program assures data compatibility for the KEEP program by providing the earth fixed trajectory comparisons and IMU error model partials in the same coordinate frame.

B. GROUND MODE RESULTS

The prelaunch, or ground mode, data provided a reliable measure of the accuracy of the GPS/MBRS range and range rate data, since the location of the reference point was known. These data also provided an indirect measure of the guidance system launch coordinates, which must be accurately known to assure proper weapon system performance.

After MBRS turn-on, satellite acquisition was achieved at approximately lift-off (T_o) minus 800 s. Ground mode operation continued until flight mode was entered, at approximately T_o - 60 s. GPS/MBRS data were available at a nominal rate of 0.09 s per sample during the ground mode. These data were corrected and compared to "ideal" values based on the surveyed location of the tracking point.

During the ground mode, three satellites were properly tracked through the Ground Antenna Group (GAG) located outside the silo (see Figure 9). Unfortunately, the fourth satellite was tracked through the MBA. Consequently, special post flight adjustments had to be made to effect a solution for the location of the GAG.

The rms noise present in the high rate GPS/MBRS data during the ground mode was estimated as 3 ft in range and 0.04 ft/s in range rate. These levels could be reduced by additional smoothing of the data.

T_o - lift-off reference time

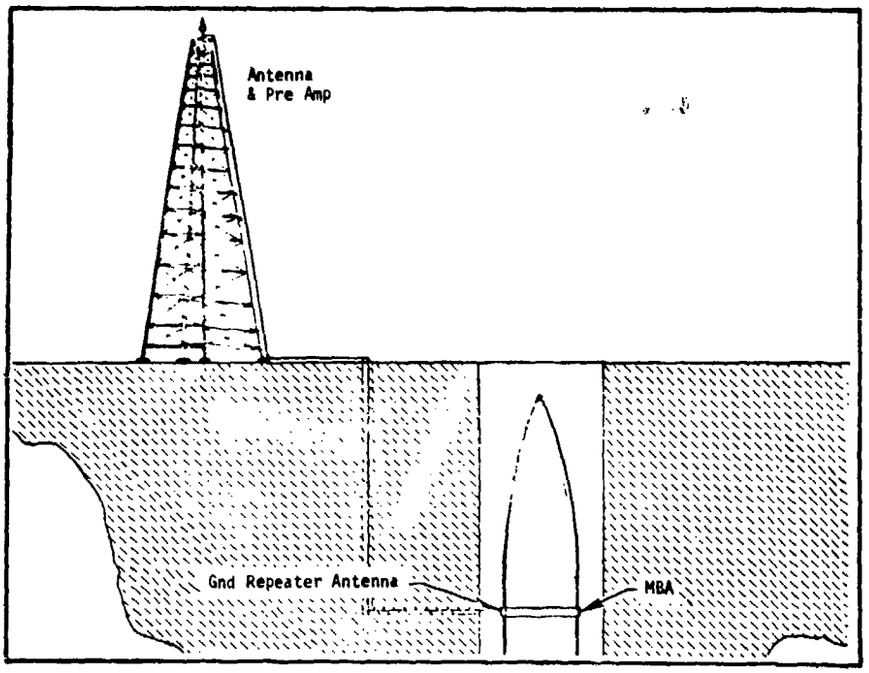

Figure 9. GPS Ground Antenna Group

The "fully-corrected" ideal minus GPS/MBRS measurements of the GAG location, obtained using the Aerospace Corporation provided ephemeris and SV clock correction data, had no undesirable trends or bows on PVM 18. The differences, or offsets, were less than 10 ft in range and 0.02 ft/s in range rate in each channel. The residual MBRS clock bias and clock drift rate (Figure 10) displayed the effects of clock thermal sensitivity. In this regard, the clock drift rate had an exponential decay effect and the clock bias appeared as the integral of the drift rate effect, plus an arbitrary initial bias. There was also an obvious discontinuity in the MBRS clock at approximately T_o - 500 s, on PVM 18, due to unknown sources.

The most interesting information obtained during the ground mode is the ideal minus GPS/MBRS measurements of the GAG location expressed in an earth fixed coordinate frame. Figure 11 illustrates the GAG position offsets in launch site centered north, west, up coordinates. The observed offsets are also presented in Table 1 together with the PVM 19 results. The PVM 19 data include four special evaluation runs performed the day before launch, and one run on launch day. The statistics on these data provide a measure of the combined error in the GPS/MBRS measurements and the GAG survey measurements.

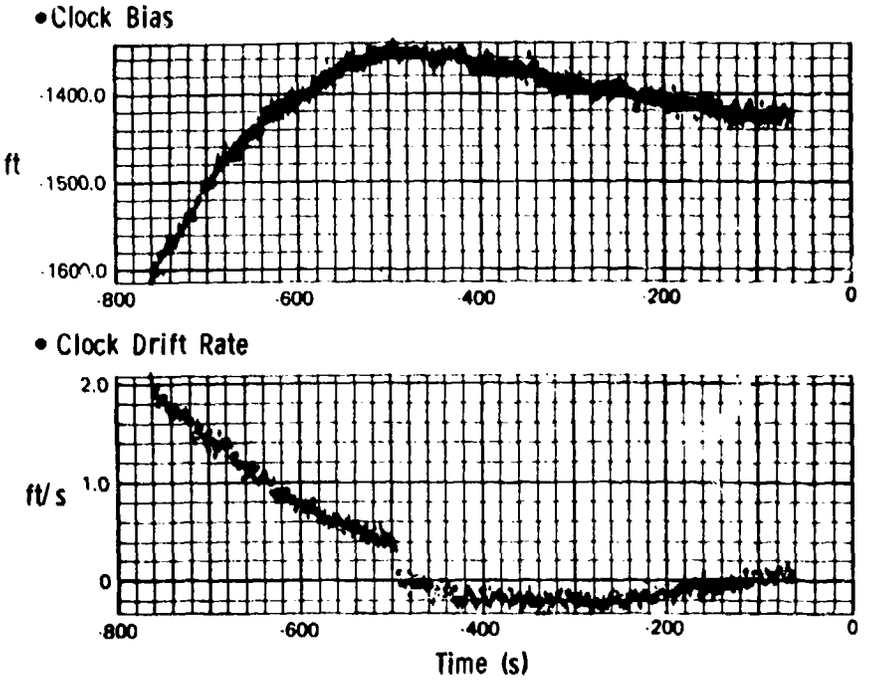

Figure 10. Residual MBRS Clock Bias and Drift Rate (PVM 18, Ground Mode)

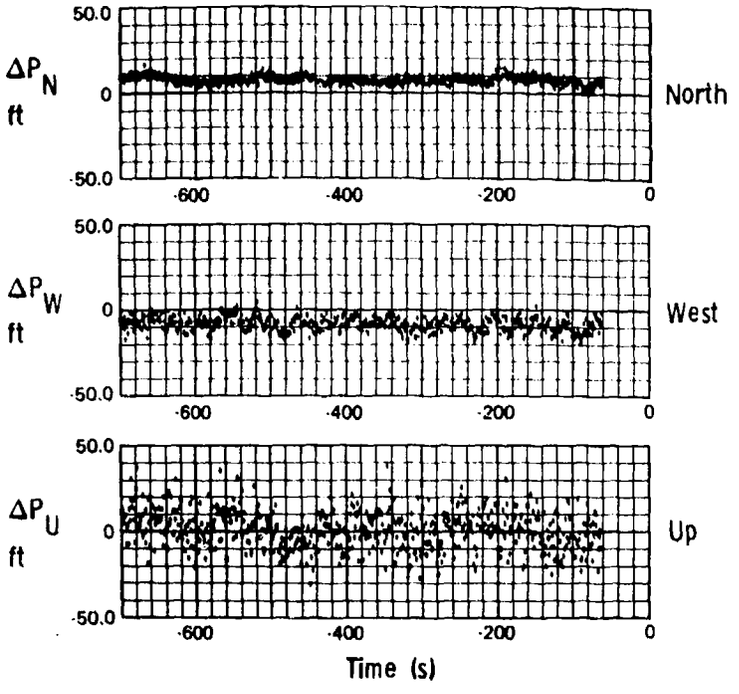

Figure 11. GAG Position Offsets (PVM 18, Ground Mode)

Table 1. Estimated Position Offsets of GAG

Run*	Satellites	Position Offsets (ft) North-West-Up-Coordinates			RSS
		N	W	U	
1	4-5-6-8	10	-12	6	17
2	4-6-7-8	12	-16	-5	21
3	4-5-6-7	10	-15	0	18
4	4-5-7-8	12	-24	0	27
Launch Day Results					
PVM 18	4-6-7-8	8	-9	0	12
PVM 19	5-6-7-8	16	-12	-10	22
Mean		11	-15	-2	
Standard Deviation		3	5	5	
rms		12	15	5	

*Day Before Launch of PVM 19

The results are consistent in each coordinate and they reflect a GPS accuracy better than that anticipated.

C. FLIGHT MODE RESULTS

1. General

All four satellites were tracked through the MBA from lift-off to T_o + 1000 s. The GPS/MBRS data received during the flight mode were at a rate of 0.03 s per sample. Several seconds of data around lift-off and each staging event were deleted from the analyses. At these times, the MBRS went out of phase lock and into frequency lock, as planned, to minimize the risk of losing lock during regions of high jerk. The deletion of the poor quality data in these regions did not detract from the GPS/MBRS performance capability.

The rms noise of the high rate data was estimated by assessing the variability relative to a second-order fit to groups of 15 points, during the process of synchronizing the data to guidance system time samples. The noise levels were 3 ft and 0.05 ft/s in range and range rate, respectively, throughout the flight.

The residual MBRS clock performance on PVM 18 is depicted in Figure 12. The drift rate plot shows the exponential decay from T_o + 0 to T_o + 600 s. The drift rate changes from approximately 2.8 ft/s at T_o + 0 to -0.8 ft/s at T_o + 600 s. A dynamic effect, apparently environmentally-induced, is superimposed over the exponential effect during boost. The plot also reveals residual MBA/IMU relative motion around the RV deployment events (T_o + 400 s). This, of course, is not receiver clock-related, but the effects of residual relative motion filtering through the deterministic solution. A similar plot was obtained on PVM 19.

The plot of residual clock bias is equal to the integral of the residual clock rate profile plus an arbitrary bias. Remember, large initial estimates of clock bias and drift rate were previously removed.

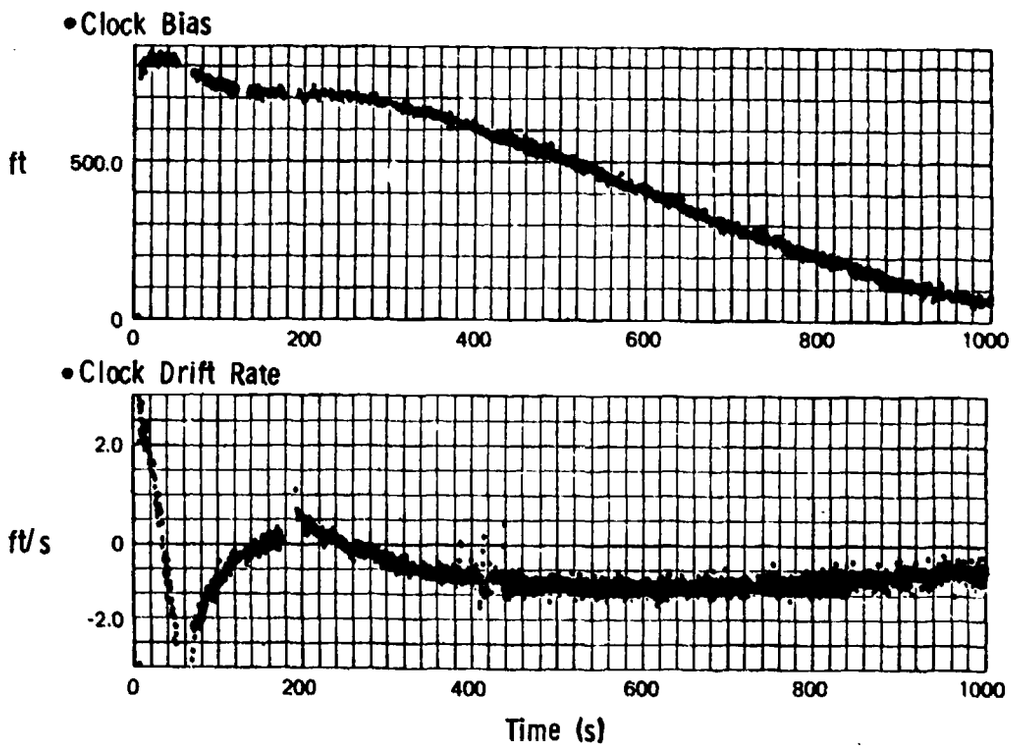

Figure 12. Residual MBRS Clock Bias and Drift Rate (PVM 18, Flight Mode)

2. IMU Hardware Evaluation

The "fully-corrected" guidance system* minus GPS/MBRS missile trajectory comparisons in the range and range rate domains were employed in regression analyses to estimate modeled IMU hardware error effects. In addition, trajectory comparisons were generated in the more visually convenient Launch Centered Earth Fixed (LCEF) coordinate frame. These comparisons, shown in Figures 13 and 14 for PVM 18, were also used in ensuing regression analyses. However, the proper characterization of measurement noise and modeling of GPS/MBRS residual errors is best achieved in the range and range rate domains.

The LCEF velocity comparisons illustrate the buildup of IMU hardware errors during boost (first 180 s) due to errors in the accelerometers, gyros, and initial alignment of the stable platform. In particular, the ΔVy plot was later determined to be caused by gyro errors acting during boost, and accelerometer bias shifts occurring at T_o + 450 s.

Preliminary estimates of the velocity and position errors at RV deployment were obtained by "eye-ball" smoothing through the comparisons. These errors were mapped into downrange and crossrange impact miss. Refined estimates were made by fitting the data with models of various IMU hardware errors. It is noted that residual MBA/IMU relative motion effects are evident during first stage and at RV deployment times. These data were deleted from further analyses.

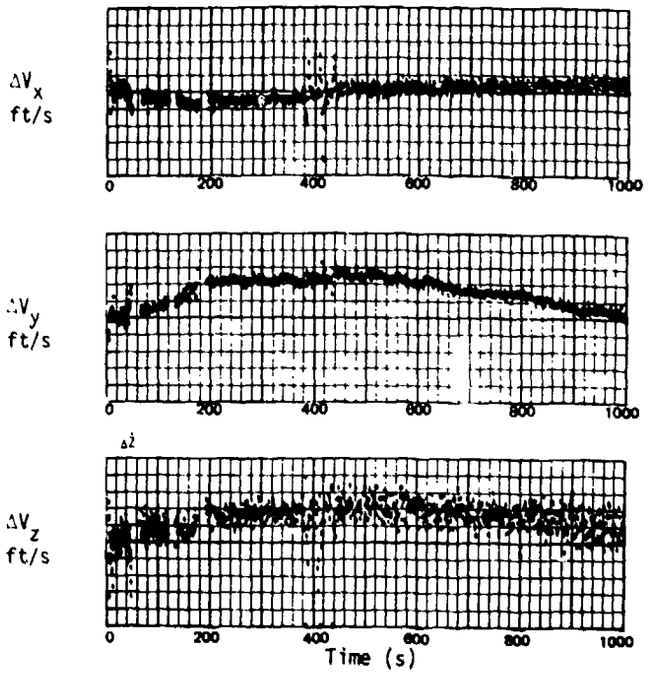

Figure 13. Guidance System Minus GPS/MBRS Velocity (LCEF Coordinates)

*Based on the post flight reconstructed guidance system indicated trajectory, which contains unknown IMU hardware error effects to be estimated.

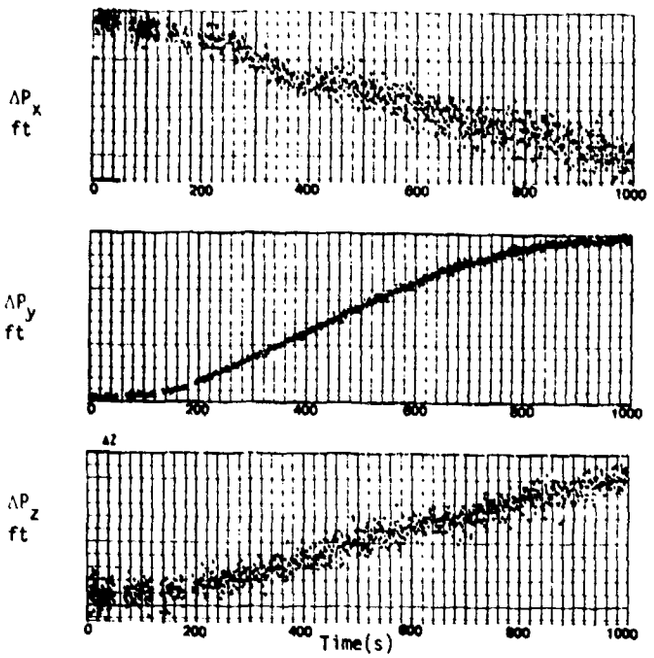

Figure 14. Guidance System Minus GPS/MBRS Position (LCEF Coordinates)

There were three types of regression analyses performed, using GPS/MBRS measurements as the instrumentation system data (in place of the radar measurements). The first used the range rate measurements only; the second used range rate and range measurements; the third used velocity data expressed in LCEF coordinates.

Preliminary runs were made to establish optimum time spans and noise profiles for the later analyses. The IMU error model contained various accelerometer, gyro, and platform misalignment terms. For the regressions performed in the range rate and range domains, the GPS/MBRS error model included residual channel-dependent biases. For the LCEF regression, there were no modeled GPS/MBRS errors; GPS/MBRS biases in LCEF coordinates have no physical meaning.

The three different regression solutions using GPS/MBRS data were compared with each other and with the results using radar tracking data. In estimating crossrange miss-type IMU hardware errors, all GPS/MBRS and radar solutions were consistent and in good agreement (within 75 ft). The estimates of IMU hardware-induced downrange miss varied; for PVM 18, the best agreement with radar data was achieved using range rate data only; for PVM 19, the best agreement with radar data was achieved using LCEF velocity data.

The estimation uncertainties (Table 2), viewed in a relative sense, showed that GPS/MBRS data were better than radar data for estimating crossrange miss-type errors. Also, GPS/MBRS is better than radars in estimating downrange miss-type errors when GPS/MBRS range and range rate data are both used. However, although this potential is shown, better modeling of GPS/MBRS errors, expecially in range, is required to realize that potential.

Table 2. Ideal Estimation Uncertainties of Total IMU Hardware-Induced Impact Miss

	Estimation Uncertainties(1) (ft)	
	Downrange	Crossrange
Radars(2)	28	33
GPS $\dot{R}$	84	21
GPS $\dot{R}$ + R	17	5
GPS LCEF Vel	30	12

(1) Ideal Values - Based on assumption that all errors in the data are modeled.
(2) Full-up radar coverage; uprange, midrange, downrange tracking.

The results of the various IMU hardware regression analyses, displayed at RV deployment and impact, using GPS/MBRS data and radar data are summarized in Table 3, for RV 1 only. The differences reflect the existence of unmodeled errors in the radar and various GPS/MBRS data sets plus differences in IMU error observability resulting from the varied observation domains. The differences in the solutions are also shown pictorially as a function of time in Figures 15 and 16. These comparisons illustrate radar minus GPS/MBRS solutions of estimated IMU hardware errors. These hardware errors can be used to correct the guidance-indicated trajectory to form Guidance Best Estimate of Trajectories (GBET). In terms of GBET comparisons, Table 3 and Figures 15 and 16 illustrate GPS/MBRS-type GBETs minus the radar-type GBET.

The plots of the different solutions during boost (T_o + 0 to T_o + 190 s) are basically driven by different solutions for gyro errors. Differences during extended mission (T_o + 450 s to T_o + 1000 s) are driven by different solutions for accelerometer bias errors at launch and, especially, at T_o + 450 s (bias shift). These extended mission errors do not affect weapon system accuracy.

Table 3. Differences at Deployment and Impact Due to Estimated IMU Hardware Errors Using Radar and GPS/MBRS Data

Solution Differences*	PVM 18 (RV 1)							
	Velocity (ft/s)			Position (ft)			Impact (ft)	
	ΔV_x	ΔV_y	ΔV_z	ΔP_x	ΔP_y	ΔP_z	M_D	M_C
Radar Minus GPS $\dot{R}$	0.0002	-0.0735	-0.0448	8.3	-13.5	-12.9	55 L	71 L
Radar Minus GPS $\dot{R}$ + R	-0.0051	-0 0684	0.0671	1.6	-10.0	19.4	111 S	72 L
Radar Minus GPS LCEF Vel	-0.0161	-0.0642	-0.0417	7.6	-13.2	-15.2	109 L	63 L
	PVM 19 (RV 1)							
	Velocity (ft/s)			Position (ft)			Impact (ft)	
	ΔV_x	ΔV_y	ΔV_z	ΔP_x	ΔP_y	ΔP_z	M_D	M_C
Radar Minus GPS $\dot{R}$	0.0060	-0.0668	-0.0480	5.5	-8.5	-3.5	25 L	64 L
Radar Minus GPS $\dot{R}$ + R	0.0245	-0.0657	0.0362	8.1	-8.4	19.9	185 S	67 L
Radar Minus GPS LCEF Vel	-0.0019	-0.0729	-0.0244	9.0	-13.2	1.7	11 L	72 L

* Also equals GPS/MBRS-Type GBET Minus Radar-Type GBET

M_D = Miss Downrange

M_C = Miss Crossrange

It is noted that in the IMU hardware evaluation using radar data, a priori knowledge** regarding the extended mission accelerometer bias shift was employed. Radar range rate data, at best, can indicate the time of such a shift, but the magnitude of the error for each accelerometer cannot be adequately estimated via radar data alone. Without some a priori knowledge, the existence of the bias shifts would corrupt the radar solution of IMU hardware errors. The alternative, assuming the problem has been recognized, is to delete all extended mission data. This would void the use of desirable PBV tracking data from midrange and/or downrange radar sites. The use of GPS/MBRS data circumvents this problem, since the detection and quantification of the bias shifts are easily determined by plotting velocity comparisons in the accelerometer coordinate frame.

**Normally obtained via an assessment of expected versus observed accelerometer counts during extended mission.

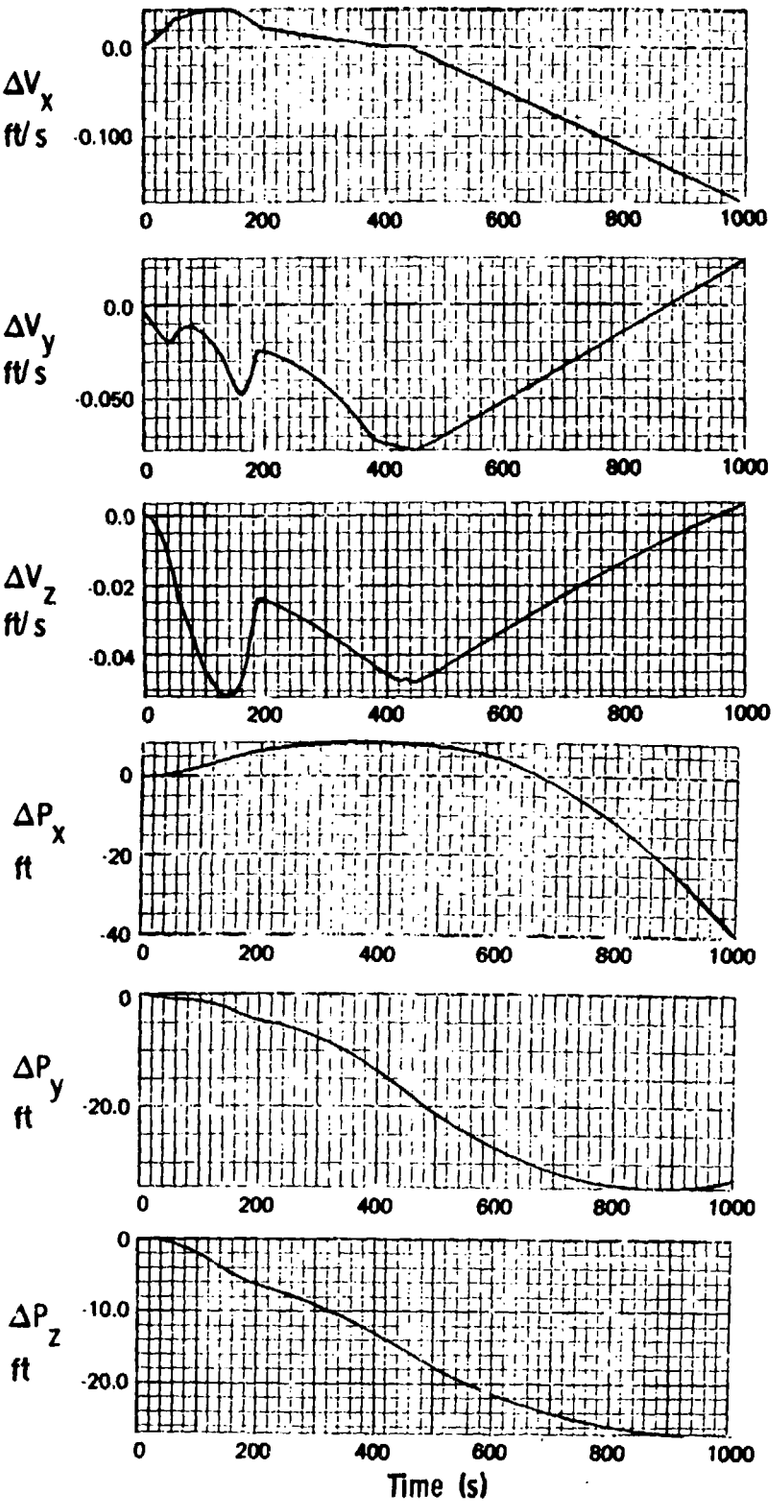

Figure 15. Difference in Estimated PVM 18 IMU Hardware Errors, Radar Solution Minus GPS/MBRS $\dot{R}$ Solution (LCEF Coordinates)

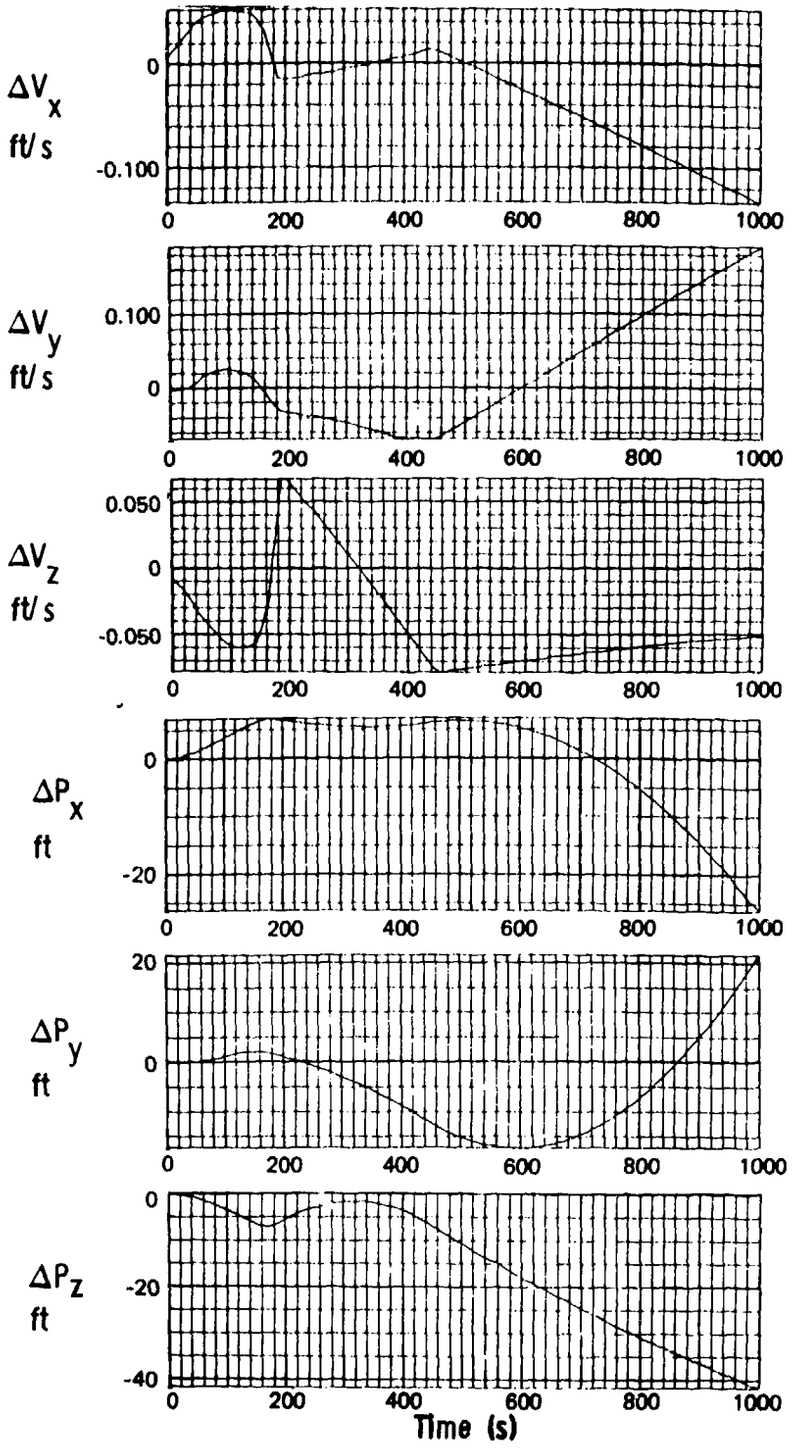

Figure 16. Difference in Estimated PVM 19 IMU Hardware Errors, Radar Solution Minus GPS/MBRS $\dot{R}$ Solution (LCEF Coordinates)

Finally, the results of the GPS/MBRS versus radar analyses of IMU hardware errors in the assessment of weapon system closed loop error analysis are shown pictorially in Figure 17, for both RV 1 and RV 2. The charts show three estimates of weapon system miss with uncertainty ellipses. The first is the impact as measured by splash detection radars, used as the reference. The second is a "radar" estimate which includes the sum of miss distances due to ground program errors, flight program errors, targeting associated errors, IMU hardware errors (estimated using radar data), residual RV deployment/separation/spin-up errors (estimated using radar data), and RV reentry errors (provided by TRW). The third is a "GPS/MBRS" estimate which includes the same components as the radar estimate, except that IMU hardware errors are based on the estimate using GPS/MBRS range rate data. Except for RV 1 of PVM 18, all three uncertainty ellipses overlap, indicating acceptable closure results with relatively small unaccountable errors in either the radar or GPS/MBRS solutions.

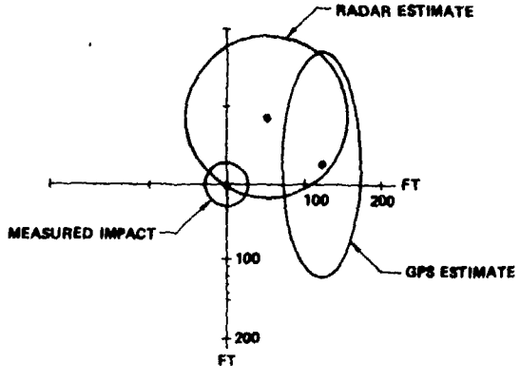

PVM 18 RV 1

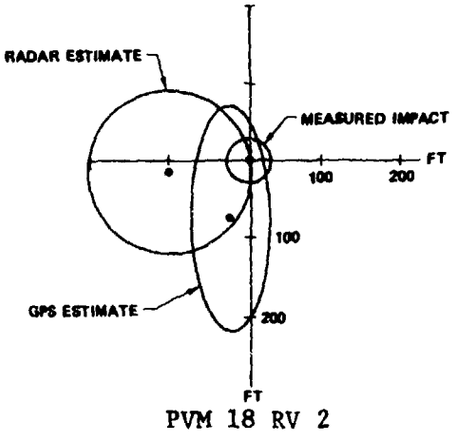

PVM 18 RV 2

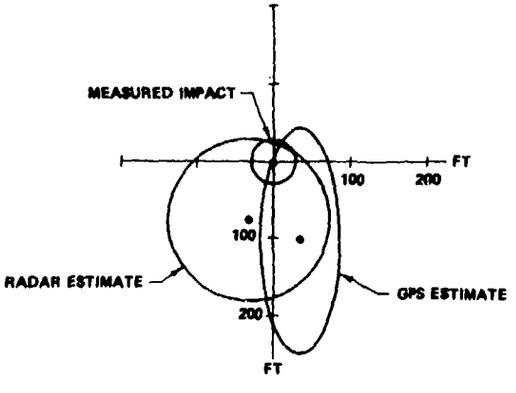

PVM 19 RV 1

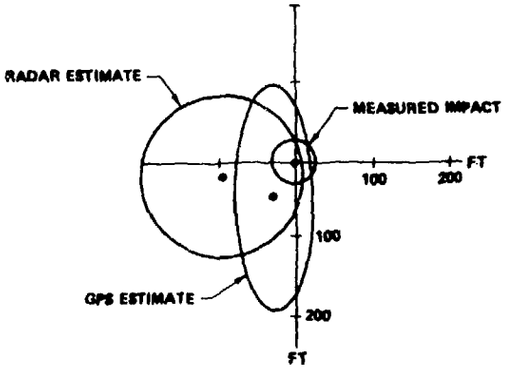

PVM 19 RV 2

Figure 17. Measured vs Estimated Weapon System Miss

3. Navigation Miss

This paragraph describes the use of GPS/MBRS data to provide an estimate of total G&C accuracy similar to the radar determined Miss Other Than Reentry (MOTR). This GPS/MBRS total accuracy estimate is termed Navigation Miss. Figure 18 illustrates the relationship of MOTR and Navigation Miss in the course of a missile flight test.

The GPS/MBRS estimate of Navigation Miss is obtained as follows:

(1) Compute a smooth estimate of the GPS/MBRS-indicated state of the PBV (position and velocity) at the time of RV mechanical disconnect.

(2) Adjust the PBV state for the targeted (nominal) RV-cg offset and the mechanical disconnect delta velocity.

(3) Free-fall the adjusted state at mechanical disconnect to RV spin-up.

(4) Adjust the state at RV spin-up for targeted (nominal) RV spin-up velocity step.

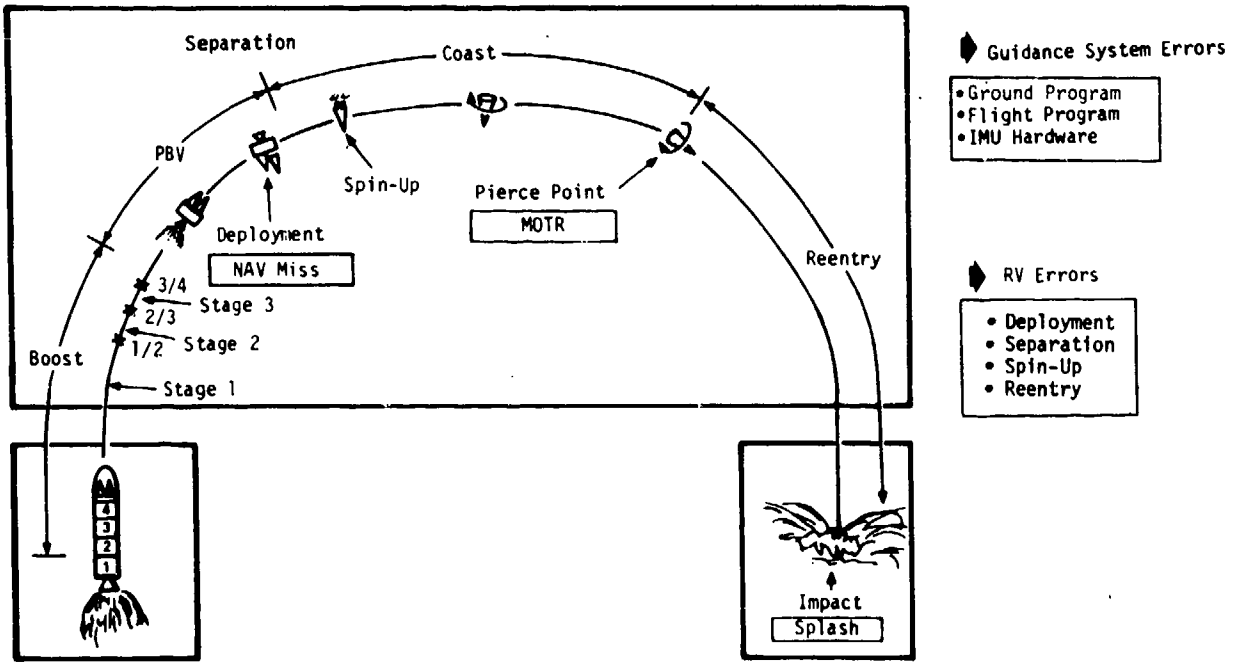

Figure 18. Missile Flight Test Mission

(5) Free-fall the adjusted state at RV spin-up to impact.

(6) Compare the impact point with the target to determine Navigation Miss.

This procedure could be followed on future flight tests in lieu of, or in addition to, radar determined MOTR assessments. The free-fall analysis employs the following:

(1) DODWGS 1972 gravity model with LRGM

(2) 1959 standard atmosphere

(3) Mark 12A RV drag model

(4) Targeted reentry climatology effects

In contrast to Navigation Miss, MOTR is obtained by free-falling a smooth estimate of radar-indicated state of the RV at top of the atmosphere (pierce point) to impact, and comparing the impact point to the target. The same free-fall analysis ingredients as those listed above are employed.

The estimated Navigation Miss differs from MOTR in that it does not include the following (basically downrange type errors).

(1) Deployment attitude error

(2) PBV limit cycle

(3) RV Tipoff error

(4) Residual RV cg offset

} Included in Flight Program RV Deployment Error Category

(5) Residual RV deployment/separation/spin-up errors

Figure 19 illustrates the comparison of Navigation Miss with Miss Other Than Reentry for both PVM 18 and PVM 19. The Navigation Miss values were based on GPS/MBRS LCEF coordinate data.

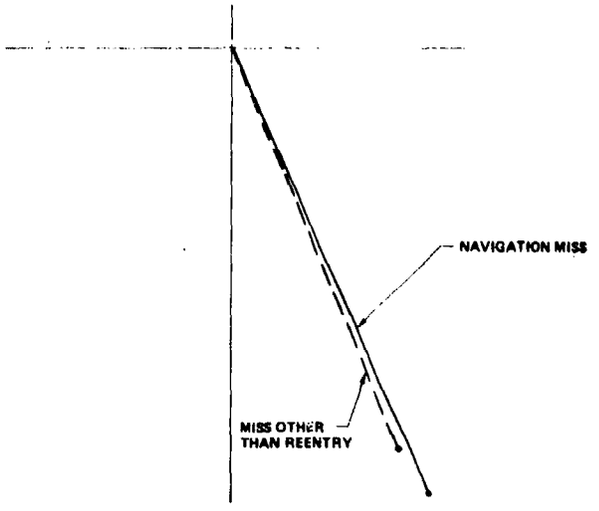

PVM 18 RV 1

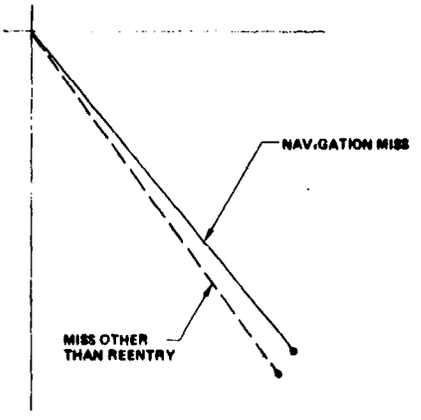

PVM 18 RV 2

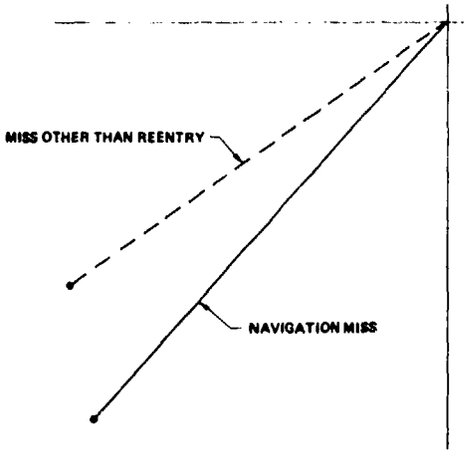

PVM 19 RV 1

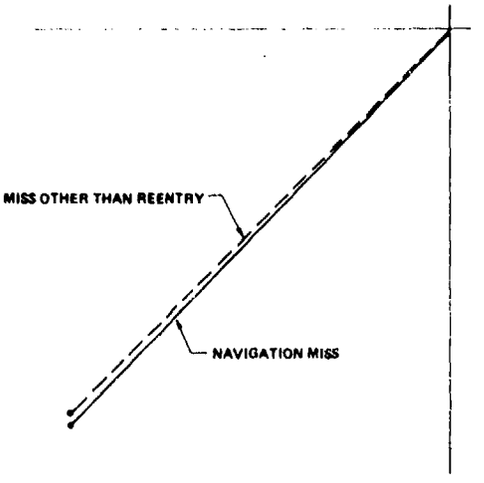

PVM 19 RV 2

Figure 19. Navigation Miss (GPS) vs Miss Other Than Reentry (Radar)

III. APPRAISAL OF GPS

The performance of the GPS/MBRS system as an instrumentation system on PVM 18 and PVM 19 was excellent. The GPS/MBRS data provided the capability to evaluate IMU hardware errors, to assess a measure of total G&C accuracy (Navigation Miss) similar to MOTR, and to observe unusual phenomena in the IMU data, namely, the time and magnitude of accelerometer bias shifts in extended mission. In this latter capability, as a diagnostic aid, the relatively simple generation of a Cartesian coordinate missile trajectory velocity and position profiles for comparison with IMU data is an obvious advantage over the use of radar data. Cartesian coordinate trajectory comparisons also provide the ability to obtain a rapid estimate of total IMU hardware error, prior to regression analyses, simply by mapping the indicated velocity and position differences at RV deployment to impact space.

The solutions for IMU hardware error using GPS/MBRS data were in very good agreement with that obtained using radar data, especially in the crossrange direction. The estimation uncertainties involved in the regression analyses show, in theory, an advantage for GPS over radar data, primarily in the crossrange direction. Also, the spans of quality GPS/MBRS data used in the estimation process were clearly evident and not subject to the sometimes arbitrary choices prevalent in the use of radar data. The advantage of this is that the analysis moves more towards a science than an art, and the results are not based on the subjective choices of the analyst.

The potential, evident in the ideal estimation uncertainties, can be achieved by adequately correcting and modeling the major GPS/MBRS errors existing in the measurement data. The corrections and models employed on PVM 18 and PVM 19 were good in generating quality GPS/MBRS data; however, additional work in this area is required. In particular, a technique for adequately correcting for ionospheric effects need be developed.* Also, more sophisticated techniques need be employed to characterize and remove receiver clock effects from the data without introducing time dilution of precision, which tends to increase the noise in the data. A lower noise level will further reduce the ideal estimation uncertainties relative to that displayed herein, and would enhance the usefulness of GPS data as a diagnostic aid and as a means to better evaluate individual IMU error contributors via regression analysis. In this regard, a technique to obtain smooth data was recently developed at Autonetics by R. L. Blanchard during follow-on GPS/MBRS studies. The technique employs an 8-state Kalman filter which operates upon observables of guidance system-indicated minus GPS/MBRS measurements of doppler cycle counts (equivalent to range rate data) to estimate the 3 components of guidance system velocity error and 3 components of guidance system position error in the LCEF coordinate frame, and residual receiver clock bias and drift rate. The end product of this processing replaces the previously defined deterministic solution and provides guidance versus GPS/MBRS trajectory comparisons in both the GPS/MBRS measurement domains (range and range rate) and the LCEF Cartesian coordinate frame for use

*This problem can be obviated via the use of dual frequency GPS data to measure ionosphere effects (such data were not available on PVM 18/PVM 19).

as smooth observables in ensuing regression analyses of IMU hardware errors. The noise content was reduced to approximately one-third of that observed in the data from the deterministic solution on PVM 18 and PVM 19. In the range rate measurement domain, the noise level achieved by this optimal processing is approximately 0.01 ft/s.

The use of GPS to provide an equivalent radar estimate of MOTR cannot be completely achieved since the GPS receiver is located in the PBV and not the RV. Consequently, certain RV deployment/separation/spin-up effects, which are included in MOTR, cannot be included in the GPS total accuracy assessment estimate, termed Navigation Miss in this document. However, the major portion of weapon system miss can be characterized via the determination of Navigation Miss.

Based on the overall performance of the GPS/MBRS system on PVM 18 and PVM 19, an estimate of its accuracy evaluation capability pertinent for these two flights is as follows:

Downrange	150 ft	Based on GPS/MBRS "Deterministic Solution" Data (PVM 18/PVM 19)
Crossrange	50 ft	

These assessments are based on judgement, using the relative GPS/radar solutions and the knowledge that the ideal estimation uncertainties are approximately three times better is crossrange then downrange. However, a definite improvement in the accuracy evaluation capability can be achieved using optimally processed data. It is estimated that this improvement equates to approximately one-half of the levels defined above, that is,

Downrange	75 ft	Based on GPS/MBRS "Optimally Processed" Data (Expected)*
Crossrange	25 ft	

In contrast, an assessment of the radar accuracy evaluation capability, using combined uprange, midrange, and downrange tracking, is as follows:

Downrange	100 ft
Crossrange	100 ft

These values are based on the observed "Unaccountable Error" (Weapon System Miss minus Total Isolated Miss Prior to Reentry) for a sample of 22 recent RVs, ie,

Downrange (ft)
rms = 77

Crossrange (ft)
rms = 75

*These values are inferred, since a complete evaluation using optimally processed data on PVM 18 and PVM 19 was not performed.

The GPS/MBRS data, although providing a good total accuracy evaluation capability, are most desirable for IMU error model signature analysis/verification. As previously mentioned, the Cartesian coordinate trajectory comparisons are easily generated for such an analysis. The velocity comparisons can be displayed in the various IMU instrument coordinate frames (accelerometer, gyro, platform) to enhance the detection of instrument errors and the verification of theoretical error models. The low noise content in such comparisons facilitates the analysis and permits the detection of unmodeled error effects. Furthermore, these signature analyses do not rely on the use of regression analysis techniques (necessary in dealing with radar data), and are therefore unbiased, since they are not forced to conform to an a priori error model.

IV. CONCLUSION

The Air Force-sponsored GPS/MBRS Test Program was successfully completed on Minuteman III missiles PVM 18 and PVM 19. The conclusion, based on the data and the results obtained, is that the concept of using such a system for missile trajectory evaluation is desirable and offers definite advantages over the conventional multilateration radar tracking configuration.

It is hoped that this step forward, in the instrumentation of ballistic missiles, is followed by further development and use of the Global Positioning System.

TITLE: TEST AND EVALUATION OF AN INERTIAL-DOPPLER-OMEGA NAVIGATION SYSTEM FOR THE CP-140 AIRCRAFT

AUTHORS: G. HITZ
L. MOELLER

LITTON GUIDANCE & CONTROL SYSTEMS
Woodland Hills, California

and

E. UNT

LOCKHEED CALIFORNIA COMPANY
Burbank, California

TEST AND EVALUATION OF AN INERTIAL-DOPPLER-OMEGA NAVIGATION SYSTEM FOR THE CP 140 AIRCRAFT

By G. Hitz*, E. Unt**, L. Moeller*

ABSTRACT

The CP-140, Aurora, aircraft developed for the Canadian Armed Forces by the Lockheed California Company (LCC) is a multimission, long-range patrol optimized for operation in the Canadian environment. It performs military ASW missions, and civil arctic surveillance, ice patrol, coastal patrol, and airlift functions. These missions, performed at high northern latitudes over water, ice, and snow surfaces, are highly dependent on the performance of the integrated navigation system that includes a doppler velocity sensor, an Omega navigation unit and two inertial navigation units. The INS units contain the navigation system integration software to provide worldwide 1.5 nm (CEP) bounded position error.

This paper discusses the results of the LCC flight acceptance test program to establish the accuracy of the navigation system and the Canadian forces operational testing that has occurred before and after delivery of the aircraft. The testing covers all modes of operation, free inertial, doppler-inertial and inertial-doppler-Omega. The flight test program for the Aurora benefitted from the testing accomplished on S-3A, P-3C and its predecessors. The number of navigation system evaluation flights were planned in accordance with Air Standardization Agreement, AIR STD 53/11.

In addition the paper describes the integrated system and the units comprising it in terms of operating modes, performance, physical and electrical characteristics and data transfer interfaces.

The system's performance in high-latitude ground- and in-air alignment and all navigation modes is controlled by an 18-state Kalman filter mechanized in the general-purpose LC-4516 digital computer of each of the inertial navigation units. A discussion of the mechanization of this filter is provided and includes Omega step-error detection and the subsequent correction of the Omega data using the inertial system as the reference, slaving of inertial navigation data to reflect the Omega position where excessive inertial system drift is detected, and use of sea current states in the filter to estimate water velocity in the doppler-inertial mode.

*Litton Guidance & Control Systems
Woodland Hills, California

**Lockheed California Company
Burbank, California

1. PURPOSE OF SYSTEM

The CP-140 Aurora aircraft system is an advanced multimission patrol aircraft derived from the U.S. Navy P-3C Orion 1 (Figure 1). Designed primarily to carry out Canada's committments to NATO defenses, it performs antisubmarine warfare (ASW) as well as arctic reconnaissance, search and rescue, coastal surveillance, earth's resources, and mapping missions. The CP-140 navigation capability includes long-term, high-accuracy geographic navigation; sonobuoy station keeping; and relative tactical navigation.

The primary geographic navigation system for the CP-140 is built around two inertial navigation systems (INS) augmented with a doppler velocity sensor (DVS) and an Omega navigation set for worldwide position reference geographical position. Velocity, attitude, heading, and steering information is generated by the navigation system and transmitted to the central navigation-tactical (NT) computer which performs ASW mission navigation and data processing [1,2]. This paper describes the primary geographic navigation system and presents flight test data of navigation performance obtained to date.

The full CP-140 weapon system navigation capabilities are provided using the combined information from the navigation system, the AN/AYK-502 central navigation and tactical (NT) computer system and the sonobuoy reference system (SRS). However the navigation system has a complete navigation capability independent of NT computer operation status. For mission activities this NT computer navigation function provides dead reckoning processing of the tactical situation in either geographical or relative coordinates, using the current aircraft most probable geographic latitude and longitude position received from the navigation system. Geographic navigation is normally used. While in the search area, sonobuoy position measurements, with respect to the aircraft, are normally provided by the SRS to the NT computer [3].

Figure 1. CP-140 Aurora

If the SRS is not functioning, a backup tactical mode of navigation may be selected at the operator's discretion. When operating in the tactical mode, navigation and tactical coordinates of elements within the tactical area are based on a tactical reference point, usually the splash point of the first expendable store deployed. When the geographic coordinates of an element of the tactical situation are required, they are based upon the aircraft as determined by the navigation system and not the tactical position as determined by the NT computer.

Mission Requirements

The ASW mission establishes the primary operational requirements for implementing the navigation functions for the CP-140 aircraft. The mission phases are executed as a series of interactions of the crew with an information processing system. The mission information is collected, processed, ordered, stored, and disseminated by the central NT computer system. Crew interfaces are an interactive graphics system that comprises keyboard and trackball integrated control trays (INCOS) and multipurpose CRT displays (MPD), together with the navigation system displays (see Figure 2) and the pilot's navigation displays.

Enroute Phase

The NAVCOM operator normally initiates ground alignment and initializes the INS elements of the navigation system. After completion of mission system readiness testing, the tactical navigation coordinator (TACNAV) loads the NT computer with the operational program, sets up the tactical display analyzes the tactical situation, and prepares the navigation plan for proceeding to the search area starting point. Commercial airways navigation procedures may be used. Geographic (latitude, longitude) coordinates, or grid mode for the polar region may be used. In-flight alignment may be used for rapid response.

Search Phase

The TACNAV orders the aircraft to be flown to the first fly-to point. During transit, if an aircraft is being relieved on station, the two aircraft can perform tactical data swap through digital and voice data link. This establishes a requirement for long-term bounded error position. During transit the TACNAV selects a sonobuoy search pattern through the computer and selects an optimum flight path for rapid sonobuoy emplacement. Completely automatic flight steering and release of selected sonobuoys are available throughout the flight. Estimated splash points of the selected stores are calculated and displayed on the multipurpose displays (MPD) of the crew. On completion of pattern drop, the TACNAV may make a computer selection of an orbit path for (1) optimum buoy revisit time, (2) continual monitoring of passive LOFAR (omidirectional) or DIFAR (directional) buoys, or (3) specific combinations of both. This orbit path sterering requires good relative position repeatability.

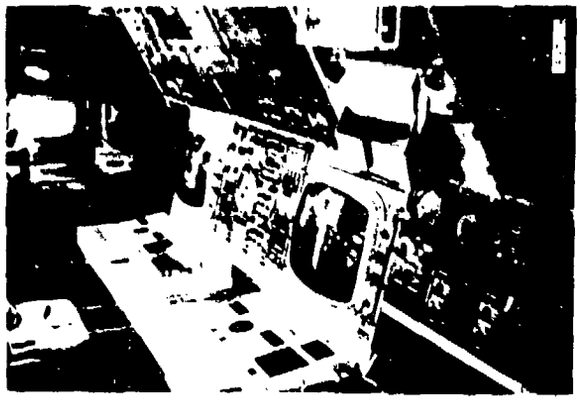

Figure 2. CP-140 TACNAV and NAV/COM Stations

Localization and Attack Phases

Depending on the type of target detected, type of search target, the TACNAV selects the next tactic via computer aided sequences. When a target position fix of sufficient accuracy has been determined, the localization phase using command-activated active (pinging) sonobuoys (CASS) follows. Fly-to-points are assigned; the sonobuoy drops are made on NT computer command; and automatic flight is directed around a constant range ring path. When a CASS fix is determined, ambiguity is resolved by a programmed flight to one of the fixes Magnetic Anamaly Detector (MAD) detection. Either a MAD mark occurs or additional CASS fixes are made, followed by automatic flight to the target intercept point. The weapon is then released at the computer-calculated closest point of approach (weapon ballistics and wind accounted for). After a weapon is dropped, continued attacks, or attack evaluation, may be ordered. For maximum target point accuracy, very low position drift is required for short to intermediate time periods. This series of calculations by the NT computer uses inputs from the INS, doppler radar, SRS, air data system and other hardware.

Specified performance requirements of the navigation system for a mission of up to 12 hours are:

a. Long-range navigation performance of the navigation system in the primary mode of operation (inertial-doppler-Omega) is bounded error of 1.5 nm (CEP) with Omega performance stipulated as 1.5 nm (CEP).

b. The doppler-inertial dead reckoning ground position radial error growth rate is not to exceed 1.5 nm/hr (95%) (0.72 nm/hr - CEP).

c. The free inertial error growth rate is not to exceed 2 nm/hr (95%) (0.96 nm/hr - CEP).

d. Accuracy of position repeatability with respect to a given location will be 0.5 nm (CEP) over a 2-hour period and within a radius of 200 nm.

e. The tactical navigation performance, that is the maintenance of the aircraft position relative to a sonobuoy field, is specified (classified) for conditions of normal SRS and for alternative OPTI operations.

Geographic Navigation vs Tactical Navigation

The navigational requirements for airborne ASW missions are complicated by the use of different frames of reference for one mission. The normal geographic reference frame is earth fixed, e.g. latitude and longitude, relative to the equator and the Greenwich meridian. However the target is usually submerged, drifting with or propelled relative to the predominant ocean current. The aircraft moves relative to an airmass which frequently has a significant velocity with respect to both the ocean surface and the airspace in the direct proximity of the ocean surface. The first contact between the aircraft and the target is usually established by sonobuoys that drift on the surface of the ocean, predominantly influenced by either surface movement or by deep currents, depending on whether the buoy has a sensor deployed into deep water by an attached cable.

The following quantitative ocean current and wind relationships approximately hold:

- Major (seasonal) ocean currents have a median value averaged over all oceans of 0.3 knot, and a peak value of 5 knots .[a]
- Wind driven water spray can reflect significant amounts of rf energy in the case of modern 13.3 GHz (wavelength - 22 mm) transmitting doppler radars. Spray "seen" by the doppler radar is not proportional to the wind velocity and is zero for winds less than approximately 2 knots (i.e. there is no significant spray). For wind of 2 knots, nearly 2-knot spray is seen by the doppler; for 10 knots of wind, the doppler sees 3 knots; and for 30 knots of wind, the doppler sees 4 knots .[b]

Even if the navigation system is operating without equipment errors - in the normal design operating environment, significant discrepancies will arise in the velocity measurement of sonobuoys because of differences with respect to what sensor measures the velocity. A simplified snapshot diagram of what is observed by airborne augmented inertial versus doppler navigation systems is given in Figure 3, for two conditions: a free floating surface buoy (e.g. a marine flare) and a sonobuoy with a hydrophone deployed.

The INS coupling between platform level errors and acceleration errors, with the well-known 84-minute Schuler period, results in relative velocity and position errors reaching maximum in 42-minute intervals. This can be troublesome for standard ASW operations. In the past, to obtain a more stable and more representative reference for targets in the ocean, classical ASW tactics have employed a tactical navigation mode for search and attack, which consists of dead-reckoning with doppler velocity and doppler-damped inertial heading and a tactical bias velocity obtained from successive OPTI of a selected reference buoy. Note that even though classical doppler-damped inertial navigation may be used, a discrepancy between the earth-fixed reference for the inertial vs the ocean-surface-fixed

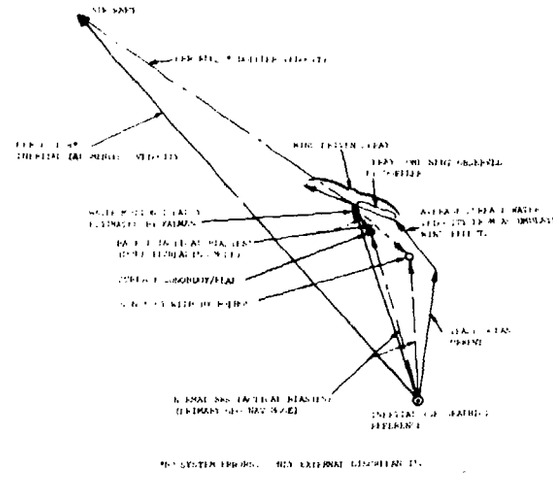

Figure 3. Velocity Vectors of Aircraft Observing Sonobuoys

reference for the doppler results. The tactical situation (buoys, submarine, etc.) is in yet another reference system differing from the navigation reference by another tactical bias or biases.

The inherent difference between the "perfect" INS (as provided by the augmented IDO) and the doppler velocities can be bridged by an ocean-current or a water-surface-velocity vector and is implemented in the CP-140 navigation system as two sea-current-state vector elements in the navigation Kalman filter, and the SRS is then used for determining aircraft-to-sonobuoy position by means of recursive estimation from passive angle-measurements, freeing the aircraft from the classical on-topping requirement for localizing and attacking the target. This also permits derivation of the individual sonobuoy tactical biases and the sonobuoy field bias.

2. NAVIGATION SYSTEM DESCRIPTION

The navigation system provides all-weather global navigation capability in the enroute, airways and tactical environments to enable the aircraft to function effectively as a surveillance and ASW weapon system. The navigation system's functional flow diagram is shown in Figure 4.

The navigation system is built around two inertial navigation systems augmented with doppler for velocity, Omega for position, and position fixes from radar, tacan or position overfly. The two INS operate independently. Each INS processor accepts data from a single doppler ground velocity sensor and Omega navigation set [c]. Each INS also accepts position update information from either the NT computer or the INS controls. These data are combined with INS data in identical recursive suboptimal Kalman filters to yield outputs of most probable position and velocity. The 18-state Kalman filter is mechanized to function during ground alignment, in-flight alignment, and normal navigation. Provisions

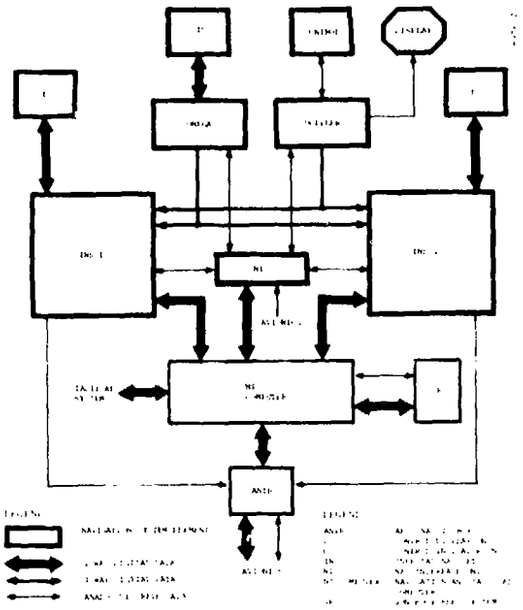

Figure 4. Block Diagram of CP-140 Navigation System

are provided for periodic calibration of inertial platform gyros and accelerometers. The navigation system units communicate with the central NT computer via the navigation interface unit (NIU) and with the flight instruments via the aircraft AFCS/navigation interconnection box (ANIB). The horizontal and vertical reference information from the INS systems can be chosen independently for the pilot's, co-pilot's, and NAVCOM operator's instruments, and for the NT computer. Navigation system mode control and selection of the INS for data output is provided by the NIU. Fault isolation to the module level is provided for each navigation system LRU. Software is also included which allows self test of the interface and aircraft systems upon demand. INS operation is designed to gracefully degrade when doppler or Omega information becomes grossly erroneous or unavailable. Unstabilized magnetic heading is provided in case of platform failure, and when the coarse align mode has not been completed.

The principal operator interface with the INS units is via the two INS control and display units. The INS generates information necessary for waypoint steering and also computes global synthetic magnetic variation. Position can be displayed in a grid coordinate system for navigation in the polar region. The Omega system, operating as an independent navigator generating position outputs to the INS elements, provides interface to the operator via the Omega control indicator unit (CIU). A doppler readout of drift angle and groundspeed is provided.

In the (fullup) inertial-doppler-Omega (IDO) navigation mode employing the 18-state Kalman filter, the navigation mode is identical to the fine-alignment portion of the in-flight alignment mode. As has been variously analyzed [4,6]; the required alignment time and resultant accuracy can be improved by maneuvers during the alignment period. Normal CP-140 aircraft maneuvers after completion of coarse align, have consistently been used for obtaining satisfactory inflight ID and IDO alignment.

Inertial Navigation System (Figure 5)

Two identical Litton LN-33L INS (AN/ASN-505) are used. The inertial navigation unit (INU) contains the P-1000 platform and associated electronics, LC-4516 computer, the 16K-word 16-bit LCM-8000 DRO core memory, and necessary analog and digital interfaces. The INU adapter (AINU) provides followup servo outputs of roll, pitch, and magnetic heading. A backup compass mode provides backup magnetic heading. Each INS has a control display unit (CDU) to provide the NAVCOM operator with continuous readout of system outputs. The INS performs self-contained ground alignment or an in-flight alignment from the doppler and/or Omega. The INS provides great circle waypoint steering commands to the flight director system whenever valid waypoints exist in the INS. It contains provisions for manual position fix during operation by overflight of a known location. Each INS contains a Kalman filter in software to combine inertial, doppler, and Omega information for navigation, in-flight alignment, velocity damping, position correction and position error bounding. Each INS possesses a self-test and failure warning capability. A battery unit provides for INS operation during interruption of aircraft power.

The following primary modes of INS operation are controlled from the INS CDU:

Standby

Power is applied to minimum circuits to keep the system in a ready state for alignment particularly under cold temperature basing conditions. The INS can be readied without being manually placed in the standby mode.

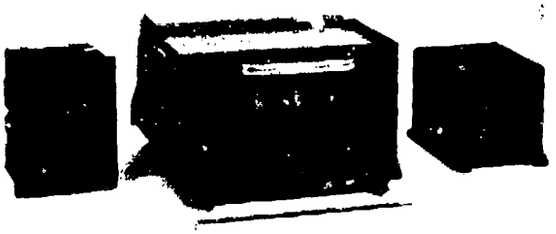

Figure 5. LN-33L Inertial Navigation System (AN/ASN-505)

Align

Ground alignment and in-flight alignment are available. The INS on the ground, at equipment ambient temperature above 0C completes alignment within 15 minutes of initiating the alignment sequence at latitudes 75° or less. For temperatures of 0C to -40C the alignment times do not exceed 20 minutes. For latitudes greater than 75°, automatic alignment is possible but may exceed these alignment times. Navigation data are transferred during coarse alignment.

Navigate

The INS operates in the best mode possible as determined by the status of external sensor data and as modified by the NIU and by operator equipment/mode selections. Order of mode priority is:

- Inertial/doppler/Omega
- Inertial/Omega
- Inertial
- Dead reckoning based on doppler information and compass heading
- Dead reckoning based on TAS, compass heading, and last remembered or manually input wind. Graceful degradation takes place automatically in accordance with the above in the event of sensor failure.

Compass Mode

Unstabilized magnetic heading is the only output.

Grid Mode

Grid mode is a submode normally selectable between latitudes of 65° and 90° North or South. All system outputs are referenced to Transverse Mercator projection coordinates with the point of tangency lying along 90° East and 90° West meridians; and the grid north pole relocated at 0° latitude and 180° longitude.

Calibrate Mode

This mode determines and corrects gyro biases, and estimates accelerometer bias to aid in improved high latitude system alignments. The INS proceeds through a normal ground alignment sequence followed by a 2-axis calibration. During the calibration process the INS platform is rotated about azimuth for biasing of both level gyros and accelerometers. The operator is provided a cue on the CDU at the completion of level gyro and accelerometer biasing and also at the completion of Z gyro biasing.

Test Mode

This mode is used during maintenance procedures only. System outputs are simulated for test purposes.

Doppler Velocity Sensor (Doppler)

The AN/APN-510 doppler (Figure 6) is produced by the Canadian Marconi Company (CMC). It employs an aircraft-fixed 4-beam, planer array antenna. The FM/CW rf transmission is at 13.3 GHz using a Gunn diode power oscillator at a radiated power output of 200 milliwatts. The doppler is composed of four LRUs:

1. The receiver-transmitter unit, mounted on the antenna and integral radome
2. The signal data converter unit including a 16-bit microprocessor with a 3K × 8-bit ROM and 26 · 8-bit RAM scratch pad for memory
3. A doppler sensor controller
4. A groundspeed/drift angle indicator.

Velocity data and status information are transmitted to the dual INUs via an ARINC 575 serial data bus. The digital velocity outputs, Vx, Vy, and Vz, are in antenna coordinates and are accurate to 0.17% rms for drift ±10°. Terrain bias scale factors are selected by a manual land/sea switch on the doppler controller. The velocity fluctuation noise is less than 0.05%, averaged over 10 nm, and is suitable for INS in-flight alignment.

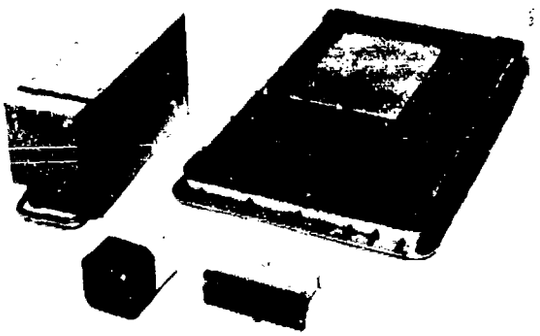

Figure 6. Doppler Velocity Sensor (AN/APN-510)

Omega Navigation Set (Omega)

The AN/ARN-511 Omega Set (Figure 7), built by Canadian Marconi Company, is composed of three LRUs:

1. A receiver/computer unit
2. A control/indicator unit (CIU)
3. An orthogonal ferrite loop antenna with a signal preamplifier.

The receiver/computer is packaged as a 1 ATR unit. The computer is a 16-bit processor with an 8K DRO core memory. The computer, together with the VLF receiver, uses a minimum of three stations, selecting the best available based on received signal strength. Synchronization and station

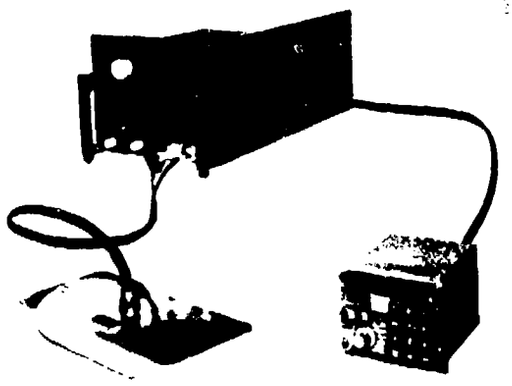

Figure 7. CM A-719(M) Omega Navigation System (AN/ARN-511)

selection is fully automatic. The receiver tracks the three Omega carrier frequencies for 72-nm lane ambiguity. TAS is used by the Omega for rate aiding and for degraded mode dead reckoning. Phase tracker bias error is ±1 centicycle (CEC) maximum. The dynamic phase tracking error is 1 CEC per 200 knots with rate aiding or 3 CEC in type II servo mode without rate aid at constant velocity. Diurnal phase correction is effected by software.

The Omega set outputs data to the two INS via a ARINC 575 output serial data bus. The NAVCOM operator also has a continuous display of aircraft position and other navigation, steering, and status information available on the Omega CIU.

Table I highlights the physical characteristics of the navigation system.

TABLE I - PHYSICAL CHARACTERISTICS OF NAVIGATION SYSTEM

	Size H × W × L (in.)	Weight (lb)	Power
Inertial Navigation System (INS), AN/ASN-108*†			
Inertial Navigation Unit	8.6 × 14.0 × 13.3	42.5	115/200V, 3Φ
Control Indicator	7.5 × 5.7 × 5.8	6.5	350W; plus
Adapter, INU	6.2 × 6.1 × 7.1	6.6	600W for
Battery Power Supply	6.3 × 9.1 × 12.2	18.5	3 Min., Max.
Mounting Base, INU		2.2	Heater Power
Navigation Interface Unit (NIU), OU-500/ASN†			
RI Electronics Unit	7.7 × 4.1 × 19.6	22.5	115v., 400 Hz,
Control Indicator	2.6 × 5.8 × 5.3	5.0	200 VA; 28Vdc, 20W
Doppler Velocity Sensor (Doppler), AN/APN-510†			
Receiver Transmitter	4.1 × 10.7 × 25.7	15.9	115v., 400 Hz
Signal Data Converter	7.5 × 9.0 × 12.5	14.0	60VA;
Drift Angle/Ground Speed Indicator	3.3 × 3.3 × 5.0	2.2	26v., 400 Hz, 8VA;
Control	1.9 × 2.8 × 3.2	0.9	28Vdc, 8W
Omega Navigation Set (Omega), AN/ARN-511†			
Receiver Computer	7.8 × 10.0 × 19.5	45.0	115v., 400 Hz
Control Indicator	4.5 × 5.8 × 6.5	6.0	250VA
Antenna	1.8 × 6.5 × 11.0	4.0	

*Litton G&S
†Litton Systems LTD (LSL), Canada
‡Canadian Marconi Co.

3. KALMAN FILTER MECHANIZATION

The best estimate of aircraft position, velocity, and heading information is obtained by augmenting the inertial system Omega- and doppler-derived information and other position fix updates. The 18-state Kalman filter in each INS provides the means of optimally combining INS and reference system information[11,17]. The errors estimated by the filter are position, velocity, heading, platform tilts, errors in the deflection of gravity, gyro biases, Omega biases, doppler bore sight and scale factor errors, and sea currents. Figure 8 presents the system state vectors and dynamic (A) matrix. Figure 9 defines the observation (H) matrix, and the state vector, and Table II provides definition of terms.

State Propagation/Kalman Update Approach

All Kalman updates are performed at the end of velocity averaging intervals. The state vector is propagated between these points where it is used in forming the Kalman residual. The observable differences, also required in forming the residuals, occur at arbitrary points during the averaging interval and are projected to the end of the interval by the "Projected H Materics" (contragradient) defined in Figure 9. When the update is complete, the state vector is propagated into the future to the end of the next averaging interval. At that time the inertial system is corrected with the appropriate state vector elements as soon as real time equals the time at the end of the interval. A new update cycle then begins.

The covariances are propagated according to the algorithm,

$$P = P + AP * DA + (AP)^T * DT + APA^T * (DT)^2 + Q$$

Because P is symmetrical, only those elements above and including the diagonal are stored. The size of the P buffer is N * (N+1)/2, where N is the state vector size. The format of each P element is the same as the format of each Q element.

Propagation occurs every 4 seconds except in coarse level where the propagation interval is 2 seconds.

The covariance and state vector updates are performed according to the following algorithm:

$$K = PH^T D^{-1}$$

$$P = P - KHP$$

$$X = X + K[Z - HX]$$

$$D = HPH^T + R$$

Since observations are uncorrelated, sequential updates are used in order to avoid a matrix inversion when computing K. The computational algorithms are constructed so that the second residual in a sequence of updates is formed using the results of the first update. Updates are performed every 8 seconds except in coarse level where the update interval is 2 seconds.

TABLE II - DEFINITION OF TERMS

Kalman state variable elements

a_x, a_y	=	accelerometer bias (calibration) or gravity anomaly states
b_x, b_y, b_z	=	gyro bias states
b_{xt}, b_{yt}	=	thermal gyro bias states (alignment)
c_x, c_y	=	sea current states
δY, δSF	=	doppler boresight, scale factor states
$\delta\rho_z$, $\delta\zeta$	=	azimuth slew rate, relative azimuth error states (calibration)
ϕ_x, ϕ_y	=	platform tilt error states (coarse level)
$\delta\theta_x$, $\delta\theta_y$, $\delta\theta_z$	=	position error states
δV_x, δV_y	=	velocity error states
ϵ_x, ϵ_y	=	platform tilt minus position error states
$\delta\Omega_x$, $\delta\Omega_y$	=	omega bias states

Definitions

A, H, P, R, Q	=	dynamic, observation, covariance, observation noise, plant noise matrices
H_i	=	observation matrix for ith sample in velocity averaging interval
$\Phi_{(i,\,e)}$	=	transition matrix from last update, e, to each valid sample i.
DT	=	propagation interval
K	=	Kalman gain matrix
N	=	number of valid observation samples
X	=	state vector
X_e	=	state vector at evaluation of velocity averaging interval
Z	=	Kalman observable difference
CO	=	$\omega_z + \Omega_z$ = corriolis coupling
G	=	gravity
R	=	radius of earth
V_{AH}, V_{CH}	=	along, cross heading average doppler velocities in velocity averaging interval
α	=	platform azimuth (wander) angle
β_a, β_b, β_{bZ}	=	accelerometer, gyro correlation times
β_1, β_2	=	sea current, gyro thermal (alignment) correlation times
β_3, β_4	=	doppler boresight/scale factor, azimuth slew (calibration) correlations
ϵ_x, ϵ_y	=	x, y gyro biases
ρ_x, ρ_y	=	craft rates
ω_x, ω_y, ω_z	=	spatial rates
Ω_x, Ω_y	=	x, y earth rate components

The filter is initialized differently for each of five different filter modes, but the same computational algorithms are used throughout. The following filter modes are configured during various operational phases.

Navigation and Position Fix Filter Mode

This filter is used for navigation following ground alignment or during in-flight alignment in order to augment inertial navigation with doppler and Omega updates and provides for Kalman position files. It uses 18 states and is the baseline for all other Kalman filters.

Coarse Level Filter Mode

This filter reduces platform tilts to less than 1° following initial platform caging. The filter is initialized with four states (two velocity and two tilt states), providing 2nd-order leveling for each axis.

Wide Angle Filter Mode

This filter is run after coarse level and is intended to estimate heading within 1° before starting fine align and gyrocompass. Platform alpha angle is computed and used to initialize the ground align, navigation or calibration Kalmans.

Ground Alignment Filter Mode

This filter, used before takeoff, is derived from the primary navigation/position fix Kalman filter by replacing the sea current states with thermal gyro bias states.

Calibration Filter Mode

This filter allows for periodic refinement of gyro biases and level accelerometer biases to meet performance requirements with high latitude alignments. It consists of the ground alignment filter with the doppler boresight and scale factor states replaced with relative azimuth and azimuth slew rate states.

In-Flight Alignment

The 18-state Kalman filter provides the capability of aligning the platform in flight. Doppler is required (at least initially) while position information (Omega or position fixes) is desirable. The alignment sequence is as follows:

- Coarse level - The pilot is required to maintain straight and level flight with constant velocity. Earth rate is modeled as noise driving the tilt states.
- Wide angle gyrocompass - The platform alpha angle is estimated to within 1°. The gyro bias states are initialized to estimate earth rate and the A matrix elements coupling the azimuth state ($\delta\phi_z$) to three other states are zeroed. Alpha angle is computed as

$$\alpha = \mathrm{Tan}^{-1}\ \frac{\Omega x + \epsilon x}{\Omega y + \epsilon y}$$

- Fine alignment - Detailed estimates of position, velocity, and heading are obtained.

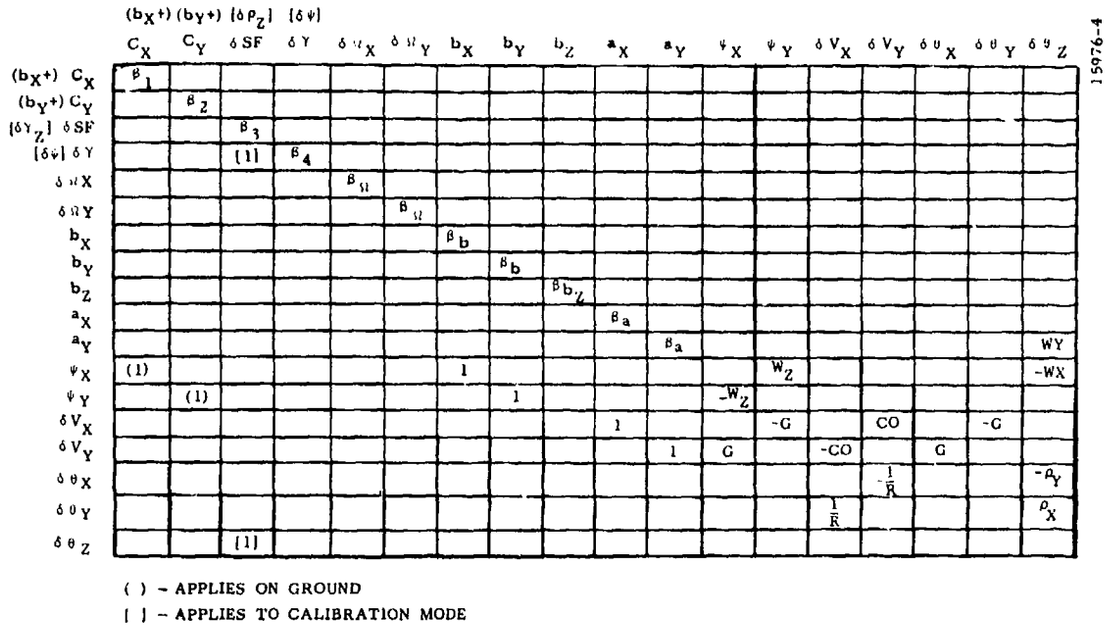

Figure 8. State Vectors and Dynamic Matrix

STATE VECTORS (TRANSPOSED)

15976-14

[C_X C_Y δSF δγ $\delta\Omega_X$ $\delta\Omega_Y$ b_X b_Y b_Z A_X A_Y ψ_X ψ_Y δV_X δV_Y $\delta\theta_X$ $\delta\theta_Y$ $\delta\theta_Z$]	IN AIR
[b_X' b_Y . . . .]	GROUND ALIGN
[. . $\delta\rho_Z$ δψ . . . .]	CALIBRATION
[ϕ_X ϕ_Y δV_X δV_Y]	COARSE LEVEL

A. STATE VECTORS (TRANSPOSED)

MEASUREMENT MATRICES

[0	0	0	0	-1	0	0	0	0	0	0	0	0	0	t/R	1	0	Y]	X	Omega
[0	0	0	0	0	-1	0	0	0	0	0	0	0	-t/R	0	0	1	Y]	Y	
[(1- t)	0	-VCH	VAH	0	0	0	0	0	-T	0	0	GT	1	0	0	GT	0]	X	Doppler
[0	(1- t)	-VAH	-VCH	0	0	0	0	0	0	-T	-Gt	0	0	1	-Gt	0	0]	Y	
[0	0	0	0	0	0	0	0	0	-T	0	0	GT	1	0	0	GT	0]	X	Ground Align
[0	0	0	0	0	0	0	0	0	0	-T	-Gt	0	0	1	-Gt	0	0]	Y	and Calibration
[0	0	0	0	0	0	0	0	0	0	$-t^2/R$	$-Gt^2/R$	0	1	t/R	$(-Gt^2/R)$	0	0]	X	Position Fix
[0	0	0	0	0	0	0	0	0	$-t^2/R$	0	0	$-Gt^2/R$	0	0	0	$(-Gt^2/R)$		Y	
[0	0	0	1	0	0	0	0	0	0	0	0	0	-t/R	0	0	0	0]		Calibration (Synchro)
[0	0	1	0]	X															
[0	0	0	1]	Y	Coarse Level														

B. PROJECTED OBSERVATION (H) MATRIX

Figure 7. Observation (H) Matrix and State Variables

Heading is estimated without an intial magnetic heading input; the magnetic heading can be unreliable because the aircraft may operate in the vicinity of the magnetic pole. With this approach a large position error can accumulate when the alpha angle estimate is poor, because the alpha estimate must be used to propagate the navigation direction cosines. Therefore position updates are highly desirable to reduce position error accumulation during the initial part of the alignment[1].

Maneuvers are allowed after completion of coarse leveling. Doppler data are considered valid for roll angles up to 30°.

Ground Align/Calibration

During ground alignment, the doppler and Omega states serve no useful function and are, therefore, redefined to improve alignment and calibration performance. The sea current states are replaced by thermal gyro bias states modeled as exponentially correlated states with a fixed correlation time and a plant noise, which is bled away as the platform warms up. In addition the gravity anomoly states are redefined as accelerometer bias states.

The calibration mode is characterized by a 2-position alignment with intermediate slew. Estimates of x, y, and z gyro biases and x, y, accelerometer biases are obtained. During slew, the increase in azimuth spatial rate causes the accelerometer biases to become observable. The platform high slew rate (400°/hr) is accomplished by hardware to ±25% accuracy, which does not permit a good estimate of accelerometer biases; ω_z is used in the dynamic matrix and for computing total angle slewed). Therefore the doppler boresight and scale factor states are redefined to be azimuth synchro error and azimuth slew rate (ω_z). By making observations of the azimuth synchro during slew, ω_z is estimated.

Navigation

Navigation performance is dependent upon the alignment mode. During ground alignment, INS inertial position and velocity errors are reduced to minimum values. At takeoff, since inertial errors are much smaller than Omega and doppler errors (as conveyed to the Kalman filter by the covariances), the Kalman is able to estimate the doppler boresight and scale factor errors (if the aircraft turns) and the Omega biases. If the aircraft is over sea, an estimate of the sea currents will also be obtained. However, since doppler and Omega errors are modeled as exponentially correlated states these initial estimates will eventually bleed off, and the modeled inertial errors will increase. Eventually the inertial position and velocity will be bounded, and the Shuler oscillation will be damped to within the doppler and Omega errors. If the aircraft transitions from sea to land, the velocity estimate will improve because the observation is no longer contaminated by the sea currents. (The sea current states are removed from the filter when land/sea is placed in the land position.) If the aircraft returns to sea, the sea currents will again be estimated.

When the system is initialized for in-flight alignment, the inertial covariances are much larger than after a ground alignment. The filter then tends to immediately bound the estimated states to the doppler and Omega derived observations.

The requirement for position repeatability to a selected point after 2 hours to within 0.5 nm (CEP) after flight within a 200-mile radius is 3 times more difficult to meet than the Omega bounding requirement of 1.5 nm (CEP). This requirement is satisfied by better than specified system performance and partially as a result of some error cancelling when the aircraft returns to the selected initial point.

Doppler Augmentation

The doppler radar unit is a fixed antenna system. It supplies x, y, z velocities in doppler antenna coordinates as well as a status word, which gives discrete information on data validity and system status. Velocity information from the doppler is rotated from antenna coordinates through platform roll, pitch, and azimuth into platform coordinates, where it is differenced with inertial velocity. Four Kalman filter states are defined for estimating doppler-related errors: doppler boresight and scale factor errors and two sea current states. In the doppler unit, the land/sea switch causes a gain change to account for the difference in average reflectivity between land and sea. In the software the switch causes the inclusion or deletion of sea current Kalman states.

Doppler boresight and scale factor errors are fixed in aircraft coordinates, while inertial velocity and sea current states are platform fixed. Therefore scale factor and boresight errors can be estimated during a turn. Sea currents, on the other hand, can be estimated only when the inertial velocity errors are small such as after a ground alignment or after flying from land to sea. The sea current states inform the filter of a doppler velocity error over sea due to the moving reflector surfaces. Once over sea, doppler velocity accuracy slowly degrades to the level determined by the sea currents, since sea currents are modeled as exponentially correlated random variables with an initial covariance of 2.5 knots and a relatively short correlation time of 1 hour. Doppler boresight and scale factor errors are also modeled as exponentially correlated random variables with initial covariances of 15 $\overset{\frown}{\text{min}}$ and 0.2%, respectively, with correlation times of 1000 hours.

A reasonableness test (3-sigma test) is performed on the doppler/inertial residual by comparing it against the Kalman residual. If the test fails, updating is suspended for 2 minutes and a light is flashed to inform the operator of the failure.

Doppler updates occur every 8 seconds. Up to 40 independent doppler velocity samples can be received during each 8-second interval. The samples are edited and prefiltered by taking a simple average. Since doppler samples can be missing (nonvalid) and since the observation matrix elements are functions of platform synchro angle, the point at

which this single point average applies varies. To project the average to the end of the interval, an observation matrix defined by the following is used for the update:

$$\bar{Z} = \frac{1}{N} \sum_{i=1}^{N} Z_i = \bar{H} X_e + R$$

where:

$$\bar{H} = \frac{1}{N} \sum_{i=1}^{N} \left(H_i \phi (i, e) \right) X_e$$

Omega Augmentation

The Omega supplies latitude, longitude, error and sigma (indications of Omega quality), time, and status. The Omega navigation set independently updates latitude and longitude from the lines of position every 10 seconds and interpolates position between updates using velocity and heading from external sources. The "time" word indicates the time since the last position update.

An Omega update is performed every 60 seconds. Updates are suspended whenever the Omega error and status words indicate a lane slip condition. In addition a reasonableness test is performed by differencing the actual IDO or IO residual against the Kalman predicted residual. If the actual residual is more than 4 times greater than the Kalman residual (about 5 miles) a lane slip (step-error) is assumed to have occurred. Large plant noise increments are then added to the Omega bias covariances so that on the next update most of the error between the Omega and inertial positions is assigned to the Omega. In other words the short term stability of the inertial system is used to calibrate out the lane slip.

Position Fix

Position fixes are processed on a one-to-one basis. That is the displayed present position is always changed by an amount equal to the total observable difference. The inertial position is changed by an amount equal to the Kalman state vector, and the display is biased by an amount equal to the difference between the total observable difference and the position state vector.

Since several minutes can elapse when performing a position fix between the time of the flyover (when the position is fixed) and the time an update is requested (i.e. when the gains are computed), an observation matrix is used similar to the observation matrix for doppler processing.

4. PERFORMANCE

Performance data for the CP-140 navigation system has been obtained from four test programs. Initial performance testing was conducted on the LN-33L inertial test system installed in a Canadian Forces (CF) Argus patrol aircraft between June and September 1979. Flight testing for performance verification of the integrated Navigation System occurred between January and June 1980 as part of the aircraft contractor CP-140 Integrated Flight Test program. Additionally there is follow-on contractor acceptance test data obtained from CP-140 acceptance flights through May 1981. Finally, limited data has been obtained from initial phases of formal Canadian Forces operational evaluation (OP/VAL) flight testing of the total CP-140 Aurora aircraft system. CP-140 OP/VAL testing will be completed in the fall of 1981.

Flight test navigation data for the LN-33L OP/VAL were automatically recorded using video cameras observing the routine navigator's station displays, including the primary LN-33L CDU the reference system Loran-C CDU, a time code generator repeater display and an alternate reference LTN-51 inertial system CDU. The video data were supplemented with manual logged data recording. Data reduction was performed with verified, corrected data using an HP 9820 computing system using several different statistical methods.

Test data for the CP-140 contractor integration test program flight tests used manual entry mark by the pilot of ground reference radio navigation aids (vortac, DME, tacan) on overfly. Position data from the two inertial systems was automatically recorded into the CP-140 central processing system for later data retrival. Backup on-top position data were manually logged by the navigator by freezing the two inertial and the Omega system readouts and recording position and time data.

Position data for the CP-140 navigation test flights reduced in accordance with procedures previously defined for the S-3A integrated navigation system using the U.S. Navy Standard CAINS. A weighted average method was used for computing the overall CEP for a group of flights of the same mode (inertial, O, ID, IDO). The flights were grouped according to the number of checkpoints in the flight. Once the CEP for each group was determined a weighted average CEP or CEP rate was determined for all flights, and data were then plotted. As a comparison the data were also computed using the maximum likelihood methods of ASCC AIR STD 53-11, with performance verified within specification using either method.

Test Results

The free inertial results obtained during the initial OP/VAL of the LN-33L yielded performance of 0.48 nm-per-hour (CEP) for the first 3-1/2 hours, increasing to 0.84 nm per hour after 10 hours, using ASCC AIR STD 53-11 maximum likelihood methods for calculation. Data were obtained from 13 flights with flight times of 3 hrs 42 min to 13 hrs 58 min with 10 flights over 10 hours, and included alignments and flights at high latitude and one polar flight. Ground alignment was performed numerous times between latitudes of 64° and 76° in 12.8 minutes. A single LN-33L unit was evaluated.

The CP-140 contractor performance verification flight tests comprised 15 flights lasting between 8 and 11 hours. Twelve of these flights were over land and three were over water or partially over water.

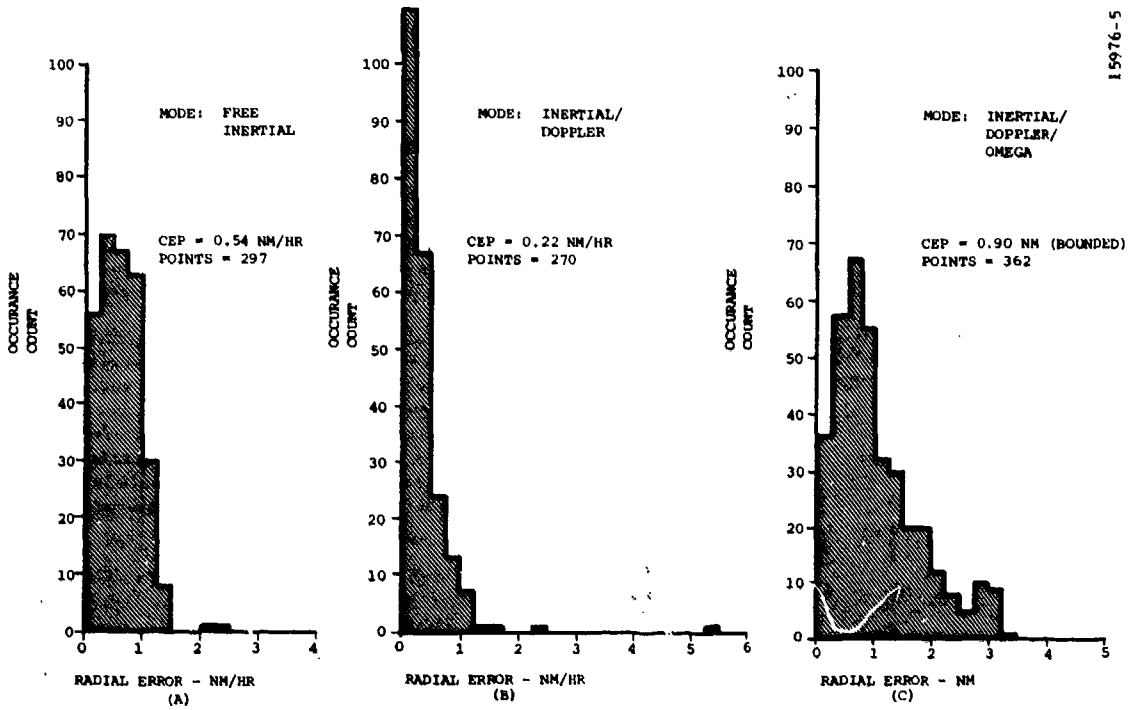

Figure 10. CP-140 Position Error Histograms

Four flights were north-south flights; five flights were east-west flights; two flights comprised a cross-country flight and return, and four flights were 2-hour repeatability flights. (Two were continuously over water.) The dual INS navigation systems were operated in various modes during the flights yielding 8 free inertial flights, 8 inertial-doppler flights (ID) and 11 inertial-doppler-Omega (IDO) flights. All of the over-water flights were performed in the ID and IDO modes. Performance was excellent, as shown in Figures 10A through 10C, yielding free inertial performance of 0.54 nm per hour (CEP), ID performance of 0.22 nm per hour (CEP), and bounded IDO performance of 0.90 nm (CEP) . All alignments were within the specified 15 minutes ground alignment requirements.

Figure 11 shows the performance of each mode compared to the specification requirements. Note that the ID performance error is reduced after 4 hours to 0.10 nm/hr indicating the velocity bounding effect of the doppler sensor becoming dominant due to Kalman filter action[15].

Performance of 11 flights in the IDO mode is shown with the composite Omega system performance during the same flights (Figure 12). Both the IDO and the Omega performance is within the 1.5 nm (CEP) requirement. The flights occurred over a 15-hour period, with some starting as early as 5:30 a.m. Although the composite Omega performance shown in Figure 12 compresses the time scale, diunal effects are apparent. Early predominance of the inertial performance shows in the first 3 hours of operation. Thereafter, IDO performance appears to track the Omega system.

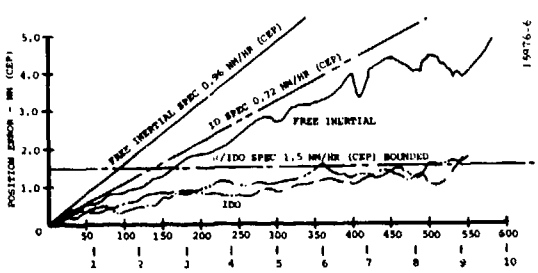

Figure 11. Ensembles of Free Inertial, ID, and IDO Flights

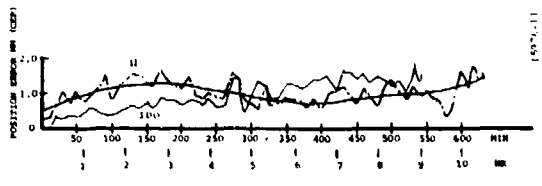

Figure 12. Composite of Ω and IDO Performance

Figure 13 shows two flights where one system was operated in the IDO mode and one in the ID mode. As predicted, after 3 to 4 hours the Omega starts to bound the inertial as the modeled inertial errors approach the Omega errors.

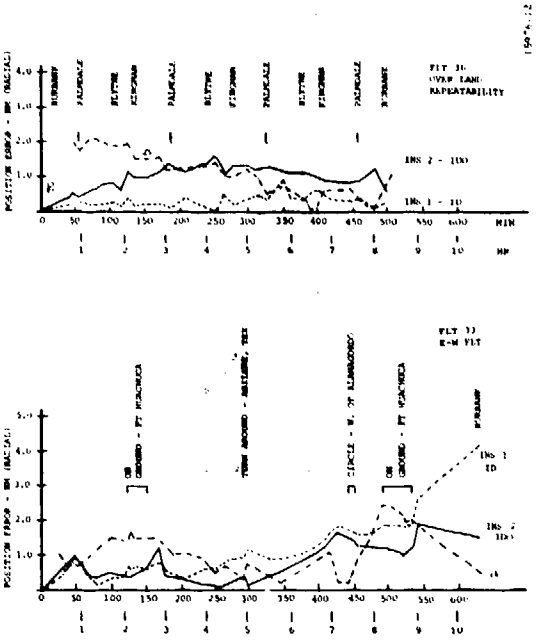

Figure 13. Comparison of ID, IDO, and Ω

One of the key performance requirements for ASW operations is a high level of repeatability during the mission to allow satisfactory return to search patterns of sonobuoys, return to reference points, etc. Figure 14 shows a flight made to evaluate repeatability performance.

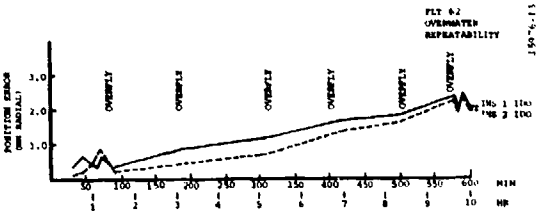

Figure 14. Overwater Repeatability Flight

Flight 62 shows a typical repeatability flight, with all flight time between reference overflies over water. There was wind of approximately 20 knots from a heading of 325° that prevailed throughout the flight. Since this occurred well after the first hour of flight when the sea currents can be detected, there is little or no sea current correction. Note that both systems track each other closely, indicating excellent determination of inertial biases, with the system then driven by the sea currents. Omega performance was less than 1 mile and reduced the rate of growth of inertial position caused by the sea currents.

Note that the augmented system error rate is much less than would be the case without the Kalman filter because a 20-knot wind generates a 3- to 4-knot doppler velocity error causing wind-driven water surface effects. Repeatability performance on this flight was excellent, averaging 0.41 nm between overflies or 0.44 nm per 2-hour intervals.

In-flight alignments have been performed during acceptance testing of each production aircraft. There have been 39 attempts and 35 successful in-flight alignments. Alignment times were between 49 and 54 minutes, except two that took over 1 hour (61 and 68 minutes). Three unsuccessful attempts were caused by improper system data inputs, and one was unsuccessful because of equipment BIT no-go.

Initial high latitude tests have been conducted by Canadian forces. High latitude in-flight alignment above 70° latitude was achieved with moderate success. The BIT-align monitor parameters apparently require some readjustments for better performance.

CONCLUSIONS

Initial performance of the CP-140 augmented navigation system has demonstrated exceptionally good performance in all primary modes of operation (inertial, ID, IDO). Two-hour repeatability performance meets the requirements of 0.5 nm (CEP). In-flight alignment is successful as a normal mode of operation. Some BIT parameter adjustment may improve high-latitude in-flight alignment.

ACKNOWLEDGEMENT

This paper addresses the design and test of a system to which several organizations and many individual engineers have contributed over several years. Flight test data and pictorial materials used in this report have been supplied by the Canadian Forces Detachment at Lockheed, Lockheed California Company, Litton Guidance and Control, Litton Systems Ltd. (Canada) and Canadian Marconi Co.

REFERENCES

1. "CP-140 Aircraft Detail Specification, Annex B," Lockheed Report LR 26662-1AB

2. "CP-140 Inertial Navigation System, Program Design Specification," Litton G&C Systems Document No. 403695, April 1980

3. R.W.H. Killer, "Precise Positioning of Sonobuoys Using AME and DME Techniques," Proceedings of IEEE Plans 76

4. "S.K. Jordan and G.N. Sherman, "Spatial Gauss-Markov Models of Ocean Currents," Transactions IEEE, Vol. AES-15, No. 6, Nov. 1979

5. D.F.H. Grocott, "Doppler Correction for Surface Movement," Journal of the British Institute of Navigation, Vol. 16, Jan. 1963

6. R.K. Moore and A.K. Fung, "Radar Determination of Winds at Sea," Proceedings IEEE, Vol. 67, No. 11, Nov. 1979

7. I.Y. Bar Itzhack and B. Poraf, "Azimuth Observability Enhancement During INS In-Flight Alignment," Technion, DDC ADR-038619, April 1979

8. J.W. Diesel, "Fundamental Accuracy Limitations in In-Flight Alignment of Inertial Sensors," Proceedings of IEEE NEACON 1979

9. R. Brown, G. Brolaugh, "An Application of Omega as a Sensor," Proceedings of IEEE Plans 76

10. J.E. Bergeson, "Experiences with the B-1 Navigation Filter," Practical Aspects of Kalman Filtering Implementation, AGARD Series, March 1976

11. A.J. Brockstein, "Preliminary Report on the Computer Program Performance Specification for the Long Range Patrol Aircraft," Litton GCS Internal Document 4JB-7409-060, Sept. 1974

12. J. Diesel, "Kalman Filter Equations for LN-33L Fine Alignment and Navigate Modes," Litton GCS Internal Memo JWD-7612-110, December 1976

13. Air Standardization Coordinating Committee, "The Specification and Evaluation of the Accuracy of Inertial Navigation Systems," ASCC AIR STD 53-11 (C), 15 March 1979

14. S.R. Ellms, M.W. Trawick, "Investigator of Inertial System Error Analysis Methods," Report No. NADC-AM-6663, 29 Dec 1966

15. L.L. Rosen, D.L. Harmer, "Inertial System Performance Evaluation," Third Inertial Guidance Symposium, CIGTF, HAFB, N. Mexico, 1966

TITLE: SLED TESTING OF THE MISSILE X ADP/AIRS SYSTEM

AUTHORS: ELDON PETERSON
CAPT ROBERT LAWRENCE

6585TH TEST GROUP
Holloman AFB, New Mexico

ABSTRACT

This paper describes some of the unique sled test methodology innovations being developed at the 6585th Test Group, Holloman AFB for systems testing on the Advanced Inertial Reference Sphere (AIRS). The extreme accuracy and sophistication of the AIRS System have been the driving force behind a series of hardware, software, and test philosophy improvements over the past two years. This paper summarizes our current state-of-the-art in sled test capability for high performance guidance systems such as the AIRS being used in the Missile X (MX) program. Many of the improvements, driven by MX requirements, are of a general nature and will be of interest to our other customers.

Specific results of the test program will not be presented in this paper due to classification. The paper will be restricted to a discussion of general findings and test techniques.

1. BACKGROUND

The Central Inertial Guidance Test Facility, more commonly known as CIGTF, has a long history of involvement in high accuracy guidance systems development. The 50,770 ft Rocket Sled Track at Holloman, which the CIGTF has used for the past twenty-five years, has been and continues to be one of the best tools for conducting dynamic tests of missile inertial guidance systems in a simulated operational environment.

As guidance system sophistication has matured, demands on the test facility capabilities and testing complexity have multiplied several fold.

Results on some recent high accuracy programs led the CIGTF to adopt a policy of taking a fresh look at our unique facility and how we conduct our test programs.

CIGTF has long been famous for its total "blue suit" unbiased evaluation of systems. This policy has not changed; however, implementation of this goal is much more difficult on complex systems such as AIRS.

Early in the test planning stages of the AIRS Dynamic Test Program, the program office, now the Ballistic Missile Organization (BMO), determined that conducting such tests would require the involvement of the entire MX guidance community. The MX Test Planning and Evaluation Team (TPET) was formed in 1978 as a planning committee of the MX Accuracy Working Group. Figure 1 shows the various government and contractor agencies who have been and continue to be part of TPET. This joint operation's philosophy has been very effective in putting together an integrated test program. This approach, as opposed to a total contractor responsibility or a total CIGTF in-house effort, will continue to be a viable management scheme for future programs. The remainder of this paper will concentrate on the sled test methodology developed by the TPET and the resulting facility improvements made at Holloman in preparation for the Advanced Development Phase AIRS Dynamic Test Program. This program is referred to in the remainder of this paper as the Dynamic Test Program or DTP.

2. ESTABLISHING THE ENVIRONMENT

In any type of dynamic operational test, establishing the test bed environment becomes a serious consideration if meaningful test data is to be obtained. Since we are trying to simulate and observe both the translational motion of a ballistic missile trajectory and the average characteristic flight vibration envelope, several complex interdependent factors come into play. The basic problem amounts to matching the spectral content of the sled vibration excitation to that experienced in flight and tailoring the sled profile to allow maximum observability of error model terms during the necessarily short duration sled run.

The MX DTP is utilizing an aluminum honeycomb type forebody. The AIRS IMU is mounted in the front section of this forebody with a specially designed fixture that permits precision case alignment during prerun calibrations. The IMU ball itself is isolated from the hardside of the forebody by two sets of isolators. The primary set is included as part of the test item itself.

JOINT TEST RESPONSIBILITIES
BEING USED ON MX PROGRAM

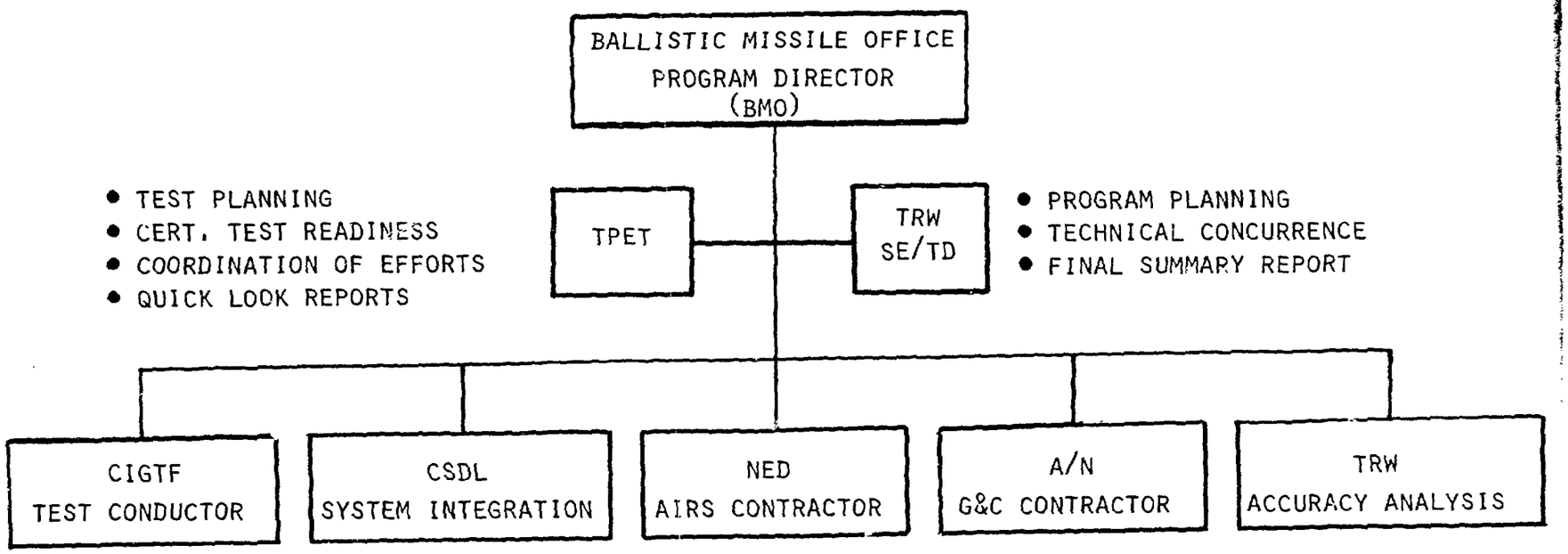

- TEST PLANNING
- CERT. TEST READINESS
- COORDINATION OF EFFORTS
- QUICK LOOK REPORTS

- PROGRAM PLANNING
- TECHNICAL CONCURRENCE
- FINAL SUMMARY REPORT

- TPET MEMBER
- TEST PLANNING
- FACILITY PLANNING
  TEST SITE INTEG
- SUPPORT HARDWARE
- SLED RUNS
- CENT. RUNS
- DATA PROCESSING
- POST-TEST ANAL/RPT

- TPET CHAIRMAN
- TEST PLANNING
- OVERALL TSE RESPONSIBILITY
  - ON BOARD EQUIP
  - TSE
  - SOFTWARE
- LAB PRE-INTEG.
- AIRS/SLED/CENT INTEG SUPPORT
- TEST SITE SUPPORT
- POST-TEST ANAL/RPT

- TPET MEMBER
- TEST PLANNING
- AIRS FAMILIARIZATION
- AIRS MAINTENANCE
- TEST SITE SUPPORT
- POST-TEST ANAL/RPT

- TPET MEMBER
- TEST ADVISOR
- FSED COMPATIBILITY
- TEST PLANNING

- TPET MEMBER
- TEST PLANNING
- TRADE STUDIES
- POST-TEST ANAL/RPT

FIGURE 1

These isolators are located between the outer sphere and the mounting case. These isolators are resonant at approximately 50 Hz and provide a significant attenuation of any high frequency excitation as evidenced in figure 2. The second set of isolators is designed to suppress predominant sled excitation in the region of 20-30 Hz by inserting an additional notch filter resonant at approximately 9 Hz. The resulting overall transmissibility, together with the sled excitation, results in a vibration spectrum input to the IMU ball itself shown in figure 2. As one can see, the resulting envelope has essentially the same shape as the predicted flight envelope. The flight data for figure 2 was provided by CSDL as a result of analysis on the MPMS program and should be a close approximation to that to be experienced in MX flights. Table 1 contains in tabular form the differences between sled and flight predominant vibration levels.

Several preliminary tests were conducted to establish the test environment. Preliminary pull tests of the isolators verified theoretical spring constants. Then an IMU mass simulator was interfaced to the sled fixture and a complete environmental laboratory vibration test was conducted. These tests resulted in data verifying the transmissibility and stiffness of the external isolators and sufficient information to predict the vibration energy input to the system. Figure 3 shows the mounting configuration of the AIRS/sled interface.

These results were verified by two sled runs using the mass simulator and several channels of tri-axial vibration transducers to measure the vibration on an actual mission. Figure 4 shows a CIGTF technician adjusting a HP 5451 Fourier Analyzer used to produce PSD plots used to verify the vibration environment. The results indicated that the input envelope was close to the expected value and was sufficiently attentuated at 50 Hz to minimize any double resonance effects. One of the problems which complicated this effort is the fact that there is no vibration transducer on the soft side of the internal isolators, so the final ball excitation must be predicted with theoretical internal isolator characteristics. Another secondary complicating effect is the softness of the springs required to provide the 9Hz resonance. This "softness" creates a significant translational motion ($\simeq$ .1"/g) of the entire system when subjected to the sled run trajectory. As will be pointed out in later sections, this necessitated mounting six linear variable displacement transducers (LVDTs) between the hardside and softside of the sled to dynamically record any sled forebody relative displacement during the run.

The other critical environmental input during the sled test is the actual translational motion run profile. This test series utilized the AJ-10 acid engine. The thrust profile and water brake profile were carefully chosen to maximize observability of expected error terms. Several operational factors also influenced the final profile chosen as shown in figure 5. One of these was the desire to separate the forebody from the pusher to simplify post run recovery operations. The acid engine problems which complicated the MPMS/AIRS Sled Test program were solved and the reliability of the acid engine to provide smooth, repeatable performance was verified on six runs conducted before the first data run.

VIBRATION LEVELS

AIRS				
	HARD SIDE		SOFT SIDE	
	g^2	g_{rms}	g^2	g_{rms}
SLED				
HARD SIDE				
10–25 Hz	0.2	0.4	0.1	0.3
25–2000 Hz	67.0	8.2	8.0	2.8
TOTAL	67.2	8.2	8.1	2.8
SOFT SIDE				
10–25 HZ	0.02	0.1	0.05	0.2
25–2000 HZ	2.37	1.5	0.56	0.7
TOTAL	2.39	1.5	0.61	0.8
FLIGHT				
10–2 HZ	0.1	0.3	0.1	0.3
25–2000 HZ	162.8	12.8	3.67	1.9
TOTAL	162.9	12.8	2.77	1.9

TABLE 1

SLED AND FLIGHT VIBRATION ENVELOPE

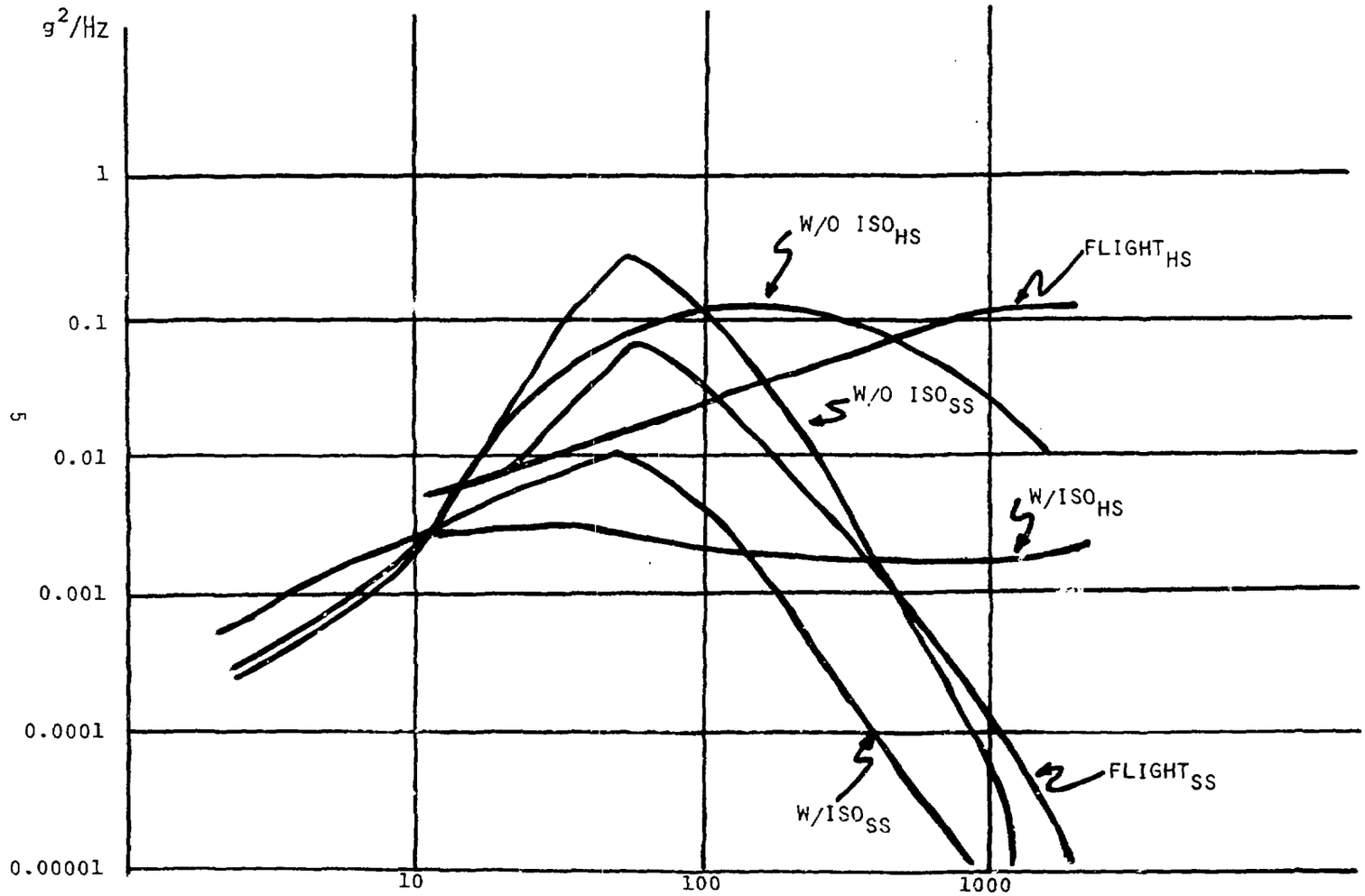

FIGURE 2

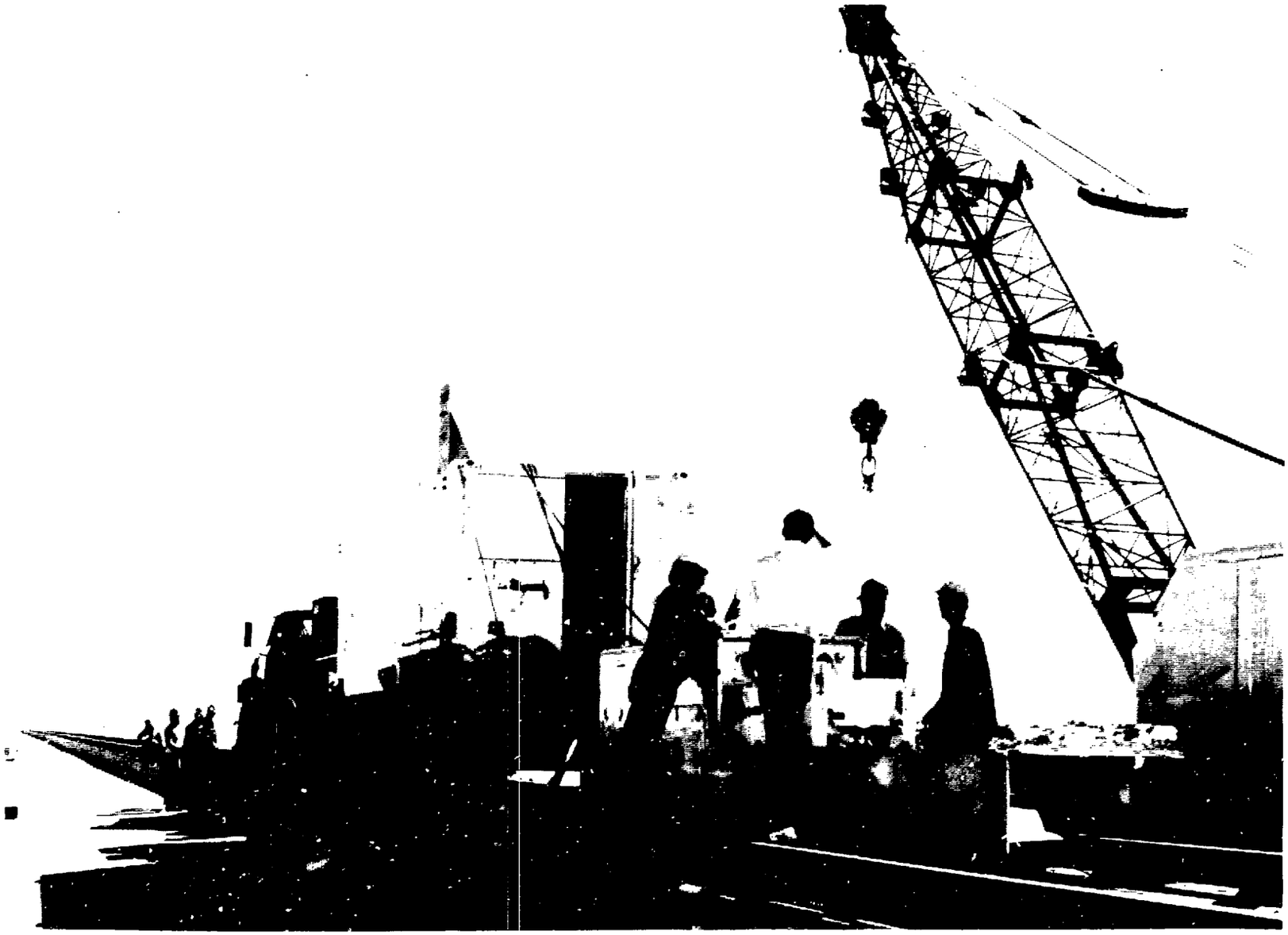

FIGURE 3. AIRS MOUNTING CONFIGURATION

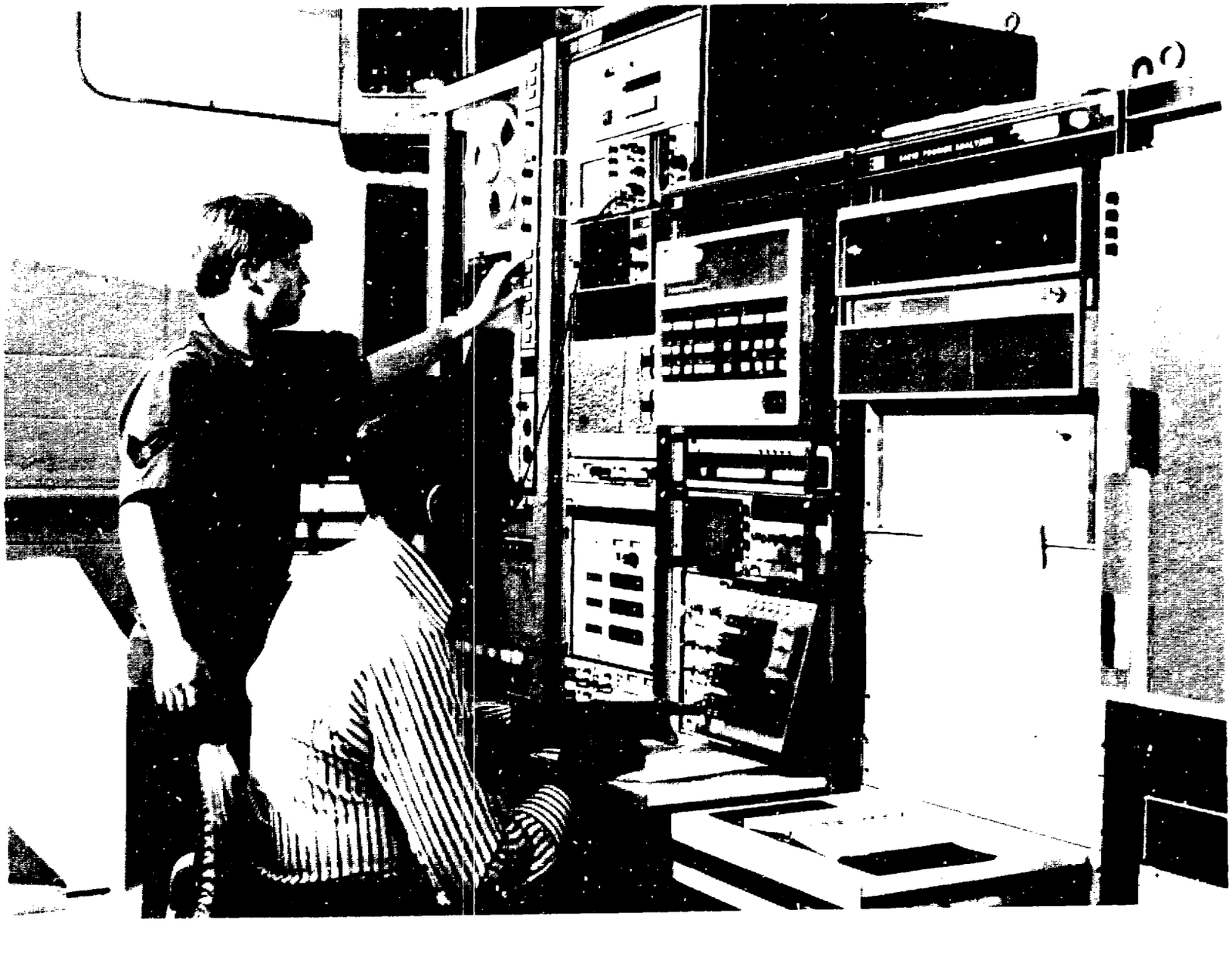

FIGURE 4. FOURIER ANALYZER

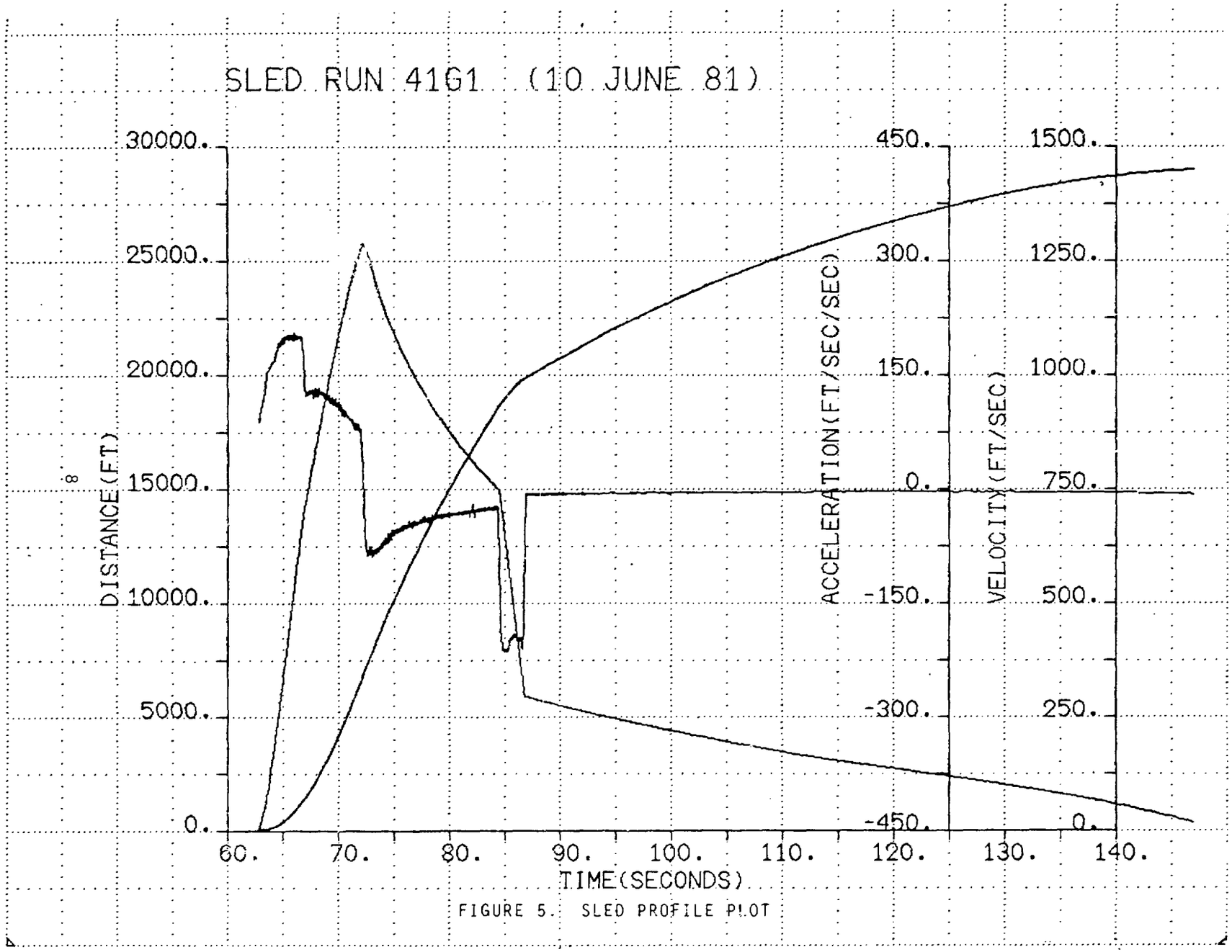

FIGURE 5. SLED PROFILE PLOT

3. TEST SUPPORT EQUIPMENT

A significant effort was put into the development of test support equipment for this program. This was due primarily to the cycle of evolution the AIRS was at when the program began. All of the other ADP equipment was designed strictly for laboratory type testing. To test the AIRS in the dynamic sled environment required the development and fabrication of several support subsystems. Many of these subsystems are shown in figure 6.

The foremost task was the development of the Test Processor. This processor interfaces to the IMU in much the same way as the MECCA processor will during the MX operational phase. It performs many of the same functions; however, it does not contain a navigational algorithm. The Test Processor design was developed by the Charles Stark Draper Laboratories (CSDL) and approved by the TPET during early design TSE reviews. It consists of a multiple microprocessor "Federated" architecture system designed to perform System Mode Control, data acquisition and formatting, and IMU safing.

The Test Processor, which is mounted below the system interface on the sled, was not designed to perform any calibration processing. This is accomplished with a data link to a Systems Engineering Lab (SEL) Model 32/55 minicomputer system via an Interface Control Console (ICC). The ICC allows either manual or computer control of system moding and provides a buffered data interface to the SEL. Both the ICC and SEL computer are located in the blockhouse some 400 feet away from the launch pad.

AIRS required the development of several new power subsystems. Both ground and sled power systems were developed. These systems feature computer control, failsafe overrides, and remote safing, as well as flexible changeover circuitry to provide glitchless power to all systems during the various phases of the test.

The AIRS system is cooled with a circulating R-12 heat exchanger system. Appropriate coolant supplies were designed and built up to provide this function on the pad, on the sled, and in the recovery van. These supplies, as well, were designed to minimize any changeover transients. The various coolant systems range from a simple controlled flow offboard dumping system used during the sled run, to a conventional closed loop recirculating system used on the pad, to a non-conventional recycling system used on the recovery van.

Another important category of test support equipment requiring considerable effort was the data acquisition interface. The entire integrated data acquisition system was designed to provide a wide variety of data products during all phases of the test.

Figure 7 shows the complex data interfaces present in the test sled setup. The SEL data products consist primarily of calibration and alignment results. To aid in processing the complex filter algorithms, a second SEL computer is located off site to batch process intermediate calibration results. The remainder of the data products are produced by the CIGTF data acquisition systems which range from analog sledborne recorders to real time PCM

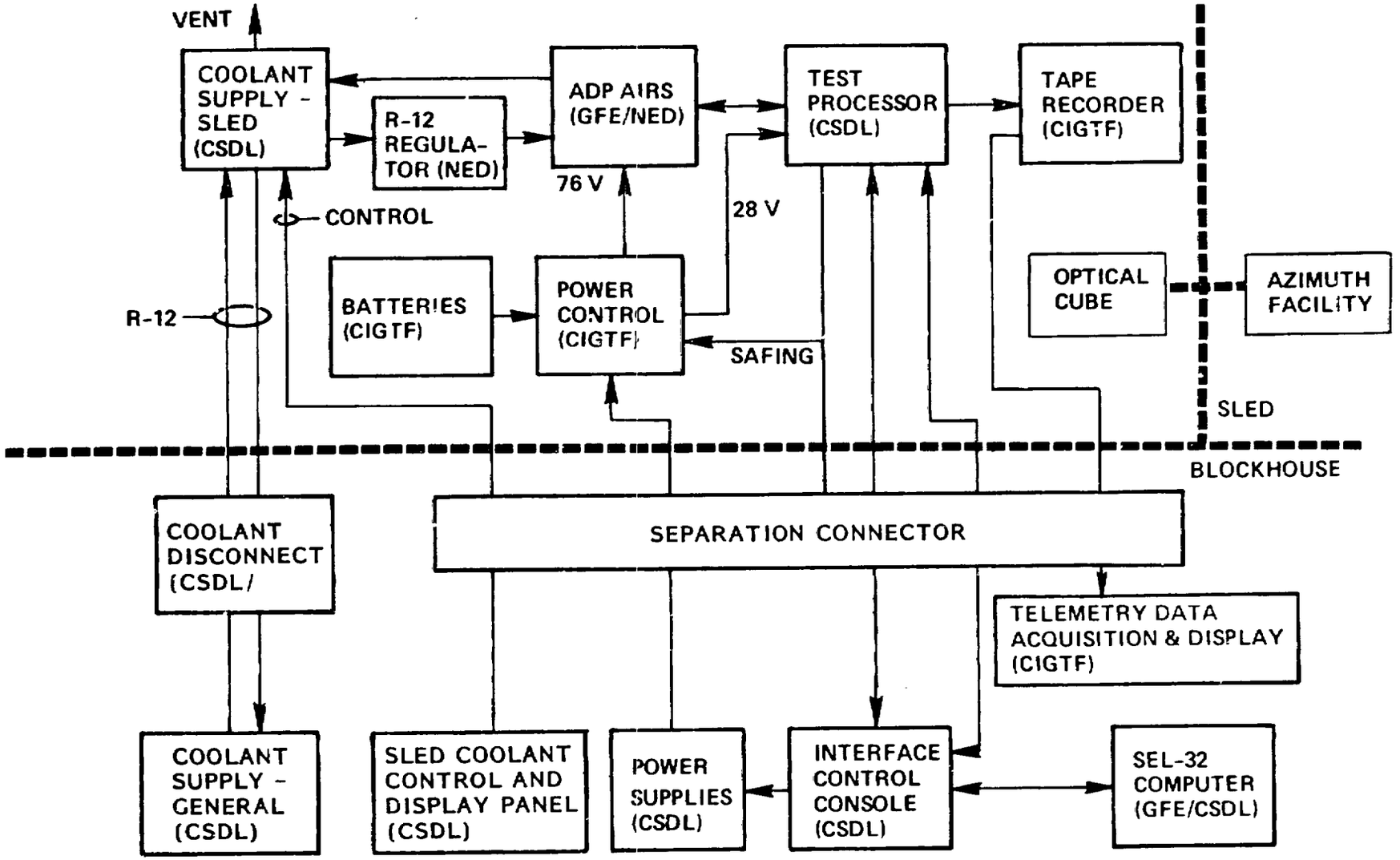

Figure 6. AIRS Dynamic Test—simplified block diagram, sled/blockhouse.

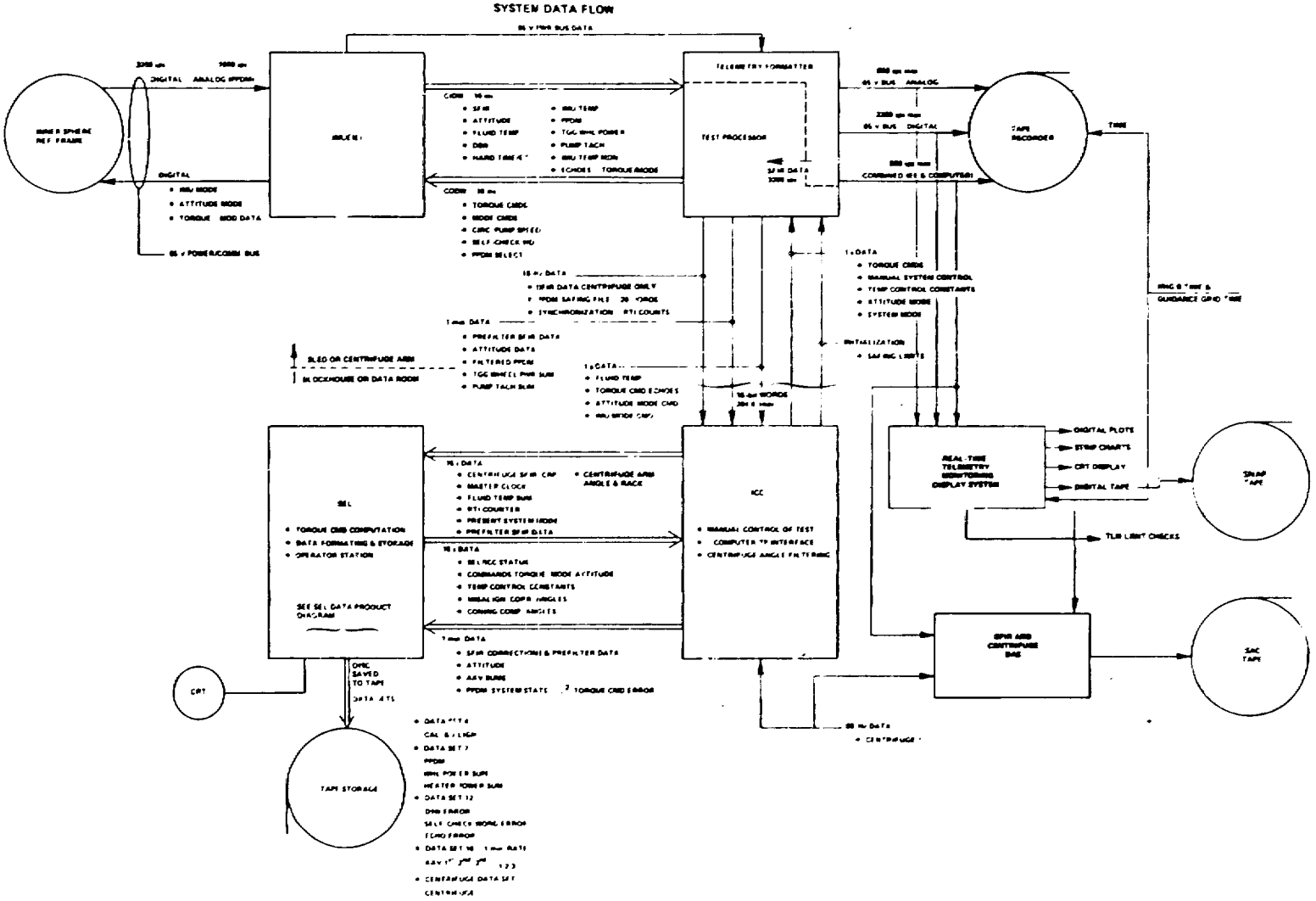

Figure 7. System data flow.

decommutation and display systems. One of the most useful pieces of equipment being used for the first time during this program was the Digital Programmable Analysis and Display (DPAD) System built by the Conic Corporation. These DPADs (see figure 8) provided the core of the real time PCM display capability. In the past we have had to rely on hardware decommutation or dedicated computers for this function. This microprocessor based instrument provided the capability in a small easily programmed subsystem. We also found that these systems complemented our Hewlett-Packard Real Time minicomputer system in providing versatile prelaunch countdown data display.

Another new Test Support system developed since the last major sled program is the Sled Test Analog Reformatting System (STARS). This is a new data reformatting system which reads back sled analog data and produces a computer compatible data file. This system is an up-to-date replacement for the General Input Converter II (GIC II) which had been in use at Holloman for several years. The STARS has the capability to reformat not only space time data, but various system analog and PCM signals. It has several built-in self-validation features not possible with the older GIC II equipment.

4. BLOCKHOUSE IMPROVEMENTS

The testing done on the Missile Performance Monitoring Systems (MPMS) in 1978 pointed out several problems in our blockhouse launch capability. Some of these problems were the results of gradually deteriorating facilities and others were due to the ever increasing complexity of system under test and resultant facility demands.

Shortly after the MPMS program was completed, the 6585th Test Group embarked on an emergency renovation program for the Alpha Blockhouse Facility. This effort culminated in April of 1981 with the dedication of an enlarged and modernized facility.

Alpha Blockhouse now has the capability of supporting sophisticated test demands of programs such as MX with adequate air conditioning, dust control, 40 KVA of uninterruptible power, three standby diesel generators, and a new 15 x 40 foot computer room exclusively for customer furnished ground support equipment. Several other improvements have been made in blockhouse communications, real time data display, and contractor working areas. Figure 9 shows a CIGTF technician testing one of the new dual backup uninterruptible power systems (UPS) in Alpha Blockhouse.

5. POST RUN HOT CALIBRATION

This is the first high accuracy inertial guidance program where we have attempted to perform a post run calibration without an intermediate power down. This requirement has been the driving force behind a completely new test technique where we recover the sled shortly after it stops, establish test support functions via a support van, pull the sled back to the blockhouse, transfer back to the blockhouse computer based test support equipment, and finally perform the post run calibration on the SEL computer.

The heart of this new capability is a 10-ton diesel tractor with a semi-trailer, both converted to ride on the sled track. The tractor is called the Low Speed Prime Mover (LSPM) and the trailer is called the Recovery Support Van (RSV). When coupled to the MX forebody, the entire train can safely travel at speeds up to 30 MPH. This approach was chosen, not only to provide the recovery capability, but to provide the capability of slow speed tests of MX and other systems in the future. The entire sequence of launch, recovery, pull back, and calibration is performed within two hours.

The RSV contains the required power, cooling, air conditioning, and data acquisition systems to support AIRS during the recovery phase. A throttled freon chiller is used on the van for maximum reliability. Environmental consideration precluded dumping this much R-12 into the atmosphere so a secondary reclaiming system is used to recompress the freon into a second tank until it can be properly disposed.

The new slow speed test support equipment is sure to become a key part of future sled test programs. Figure 10 shows the LSPM and RSV being mounted on the track during a recovery operation.

6. PUSHING THE SPACE-TIME REFERENCE TO THE LIMIT

The accuracy of the space-time reference provides the capability to perform a quantitative performance evaluation of the AIRS guidance system. The maintenance and improvement of the reference accuracy are dependent upon three sets of measurements:

a. Defense Mapping Agency (DMA) Survey: This is considered the reference standard, and defines the distance between Interrupter Control (IC) Benchmarks (nominal 2600 feet). This survey is performed periodically, and DMA has established a data base which extends from 1975 through 1981 with accuracy to about 1.24 PPM over a nominal interval. Also the track azimuth (Fiducial line) is surveyed by DMA to less than 1 arc-second.

b. Laser Interferometer Survey: This measures each interval between all interrupters, nominally 13.0 and 4.33 feet. The interrupters located adjacent to the IC benchmarks are adjusted to be exactly at the IC position using the DMA survey as a reference. Analysis is performed using the DMA and laser data to generate a Position Vector of the sled run. It is expected that a Laser survey will be performed prior to each sled run, weather permitting, to provide the most accurate Position Vector possible for each test. A rough measure of the reproducibility of the survey data is given by the fact that the sigma of the residuals of 7294 interrupter locations from their respective averages is about 0.274 milli-inches or about 1.75 PPM of a nominal 13.0 foot interval. Figure 11 shows Test Track personnel setting up the laser interferometer survey equipment.

c. Space-Time Measurements: These are made as the sled proceeds down the track during the sled run. Specific sensing heads, which generate pulses from interrupter passage, have been selected for the DTP based on past performance and lab tests.

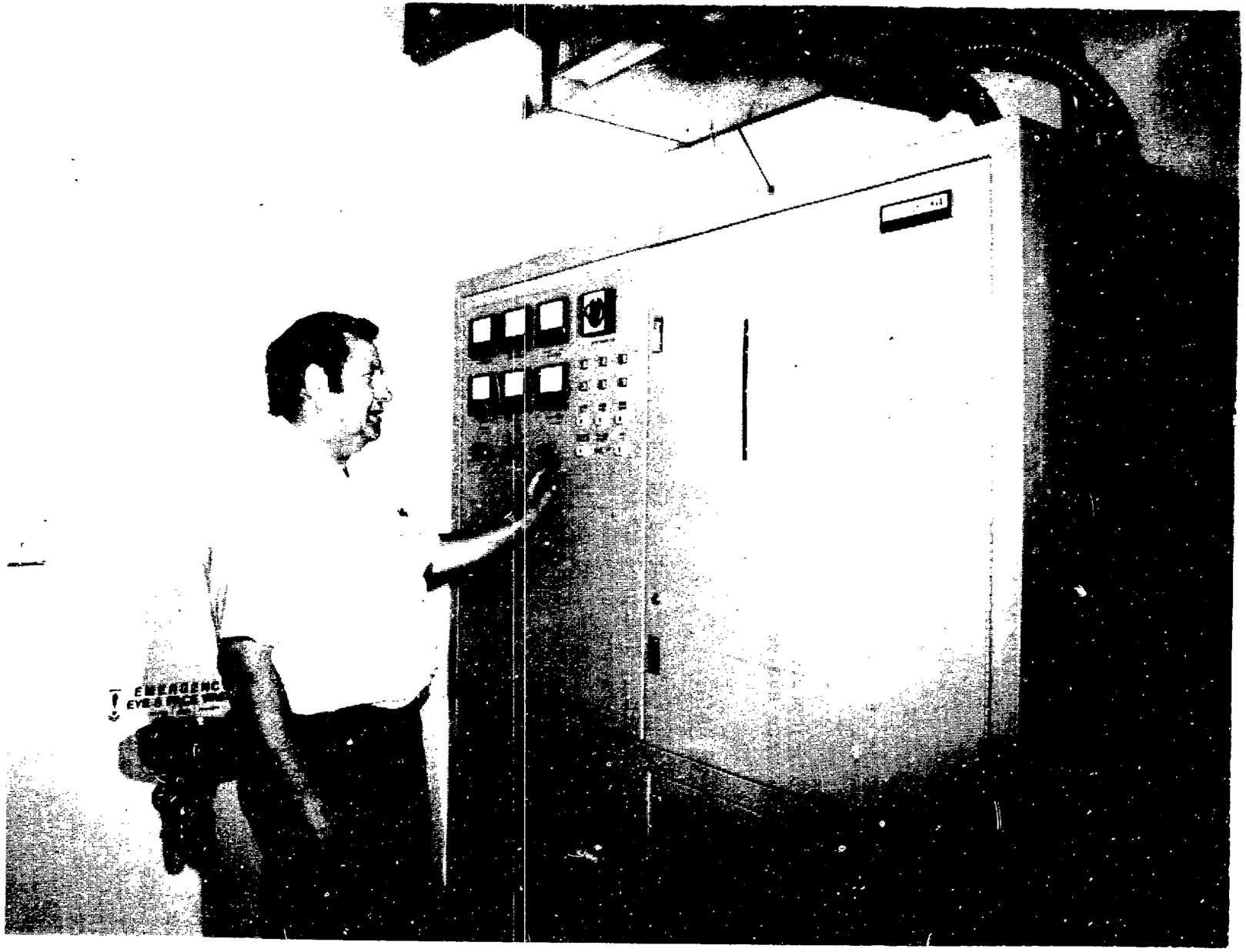

FIGURE 9. DUAL UPS SYSTEM

The sledborne reference time base has been upgraded and modified so its performance can be observed. This is critical when reducing the data recorded on the sled analog recorders by the STARS.

The accuracy of the space-time reference during earlier sled tests is shown in Table 2. The following improvements have been, or will be, made to increase the accuracy:

a. DMA is required to survey the track azimuth to less than 1 arc-sec.

b. Laser survey and analysis techniques allow a full track survey (35,000 ft) prior to each sled run.

c. Interrupter density will be increased a nominal 4.33 ft for the first 35,000 ft of track.

d. Time correlation of reduced data will be accurate to less than 0.001 PPM.

The space-time accuracy improvement is an ongoing effort at CIGTF to perform a quantitative performance evaluation of guidance systems with high accuracy requirements.

7. TIME CORRELATION OF DATA

The time correlation of data is the method in which reference space time data is correlated with AIRS data. The problem arises because the AIRS and reference clocks are different, both having different scale factors and asynchronous origin times. This problem caused considerable difficulty in earlier programs. A new technique has been developed for the DTP. The basic procedure is to align the space-time data using a flight mode entry discrete (FIMK) generated by the guidance system. This discrete can then be associated to a specific PCM frame relating to system flight mode entry.

The system (AIRS) data is digitized with respect to the RTI (AIRS reference) clock, 10 msec nominal interval. A software counter in the PCM data correlates each PCM frame with cumulative RTI counts. The PCM data can then be associated with the FIMK discrete relating to a specific RTI count. The AIRS time grid is a nominal 1 second period square wave which originates at the occurrence of FIMK. It changes state every 50 RTI counts and is used to calibrate the AIRS clock and time correlate data to system flight mode entry.

The space-time, AIRS time grid, and cesium reference clock are processed by the STARS (ETR mode) with the origin time arbitrarily set to precede computational zero (FIMK) by a few milliseconds. The STARS is used to digitize the data using the 100 KHz sled reference clock recorded on the analog tape to compensate for tape speed errors. The reference clock scale factor and run stability are determined using the cesium standard 1 second square wave, recorded on the analog tape which is transmitted to the sled via the ITS line. In summary, the space-time and AIRS time grid data are corrected for reference clock errors and VCO delays to allow the FIMK event time to be subtracted from the space-time event times to reference the space time origin to system flight mode entry

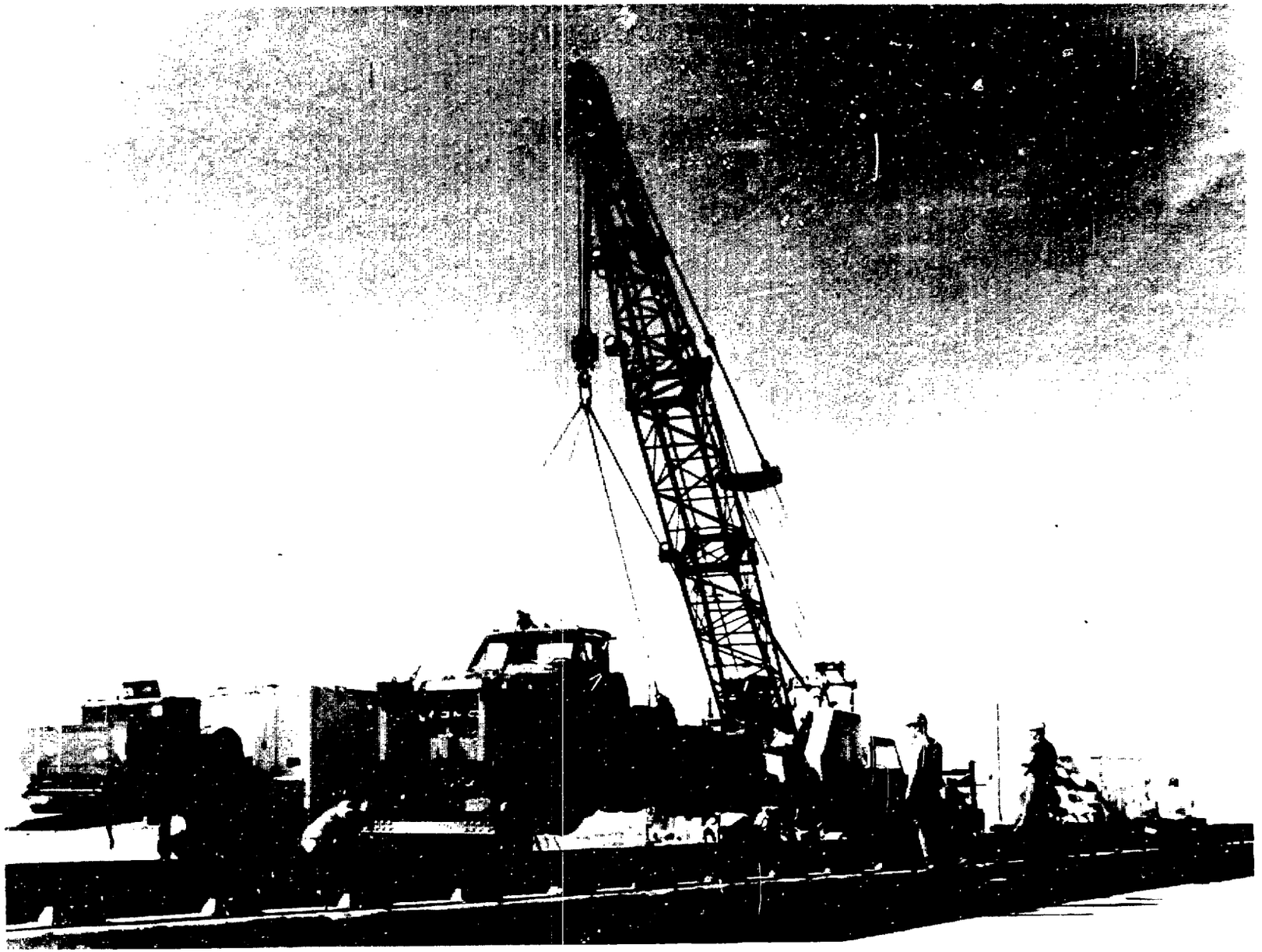

FIGURE 10. RECOVERY SUPPORT VAN

FIGURE 11.
LASER INTERFEROMETER REFERENCE SURVEY

SPACE TIME REFERENCE SYSTEM ACCURACY				
DIRECTION	POSITION (FT)			VELOCITY (FPS) 0.5 Hz
	SHORT-TERM (13 Ft Interval)	MID-TERM (2600 Ft Intervals)	LONG-TERM (35000 Ft Interval)	
DOWNTRACK	0.006	0.005	0.031	0.004
CROSSTRACK	0.009	0.008	0.059	0.010
VERTICAL	0.009	0.008	0.023	0.008
AZIMUTH <1.5 ARC-SEC				

TABLE 2

as shown in figure 12. The end result is a timing system providing microsecond accuracy and correlation during the dynamic test. The LVDT data which measures the system pallet motion with respect to the sled is also processed with the AIRS time grid to align to system flight mode entry.

8. ANALYSIS

The majority of the test objectives will be verified by analysis. This will be performed in the distance and velocity domain for both the platform and track coordinate frame. Specific error signatures will be verified and unanticipated errors modeled to determine system performance.

The data taken during pre-and post-run, while the AIRS is in a static environment, will be used to determine an accurate estimate of such quantities as platform tilt and drift. This will serve to help diagnose anomalies during the dynamic part of the sled run. The analysis for the dynamic part of the run will utilize models developed for specific errors. The primary driving function for the models will be downtrack distance, velocity and acceleration.

The system data will be corrected for the following errors:

a. Servo Driven Member-to-SFIR misalignment
b. Gyro fixed G and G^2 drift rates
c. Gyro float motion
d. SFIR bias and scale factor
e. SFIR FI1 and FX1 nonlinearities
f. Platform with respect to inertial space rate
g. Pallet with respect to sled motion

These errors will be determined using pre-run coefficients and dynamic run measurements.

Therefore, analysis based on two or more sled runs should verify the test objectives and possibly uncover new errors produced from the dynamic environment of the sled run.

9. CONCLUSIONS

As this paper reached the publishing deadline, three successful DTP tests had been accomplished at Holloman. The results obtained from these tests lend ample evidence to the desirability of conducting a well planned sled test program before flight testing begins.

10. ACKNOWLEDGMENT

The advances reported in this paper are the result of outstanding work done by the entire MX Guidance community. The CIGTF gratefully acknowledges those contributions made by the various contractors and government agencies which are reported herein.

SYSTEM/REFERENCE TIME CORRELATION

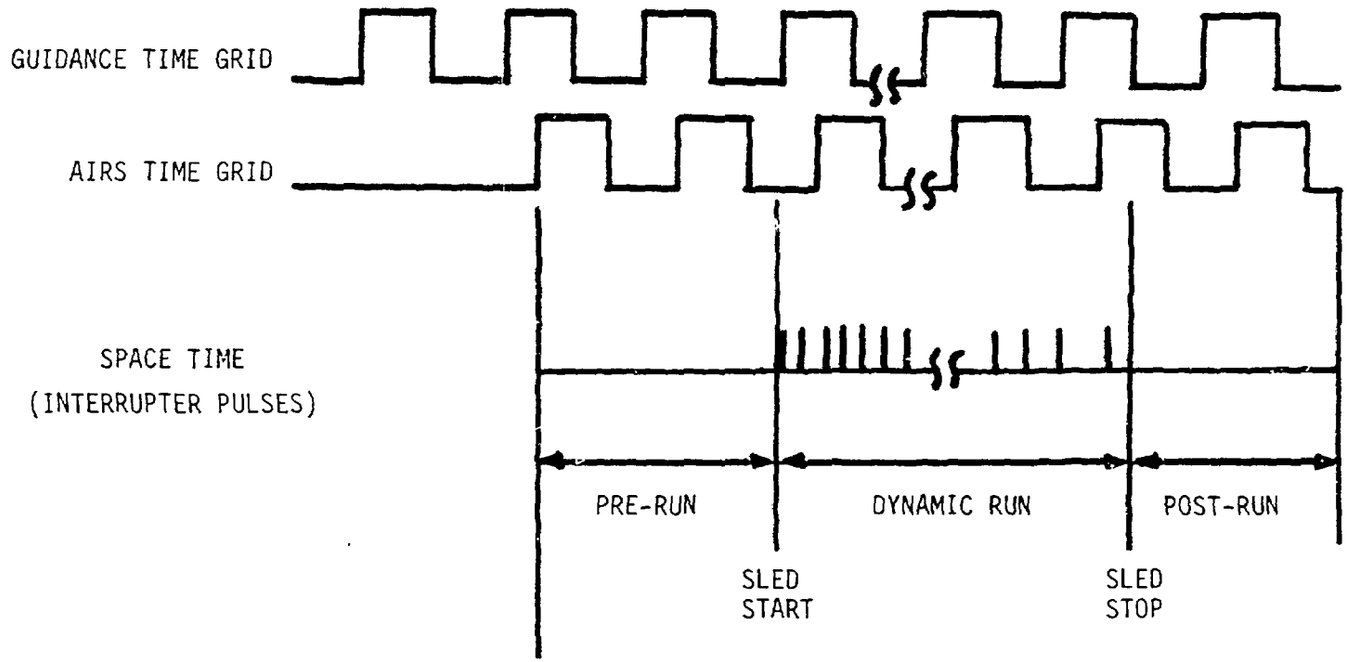

FLIGHT MODE ENTRY (CO)

FIGURE 12.

TITLE: PRECISION CENTRIFUGE TESTING USING AN ACCELERATION REFERENCE STANDARD

AUTHOR: KURT E. STEINKE

SUNDSTRAND DATA CONTROL, INC.
Redmond, Washington

PRECISION CENTRIFUGE TESTING USING AN ACCELERATION REFERENCE STANDARD

by

Kurt E. Steinke
Design Engineer
Instrument Division

The author is indebted to Joe Hunter, Guidance and Control, Army Missile Command, and Norm Klein, Instrument Division Director of Engineering, Sundstrand Data Control, for their pioneering work in this approach to precision centrifuge testing.

PRECISION CENTRIFUGE TESTING USING AN ACCELERATION REFERENCE STANDARD

SUMMARY

This paper describes an extremely accurate automated centrifuge system. Absolute accuracy capability of the system with data reduction techniques presently in use is below 50 ppm and repeatability is less than 5 ppm. A reference accelerometer centrifuge system is very simple and cost effective compared to a speed measurement centrifuge system for a given accuracy, since many significant equipment errors are reduced or eliminated. Calibration of the reference accelerometer system to allow correction of observed systematic errors will result in further significant improvements in accuracy.

FUNDAMENTALS OF CENTRIFUGE TESTING

The primary utility of a centrifuge is due to the property that it can provide a quasi-static high level of acceleration. This property can be useful for testing accelerometer parameters such as scaling, linearity, range, hysteresis, and sensitivity to cross-axis acceleration. To be useful for such testing, the acceleration at the accelerometer under test must be known to a very high degree of precision.

Any point on the arm of a centrifuge experiences an acceleration of $R\omega^2$ toward the axis of rotation, where R is the radius of the point from the axis of rotation and ω is the speed of rotation of the arm in radians per second. Centrifuge speed is calculated from the time per revolution, or from counting pulses from a high resolution encoder attached to the centrifuge axle during a predetermined time interval. It is seldom practical to determine the radius at the center of mass of the seismic element of the accelerometer under test by direct measurement to better than 1000 ppm. The radius is normally determined indirectly by spinning the accelerometer under test at a low enough speed that the acceleration it sees may be determined based on its scaling from calibration in a 1g field. With acceleration known for one centrifuge speed, the radius may be calculated.

The measurement technique discussed herein is a logical extension of the latter method. It is based on the principle that the ratio between acceleration levels at any two points on the centrifuge arm is a constant, independent of centrifuge speed, equal to the ratio of the two radii. If a second accelerometer is placed on the centrifuge arm as a reference at a short radius arm

so that it remains within its calibration range, and the ratio between the acceleration levels (radii) at the two instruments is determined by a measurement at low acceleration, high acceleration levels may then be calculated by multiplying the acceleration at the standard times that ratio.

DESCRIPTION OF THE CENTRIFUGE SYSTEM

The operation of our centrifuge test facility (see Figure 1) is largely automated. The centrifuge itself is driven by a DC motor which is speed controlled by an analog servo with tachometer feedback. It was modified for computer control by using a digital-to-analog converter to provide a reference signal to the speed control amplifier. The reference accelerometer is mounted on a 10-inch radius, and the accelerometers or units under test (UUT) are mounted on radii of approximately 30 inches. The reference accelerometer and the accelerometers under test are monitored by one of two identical voltmeters selected for maximum repeatability in this application. A scanner is used to switch one voltmeter sequentially to monitor each of several instruments under test. An HP9825 computer reads the voltmeters, adjusts the centrifuge speed to achieve the desired output of one accelerometer, controls the scanner, and reduces the data. Program and data storage is on a floppy disk.

Acceleration Standard

The primary consideration in selection of an acceleration standard is extreme repeatability. Our system uses a Sundstrand Q-Flex (an instrument which exhibits virtually no mechanical hysteresis and which has a very tightly constrained proof mass) in a temperature controlled oven.

Although placing the reference accelerometer on a shorter radius (10" vs. 30") largely compensates for its nonlinearity (90% of the second-order coefficient, and 97% of the third-order coefficient), its nonlinearity has been measured to be less than 35 ppm and averages about 9 ppm over the 13g range it sees in our system (see Figure 2). This is the most significant systematic error in our centrifuge system. The reference accelerometer is calibrated every six months against a transfer standard (see Figure 3).

Voltmeters

Repeatability again is the primary consideration in selection of voltmeters for this application. In order to avoid errors induced by speed drift of the centrifuge, it is necessary to

measure the output of both accelerometers simultaneously. As the centrifuge was originally set up, this was accomplished by comparing the two signals using a Fluke 895 differential voltmeter in the ratio mode. This method was not suited to automatic data acquisition. Several different voltmeters were evaluated in this application and compared with the original ratio method. Repeated runs were made on the same accelerometer with each type of voltmeter. The second-order coefficients were calculated for each run, and their mean and standard deviation were calculated for each type of voltmeter (see Figure 4).

It is apparent that there are systematic linearity differences among the various types of instruments evaluated for this application. For the instruments chosen, this characteristic nonlinearity is less than 16 ppm and typically 6 ppm. This is the only significant systematic error besides nonlinearity on the reference accelerometer on our centrifuge. Relatively high levels of noise on the signal lines made it necessary to use whatever input filtering mode was provided on each voltmeter. Instruments with analog filters on their inputs (Fluke, Dana) exhibited approximately three times better repeatability than those with digital filters (HP, Guildline). Dana 6000's were chosen because of their excellent repeatability and the correlation with the previous method. This selection should not be considered final for a new application, since neither Fluke's, HP's, nor Datron's newest meters have been evaluated.

DATA ACQUISITION AND REDUCTION

The outputs of the reference accelerometer and the accelerometer under test are measured simultaneously, triggered by the computer. Thirty-eight sets of readings are taken (this requires about 10 seconds) and averaged at each data point. Data is reduced automatically by the computer. The system is capable of calculating nonlinearity as deviation from an extrapolated low g-level measurement, but this effectively bases the scaling of the run on a single measurement. Greater repeatability is achieved by fitting polynomials to the data, which reduces the effect of data scatter (see Appendix A). The polynomials may then be scaled to the known $\pm 1g$ scale factors of the units under test. The system is capable of providing a highly accurate polynominal characterizing the tested accelerometer or of generating corrections to the $\pm 1g$ scale factor and null offset to provide a best-fit straight line over any portion of a $\pm 40g$ range.

Polynomial curve fitting is an excellent tool for measuring cross-axis sensitivity to acceleration. Ordinarily it is very difficult to separate the effect of cross-axis sensitivity from

that of axis misalignment. The usual technique is to rotate the accelerometer under test for a zero g output at low acceleration to eliminate axis misalignment. This must be done by trial and error and is both difficult and time consuming. The accelerometer is then spun to the test level and the cross-axis sensitivity is measured. The test is ambiguous at best, since the accelerometer can always be rotated to give a zero g output at any given acceleration level. For a linear accelerometer, axis misalignment is simply the first-order term of a polynomial fit to the data, and cross-axis sensitivity is the sum of the higher order terms.

SYSTEM ADVANTAGES

The reference accelerometer centrifuge system offers significant merit in comparison to a speed measurement centrifuge system in terms of measurement accuracy and system complexity.

In the reference accelerometer system, the test acceleration is exactly proportional to the acceleration experienced by the reference accelerometer. In a speed measurement system, the test acceleration is proportional to the square of the centrifuge speed. Thus for a given measurement resolution, the reference accelerometer system offers an inherent 2:1 improvement in accuracy of acceleration determination, since the speed measurement (plus its error) must be squared.

Control of the centrifuge speed in a reference accelerometer system is much less critical than in a speed measurement system. Speed drift contributes to an error in the speed measurement centrifuge system, since the square of the average speed is not exactly equal to the average of the speed squared during the measurement interval (a 1% speed drift contributes 33 ppm error). Furthermore, a speed measurement system normally requires that two different types of instruments be used, a voltmeter to measure the output of the accelerometer and a frequency meter or counter to measure speed. It is difficult to make measurements over exactly the same time interval with different types of instruments. If the measurement intervals are not exactly coincident, speed drift will cause a difference in average acceleration levels at the instrument under test between the time intervals during which the speed is measured and during which the output of the accelerometer is measured. Since the measurements of the outputs of the reference and the accelerometer under test are proportional and can be made over exactly the same time intervals, speed drift errors are virtually eliminated.

The reference accelerometer system has a distinct advantage in that the same type of measurements are made on the same type of

signals using the same type of instrument. Since identical meters may be used, there is a much greater tendency for environmentally induced reading errors to track and cancel.

The reference accelerometer system automatically compensates for stretch of the centrifuge arm as acceleration levels increase, since both accelerometers experience the same effect.

SYSTEM PERFORMANCE

Except for the characteristic nonlinearities associated with the reference accelerometer and voltmeters, the absolute accuracy of the reference accelerometer centrifuge system approaches the accuracy to which the ±1g scale factor can be determined. Relative accuracies are, of course, much higher. Repeatability of the second order coefficients generated in subsequent runs on the same accelerometer is less than $\pm 0.2 \mu g/g^2$ (equivalent to characterizing the accelerometer to within 1.6 mg at 40g's). Differences between non-linearity measurements from run to run (differences between deviations of the raw data from the best-fit second-order curves generated by the system) are less than 5 ppm and typically 2 ppm of the input acceleration.

The extreme repeatability of this system suggests that characterizing and compensating for systematic nonlinearities would significantly improve the system accuracy. High linearity of the reference accelerometer is a convenience in data reduction, but is not a necessity in a system in which that function is automated, as long as the nonlinearity is known. Nonlinearity of the reference accelerometer may be characterized to within 3 ppm. Since the voltmeters see virtually proportional signals, their nonlinearity could be characterized to about 1 ppm automatically by using fixed precision voltage divider and a programmable voltage source. Simple modification of the data reduction program to correct for these effects would achieve accuracies below 10 ppm.

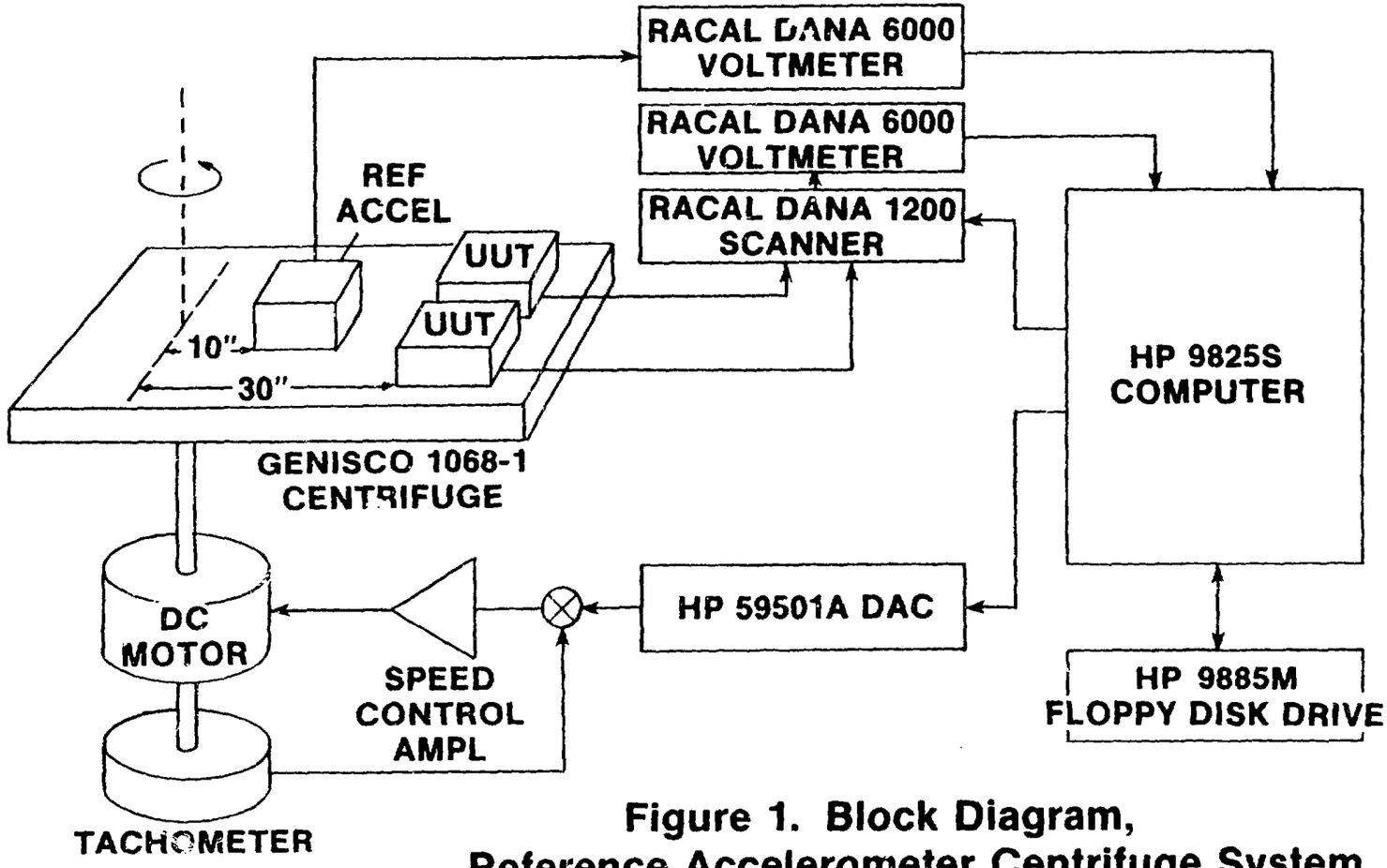

Figure 1. Block Diagram, Reference Accelerometer Centrifuge System

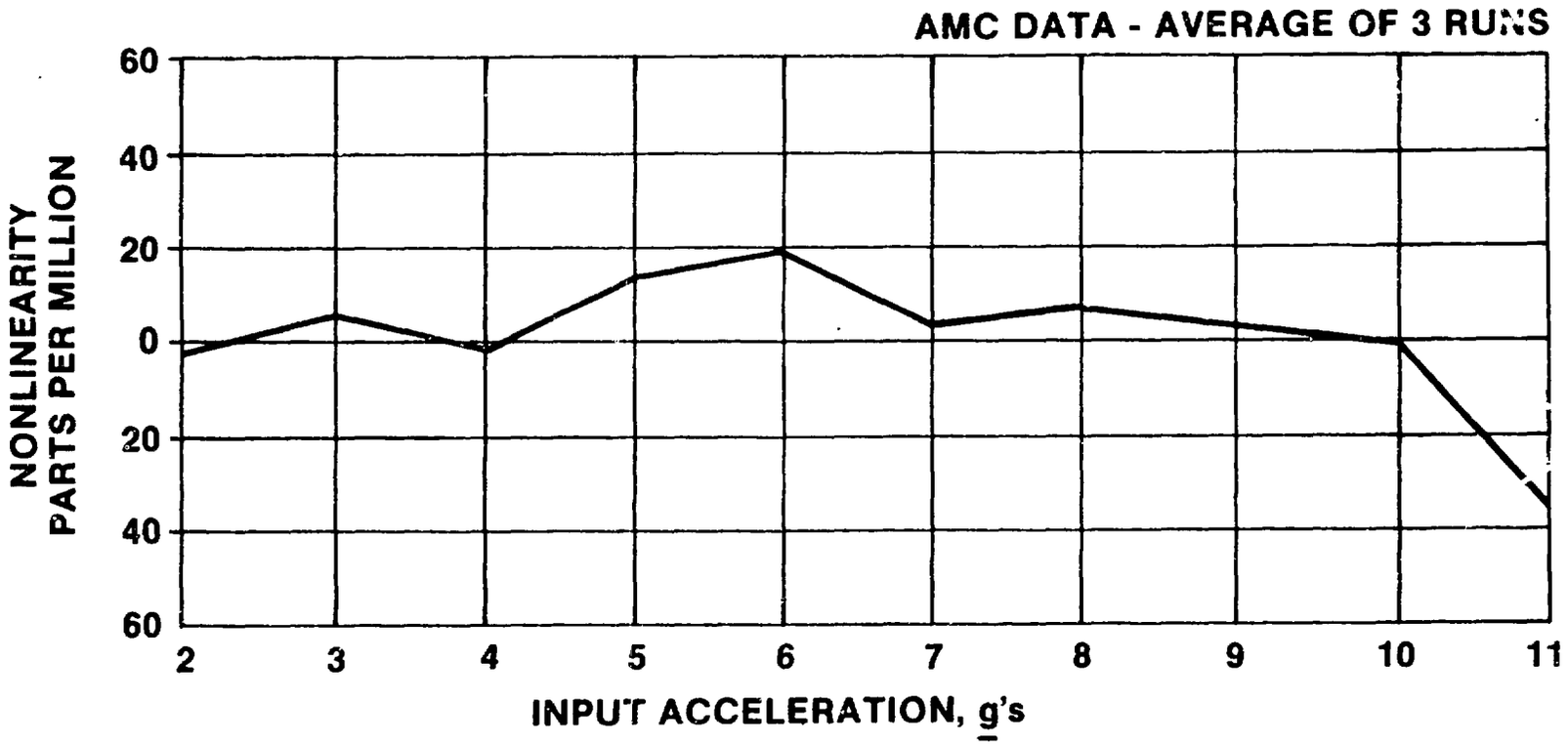

Figure 2. Average Linearity, Sundstrand Q-Flex Reference Accelerometer SN E-1

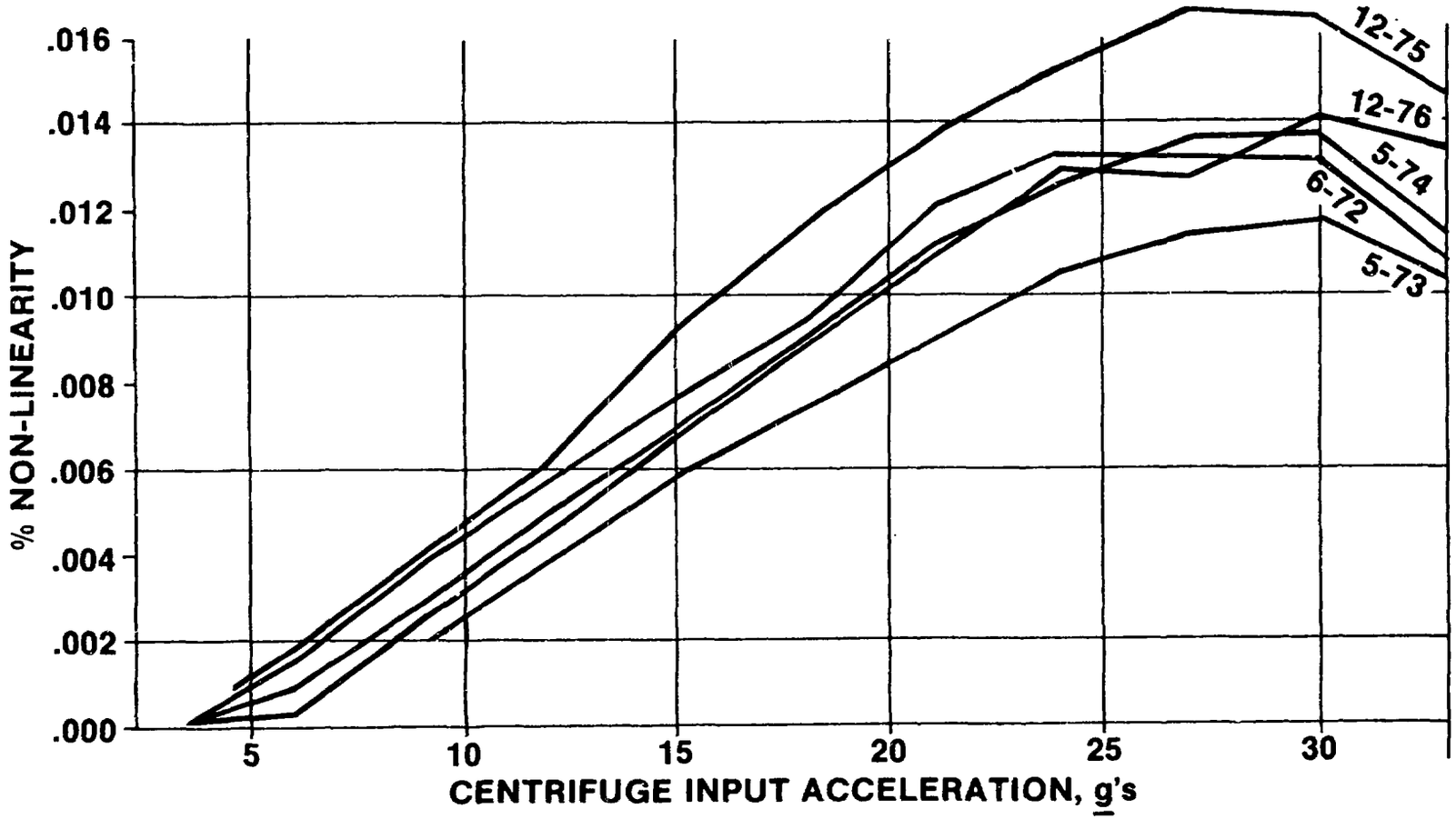

Figure 3. Long-Term Linearity Repeatability, Sundstrand Q-Flex Reference Accelerometer SN E-1

	MEAN 2ND-ORDER COEFFICIENT	STANDARD DEVIATION
A. Fluke 895, Ratio Mode and Fluke 8502A for V_T	1.75	.24
B. HP 34SS A, Simultaneous	.87	.70
C. Fluke 8502A, Ratio Mode	2.90	7.23
D. Fluke 8502A, Simultaneous	3.13	.08
E. Dana 6000, Simultaneous	1.45	.10
F. Guildline 9576, Simultaneous	2.54	.37

Figure 4. Digital Voltmeter Evaluation Data

APPENDIX A

POLYNOMIAL CURVE FIT : DATA REDUCTION ALGORITHM

An equation of the form $y = a + bx + cx^2 + \ldots + k_n x^n$ may be fitted to data if Σx, Σx^2, Σx^3, ..., Σx^{2n} and Σy, Σxy, $\Sigma x^2 y$, ..., $\Sigma x^n y$ are computed and the following simultaneous equations are solved:

$$\Sigma y = ma + b\Sigma x + c\Sigma x^2 + \ldots + k_n \Sigma x^n$$

$$\Sigma xy + a\Sigma x + b\Sigma x^2 + c\Sigma x^3 + \ldots + k_n \Sigma x^{n+1}$$

(where m = # data points and n = degree of polynomial to be fitted)

$$\Sigma x^n y = a\Sigma x^n + b\Sigma x^{n+1} + c\Sigma x^{n+2} + \ldots + k_n \Sigma x^{2n}$$

The solution of the preceeding equations for a, b, c, ..., k_n is readily accomplished with a computer capable of performing matrix operations.

For a second order equation:

$$\Sigma y = ma + b\Sigma x + c\Sigma x^2$$

$$\Sigma xy = a\Sigma x + b\Sigma x^2 + c\Sigma x^3$$

$$\Sigma x^2 y = a\Sigma x^2 + b\Sigma x^3 + c\Sigma x^4$$

The solution for these simultaneous equations is:

$$a = \frac{(\Sigma x^2 \Sigma x^4 - \Sigma x^3 \Sigma x^3)\Sigma y + (\Sigma x^2 \Sigma x^3 - \Sigma x \Sigma x^4)\Sigma xy + (\Sigma x \Sigma x^3 - \Sigma x^2 \Sigma x^2)\Sigma x^2 y}{D},$$

$$b = \frac{(\Sigma x^2 \Sigma x^3 - \Sigma x \Sigma x^4)\Sigma y + (m\Sigma x^4 - \Sigma x^2 \Sigma x^2)\Sigma xy + (\Sigma x \Sigma x^2 - m\Sigma x^3)\Sigma x^2 y}{D},$$

$$c = \frac{(\Sigma x \Sigma x^3 - \Sigma x^2 \Sigma x^2)\Sigma y + (\Sigma x \Sigma x^2 - m\Sigma x^3)\Sigma xy + (m\Sigma x^2 - \Sigma x \Sigma x)\Sigma x^2 y}{D},$$

Where $D = m\Sigma x^2 \Sigma x^4 + 2\Sigma x \Sigma x^2 \Sigma x^3 - (\Sigma x^2)^3 - (\Sigma x)^2 \Sigma x^4 - m(\Sigma x^3)^2$

TITLE: DEVELOPMENT OF ROCKET SLEDS TO IMPLEMENT THE REVERSE VELOCITY TECHNIQUE FOR INERTIAL GUIDANCE SYSTEM TESTING

AUTHOR: JACK E. MYERS

TEST TRACK DIVISION, 6585TH TEST GROUP
Holloman AFB, New Mexico

ABSTRACT

A typical rocket sled test of an inertial guidance system involves 3 phases: boost, coast, and braking. The resulting accelerations allow propagation and eventual identification of system errors. Analysis of these errors provides the basis for quantitative evaluation of the system. Previous work by Mr. Norman Ingold of the Central Inertial Guidance Test Facility has shown that the sled test phases may be optimized for inertial guidance system evaluation. Results of this optimization analysis showed that the deceleration required during the braking phase would result in a negative sled velocity (the sled would have to reverse its direction and travel backwards). Conventional braking methods are incapable of producing the desired result. A concept using retropropulsion to provide the necessary deceleration was formulated: the reverse velocity technique.

This paper discusses the engineering development of equipment and test procedures to demonstrate the reverse velocity sled test concept as summarized below: no attempt will be made to test an inertial guidance system until equipment and test procedures are fully developed. To conduct a representative reverse velocity sled test, an outrigger sled will tow a smaller monorail test sled (which normally would carry the inertial guidance system) backwards down the track. After burnout of the motor on the outrigger sled, the coupled sleds will coast, slowed by aerodynamic drag and rail friction, until they reach a low velocity. The monorail sled will then be released from the outrigger sled and rocket motors on the monorail sled will be fired to send it back in the opposite direction. A series of sled tests of increasing complexity is planned, so that the proper function of several necessary components can be verified before they are all assembled and a sled test truly representative of the reverse velocity test concept is conducted. To reduce costs, risks, and development time, existing sleds and other hardware (modified as required) will be used wherever possible.

TABLE OF CONTENTS

LIST OF ILLUSTRATIONS

1. INTRODUCTION

The first series of rocket sled tests at the Holloman High Speed Test Track which was clearly related to inertial guidance system testing (in this case gyroscope testing) was accomplished in 1955. The objective was "to determine what linear accelerations can be imposed on the vertical gyros and flight controllers that are being used, and those contemplated for use, in aircraft and guided missiles scheduled to be zero length launched." In late 1956 a sled test series was initiated to evaluate performance of an experimental inertial guidance system under simulated launch conditions of the Mace missile. The utility of rocket sled testing of inertial guidance systems was vigorously investigated in the following years and basic test procedures were developed. Rocket sled tests have become a very important aspect of the test and evaluation accomplished by the Central Inertial Guidance Test Facility (CIGTF) since its establishment in 1959. (Reference 1)

Refinement of basic sled test methods has continued, and new techniques have been investigated to maintain up to date evaluation capabilities. One such investigation concerned the reverse velocity technique of sled testing; an aspect of which is the subject of this paper.

2. ROCKET SLED TEST CHARACTERISTICS

Sled testing of inertial guidance systems (or components) is based on the ability of a rocket sled to expose the test item to controlled linear acceleration, velocity, and displacement. Test conditions can be tailored to simulate the operational environment a system or component would experience in its intended application. Test conditions can also be designed specifically to excite and propagate system errors, allowing identification and quantification of the errors. It is possible to measure test conditions and system response very accurately since the sled's trajectory is closely controlled by the slippers that guide it down the track. Test instrumentation has been developed which takes advantage of this fact. An electro-optical velocity measurement system (VMS) in which a sledborne light beam is interrupted by very precisely located metal plates placed at nominal 13 ft intervals along the track is representative of this instrumentation. Sled position as a function of time is thereby measured and telemetered to a ground station. After a sled test, the system or component can be recovered undamaged for study or further testing.

A typical rocket sled test of an inertial guidance system or component consists of a boost phase, coast phase, and braking phase. The boost phase is provided by rocket motors chosen to produce a desired acceleration for a suitable time period. After the motors burn out, the sled enters the coast phase. The sled is slowed by aerodynamic drag and rail friction until a momentum exchange water brake can be safely used to provide a controlled deceleration (braking phase).

Sled tests fall into three acceleration regimes: Low (< 10 G), Medium (10 to 50 G), and High (> 50 G). Low G tests are typically conducted using a dual rail sled, designed to carry a variety of large precision guidance systems,

and a "pusher" sled using liquid or solid fuel rocket motors (Figure 1). The sleds are normally coupled together and a water brake on the "pusher" sled is used. The water brake engages water held by dams in the trough between the rails. A typical test profile using the liquid engine "pusher" sled illustrated in Figure 1 is shown in Figure 2. Medium G tests have been accomplished using the sled in Figure 3, which carries solid fuel rocket motors on board. This sled has its own water brake. A typical test profile is shown in Figure 4. High G tests require high performance solid fuel rocket motors and a small, low mass, streamlined sled. The High G Monorail Sled shown in Figure 5 was developed for this purpose. It has a braking scoop on the front end which engages water in trays placed on the rail. Figure 6 illustrates a profile which has been achieved by this sled.

3. REVERSE VELOCITY TECHNIQUE FOR SLED TESTS

As conventional sled testing techniques were refined, it became clear that the water braking, or deceleration phase was crucial to error separation and identification. When sled tests were conducted at increasing G levels, the practical limitations of water braking became more pronounced. High G deceleration required a large braking force and minimum sled mass. To maximize the duration of the deceleration, higher water brake entry velocity was necessary. Structural, aerodynamic, hydrodynamic, and economic limitations were recognized as barriers to the extension of conventional braking techniques to the high G regime.

Concern for the limitations of existing techniques when applied to high G levels led Mr. Norman Ingold of CIGTF to explore the problems and seek solutions. An optimization analysis of the different phases of a high G sled test was performed (Reference 2). Results of the analysis showed that for optimum error separation, the decelaration required during the braking phase would result in a negative sled velocity (the sled would actually have to reverse its direction and travel backwards). Momentum exchange water braking is incapable of producing the desired result, and after considering several alternatives, a concept using retropropulsion to provide the necessary deceleration (or acceleration in the direction opposite to the boost acceleration) was formulated: the reverse velocity technique. The reverse velocity technique appeared to overcome high G water braking limitations and would allow optimization of deceleration during the braking phase. A further result of the optimization analysis was that the reverse velocity technique showed promise for improving the sled testing of guidance systems and components at all acceleration levels; not just for the high G regime. The proposed technique also has other benefits which are discussed in detail in Reference 2.

4. REVERSE VELOCITY FEASIBILITY DEMONSTRATION

Because the reverse velocity technique showed such promise as an improved test and evaluation procedure, the Test Track Division of the 6585th Test Group was approached by CIGTF to determine whether or not it was possible (and practical) to implement the technique.

It was determined to be technically feasible and a joint decision was made that the Test Track would conduct a practical demonstration of a suitable sled test profile using available rocket sleds and other equipment, to the maximum extent possible, before attempting to develop and design rocket sleds specifically for reverse velocity testing. The demonstration would provide an opportunity to explore unique design and operational requirements of the new technique.

Three primary considerations in conducting a feasibility demonstration were: 1) What performance would be required of the test sled to adequately demonstrate technical feasibility of the reverse velocity technique? 2) What sleds and equipment were available, and what modifications or new equipment items were necessary to meet performance requirements (and measure performance)? 3) What was the most economical and timely approach to conducting the demonstration based on performance requirements and available resources? The answers to these questions follow:

Performance Requirements

Since the high G regime of sled testing appeared likely to benefit immediately from the new technique, it was decided to aim for the highest practical acceleration levels. The optimization analysis showed that acceleration in the reverse direction should be two to four times the initial acceleration. Achieving the desired accelerations under practical conditions, using retropropulsion, was considered to be the primary success criterion of the feasibility demonstration.

Sled and Equipment Development

A preliminary sled performance analysis conducted by the Test Track Engineering Branch identified two rocket sleds that could be used in combination (with modifications) to meet the desired performance requirements most easily. The sleds were made available and the towing sled has already been modified. A structure (towing truss) with large slippers to react side forces caused by the towing operation is under construction. A release mechanism has been designed which will decouple the towed sled at the proper time.

Figure 7 illustrates the hardware to be used for the feasibility demonstration.

The large general purpose "outrigger" sled used as the towing vehicle was originally designed to use four high performance rocket motors or one medium performance motor. The medium performance motor would not give desired acceleration, and the four high performance motors were too expensive for use in the feasibility demonstration. The sled was modified to use an Improved Honest John motor which is available as a surplus item and is quite economical for this application. It has a peak thrust of more than 100,000 pounds and will give an acceleration of approximately 20 G for the configuration of Figure 7.

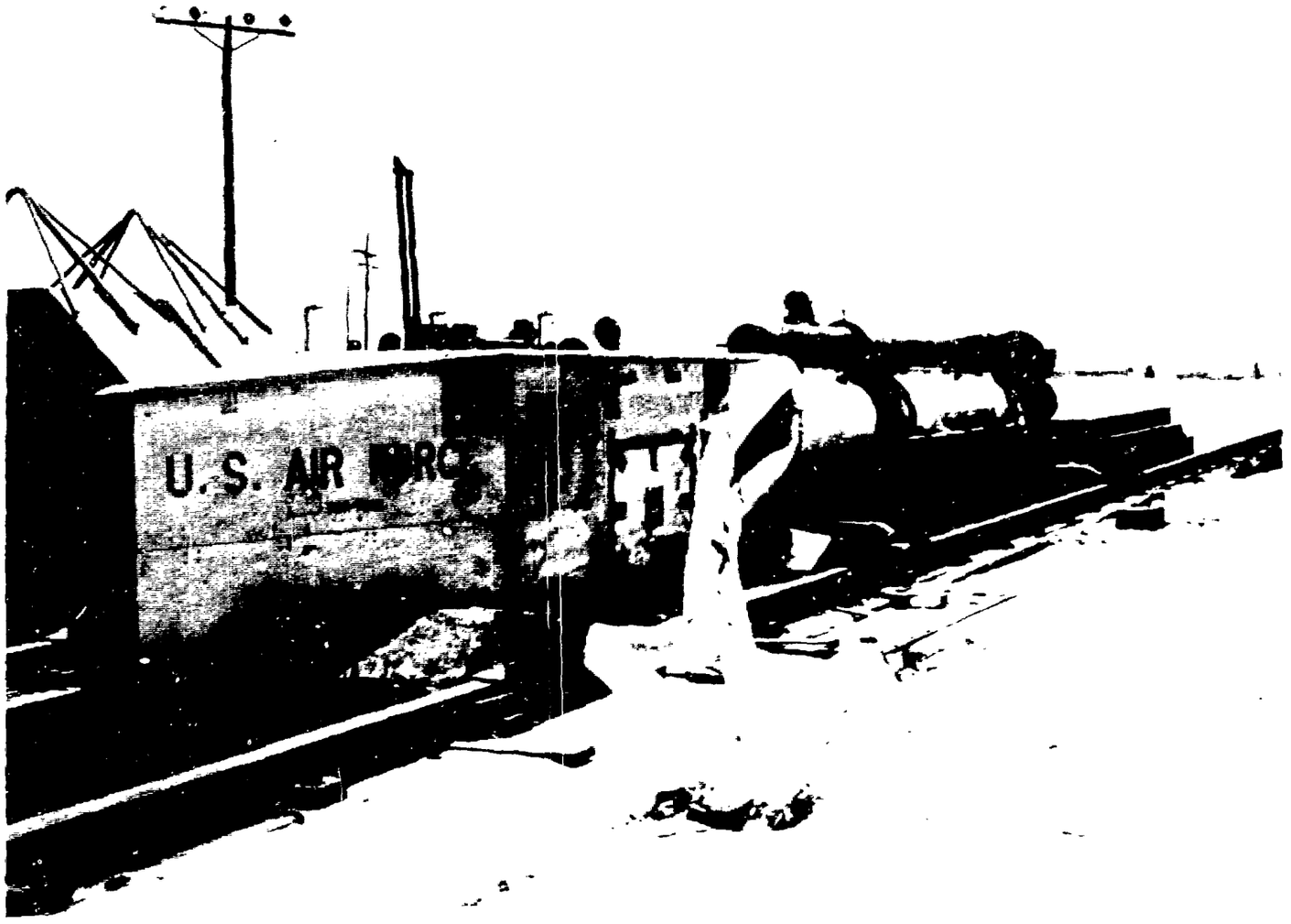

Figure 1. Low G Test Sled With Liquid Fuel Pusher

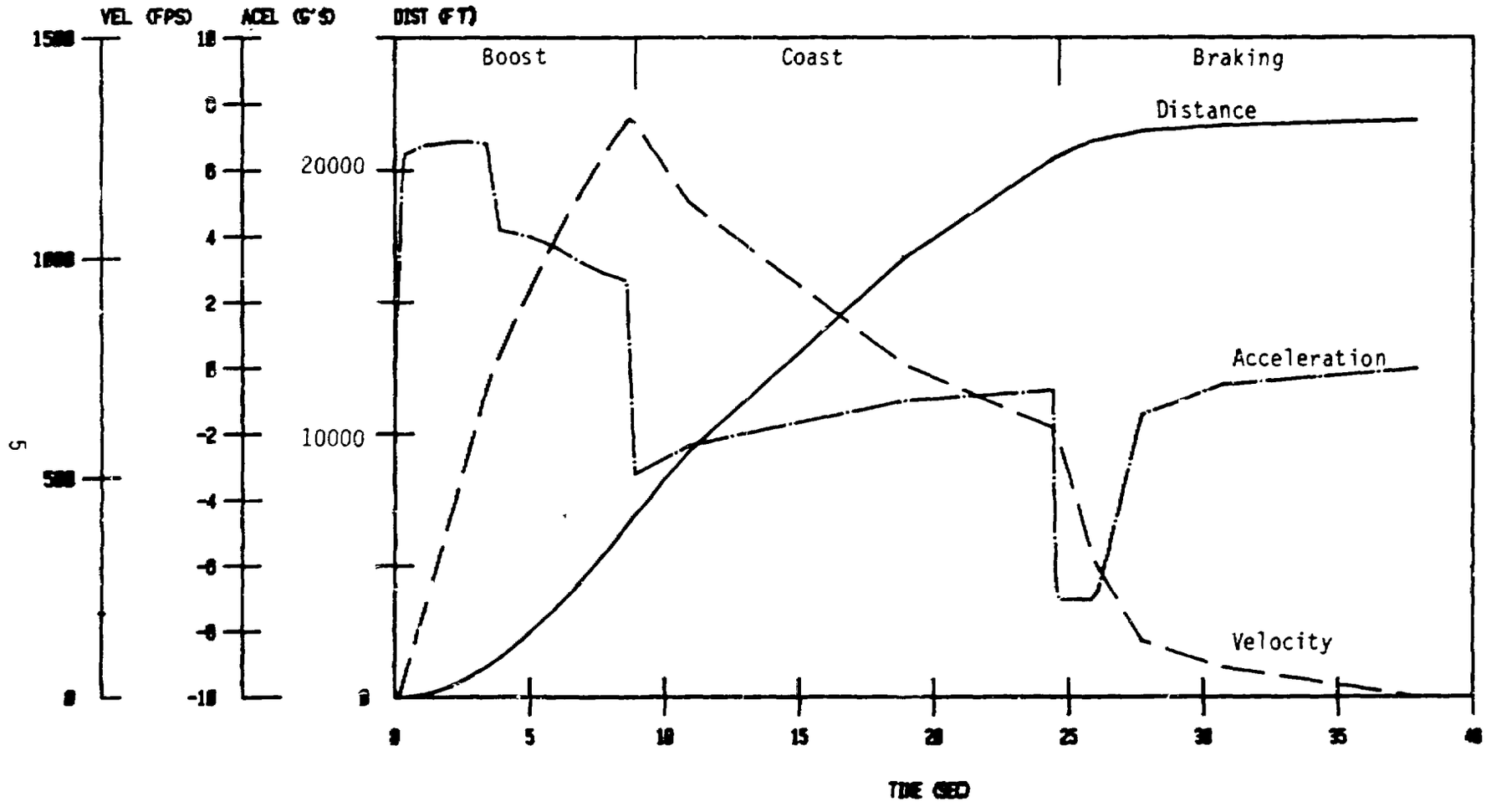

Figure 2. *TYPICAL LOW G SLED TEST PROFILE*

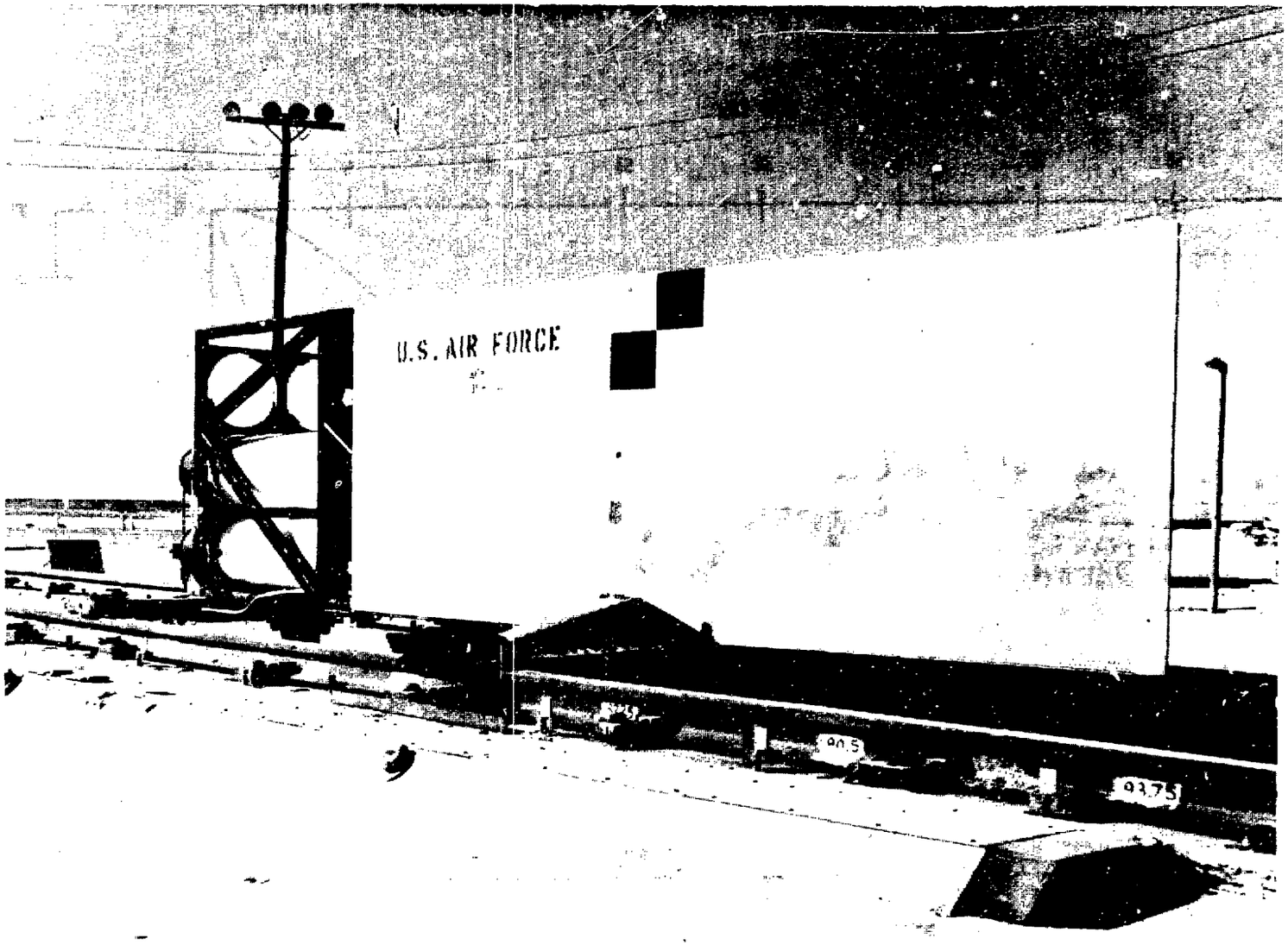

Figure 3. Medium G Test Sled

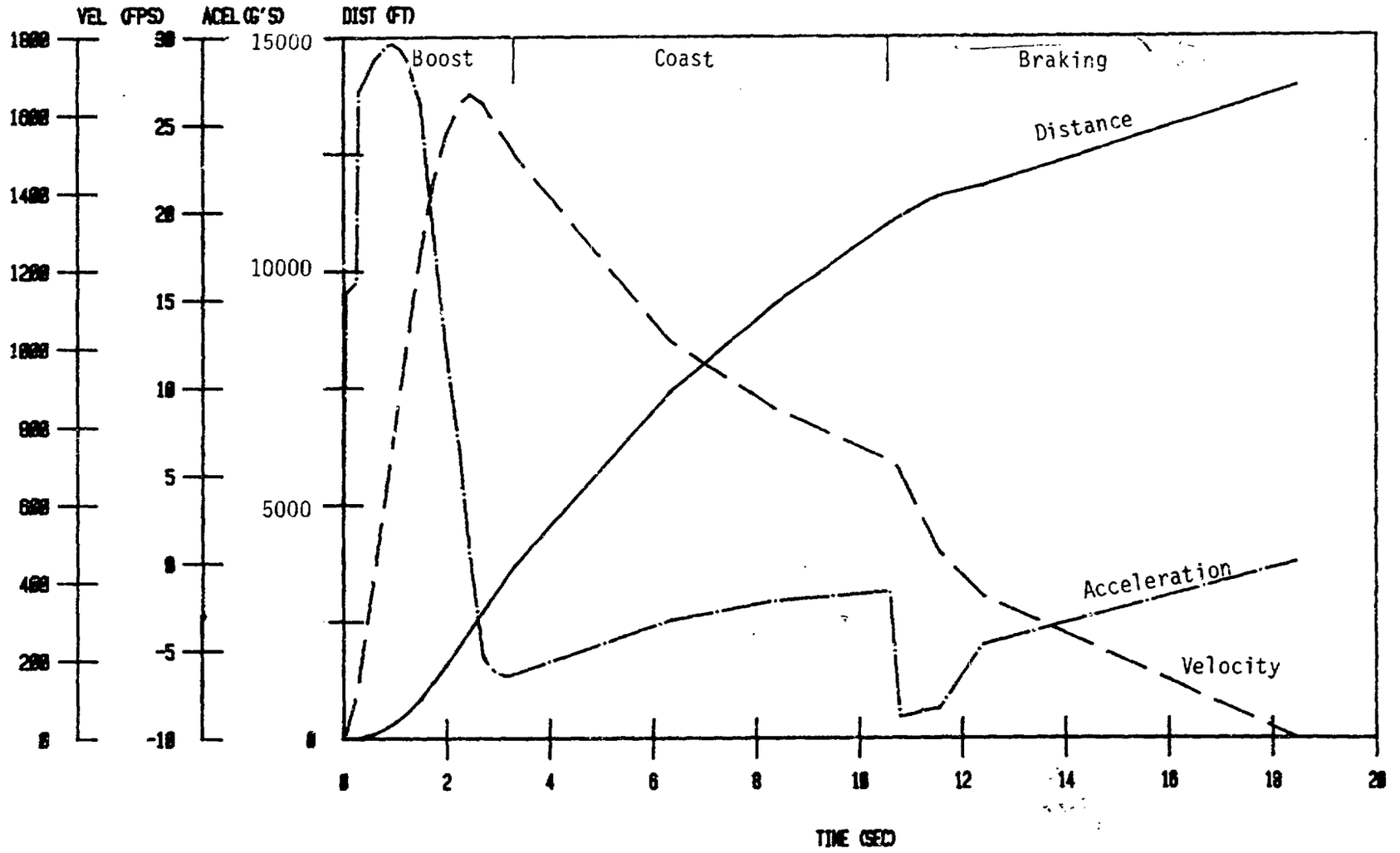

Figure 4. *TYPICAL MEDIUM G SLED TEST PROFILE*

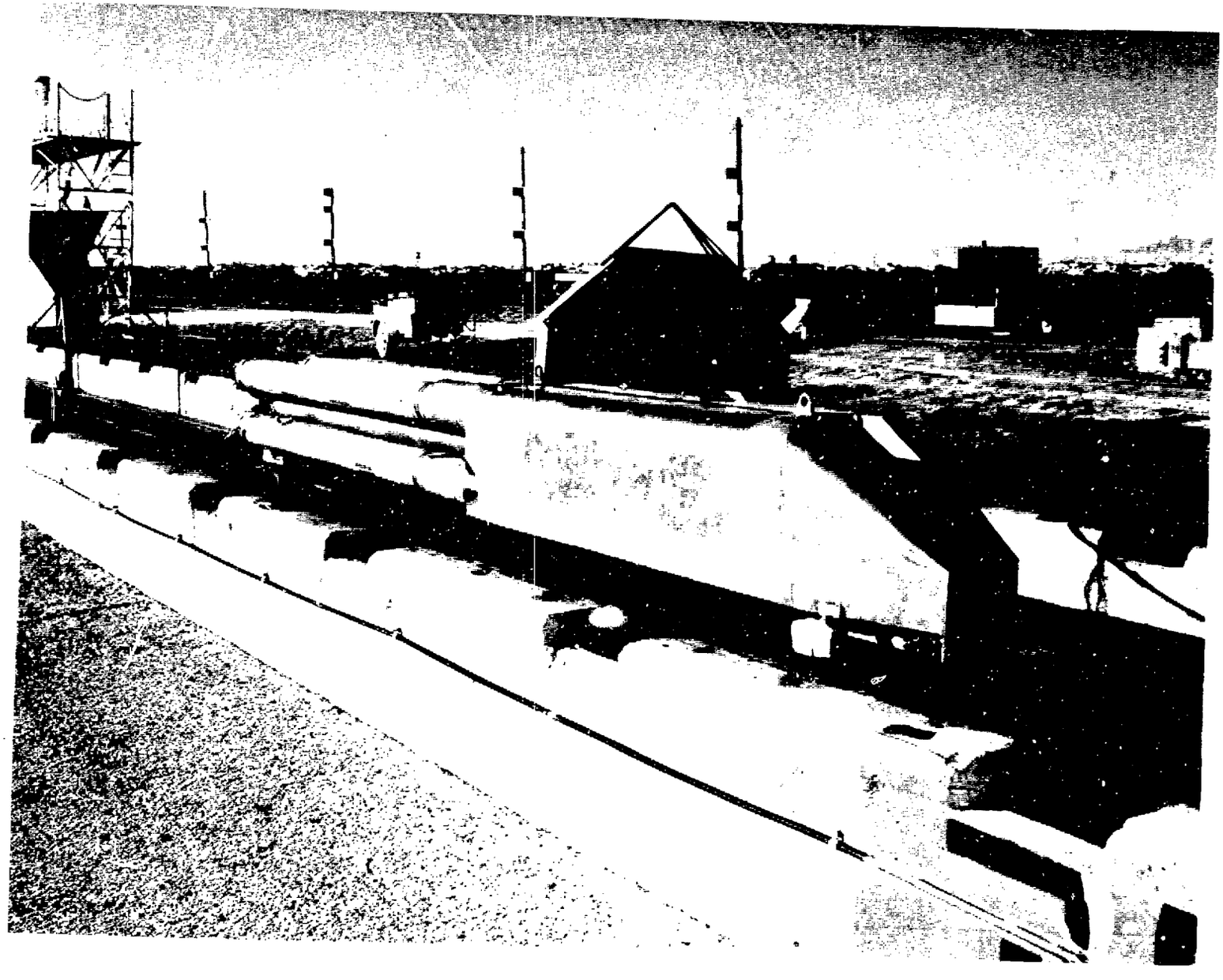

Figure 5. High G Monorail Test Sled

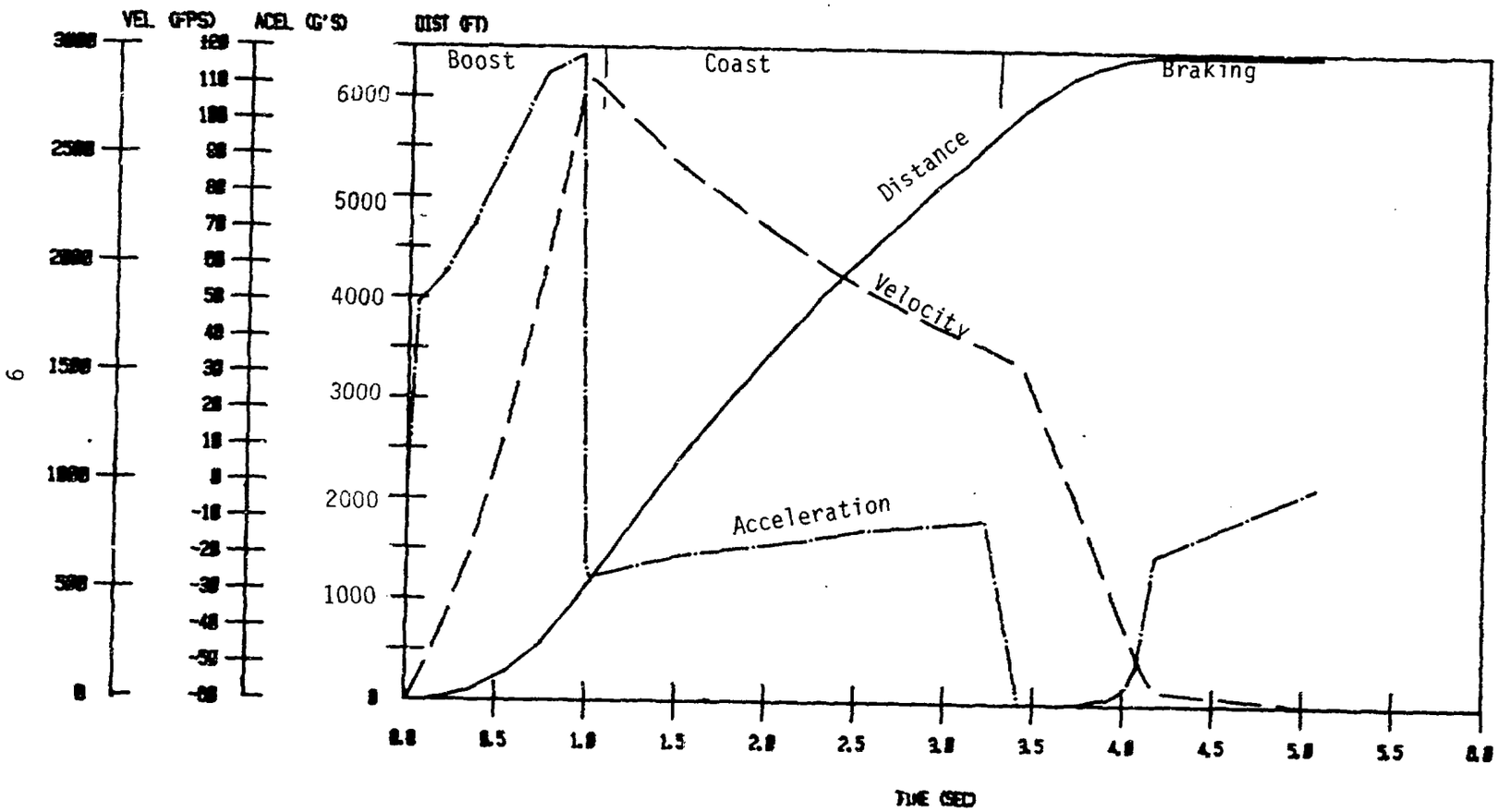

Figure 6. *TYPICAL HIGH G SLED TEST PROFILE*

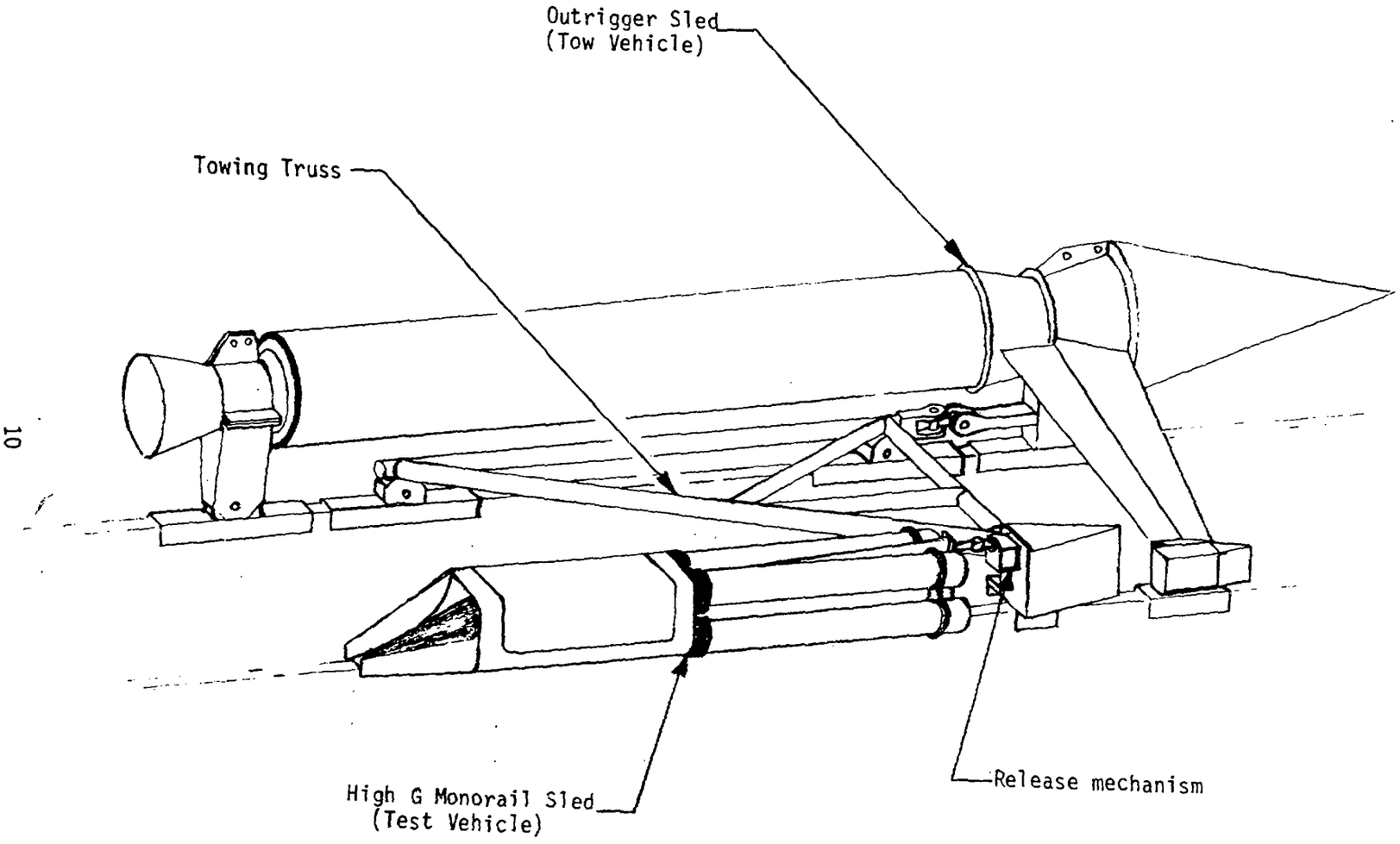

Figure 7. Reverse Velocity Sled Configuration

The monorail sled, used as the test vehicle, is the same type as the one shown in Figure 5. This sled would carry an inertial guidance system or components for actual reverse velocity tests. Five surplus Zuni rocket motors giving a peak thrust of about 35,000 pounds will give this sled an acceleration of about 60 G after it is released from the towing vehicle. The built-in water brake will not be used. Minor modifications will be required in order to tow the sled backward. Electrically insulated knifeblades will be installed on the monorail sled and connected to igniters on its rocket motors. These knifeblades pass through trackside "screenboxes" to complete an electrical circuit that will ignite the motors after the sled has been released. This method is commonly used to ignite rocket motors on moving sleds and has proven to be extremely reliable.

An analysis of the structural loads in the outrigger sled caused by the towing operation showed that it was not possible to tow the monorail sled directly from the outboard end of the outrigger arm without extensively modifying the outrigger sled. In order to reduce structural loading on the outrigger sled to an acceptable level, without greatly modifying it, an independent structure (towing truss) with large slippers to react the yawing moment caused by the towing operation was incorporated. The towing truss will be attached to the main body of the outrigger sled and can be easily removed so that this sled would be available for other purposes. A wedge shaped aerodynamic fairing is attached to the outboard end of the towing truss to reduce drag and protect the towed monorail sled. The connections between the towing truss and the two sleds will be universal joints to allow for relative motion as slippers wear.

A release mechanism will be installed on the outboard end of the towing truss. A mechanical release in which a link of the mechanism is cut by a track side knifeblade at the desired location on the track, thereby releasing the monorail sled, has been designed. Pyrotechnic, hydraulic, pneumatic, and electro-mechanical devices were considered for the release mechanism before a mechanical release was decided upon. A combination of concerns for reliability, safety, and economics led to this choice. A mechanical release system using the same general principles has been used very successfully at the Holloman Test Track to decouple moving sleds. Provisions will be incorporated to insure the motors on the monorail sled cannot be fired unless the release mechanism has functioned properly. The release mechanism can be removed from the towing truss for independent testing, adjustment, or modification.

The outrigger sled will carry a telemetry system and instrumentation to measure forces on the couplings between the towing truss and the two sleds. The monorail sled will carry a telemetry system and accelerometers to measure linear accelerations and vibration levels. Velocity of the monorail sled will be measured by the electro-optical velocity measuring system (VMS). Both sleds have existing provisions for installation of the required instrumentation systems.

During the feasibility demonstration no attempt will be made to actually install an inertial guidance system or components.

Development Test Program

It was determined that the feasibility demonstration should consist of a series of six track tests of increasing complexity in order to reduce technical risk.

Test 1 verified the structural integrity of the outrigger sled after its modification to use the Improved Honest John motor. This test was conducted in July 1980.

Test 2 is intended to verify the structural integrity of the towing truss and provide data from which actual slipper loads and wear rates can be determined. For this test a low cost "dummy" sled (which has no motor) will replace the high G monorail sled. The release mechanism will not be installed, so the sleds will remain coupled together.

Test 3 is a planned series of dynamic tests of the release mechanism in which the towing truss will be pulled along the test track by a truck tractor that has been modified to operate on the track (Low Speed Prime Mover). The above mentioned dummy sled will be released to verify proper operation of the release mechanism and its safety features under dynamic conditions (up to 70 ft/sec).

Test 4 will be a test of the release mechanism using the outrigger sled, towing truss, and dummy sled. The dummy sled will be released when the coasting sleds slow to about 200 ft/sec. Both sleds will continue on in the original direction until they stop.

Test 5 will consist of towing and releasing the high G monorail sled which will carry empty rocket motor cases that have been ballasted to simulate propellant weight. This test will verify structural integrity of the high G monorail sled as modified for towing in reverse. The monorail sled will be released at a velocity of about 200 ft/sec as in Test 4.

Test 6 will be the actual attempt to produce a sled test profile which would be suitable to implement the reverse velocity technique (see Figure 8 and Figure 9). The outrigger sled, towing truss, release mechanism, and high G monorail sled will be used. The high G monorail sled will be released after the coupled sleds have slowed to about 200 ft/sec. The outrigger sled and towing truss will continue to coast until they stop. The rocket motors on the high G monorail sled will fire, stopping the sled and then propelling it back in the opposite direction. After motor burn out the sled will coast to a stop.

5. FURTHER DEVELOPMENT OF THE REVERSE VELOCITY TECHNIQUE

Successful completion of the feasibility demonstration will be followed by tests of representative inertial guidance system components using the sleds, other hardware, and procedures developed during the feasibility

demonstration. These tests should fully verify that the reverse velocity technique can be implemented as an improved method for testing inertial guidance systems or components.

The sled train configuration chosen for the feasibility demonstration (Figure 7) is not the only one that could be used for reverse velocity testing. An outrigger sled could be designed to tow a monorail sled directly, without need for an intermediary towing truss. Lighter, more efficient designs would allow higher G levels to be attained. Larger and heavier test items could be carried for tests conducted at lower G levels.

While an outrigger sled towing a monorail sled is convenient, it is not the only possible configuration. Schemes for using dual rail or monorail sleds can be visualized in which one sled carries motors for a boost phase and motors which would provide thrust in the opposite direction. This has been accomplished in practice, primarily as a means of stopping sleds when the more conventional water braking is not suitable. An application of this general technique to guidance system testing was proposed in 1958 (Reference 3). The intent was to provide higher acceleration in the boost phase, for a longer duration, than was practical at that time because of track length and sled velocity limitations. The forward velocity at the end of boost phase was expected to be reduced significantly though the acceleration level during boost was higher. By initially propelling a dual rail sled backwards with solid fuel rocket motors until they burned out and then igniting the liquid fuel motor of the test sled, a test profile similar to that of Figure 2 would result, except it would have an initial negative velocity instead of zero velocity and a higher boost phase acceleration. It is also possible that two dual rail sleds, one towing and releasing the other, could be designed.

Another possibility that has been considered is a test consisting of two separate sled runs. This could be done either by quickly removing burned out motors at the location where the first run stops and then installing and firing motors to propel the sled back in the opposite direction; or by returning the sled to its original launch point, reloading it with new motors, reorienting the guidance system, and firing it again. The dual sled run approach seems impractical due to the necessary elapsed time between runs and the likelihood of disturbing the alignment of the test item. Reference 2 discusses the objections to this approach in greater detail.

6. SUMMARY

An analytical study by CIGTF has identified a very promising new sled test method for the evaluation of inertial guidance systems: the reverse velocity technique. A cooperative effort with the Test Track Division of the 6585th Test Group will attempt to demonstrate that the reverse velocity technique can be implemented. Rocket sleds could be specifically designed to meet requirements of testing at G levels of current interest; the low, medium, and high G regimes. While the outrigger tow sled/small monorail test sled configuration appears to be the optimum for high G testing, other configurations are possible and much larger sleds could be used for lower G levels.

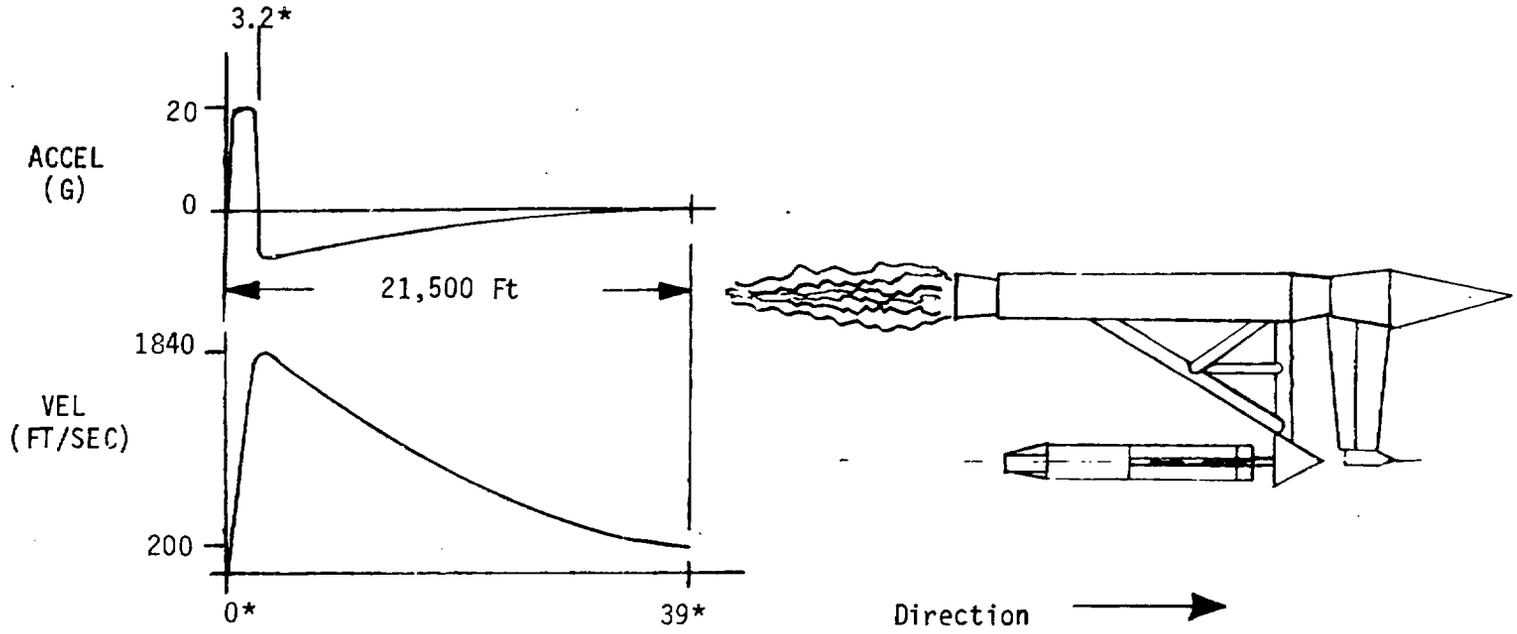

* Time from launch of Tow Sled (Sec)

Figure 8. Reverse Velocity Sled Test Profile (First Part)

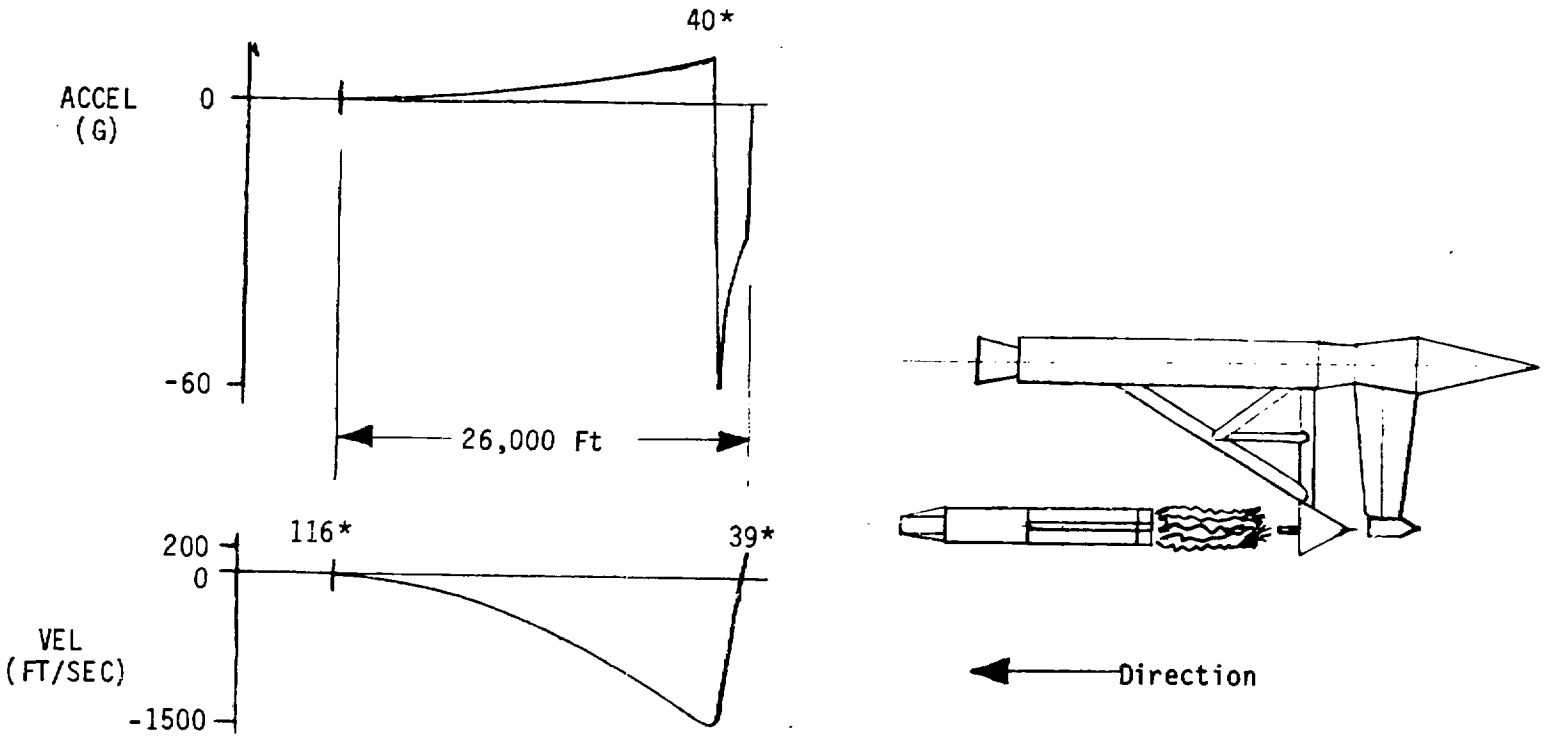

* Time from Launch of Tow Sled (Sec)

Figure 9. Reverse Velocity Sled Test Profile (Second Part)

REFERENCES

1. Bushnell, Dr. David, The Beginning of Guidance System Testing at the Air Force Missile Development Center, 1955-1959, Historical Branch, Office of Information, Air Force Missile Development Center, Air Research and Development Command, United States Air Force, February, 1960.

2. Ingold, Norman L.,"Proposed Use of Retro Rockets for Optimizing Analysis of Inertial Guidance System Errors in 100-G Sled Tests", Proceedings of the Ninth Biennial Guidance Test Symposium (Holloman Air Force Base) October, 1979.

3. Pickles, A.M. and Poland, H.M. (Aerojet-General Corporation), "Three Methods of Controlling Rocket Sled Acceleration Without Varying Thrust", Proceedings of the Fifth Annual Supersonic Track Symposium, (Cloudcroft, New Mexico) October, 1958.

TITLE: A HARDWARE-IN-THE-LOOP SIMULATION FOR TESTING THE GUIDANCE, CONTROL, AND WARHEAD EQUIPMENT OF THE VOUGHT CORPORATION ASSAULT BREAKER MISSILE

AUTHOR: PETER SCHAAR

VOUGHT CORPORATION
Dallas, Texas

INTRODUCTION

The Vought Assault Breaker T-22 missile contains a guidance system and a warhead designed to eject up to 24 submunitions in a pre-determined pattern. In order to prove that the inertial guidance software, the inertial guidance hardware, the actuators, the warhead sequencer and dispenser, and the mobile data gathering computer are properly integrated and that they operate together as intended, a real-time hardware-in-the-loop (HWIL) Simulation was created. This paper describes the HWIL Simulation and presents enough results from its operation and from a corresponding flight test to illustrate its usefulness and demonstrate its validity.

THE ASSAULT BREAKER MISSILE

The T-22 Missile Configuration

The Assault Breaker T-22 flight test vehicle, shown in Figure 1, uses the same airframe as the LANCE missile. The T-22 differs from LANCE in its external aft control surfaces (elevons), fixed wing surfaces, solid rocket motor, and improved guidance system. The strapdown inertial guidance system, which uses three ring laser gyroscopes, is supplied by Honeywell Incorporated and is mounted within the guidance shell (Figure 1). The pneumatic elevon control system, supplied by AiResearch Corporation, is placed around the rocket nozzle and is enclosed within an aluminum boattail. The warhead section contains 24 submissiles or submunitions assemblies and a programmable sequencer capable of dispensing them in various pre-selected patterns. Pertinent characteristics of the T-22 are presented in Figure 2.

The Inertial Guidance System

The inertial guidance system is called the Laser Inertial Measurement Unit (LIMU) and includes the accelerometers and the gyroscopes, a pulse accumulator module (PAM), the flight computer, and a power conditioner (not shown in Figures 3 and 4). The accelerometers and gyroscopes generate pulses in quantities proportional to their outputs. These pulses are accumulated asynchronously by the pulse accumulator module, where they are periodically sampled by the flight computer. The flight computer uses these pulses as inputs and produces steering signals to be sent to the actuators as outputs.

The Actuation System

The Control Actuation System (CAS) and its associated Power and Control Electronics (PACE) constitute the elevon actuation system. The CAS, including the elevons, resides in the boattail section surrounding the rocket motor nozzle at the aft end of the missile. The PACE resides on the Guidance and Control plate with the inertial guidance gear. The PACE receives the steering signals from the flight computer and issues the command signals to move the elevons. The CAS contains potentiometers which sense and report the elevon positions to the PACE for broadcast over the telemetry system.

The Warhead Sequencer and Dispenser

During a flight a discrete arming signal is issued by the LIMU at the appropriate point in the flight. Upon receipt of this discrete signal by the sequencer, the sequencer software is turned on and monitoring of the serial data line from the LIMU begins. The sequencer issues a signal to fire the skin at a preset altitude and then issues firing signals to the dispenser to fire the submunitions at preset roll angles designed to achieve the desired laydown pattern. Data is sent continuously from the LIMU which enables the sequencer software to correct for variations in the actual roll rate.

The Mobile Data System

The mobile data system is a Xerox Sigma 3 computer mounted in a van at the launch site. Its function is to receive telemetry data from the missile and reduce, manipulate, store, and plot the data in real time. This system has the ability to display plots of several telemetered quantities in real time on CRT terminals.

THE HARDWARE-IN-THE-LOOP (HWIL) SIMULATION

Simulation Configuration

The real time hardware-in-the-loop (HWIL) simulation was created to test the guidance system, the control actuation system, the warhead sequencer and dispenser, and the data reduction system in as realistic an environment as possible. This simulation is sketched in block form in Figures 3 and 4.

The simulation configuration shown in Figure 3 will be referred to as the "complete" configuration. It includes the inertial guidance system, the actuators plus an elevon loader, the warhead sequencer and dispenser, and the telemetry data reduction system in the simulation loop. The simulation configuration shown in Figure 4 will be referred to as the "LIMU-only" configuration. It includes only the inertial guidance system, or Laser Inertial Measurement Unit (LIMU), and the data reduction system.

The simulation computer consists of a PDP 11/70 and a Floating Point AP120B array processor. The PDP 11/70 contains the models of the missile, the earth, the atmosphere, the accelerometers and gyroscopes, and it also contains the pre-launch simulation. The AP120B contains all the table lookup functions, including aerodynamic, inertial, and propulsion functions, and the equations of motions are integrated in the AP120B. The output of the simulator computer consists of three accelerometer values and three gyroscope values which are sent to a six-channel pulse generator. The simulation computer and the pulse generator are both synchronized with the flight computer by a clock discrete from the flight computer. When the clock discrete is received the pulse generator sends pulses to the guidance system. The number of pulses sent by each of the six channels is proportional to the accelerometer or gyroscope signal sent to that channel by the simulation computer. The guidance system (flight computer) uses the sensor pulses to compute steering signals, which are either sent to the actuation system (Figure 3) or back to the simulation computer (Figure 4). In the latter case (LIMU-only configuration), "ideal" actuators are assumed in which the elevon positions are identical to the steering signals at all times. An earlier version of the LIMU-only configuration included an analog model of the actuators, but this did not provide any improvement over the ideal actuator and was discontinued.

Missile Hardware

For simulation purposes, the connections in the inertial guidance unit (LIMU) between the sensors and the pulse accumulator module are interrupted and pulses generated by the simulation pulse generator are substituted. Thus, the accelerometers and gyroscopes are not tested by the simulation; they are tested in a separate test. The inertial guidance system excepting the sensors is the component most extensively tested by the HWIL simulation.

The actuation system, composed of the Control Actuation System (CAS) and the Power and Control Electronics (PACE) is tested in the complete configuration (Figure 3). During HWIL testing the PACE resides on the Guidance and Control plate with the LIMU, just as it does in the missile (Figure 1). The CAS resides in a hydraulically actuated spring-and-pulley loader which mechanically simulates the aerodynamic loads on the elevons. The flight computer issues steering command signals, which in the complete configuration are fed to the actuators, causing them to move. The PACE contains potentiometers which sense and report the elevon positions in the form of electrical signals. These signals are fed back to the simulation computer where they close the loop by moving the simulated missile.

The warhead sequencer and dispenser are tested as a unit. The firing signals issued by the sequencer are monitored by a test set and are also sent to the simulation computer for recording.

A replica of the mobile data system computer hardware and software is included in the HWIL Simulation. The main difference between it and the field system is that, in the Simulation, data from the flight computer is sent over a hard line rather than telemetered. This replica is referred to as the "data reduction system" in this paper.

Pre-Launch Simulation

In addition to simulating the missile during flight, the simulation computer simulates the missile and part of the Launch Control Unit (LCU) function during pre-launch operations. The LCU is a teletype which is connected to the LIMU until lift-off and which commands the LIMU to go from one mode to the next, and which also receives and prints certain data from the LIMU during each mode. A real LCU was included in the simulation for the receiving and printing functions; the commanding function was performed by the simulation computer.

The first pre-launch mode is an alignment while the missile is attached to the launcher in a (geodetically) horizontal position. During this mode, labeled A1, the velocity components are clamped to zero while the flight software searches for an alignment which agrees with the known azimuth and accelerations. The second mode is a navigation mode, labeled N1. The missile is erected to its launch elevation angle during this mode, and the flight software navigates. The third mode, labeled A2, is a re-alignment while the missile is held at the launch angle. The fourth and final pre-launch mode is the second navigation mode, labeled N2, while the missile awaits firing.

Since the missile is fixed to the earth during pre-launch and is stationary on the earth during the alignment modes, these modes proved very useful in checking out and trouble-shooting much of the software and hardware in the simulation. In particular, several problems with the simulation pulse generator were found this way.

TEST RESULTS

Flight Conditions

The LIMU-only configuration (Figure 4) was used in all eleven flight conditions shown in Table 1 below. The complete configuration (Figure 3) was used only in the first three of these conditions, nominal, overshoot, and undershoot, in order to avoid prolonged testing of the pneumatic actuators. The definitions of nominal, overshoot, and undershoot cases are given at the bottom of Table 1.

Simulation Results: Guidance and Control

Selected test results are shown for two flight conditions, nominal and overshoot. Although a great deal of data is available, only strip chart records of elevon positions and X-Y plotter records of altitude are included in this paper.

Figure 5 is a plot of altitude vs. down-range distance recorded during a LIMU-only run under nominal flight conditions. The apogee and pushover features of the trajectory are identified. The missile guidance is designed to bring the missile down vertically over the target. During the vertical dive the missile is spun at a pre-set rate and the submunitions are dispensed by the warhead sequencer in the pre-set pattern. The elevon position records from the same LIMU-only nominal run are shown in Figure 6 with the trajectory features identified. The elevons are limited to 19 degrees deflection, and their relieved condition during the dispense phase indicates that the navigation routine in the LIMU computes missile position to be directly over the target.

Figures 7 and 8 are records of altitude and elevon positions for an overshoot flight condition. The run was again a LIMU-only run. A comparison of elevon positions run under nominal and overshoot flight conditions reveal several differences. Under the overshoot condition, the maximum elevon deflection at the end of boost, when guidance is activated, is larger than the maximum deflection under nominal conditions. The elevons go into maximum, limited, deflection for a shorter time than they do under nominal conditions, and the elevons are relieved somewhat later during pushover than they are under nominal conditions. These differences are pertinent to the flight data discussed below.

Figures 9 and 10 are records of elevon positions from nominal and overshoot runs of the complete configuration, including the flight actuators. Altitude plots are not included because they are identical to the corresponding altitude plots from the LIMU-only runs (Figures 5 and 7). Close comparison of the LIMU-only runs and the corresponding runs with the actuators included reveal no significant differences, although a slight loss of stability due to the inclusion of the actuators can be seen.

Flight Results: Guidance and Control

Figure 11 is the altitude plot obtained from the LIMU via telemetry during the flight test of the missile. Figures 12 and 13 are telemetry records of elevon positions during the first flight. The different scaling of the axes makes comparison with simulation runs awkward, but such comparison shows that both the altitude and the elevon positions are qualitatively similar to the overshoot flight condition runs discussed above, but exaggerated. This is consistent with the discovery that the missile coating failed to ablate as expected, with the result that the missile drag was significantly less than that assumed in the simulation nominal condition. As a consequence the missile flew in an extreme overshoot condition, and comparison of the flight records, especially the elevon positions, with the simulation results bear this out.

Simulation and Flight Results: Warhead

A summary of the sequencer results from a simulation run and from the first flight test are shown in Figure 14. The time intervals between firing signals as recorded by the test set and by the simulation computer are compared with each other and with the actual timing during flight. The test set results agree with the actual flight results fairly well, the largest difference being 17 ms. At a nominal spin rate of 150 degrees/sec for this particular flight, 17 ms corresponds to an error of 2.55 degrees in predicted ejection direction. The time intervals recorded by the simulation computer did not agree quite as well with the flight data.

This problem is under investigation; however, it is a minor one and does not prevent the HWIL simulation from providing the sequencer and dispenser with the flight environment necessary for test.

OBSERVATIONS AND CONCLUSIONS

It was found necessary to time the flight computer, the simulation computer, and the pulse generator from a master clock in order to operate them in real time. A simulation involving several computers such as this one can easily become overly complicated; the use of simple models such as the digital ideal actuator model is desirable and proved quite adequate for a significant part of the production and flight qualification testing.

The original purpose for including the data reduction system was to integrate it into the flight system and test it under flight conditions in the same way as the other flight system components were integrated and tested. However, the data reduction system also proved to be a useful tool for trouble-shooting both the flight computer and the HWIL Simulation, since it provides the only access to the flight computer software during operation..

The HWIL simulation has been validated as a useful tool for testing the operation of the guidance and control system, the warhead sequencer and dispenser, and the data reduction system under simulated flight conditions. Its success in providing a flight environment has been demonstrated by comparison with the first flight test results. Its usefulness as a design aid has been established as well; several system design problems have been discovered and solved during testing.

Table 1. Flight Conditions Used in Assault Breaker HWIL Verification and Testing.

CONDITION NUMBER	DESCRIPTION
1	Nominal
2	Overshoot*
3	Undershoot**
4	Overshoot + 1.01 total impulse + 1.10 thrust level
5	Undershoot + 0.99 total impulse + 0.90 thrust level
6	Overshoot + 0.90 pitch/yaw control effectiveness + 1.05 normal force effectiveness + 1.05 pitch/yaw inertia
7	Undershoot + 1.10 pitch/yaw control effectiveness + 0.95 normal force effectiveness + 0.95 pitch/yaw inertia
8	Overshoot + static margin shift: Boost: +0.5 cal, Coast +0.25 cal
9	Undershoot + static margin shift: Boost -0.5 cal, Coast -0.25 cal
10	Nominal + 1.10 roll control effectiveness + 0.95 roll inertia
11	Nominal + 0.90 roll control effectiveness + 1.05 roll inertia

Definition:

*Overshoot:
- Tailwind and crosswind: 50% of WSMR 95th percentile scalar wind profile.
- Drag: -5%
- Thrust misalignment: 0.003 radians (nose up, nose left)
- Tipoff rate: +0.1 radians/sec

**Undershoot:
- Headwind and crosswind: 50% of WSMR 95th percentile scalar wind profile
- Drag: +5%
- Thrust misalignment: 0.003 radians (nose down, nose left)
- Tipoff rate: -0.1 radians/sec

Figure 1. Inboard Profile
Vought Assault Breaker
T-22 Missile

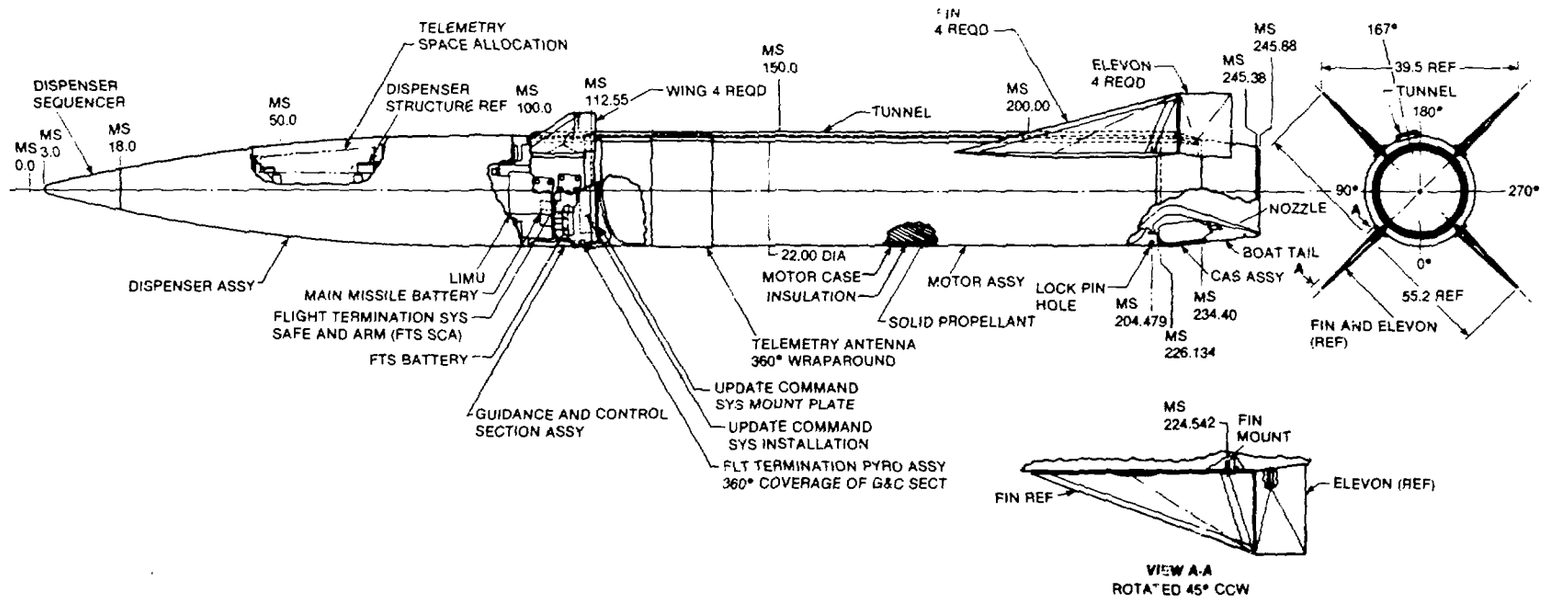

G1-1659-1

T-22 FLIGHT TEST VEHICLE CHARACTERISTICS

Length	6.2m	242.88 inches
Diameter	55.88cm	22 inches
Width-Fin Span	139.70cm	55 inches
Propulsion	Solid, Single Stage	
Control Surfaces	External Aft Elevons in cruciform (X) configuration, pneumatically actuated; fixed wings at midsection in cruciform (X) configuration.	
Guidance	Strapdown Inertial	
Maximum Acceleration	24g	
Spin Rate	Zero (Roll Stabilized)	
Weight-Launch	3800 lbs. (Nominal)	
Weight-Burnout	2057 lbs. (Nominal)	

Figure 2

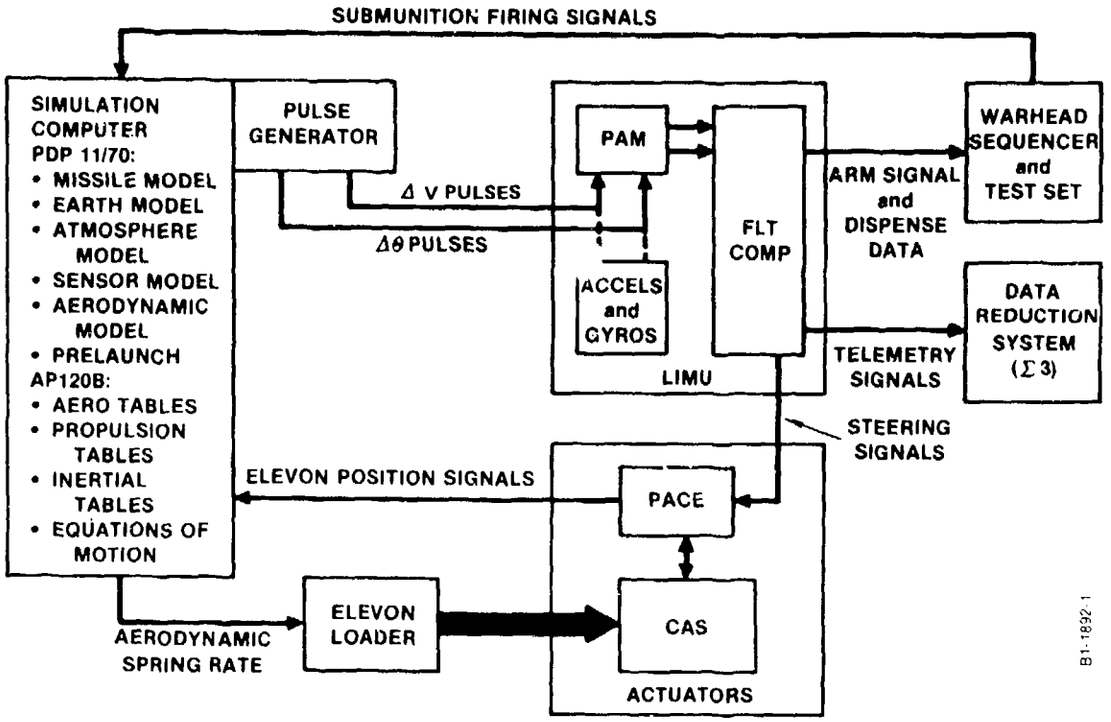

Figure 3 Assault Breaker Hardware-in-the-Loop Simulation Complete Configuration.

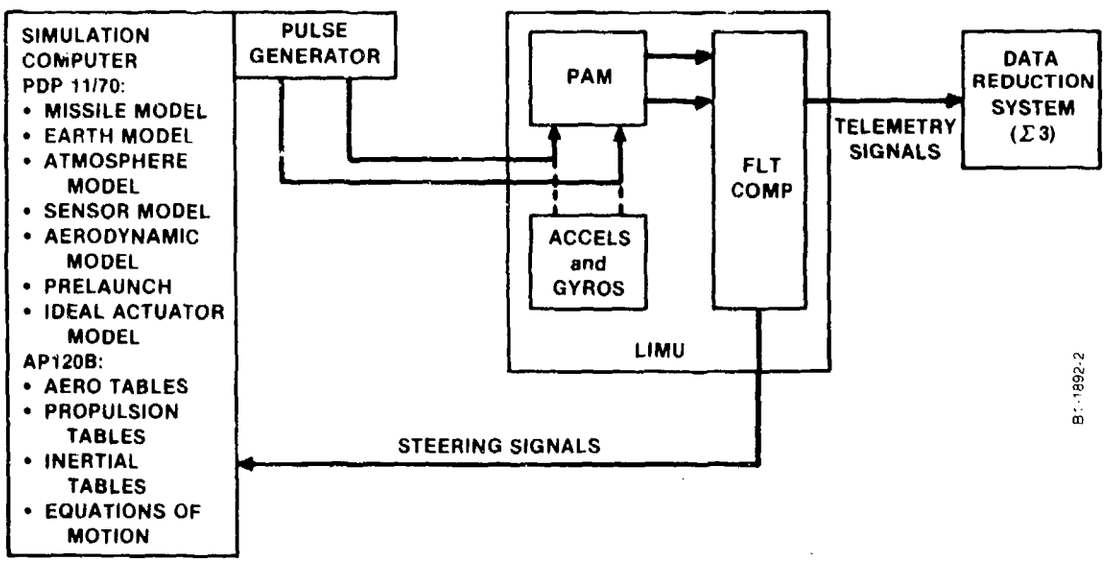

Figure 4 Assault Breaker Hardware-in-the-Loop Simulation LIMU - Only Configuration

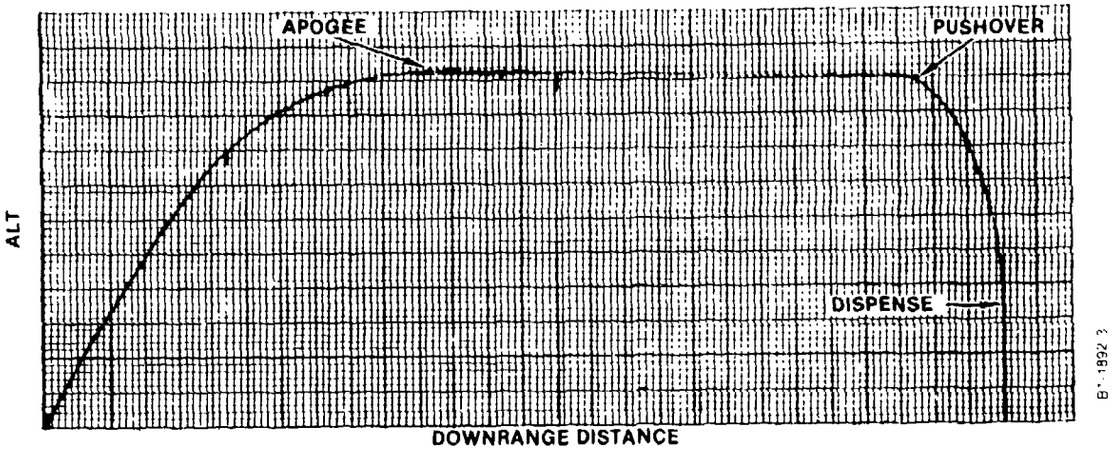

Figure 5 HWIL LIMU Only Configuration. Altitude vs Downrange Distance. Flight Condition 1 (Nominal).

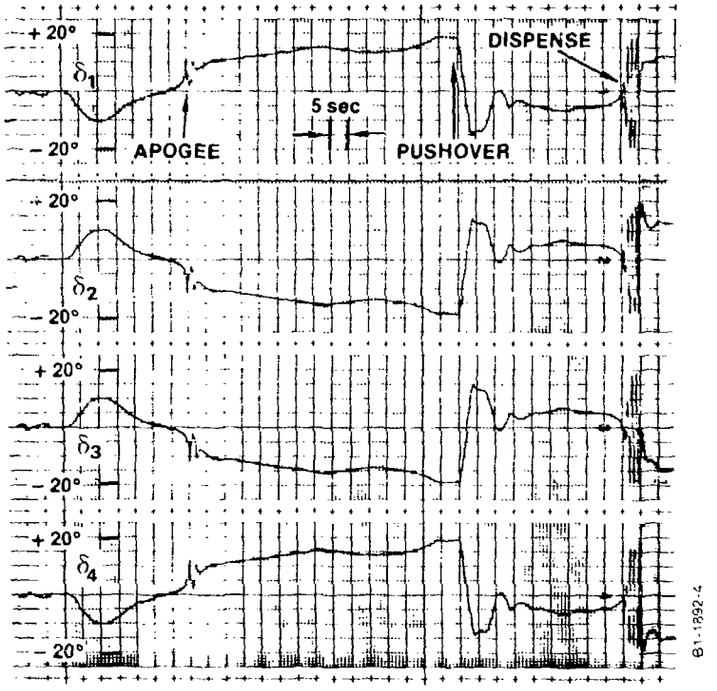

Figure 6 HWIL LIMU Only Configuration. Elevon Positions, Elevons 1-4 (Top to Bottom). Flight Condition 1 (Nominal).

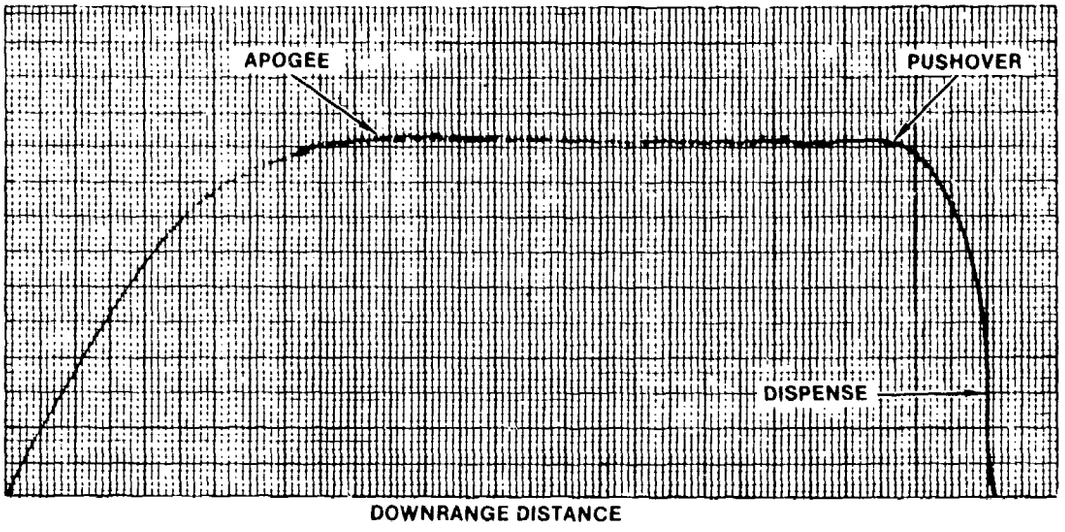

Figure 7 HWIL LIMU Only Configuration. Altitude vs Downrange Distance. Flight Condition 2 (Overshoot).

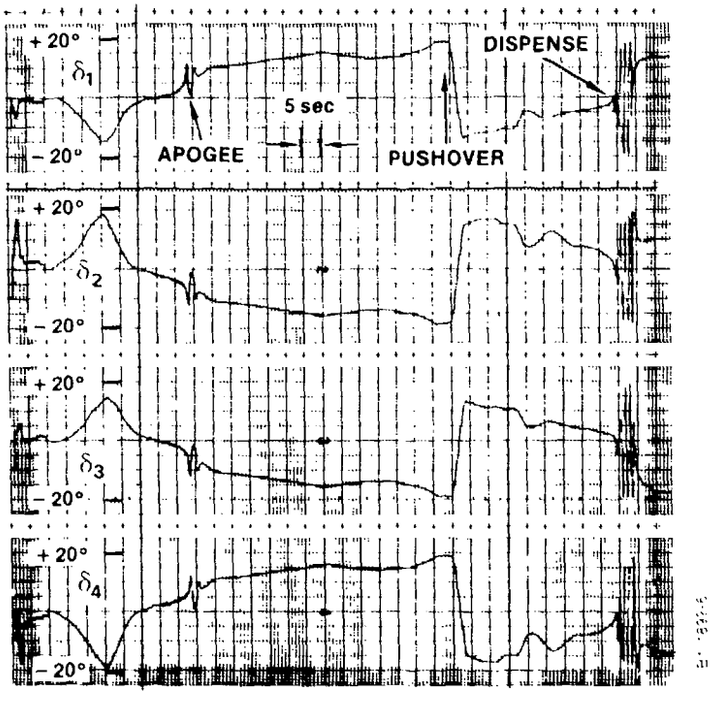

Figure 8 HWIL LIMU Only Configuration. Elevon Positions, Elevons 1-4 (Top to Bottom). Flight Condition 2 (Overshoot).

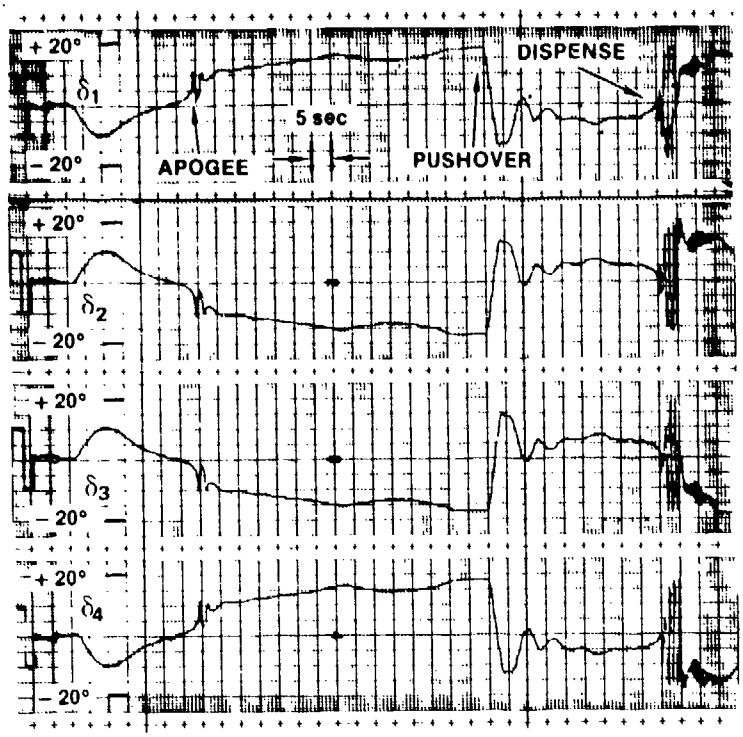

Figure 9 HWIL Complete Configuration (LIMU and Actuators). Elevon Positions, Elevons 1-4 (Top to Bottom). Flight Condition 1 (Nominal).

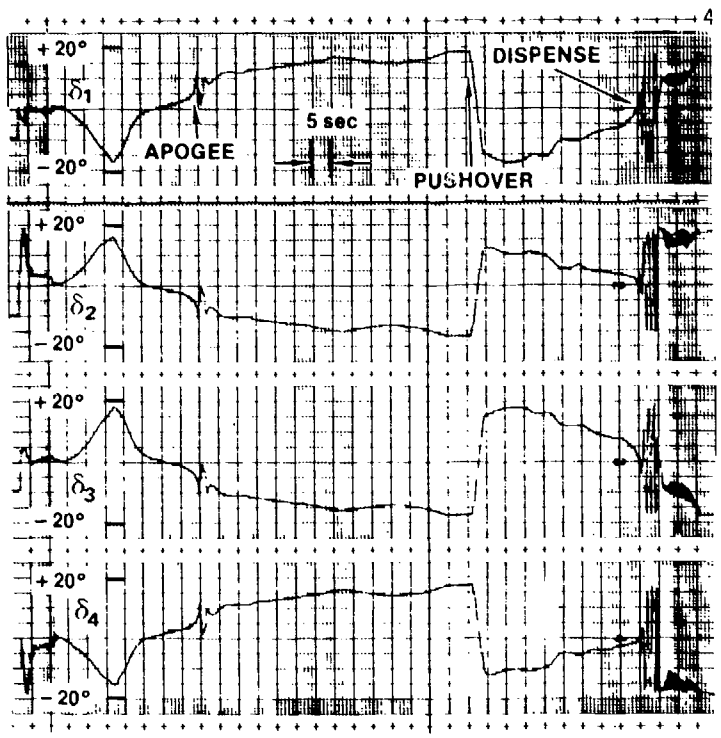

Figure 10 HWIL Complete Configuration (LIMU and Actuators). Elevon Positions, Elevons 1-4 (Top to Bottom). Flight Condition 2 (Overshoot).

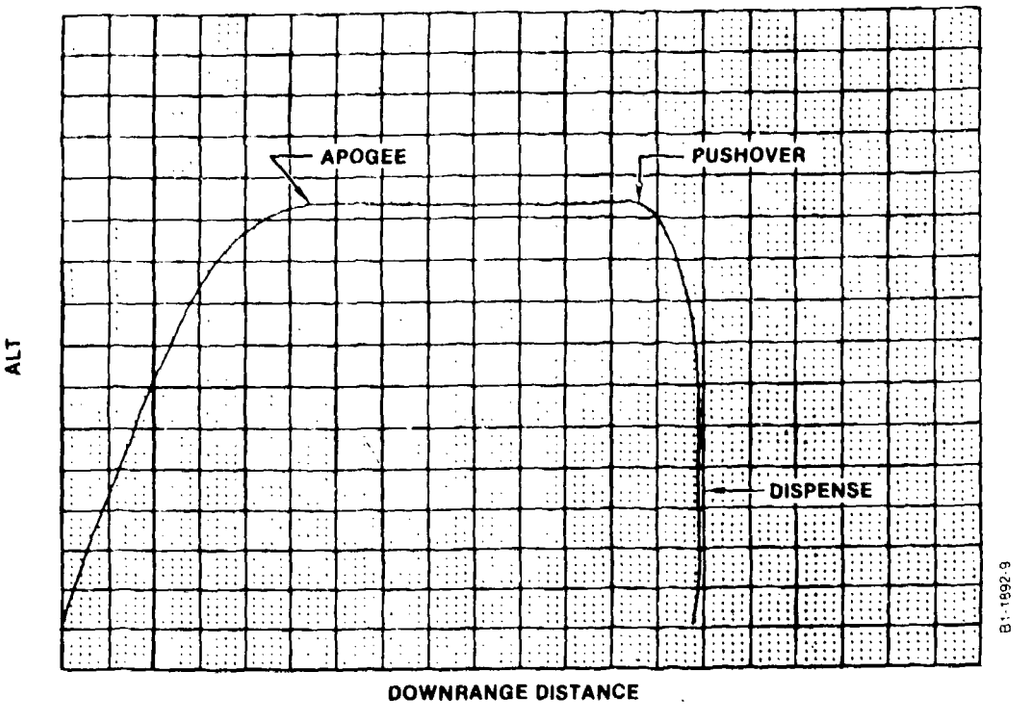

Figure 11 Flight Test Data. Altitude vs DownRange Distance.

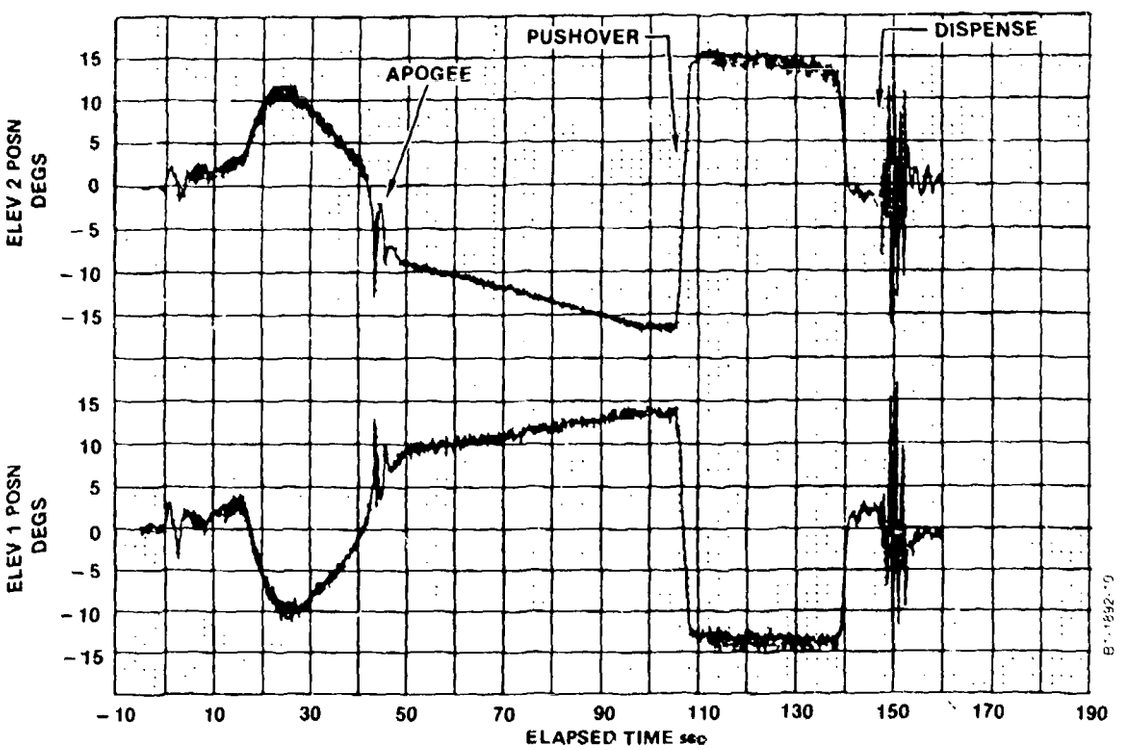

Figure 12 Flight Test Data. Elevon Position, Elevons 1, 2.

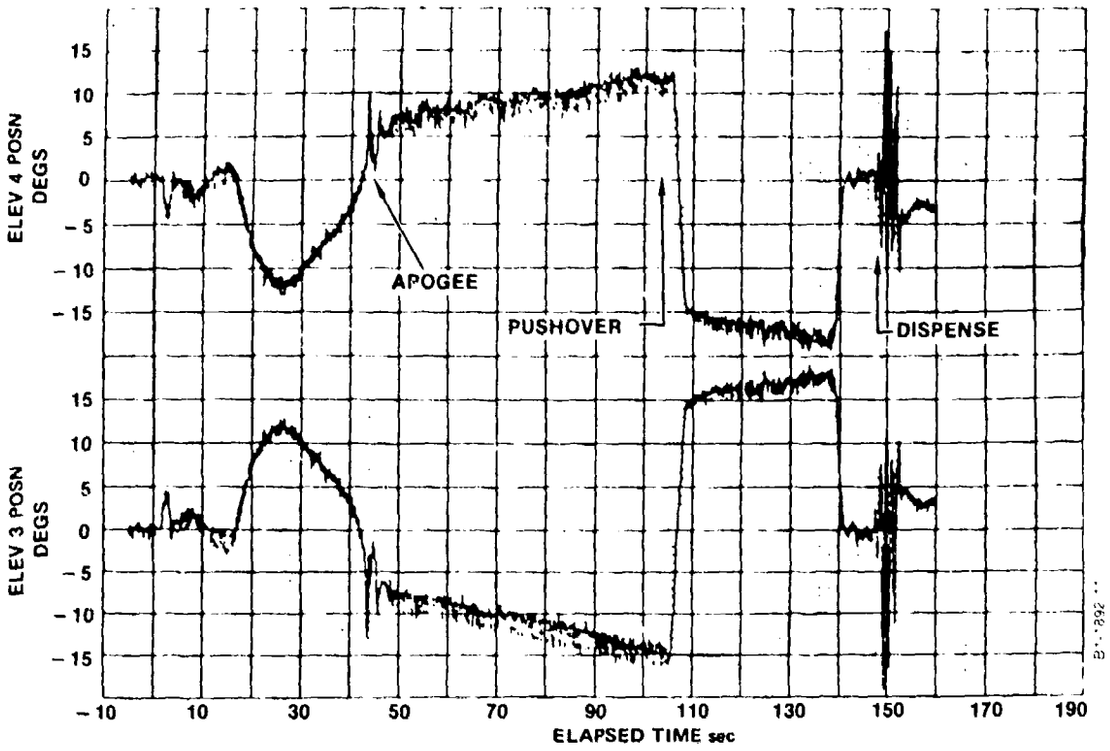

Figure 13 Flight Test Data. Elevon Position, Elevons 3, 4.

SUBMISSILE SKINS	TIME DIFFERENCE (ms) HWIL	SEQUENCER TEST SET	FTV-1
14	1629.1	1709	---
13	99.9	109	102
22	60.0	58	50
24	979.4	1038	1051
19	30.0	35	35
20	30.0	28	24
17	569.7	608	617
23	40.0	32	35
16	149.9	150	133

Figure 14. Timing of Ejection Pulses in HWIL Simulation, Sequencer Test Set, and During FTV-1.

BIOGRAPHY

Peter Schaar received his B.S. degree in Physics from Texas A&M University in 1959, after which he studied heat transfer in missile hydrogen and oxygen tanks for Douglas Aircraft Company. In 1964 he completed a M.S. degree in physics at California State University at Los Angeles and worked in acoustic radiation and scattering theory for Wyle Research Laboratories for a year. Beginning in 1965 he studied mathematics at the University of Texas at Austin and taught mathematics there and at El Centro College in Dallas. In 1977 he obtained the Ph.D degree in biophysics from the University of Texas Health Science Center in Dallas, following which he obtained a National Science Foundation Postdoctoral Fellowship at the Weizmann Institute in Israel, where he performed research in contractile proteins in non-muscle cells. During the last three years he has worked in the aerospace industry, most recently on the Assault Breaker Program for Vought Corporation. Other interests of Dr. Schaar include theater and movies, real estate investing, and landscape design.

TITLE: AN INTEGRATED PROGRAM FOR DEVELOPMENT OF A LASER GYRO IMU WITH SUB-ARC SECOND AZIMUTH FINDING CAPABILITY

AUTHORS: JIM MATTHEWS
M. GNESE
I. SMITH
T. TAYLOR

RAYTHEON, INCORPORATED
Sudbury, Massachusetts

R-7

TITLE: CONSTRUCTION OF APPROXIMATE ERROR BUDGETS FOR MULTIPLE-COMPONENT GUIDANCE SYSTEMS

AUTHOR: WILLIAM J. FITZPATRICK

LOXICON, INCORPORATED
San Pedro, California

R-4

CONSTRUCTION OF APPROXIMATE ERROR BUDGETS FOR MULTIPLE-COMPONENT GUIDANCE SYSTEMS

by

Dr. William J. Fitzpatrick

Logicon, Inc.
San Pedro, California 90733

ABSTRACT

Analyzing guidance and control contributors to impact error for strategic missile systems usually entails compiling detailed error budgets. In practice, the compilation frequently involves executing a Kalman-like error covariance computer program. While a single run can provide a projection of overall system performance for a given mission scenario, a sequence of such runs is necessary to generate an error budget. If the number of scenarios under investigation is itself large, the required computer time can be excessive.

Several special factorization methods have been developed to allow determining error budgets more efficiently. These methods in general aim to: 1) increase numeric stability, 2) reduce computer memory and time burdens, and 3) yield more usable information per run. Nonetheless, the inherent nonlinear nature of optimal-filter error covariance equations still presents a significant problem to the error analyst, especially if the candidate systems under investigation are previously untested, since little a priori knowledge of significant error sources may be available. In such instances, a detailed investigation of all possible error drivers is vital.

This paper presents an alternative to the standard approach for constructing an error budget. It develops a method of decomposing a time-varying state covariance matrix that allows compiling detailed error information within a single run. The design of a computer program that determines error contributions due to individual initial state uncertainties, measurement noise, and state noise is presented. Regions of stability and applicability are defined.

The procedures are applied to the problem of defining guidance system requirements for candidate weapon systems incorporating maneuvering reentry vehicles. A number of top-level components affect the performance of such systems; these include boosters, reentry vehicle inertial measurement units, navigation update systems, and reentry trajectories. When variations in the number and quality of external updates are also taken into account, the list of possible mission scenarios becomes lengthy. Results are outlined here for selected scenarios, and the efficiency and usefulness of the technique are discussed in conjunction with this illustration.

1. INTRODUCTION

Analysts often compute error budgets for guidance and control systems with Kalman-like error covariance computer programs. The program is exercised many times to generate the error budget. This paper presents a variation to this traditional approach. Features of the alternate method include:

1) Computer Resources

   - o Computation of the entire error budget with a single program execution
   - o Significantly reduced execution time
   - o A modest increase in required memory
   - o Substantial cost reduction for multierror systems

2) Performance

   - o The single execution results in fewer user input errors
   - o Evaluation of many mission scenarios is possible
   - o Convenient presentation of data facilitates analysis
   - o Data can be extrapolated to off-nominal initial conditions, within limits

3) Applications

   - o Prediction of system performance
   - o Tradeoffs between candidate subsystems
   - o Design of suboptimal filters
   - o Resource allocation for instrument design

The method was used to evaluate potential reentry vehicle inertial measurement units during the Guidance System Requirements Study (GSRS). The last section of this paper applies the method to GSRS.

2. ESTIMATION PROBLEM

Consider the dynamic system defined by the linear differential equation:

$$\dot{\underline{x}}(t) = A(t)\underline{x}(t) + B(t)\underline{y} + \underline{w}(t) \qquad (1)$$

where

$\underline{x}$ = n-dimensional state vector

$\underline{y}$ = k-dimensional vector of constant parameters

A,B = matrices determined by the system

$\underline{w}$ = n-dimensional random disturbance vector

Further, suppose that at discrete times t_i there are measurements linearly related to the state by:

$$\underline{z}(t_i) = C(t_i)\underline{x}(t_i) + D(t_i)\underline{b} + \underline{\nu}(t_i) \tag{2}$$

where

$\underline{z}$ = m-dimensional measurement vector

$\underline{b}$ = ℓ-dimensional vector of constant parameters

C,D = matrices determined by the system

$\underline{\nu}$ = m-dimensional random sequence

The model of eqs. (1) and (2) may be rewritten as:

$$\begin{bmatrix} \dot{\underline{x}} \\ \dot{\underline{y}} \\ \dot{\underline{b}} \end{bmatrix} = \begin{bmatrix} A & B & 0 \\ 0 & 0 & 0 \\ 0 & 0 & 0 \end{bmatrix} \begin{bmatrix} \underline{x} \\ \underline{y} \\ \underline{b} \end{bmatrix} + \begin{bmatrix} \underline{w} \\ 0 \\ 0 \end{bmatrix} \tag{3}$$

$$\underline{z}_i = \begin{bmatrix} C_i & 0 & D_i \end{bmatrix} \begin{bmatrix} \underline{x} \\ \underline{y} \\ \underline{b} \end{bmatrix} + \underline{\nu}_i \tag{4}$$

The subscript i denotes the related quantity at time t_i. Eqs. (3) and (4) are of the form:

$$\dot{\underline{X}} = F\underline{X} + \underline{\omega} \tag{5}$$

$$\underline{Z}_i = H_i\underline{X}_i + \underline{\nu}_i \tag{6}$$

The state vector propagates from t_{i-1} to t_i by:

$$\underline{X}_i = \Phi_{i-1}\underline{X}_{i-1} + \underline{w}_{i-1} \tag{7}$$

where the state transition matrix satisfies the initial value problem:

$$\dot{\Phi} = F\Phi, \qquad \Phi(t_{i-1},t_i) = \Phi_{i-1}$$

Finally, assume that $\underline{w}$ and $\underline{\nu}$ are uncorrelated between distinct times. A standard Kalman filter mechanization solves the optimal estimation problem defined by eqs. (6) and (7). Following a measurement update, the state estimate, $\hat{\underline{X}}$, satisfies:

$$\hat{\underline{X}}_i^- = \Phi_{i-1}\,\hat{\underline{X}}_{i-1}^+ \tag{8a}$$

$$P_i^- = \Phi_{i-1}\,P_{i-1}^+\,\Phi_{i-1}^T + Q_{i-1} \tag{8b}$$

$$K_i = P_i^-\,H_i^T\,(H_i\,P_i^-\,H_i^T + R_i)^{-1} \tag{8c}$$

$$P_i^+ = P_i^- - K_i\,H_i\,P_i^- \tag{8d}$$

$$\hat{\underline{X}}_i^+ = \hat{X}_i^- + K_i\,\underline{Z}_i - H_i\,\hat{\underline{X}}_i^- \tag{8e}$$

where

$$Q_{i-1} = E(\underline{w}_{i-1}\,\underline{w}_{i-1}^T), \text{ state noise}$$

$$R_i = E(\underline{\nu}_i\,\underline{\nu}_i^T), \text{ measurement noise.}$$

The subscripts - and + denote before and after the measurements, respectively. The error covariance matrix, P_i of eq. (8), is a measure of the accuracy of the estimate $\hat{X}_i$. It follows from eq. (8) that the state uncertainties at time t_i are functions of P_0, the initial uncertainty of the state. We are interested in determining what effect changes in the nominal uncertainties of the parameter states $\underline{y}$ have upon the final uncertainties of the dynamic states $\underline{x}$.

3. SOLUTIONS

Assume that the dynamic states, state parameters and measurement parameters are initially uncorrelated. From the preceding discussions, P_0 may be partitioned in block diagonal form as:

$$P_0 = \begin{bmatrix} P_0^x & 0 & 0 \\ 0 & P_0^y & 0 \\ 0 & 0 & P_0^b \end{bmatrix}$$

If the parameters y are initially uncorrelated, then P_0^y may also be written as a diagonal matrix:

$$\tilde{P}_0^y = \text{diag}(p_0^1, p_0^2, \ldots, \tilde{p}_0^j, \ldots, p_0^k) \quad .$$

The methods described below can be generalized to correlated states. In the general case, diagonal blocks replace the single diagonal elements of P_0^y.

Method A

In theory, eq. (8) must be exercised many times to separate the effects of individual parameters. Set:

$$\tilde{P}_0^y = \text{diag}(p_0^1, p_0^2, \ldots, \tilde{p}_0^j, \ldots, p_0^k),$$

then propagate $\tilde{P}$ by eq. (8). The difference between P_i and $\tilde{P}_i$ is solely attributable to the change in p_0^j. The result is exact. However, a different perturbation of p_0^j requires a different run. More importantly, this procedure must be repeated for each parameter. For k large, the procedure becomes unwieldy.

Method B

Eq. (8d) is equivalent to:

$$P_i^+ = (I - K_i H_i) P_i^- (I - K_i H_i)^T + K_i R_i K_i^T \qquad (9)$$

An error budget is computed as follows (Reference 1):

1) Exercise eqs. (8b), (8c) and (8d) to generate a set of filter gains, K_i.
2) Set $P_0^y = \text{diag}(0, 0, \ldots, p_0^j, \ldots, 0)$.
3) Set all other entries of P_0, as well as Q and R, equal to zero.
4) Propagate P_i, using eqs. (8b) and (9), with K_i, P_0, Q_i and R_i as determined by steps 1 - 3.
5) Repeat steps 2 - 4 for each of the k parameters.

The filter gains are only computed once; eqs. (8b) and (9) are exercised k times. The value of P_i which results from step 4 depends solely on P_0^j .

Method C

Eq. (8b), (8c) and (8d) may be decomposed as follows:

$$P_i^+ = B_0 P_0 B_0^T + \sum_{\ell=1}^{i} C_\ell R_\ell C_\ell + \sum_{\ell=1}^{i} A_\ell Q_\ell A_\ell^T \qquad (10)$$

where

$$A_\ell = \begin{cases} (I - K_i H_i) \prod_{j=i}^{\ell} \Phi_j (I - K_{j-1} H_{j-1}), & 1 \le \ell \le i-1 \\ I - K_i H_i, & \ell = i \end{cases}$$

$$B_\ell = \begin{cases} A_{\ell+1} \Phi_\ell , & 0 \le \ell \le i-1 \\ I \quad \text{(identity matrix)}, & \ell = i \end{cases}$$

$$C_\ell = B_\ell K_\ell , \quad 1 \le \ell \le i$$

To prove eq. (10), first recall eq. (9). For i = 1,

$$P_1^- = \Phi_0 P_0 \Phi_0^T + Q_0$$

and

$$P_1^+ = (I - K_1 H_1) P_1^- (I - K_1 H_1)^T + K_1 R_1 K_1^T$$

$$P_1^+ = (I - K_1 H_1)\Phi_0 P_0 \Phi_0^T (I - K_1 H_1)^T + K_1 R_1 K_1^T + (I - K_1 H_1) Q_0 (I - K_1 H_1)^T$$

Let:

$$A_1 = I - K_1 H_1$$

$$B_0 = A_1 \Phi_0$$

$$B_1 = I$$

$$C_1 = B_1 K_1$$

Then eq. (10) is true for i = 1. For i > 1, eq. (10) follows from induction. An error measure is computed as follows:

1) Propagate the A matrix using baseline values of P_0, Q, and R.

2) Choose P_0 as in steps 2 - 4 of method B.

3) Compute the quantity $B_0 P_0 B_0^T$ for each of the k parameters. For the jth parameter, this quantity depends only on p_0^j and the jth column of B_0.

Note that all of the information needed to evaluate the jth error parameter is contained in the jth column of B_0. A single propagation yields this matrix.

Useful information is obtained about each parameter from both methods B and C. The data obtained by these methods do not directly answer the question at hand, however. The gain matrices, K_i, are determined from the full set of baseline values for P_0, Q, and R. Thus these techniques provide a component error breakdown only in a neighborhood of the nominal conditions. If P_0 changes, the gains also change. The size of the neighborhood is problem dependent. For the application discussed in the next section, method C works well (as would B). Table 2 in Section 4, which compares the accuracy of method C with method A, supports this statement. Reduced computer time is the real advantage of method C.

The important features of each method are summarized in Table 1.

Table 1. Method Comparison

Parameter	A	B	C
accuracy	exact K_i	nominal K_i	nominal K_i
computer time	k runs	1 gain run, k covariance runs	1 run
computer memory	nominal	nominal plus storage of gain file	nominal plus B_0

Computer time versus accuracy is the major consideration here. The choice of method depends on the size and complexity of the problem. As mentioned, the next section describes a partricular example, and shows why method C was an appropriate choice for that example. Large time savings were achieved, yet little accuracy was lost.

4. GSRS APPLICATION

Several factors contribute to the total accuracy achievable by ICBM weapon systems that incorporate maneuvering reentry vehicles (MaRVs). These include the reentry vehicle navigation instruments, navigation update systems, booster performance, and reentry maneuvers. High accuracy is achieved at the expense of increased complexity in one or more of these areas. To determine the degree to which each of these areas influences total weapon system accuracy, the Guidance System Requirements Study (GSRS) was undertaken.

The GSRS objective was to determine by analysis and simulation:

1) Performance requirements for inertial measurement guidance components and guidance update systems

2) Weapon system performance sensitivies to changes in MaRV subsystem performance requirements

Several classes of MaRV guidance systems and MaRV mission concepts were investigated. Key analysis parameters included weapon system accuracy, booster performance, reentry environments, reentry trajectory, and guidance system update type and quality. The remainder of this paper describes selected study parameters, reviews relevant facts from linear estimation theory, and describes analysis techniques and tools used within the course of the study.

GSRS developed and executed simulations of operational versions of Air Force maneuvering reentry vehicles. The study focused on determining the total weapon system performance of several MaRV mission concepts, and on determining the sensitivity of this performance to specific inertial navigation system error sources. Figure 1 identifies the areas studied in each of four categories: RIMU, booster, reentry maneuvers, and update systems.

Generic models of three reentry, inertial, measurement units (RIMU) were considered: four gimbal, strapdown, and roll isolated. The four-gimbal RIMU is a completely inertial platform with three single-degree-of-freedom rate-intergrating gyros and three linear accelerometers; all six instruments are mounted on the stabilized platform. The strapdown navigation system uses single-axis integrating accelerometers to measure incremental sensed velocity and single-axis gyros to provide incremental attitude measurements. The roll-isolated RIMU is a hybrid IMU in which the platform axes along the pitch and yaw directions are strapdown and the roll axis is gimbaled. Two two-degree-of-freedom gyros and three single-degree-of-freedom accelerometers are mounted on the platform.

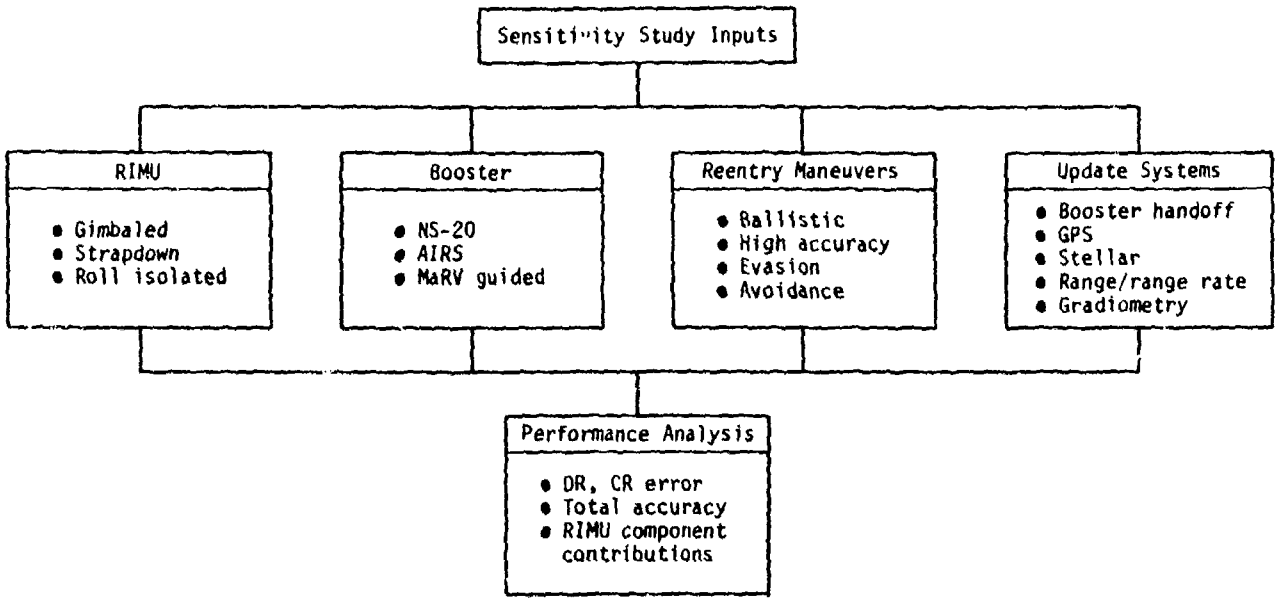

Figure 1. Sensitivity Analyses Schematic

Three booster models were studied: MMIII, MX, and MaRV guided. The IMU used in the MMIII booster is the NS-20 guidance set. The NS-20 platform is aligned in the silo to the guidance coordinate system, and this alignment is G6B4 maintained in flight by two GP4 dual-axis gyros. The sensed acceleration of the vehicle is measured by three PIGA MOD G accelerometers mounted to the platform.

The IMU used in the MX booster is the advanced inertial reference sphere (AIRS). AIRS is an all-attitude floated-inertial platform with no gimbal constraints. It contains three TGG (third-generation gyro) integrating gyroscopes and three SFIR-J (specific-force integrating receiver) accelerometers. The TGGs, as well as the SFIR-Js, are mounted mutually orthogonal. The input axes of the SFIR-Js lie nominally along the respective platform axes.

The third booster alternative considered the performance of weapon systems using the RIMUs as the sole source of navigation and guidance data. This alternative included a scheme for pooling and filtering navigation data from multiple MaRVs.

For all simulated missions the reentry vehicle was assumed to be deployed from a booster vehicle flying an ICBM trajectory with range at impact of 5500 nmi. The booster is a three-stage vehicle plus a post-boost vehicle that thrusts to the proper deployment point for each MaRV, orients to the desired reentry attitude, and deploys the MaRV. The MaRV is spun up in this attitude to 2 RPS, coasts on a ballistic patch to the pierce point, reenters the

atmosphere ballistically while spinning, despins at despin altitude, and then commences maneuvers according to the mission type and the target to be achieved.

Guidance system performance was investigated for reentry missions having the following goals:

1) Enhanced Weapons System Accuracy: Reduce weapon system impact error by preferential alignment of weapon system error covariance and terminal velocity vector.

2) Evasion: Avoid negation by defensive interceptors.

3) Low Collateral Damage: Provide as low a CEP as possible.

4) Avoidance: Avoid detection by defensive systems by quickly achieving a low altitude.

Eight reentry trajectories were defined to accomplish the different reentry missions, and a ballistic reentry trajectory was also determined.

Finally, the external aiding subsystems considered for GSRS included booster handoffs, GPS, range-rate sensors (exoatmospheric and endoatmospheric), stellar sensors, and gradiometers. Each of these aids was modeled as employing optimal data processing techniques to estimate the position, velocity, and/or alignment of the reentry vehicle.

The differential equation of motion solved by navigation is:

$$\ddot{\underline{P}} = \dot{\underline{V}} = \underline{A}_S - \frac{GM}{|\underline{P}|^3}\underline{P}$$

where

$\underline{P}$ = position vector

$\underline{V}$ = velocity vector

$\underline{A}_S$ = sensed acceleration vector

GM = earth's gravity constant

The dynamics of this system of nonlinear equations is not suited to linear estimation techniques. Instead, we use the set of linear equations obtained by perturbing the dynamical system about a nominal value.

Let:

$$\underline{A}_S = \underline{A}_S^A + \delta \underline{A}_S$$

$$\underline{V} = \underline{V}^A + \delta \underline{V}$$

$$\underline{P} = \underline{P}^A + \delta \underline{P}$$

where superscript A signifies the actual value (assuming no errors) and δ represents an error term about the actual value.

Therefore:

$$\dot{\underline{V}}^A + \delta \dot{\underline{V}} = A_S^A + \delta A_S - \frac{GM}{|\underline{P}^A|^3} \underline{P}^A - \frac{GM}{|\underline{P}^A|^3} \underline{P} + \frac{3GM}{|\underline{P}^A|^5} (\delta \underline{P} \cdot \underline{P}^A)\underline{P}^A$$

Subtracting out the actual terms:

$$\delta \dot{\underline{V}} = \delta \underline{A}_S - \frac{GM}{|\underline{P}^A|^3} \delta \underline{P} + \frac{3GM}{|\underline{P}^A|^5} (\delta \underline{P} \cdot \underline{P}^A)\underline{P}^A$$

The term $\underline{A}_S$ is due to alignment, platform, and accelerometer errors:

$$\delta \underline{A}_S = \delta \underline{\phi} \times \underline{A}_S + \delta \underline{A}_P + \delta \underline{A}_A$$

where

$\delta \underline{\phi}$ = platform alignment errors

$\delta \underline{A}_P$ = sensed acceleration errors due to platform errors

$\delta \underline{A}_A$ = sensed acceleration errors due to accelerometer errors

The $\delta \underline{A}_P$ term is modeled as a function of the sensed acceleration and platform errors:

$$(\delta A_P)_i = f_i(\underline{A}_S, \underline{E}_P), \quad i = X, Y, Z$$

Similarly, $\delta \underline{A}_A$ can be written as:

$$(\delta A_A)_i = g_i(A_S, E_A), \quad i = X, Y, Z$$

$\underline{E}_P$ and $\underline{E}_A$ represent constant RIMU platform and accelerometer errors.

The sensed acceleration errors can therefore be expressed as:

$$\delta \underline{A}_S = \delta \underline{\phi} \times \underline{A}_S + f\, \underline{E}_P + g\, \underline{E}_A$$

where f and g are matrices given by:

$$f = \frac{\partial \underline{A}_S}{\partial \underline{E}_P}$$

$$g = \frac{\partial \underline{A}_S}{\partial \underline{E}_A}$$

Writing the previous equation of motion in terms of the individual components, the errors in RIMU position and velocity propagate in time by:

$$\delta \dot{P}_i = \delta V_i \qquad i = X, Y, Z \tag{11}$$

$$\delta \dot{V}_X = (\alpha + \beta P_X^2)\,\delta P_X + \beta P_X P_Y \delta P_Y + \beta P_X P_Z \delta P_Z + A_{SZ}\delta\phi_Y - A_{SY}\delta\phi_Z + \sum_j f_{Xj}(E_p)_j + \sum_j g_{Xj}(E_A)_j$$

$$\delta \dot{V}_Y = \beta P_Y P_X \delta P_X + (\alpha + \beta P_Y^2)\,\delta P_Y + \beta P_Y P_Z \delta P_Z + A_{SX}\delta\phi_Z - A_{SZ}\delta\phi_X + \sum_j f_{Yj}(E_p)_j + \sum_j g_{Yj}(E_A)_j$$

$$\delta \dot{V}_Z = \beta P_Z P_X \delta P_X + \beta P_Z P_Y \delta P_Y + (\alpha + \beta P_Z^2)\delta P_Z + A_{SY}\delta\phi_X - A_{SX}\delta\phi_Y + \sum_j f_{Zj}(E_p)_j + \sum_j g_{Zj}(E_A)_j$$

where

$$\alpha = \frac{-GM}{|\underline{P}|^3}$$

$$\beta = \frac{3GM}{|\underline{P}|^5}$$

The alignment in the above equations is expressed in the same coordinate system as the position and velocity errors. By means of an orthogonal coordinate transformation, the alignment errors can be easily expressed in platform coordinates even if these differ from the position and velocity coordinates.

The RIMU platform alignment errors are modeled as functions of the sensed acceleration and the gyro errors:

$$\delta\phi_i = h_i\,(\underline{A}_S, \underline{E}_G) \qquad i = X, Y, Z \tag{12}$$

$\underline{E}_G$ represents the constant RIMU gyro errors. Also, each update system has associated errors, $\underline{E}_{AID}$. In the notation of Section 2,

$$\underline{x} = \begin{bmatrix} \delta \underline{P} \\ \delta \underline{V} \\ \delta \underline{\Phi} \end{bmatrix}$$

$$\underline{y} = \begin{bmatrix} \underline{E}_P \\ \underline{E}_A \\ \underline{E}_G \end{bmatrix}$$

$$\underline{b} = \underline{E}_{AID}$$

The matrix F is defined by eqs. (11) and (12). The measurement matrix is determined by the choice of update system.

To calculate system accuracy, a linear system error analysis was performed. A Kalman filter scheme was employed to accommodate the various types of external measurements. A flow diagram indicating the computer programs used in the system performance evaluation is shown in Figure 2.

The modular simulation system (MSS) generates the boost and reentry trajectories, which are described in Section 2. The linear error analysis program (LEAP) generates the RIMU transition matrices for the boost and reentry portions of flight. The free-flight error analysis program (FEAP) determines the RIMU free-flight transition matrix for the strapdown and roll-isolated systems. FEAP employs a spherical harmonic expansion of the earth's gravitational field to calculate vehicle position and velocity. Several support programs generate the measurement matrices. The system error analysis program (SEAP) uses the Kalman filter formulation to evaluate performance. Covariance matrices at the points of interest are output by SEAP. The covariance matrices describe the system performance.

The final covariance matrix, P_f, is propagated using eq. (8). The primary figure of merit used to judge system performance is CEP. If Λ_S represents the submatrix of the covariance matrix that contains position and velocity errors $\delta \underline{P}$ and $\delta \underline{V}$, then this covariance is mapped into a downrange, cross-range, time-coordinate frame by an orthogonal rotation followed by a projection of the altitude errors along the nominal impact velocity, viz:

$$\frac{\partial I}{\partial S} = \left[\begin{array}{ccc:c} 1 & 0 & -\frac{V_D}{V_H} & \\ 0 & 1 & -\frac{V_C}{V_H} & 0_{3x3} \\ 0 & 0 & \frac{1}{V_H} & \end{array}\right] \left[\begin{array}{c:c} T & 0 \\ \hline 0 & T \end{array}\right]$$

$$\Lambda_I = \frac{\partial I}{\partial_S} \Lambda_S \frac{\partial I}{\partial S}^T$$

where

$\frac{\partial I}{\partial S}$ is the mapping of state errors into impact coordinates (downrange, crossrange, and time)

V_D, V_C, V_H are the nominal velocity components along downrange, crossrange, and altitude

T is the orthogonal 3x3 rotation of navigation coordinates into downrange, crossrange, and altitude

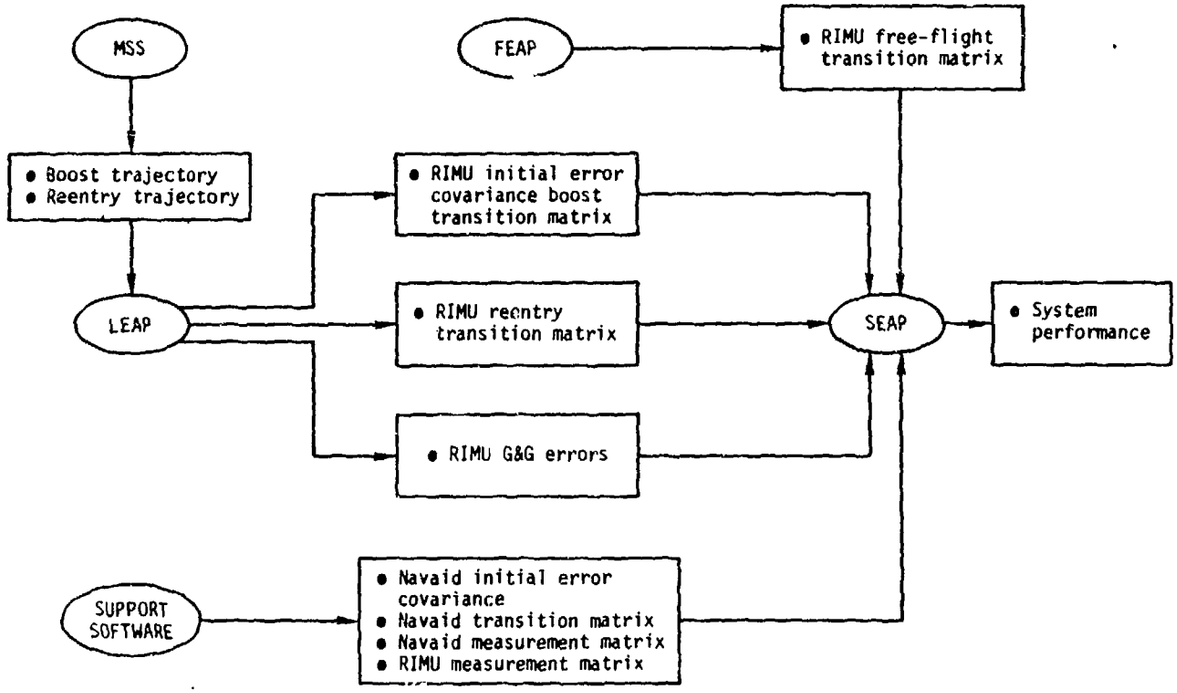

Figure 2. Program Organization

The CEP can be approximately calculated as:

$$CEP = 0.59\left(\sqrt{\Lambda_{I_{11}}} + \sqrt{\Lambda_{I_{22}}}\right)$$

where

$\Lambda_{I_{ij}}$ is the element of Λ_I in the ith row of the jth column

This formula assumes no bias in impact.

There are 350 feasible combinations of the four major mission parameters defined at the beginning of this section. For each combination, it was necessary to determine the sensitivity of weapon system accuracy to the individual RIMU error sources. A typical case consisted of 100 such error sources. Both methods A and B of Section 3 would have resulted in 35,000 computer runs. This number was unacceptable from both a time and logistic standpoint. Method C was the primary technique used for the study.

Method C is valid as a sensitivity analysis to the extent that filter gains are unaffected by changes in the initial state covariance matrix. Determination of the gain stability region requires that gains be recomputed many times for each error source of interest. As noted, this is not practical. Several additional covariance propagations were done, however, as a check on the larger error drivers. Table 2 shows sample results of these checks.

To provide an estimate of the region of linearity, system errors were evaluated for certain off-nominal conditions. Selected components of the initial state covariance matrix were increased by a factor of 100 (a tenfold increase in uncertainty), and the final covariance was propagated according to eq. (8). Normalized weapon system CEPs for these perturbed initial conditions are shown in Table 1 under the heading "filter simulation." To extrapolate from nominal conditions, it was assumed that a tenfold increase in the uncertainty of a group of IMU error drivers would cause a like increase in the CEP figure attributable to these errors. It was further assumed that no other error source contributions would be affected by the perturbation. A new RSS total was then calculated; this number is shown in the column "linear extrapolation."

Table 2 contains the largest percentage differences observed during the study. Percentage differences for less significant error sources were much less for all trajectories. In light of the large perturbations, the extrapolated results did a good job of predicting true filter performance.

The information obtained by method C provides a useful indicator of both major and minor error contributors. The data shows component error contributions to weapon system error. This is useful in the initial design of suboptimal filters. Extrapolated data shows which instrument design improvements will be most beneficial.

Table 2. Extrapolation-Filter Comparison for Normalized Weapon System CEP, Four-Gimbal RIMU, and MX Implicit Update

Trajectory	Linear Extrapolation	Filter Simulation	% Difference
Fixed Gyro Drift Perturbation*			
A	.269	.284	5
B	.359	.394	9
C	.976	.793	23
D	.924	.909	2
E	2.020	1.726	17
F	.771	.780	1
G	.649	.628	3
H	2.593	2.446	6
I	.439	.428	3
Platform Compliance Perturbation*			
A	.262	.267	2
B	.348	.357	3
C	.867	.967	10
D	.991	1.038	5
E	3.246	3.695	12
F	.580	.633	8
G	.594	.681	13
H	1.755	2.021	13
I	.357	.359	0.4

*Uncertainty increase of 100% from nominal

ACKNOWLEDGEMENT

The work described in this paper was performed for the Ballistic Missile Office under Contract F04701-78-C-0045. The author wishes to express his appreciation to Lt. Col. Melvin A. Nosal, Chief Concepts and Technology Plans Division (SYC), and his organization for guidance and support. In addition, the technical support provided by Robert E. Brooks and David P. Stewart of Logicon is greatly appreciated.

REFERENCE

1) "Applied Optimal Estimation," A. Gelb, ed., MIT Press, 1974.